DISS. ETH NO. 26371

A SCALED BOUNDARY APPROACH TO FORWARD AND INVERSE PROBLEMS

With Applications in Computational Fracture Mechanics,

Damage Localization and Topology Optimization

A thesis submitted to attain the degree of

DOCTOR OF SCIENCES of ETH ZURICH
(Dr. sc. ETH Zurich)

presented by

Adrian Walter Egger
MSc ETH Civil Eng, ETH Zurich
born on 30.03.1987
citizen of
St. Gallen-Tablat, SG and Canada

accepted on the recommendation of

Prof. Dr. Eleni Chatzi (ETH Zurich, Zurich, Examiner)
Prof. Dr. Savvas Triantafyllou (University of Nottingham, Nottingham, Co-examiner)
Prof. Dr. Chongmin Song (University of New South Wales, Sydney, Co-examiner)

2019

Abstract

The demand for sustainable design in, e.g., the aerospace, automotive and construction industries has lead to the development of lighter, stronger and more resilient structures, spawning the need to guard against failure processes by leveraging robust, economical and high-fidelity numerical simulations.

Since its inception, the finite element method (FEM) has been advanced to handle a multitude of structural analysis problems ranging from linear to nonlinear, static to dynamic, fracture and contact problems among others. Within the context of fracture mechanics, it has been demonstrated that modeling of damage-related phenomena such as crack initiation, crack propagation and delamination can successfully be accomplished by means of the FEM. Nonetheless, various undesirable characteristics persist, which render this method computationally prohibitive for more involved analyses. As a result, alternative methods have been pursued; the scaled boundary finite element method (SBFEM), is a little explored, yet highly capable alternative within the domain of linear elastic fracture mechanics (LEFM). Hence, the objective of this thesis is to accelerate computationally intensive numerical problems harnessing the merits and further extending the capabilities of the SBFEM to a wide class of forward and inverse problems, specifically with applications in computational fracture mechanics, damage localization and topology optimization.

The increasing importance of sustainability implies the prudent use of existing resources, such that efficient computation schemes are sought. This thesis proposes several novel schemes to accomplish this goal. The Hamiltonian Schur decomposition is first adopted, to reverse the computational toll incurred during an SBFEM analysis, due to the linearization of the underlying quadratic eigen-problem. Further, an efficient recovery based error estimator is proposed, which additionally permits calculating the generalized stress intensity factors (gSIFs) at increased accuracy, using fewer degrees of freedom (DOF). The use of linear quadtree (QT) meshes, pioneered by previous authors, to overcome SBFEM's unique meshing requirements, can lead to reduced accuracy in calculated gSIFs for crack propagation problems. A method of internally elevating the approximation space of a crack tip element is proposed, which is shown to greatly improve the accuracy with which gSIFs are calculated on highly coarse QT meshes. These approaches are exploited to develop the multiscale scaled boundary finite element method (MSBFEM), which harnesses the SBFEM to incorporate fracture on the fine scale and the enhanced multiscale finite element method (EMsFEM) to construct a coarse scale representation, where the governing equations are solved at a reduced computational cost. The newly developed MSBFEM is then extended to a highly efficient crack propagation scheme, which resolves only regions directly surrounding the crack tip, and incorporates the remaining domain via coarse scale macro-elements. In doing so, the amount of DOFs present during analysis are drastically reduced, while the crack path is still accurately captured.

These novel insights in accelerating the forward problem are then applied to inverse analyses. Due to its domain specific advantage, SBFEM is subsequently applied to damage localization schemes. Taking advantage of the parallel nature with which heuristic algorithms approach damage localization, combined with precomputation of the undamaged domain by SBFEM and updating the effects of varying crack candidates by reanalysis techniques, a highly efficient and effective scheme is devised to accelerate damage localization analyses to near real-time levels.

Topology optimization (TO), which similarly to damage localization, is often marred by the repeated solution of an expensive forward problem, stands to benefit from efficient solvers. Automated adaptive analysis-ready meshes are achieved by harnessing image compression techniques. The proposed drop-in replacement for the forward solver, reduces the amount of DOF during present during analysis by over an order of magnitude. This approach is successfully extended to 3D problems.

Kurzfassung

Die Nachfrage nach nachhaltigem Design in z.B. der Luft- Raumfahrt-, Automobil sowie der Bauindustrie haben zur Entwicklung leichterer, beständiger und belastbarerer Strukturen geführt, deren Simulation mittels robuster, wirtschaftlicher und präziser numerischer Simulationen gewährleist werden müssen.

Seit ihrer Einführung wurde die Finite-Elemente-Methode (FEM) weiterentwickelt, um unter anderem eine Vielzahl von Strukturanalyseproblemen zu lösen, die von linearen über nichtlineare, statische bis hin zu dynamischen, Bruch- und Kontaktproblemen reichen. Auf dem Gebiet der Bruchmechanik wurde gezeigt, dass die Modellierung von schadensbedingten Phänomenen wie Rissentstehung, Rissausbreitung und Delaminierung mit der FEM erfolgreich simuliert werden kann. Dennoch bleiben verschiedene limitierende Eigenschaften bestehen, die diese Methode für aufwendigere Analysen unatraktiv machen. Daher wurden Alternativemethoden erforscht: Eine solche Methode ist die skalierte Rand-Finite Elemente Methode (SBFEM), eine wenig erforschte und dennoch hochleistungsfähige Alternative im Bereich der linear-elastischen Bruchmechanik (LEFM). Ziel dieser Arbeit ist es daher, die Vorzüge der SBFEM zur Beschleunigung von rechenintensiven numerischen Problemen zu nutzen sowie ihre Anwendbarkeit auf eine breite Klasse an Vorwärts- und Rückwärtsproblemen auszuweiten, insbesondere bei Anwendungen in der rechnergestützten Bruchmechanik, Schadenslokalisierung (SL) und Topologieoptimierung (TO).

Die zunehmende Bedeutung der Nachhaltigkeit setzt den umsichtigen Einsatz vorhandener Ressourcen voraus, sodass effiziente Berechnungsschemata angestrebt werden. Diese Dissertation schlägt mehrere neuartige Schemata vor, um dieses Ziel zu erreichen. Die Hamiltonsche Schur-Zerlegung wird zuerst angewendet, um den während einer SBFEM-Analyse aufgrund der Linearisierung des quadratischen Eigenproblems anfallenden Rechenaufwandes zu beseitigen. Ferner wird ein effizienter Fehlerabschätzer vorgeschlagen, der es zusätzlich ermöglicht, die verallgemeinerten Spannungsintensitätsfaktoren (gSIF) mit erhöhter Genauigkeit selbst unter Verwendung von wenigen Freiheitsgraden (DOF) zu berechnen. Die Verwendung von linearen Quadtree-Netzen (QT), die von früheren Autoren entwickelt wurden, um die einzigartigen Netzanforderungen von SBFEM zu überwinden, kann zu einer verringerten Genauigkeit der berechneten gSIFs bei Rissausbreitungssimulationen führen. Es wird ein Verfahren zum internen Erhöhen des Approximationsraums eines Rissspitzenelements vorgeschlagen, das die Genauigkeit, mit der gSIFs auf äusserst groben QT-Netzen berechnet werden, erheblich verbessert. Diese Ansätze werden genutzt, um die Multiskalen-SBFEM (MSBFEM) zu entwickeln, welche mittels SBFEM Diskontinuitäten in der Mikroskala berücksichtigt, und die erweiterte Multiskalen-Finite-Elemente-Methode (EMsFEM) verwendet, um eine Makroskala-Representation des Systems zu erstellen, welches anschliessend mit reduziertem Rechenaufwand gelöst wird. Das neu entwickelte MSBFEM wird dann auf ein hocheffizientes Rissausbreitungsschema erweitert, das nur Regionen auflöst, welche die Rissspitze direkt umgeben, und die restliche Domäne über Makroelemente berücksichtigt. Auf diese Weise wird die Anzahl der DOFs drastisch reduziert, während der Risspfad ausreichend genau erfasst wird.

Diese neuartigen Erkenntnisse zur Beschleunigung des Vorwärtsproblems werden dann auf Rückwärtsprobleme angewendet. Aufgrund seines domänenspezifischen Vorteils wird SBFEM folglich auf SL-Schemata angewendet. Ausgehend von der Parallelität, mit der heuristische Algorithmen SL begegnen, kombiniert mit der Vorberechnung der unbeschädigten Domäne durch SBFEM und der Aktualisierung der Auswirkungen verschiedener Risskandidaten durch Reanalysetechniken, wird ein hocheffizientes und effektives Schema entwickelt, um die SL-Analysen fast auf Echtzeitberechungen zu beschleunigen.

Die TO, die ähnlich wie die SL häufig durch die wiederholte Lösung eines teuren Vorwärtsproblems beeinträchtigt wird, profitiert von effizienten Solvern. Automatisierte, adaptive, analysebereite Netze werden durch die Nutzung von Bildkomprimierungstechniken erzielt. Der vorgeschlagene Drop-In-Ersatz für den Vorwärtssolver verringert die Anzahl an DOF, welche während der Analyse behandelt werden müssen um eine Grössenordnung. Dieser Ansatz wird erfolgreich auf 3D-Probleme ausgeweitet.

Acknowledgements

First and foremost, I would like to thank my supervisors and co-examiners Prof. Dr. Eleni Chatzi, Prof. Dr. Savvas Triantafyllou and Prof. Dr. Chongmin Song. To this day, I am supremely thankful to both Eleni and Savvas for repeatedly taking action in my best interests, starting with our successful bid for the grant, which permitted me to carry out this thesis in the first place, and continuing to the present day. Their guidance and mentoring extended beyond the mere subject matter of this thesis to additional aspects of academic life. I further express my sincerest gratitude to both for allowing me ample freedom to pursue select topics of interest initially outside the scope of the intended research.

I am deeply indebted to Chongmin for hosting me at UNSW for three months and sharing his vast knowledge of SBFEM in the process. His and his family's hospitality cannot be overstated. My only regret is not visiting earlier.

It was through Chongmin that I was introduced to the larger SBFEM community. Most fortunately, my stay at UNSW overlapped with Prof. Dr. Philippe Devloo's. He showed me just how vast the field of FEM is, how much there is still to learn and invigorated me to explore the mathematical side of FEM. In this spirit, under the guidance of Prof. Devloo, I conducted preliminary numerical experiments for the proposed tip enrichment employed for multiscale crack propagation scheme. Beyond the brief academic patronage, I am deeply grateful for the hospitality and kindness that Prof. Devloo and his family repeatedly extended me. Dr. Albert Saputra, with who I co-developed the 3D topology optimization codes, and who primarily mentored me in SBFEM during my stay at UNSW, permitting the development of the damage localization codes, has been a constant friend since. Together with Dr. Hauke Gravenkamp, we have shared countless formal and informal gatherings and fruitful discussions on SBFEM, across the globe, for which I am deeply grateful. To Dr. Konstantinos Agathos, I extend my deepest gratitude for too many reasons to remember individually: Mentoring and accompanying me, always being available for questions, guidance on XFEM and design of experiment related issues of damage localization, to name a few.

To my family, which has grown substantially over the duration of this thesis, thank you for your understanding, unrelenting support, love and laughter. To my old friends of high school and college, who I am honored to still count as my closest friends after all theses years and to my new friends I met during my studies at ETH Zurich, I thank you for helping shoulder the weight of my endeavour with lightheartedness and much needed decompression. To the civil engineering students of ETH whose studies I have shaped and overseen, it was my pleasure. Only few things make me prouder than seeing these students succeed and proceed to shape the future for the better.

Last, but certainly not least, I would like to acknowledge the support of the Swiss National Science Foundation via grant # 200021_153379. The presented thesis was completed under its auspices. Further, I would like to extend my gratitude to Dr. Sassan Mohasseb who first introduced me to SBFEM and sparked my interest in pursuing it as a capable alternative within the context of LEFM.

Nomenclature

Acronyms

BEM	Boundary element method
BESO	Bi-directional evolutionary structural optimization
CMA-ES	Covariance matrix adaptation evolution strategy
CMX	Course multiscale element with X nodes
CONLIN	Convex linearization method
CSchur	Hamiltonian Schur decomposition according to [75]
CSM	Cohesive segment method
CZM	Cohesive zone method
DOF	Degree of freedom
EMsFEM	Enhanced multiscale finite element method
FEM	Finite element method
GA	Genetic algorithm
GFEM	Generalized finite element method
gSIFs	Generalized stress intensity factors
HMsFEM	Hysteretic multiscale finite element method
HSchur	Hamiltonian Schur decomposition according to [193]
IGA	Isogeometric analysis
LEFM	Linear elastic fracture mechanics
LSM	Level set method
MM	Meshless methods
MMA	Method of moving asymptotes
MPM	Material point method
MSBFEM	Multiscale scaled boundary finite element method
MsFEM	Multiscale finite element method
NBF	Numerical basis function
nDOF	Number of degrees of freedom
NURBS	Non-uniform rational basis spline
OC	Optimality criterion
PDE	Partial differential equation
PFM	Phase-field method
PS	Pattern search
PSO	Particle swarm optimization
PUM	Partition of unity method
QT	Quadtree
ROM	Reduced order modeling
RVE	Representational volume element
SBFEM	Scaled boundary finite element method
SERA	Sequential element rejection and admission
SHM	Structural health monitoring
SIFs	Stress intensity factors
SIMP	Solid isotropic material with penalization
SPR	Superconvergent patch recovery
TO	Topology optimization
XFEM	Extended finite element method

Notation

$\lceil\cdot\rfloor$	Diagonal matrix
$[\cdot]$	Matrix
$.^{-1}$	Inverse
$.^{[\cdot]}$	Matrix exponential
$.^{T}$	Transpose
$\mathtt{diag}(\cdot)$	Form diagonal matrix
$\cdot$	Placeholder for mathematical expression
$\cdot,_{\cdot}$	Derivative with respect to
$\leftarrow$	Update
∇	Gradient operator
∇_s	Symmetric gradient operator
$\partial/\partial\cdot$	Partial derivative
$\partial\Omega$	Domain boundary
$\{\cdot\}$	Vector

Upper-case Roman Letters

$\mathscr{G}$	Energy release rate
$\mathscr{G}_c$	Critical energy release rate
[B$^{\cdot}$]	Scaled boundary strain-displacement matrix component
[D]	Constitutive matrix
[E$^{\cdot}$]	Scaled boundary coefficient matrix
[H]	Hamiltonian matrix
[I]	Identity matrix
[K]	Stiffness matrix
[L]	Linear differential operator
[P]	Matrix of powers in least squares scheme
[Q]	Influence matrix of unit changes in reanalysis scheme
[S]	Real Schur form
[Z]	Hamiltonian matrix
{F}	Force Vector
{P}	Boundary forces resulting from the nodal force modes $\{q\}$
D	Measure of detectability
E	Young's modulus
E'	Effective Young's modulus
H_{ei}	Weight factor
J	Jacobian
K_c	Critical stress intensity factor
K$_{\cdot}$	Stress intensity factor
K_{eq}	Equivalent stress intensity factor
L	Length
N	Shape function
O	Scaling center
V	Volume

Lower-case Roman Letters

$.^{(s)}$	Singular quantities
$.^{h}$	Numerically computed quantities
$.^{m}$	Measured quantities
$\cdot_0$	Initial value
$\cdot_{max}$	Maximum value
$\cdot_{min}$	Minimum value
[b$^{\cdot}$]	Scaled boundary strain-displacement matrix component
[b]	Boolean matrix
[x]	Design variables

{a}	Vector of undetermined coefficients
{b}	Body loads
{c}	Integration constant of SBFEM solution
{n}	Normal vector
{q}	Scaled boundary nodal force modes
{t}	Traction
$\{u_h\}$	Displacements calculated by finite element method
{u}	Displacements
a	Crack length
c	Crack
c([x])	Compliance
e	Element
e^*_σ	Error estimator for generalized stress intensity factors
eps	Machine precision
f	Volume fraction
l_0	Characteristic length
m	Positive move limit
n_{par}	Number of parameters
p	Penalty parameter
r	Radius
$r_b(\theta)$	Distance to the boundary given θ
r_d	Radius of integration
r_e	Radius of enrichment
t	Thickness
tol	Tolerance
$u(\xi)$	Analytic displacements along ξ

Upper-case Greek Letters

$[\Psi]$	Transformation matrix
$[\Psi_\sigma]$	Stress mode
$[\Psi_q]$	Force mode
$[\Psi_u]$	Displacement mode
Δ	Increment
Γ	Boundary
Ω	Domain
Π	Total potential energy
$\{\Gamma\}$	Stress mode

Lower-case Greek Letters

δ	Variation
ϵ	Very small parameter
η	Numerical damping coefficient
$\eta(\theta)$	Scaled boundary coordinate in tangential direction
κ	Condition number
λ	Eigen-value
ν	Poisson's ratio
σ_{raw}	Raw stresses
σ_{rec}	Recovered stresses
τ	Shear stress
θ	Realization parameters of a flaw
θ_c	Crack propagation angle
ξ	Scaled boundary coordinate in radial direction
$\{\epsilon\}$	Strain vector
$\{\phi\}$	Modal displacement vector
$\{\sigma\}$	Stress vector

Contents

Part I

Introduction

1 Introduction

1.1 Motivation

Since its inception, the finite element method (FEM) has been advanced to handle a multitude of structural analysis problems ranging from linear to nonlinear, static to dynamic, fracture and contact problems amongst others ([33], [140], [366]). Pertaining to the field of fracture mechanics, it has been demonstrated that modeling of damage-related phenomena such as crack initiation, crack propagation and delamination can successfully be accomplished by means of the FEM [159]. Further, with the introduction of singular elements, stress singularities about crack tips may be more accurately quantified [366]. Nonetheless, various undesirable characteristics persist, which render this method computationally prohibitive for more involved analyses. Extensive mesh refinement and remeshing, as well as mesh-dependent projection errors, result in decreased accuracy and increased implementational complexity. As a result, alternative methods have been pursued such as the Boundary Element Method (BEM) ([59], [326]), the Discrete Element Method (DEM) [79], meshless methods [263], cohesive elements [226] and phase field models [132]. In general, these alternatives are not supported in commercial structural analysis software packages and are more likely to be encountered in special purpose applications.

In mitigating the aforementioned issues of the FEM, the extended finite element method (XFEM) [207] was introduced. A combination of the level set method (LSM) [305] for tracking discontinuities, combined with jump and tip enrichment for the displacement solution, is utilized to decouple both weak (material interfaces) and strong (cracks) discontinuities from the mesh. The popularity of XFEM, currently available in numerous commercial software packages, may largely be attributed to the fact that the core steps of FEM as well as its robustness are left intact, which facilitates implementation and end-user understanding alike. Although this method has aggregated significant academic interest and resolved most shortcomings of FEM-based damage simulation, a number of issues still remain. The most notable include the extension to 3D problems when using the LSM ([118],[5]), the larger condition number of the stiffness matrix ([124],[6]) and the a priori assumption for the type of tip enrichment [209]. Additionally, special integration schemes are required in order to determine the stress intensity factors (SIFs).

An alternative approach, namely the scaled boundary finite element method (SBFEM), attempts to fuse the advantageous characteristics of FEM and BEM into one method, while simultaneously introducing features that facilitate the modeling of damage-related phenomena. This method's key feature, the introduction of a scaling center, has long been exploited for the solution of electric field problems [286]. After refinement and application to solid mechanics it was initially termed the "Cloning Algorithm" by Dasgupta [80], where it was used to model wave propagation in unbounded soils and found applications in soil-structure interaction and earthquake engineering. Subsequent work by Wolf resulted in a similar formulation named the "infinitesimal finite element method" [343]. Wolf and Song, first coined the term SBFEM, once the derivations for various types of problems were standardized using the minimum weighted residual method ([344],[342]). Deeks and Wolf employed a virtual work formulation, facilitating the practical implementation of the method [82]. Though early work on SBFEM was intended for modeling unbounded domains, it soon became apparent that it is at least equally effective for bounded domains [342]. Prior to the work presented presented as part of this thesis, no comprehensive, direct comparison between SBFEM and XFEM existed, though in [242] a polygon-based SBFEM is contrasted to XFEM, while [221] compares XFEM with SBFEM tip enrichment to standard XFEM.

The SBFEM belongs to the class of semi-analytical methods and is therefore related to the thin layer method [148], the Trefftz method [152], the BEM [192], spectral elements [248] and the semi-analytical finite elements [223]. Although much of the early research focused on the treatment of unbounded domains, it was soon discovered that SBFEM is more effective at modelling bounded domains [342], particularly in

the context of linear elastic fracture mechanics (LEFM). This is apparent, since the fracture parameters, e.g., SIFs, T-stress as well as the coefficients of higher order terms, can be directly extracted from the singular components of the stress field [72, 293]. The method is able to robustly transition between power and power-logarithmic singularities [293]. It has thus been applied for computing the order of singularity and SIFs in multi-material plates under both static and dynamic loading [292], for predicting the crack propagation direction at bi-material notches [215], and for determining the free-edge stresses about holes in laminated composites [173].

Yang et al. [354] first modelled crack propagation via use of SBFEM and few large sized subdomains, whose initial meshes were manually specified. This approach was extended to model nonlinear cohesive fracture in concrete [353, 352, 237, 236, 364], dynamic fracture [233, 234] and crack propagation in reinforced concrete [240]. Reaching the limits of the laborious meshing approach, fully automated modelling of crack propagation was achieved by repurposing newly proposed meshers [242] for polygonal elements [317]. Currently, the most widely adopted meshing procedure combines the use of a quadtree (QT) decomposition with polygon clipping, to accurately represent curved geometries [238] with coarser meshes. The advantage of adopting balanced quadtree meshes as a basis lies in the limited amount of possible element realizations, whose pre-computation greatly enhances computational efficiency. Having resolved most mesh related issues, SBFEM was most recently extended to treat functionally graded materials [73, 67] and non-local damage [361, 360]. However, the accurate calculation of generalized SIFs (gSIFs) requires sufficient angular resolution of the singular stress field. This issue is traditionally circumvented by refining an area around the crack tip with subsequent homogenization into a cracked macro element. In conjunction with the balancing operation performed on the QT meshes, this introduces a significant amount of degrees of freedom (DOFs) thus increasing the computational toll of analysis. Although the direction of crack propagation is accurately determined by the ratio of gSIFs, the load-deflection curve can exhibit significant errors. Hence, we aim to increase the accuracy of the calculated gSIFs, utilizing the same global mesh as previously for analysis. This may be achieved by enforcing the external boundaries of the cracked element to be compatible with the linear shape functions, yet internally permit the use of arbitrary higher order approximations to model the singular stress field.

An interesting development pertains to the fusion of scaled boundary principles with isogeometric analysis (IGA), which is shown to provide lower error in displacement and energy norm per degree of freedom. The method ensures exact treatment of curved boundaries [172, 222], delivers additional refinement possibilities and the ability of adjust continuity as required. However, the computational cost is increased as compared against the standard SBFEM due to the integration procedure associated with IGA [23] partially due to the non-uniform rational b-splines (NURBS) basis forming a larger support for calculation of element related quantities [77]. When contrasted to established methods (e.g. FEM, IGA), this draw-back is negated as only the boundary need be discretised.

The demand for sustainable design in, e.g., the aerospace, automotive and construction industries has led to the development of lighter, stronger and more resilient structures, spawning the need to guard against failure processes by leveraging robust, economical and high-fidelity numerical simulations. While SBFEM significantly accelerates LEFM-related computations [92], the simulation of more involved problems bridging multiple scales still poses a considerable challenge. Upscaling techniques [191], which derive an analytic formulation to inscribe micro-scale information onto a macro-scale model, or multiscale methods [19, 321, 145], which define a numerically equivalent macro-scale problem based on micro-scale properties may be harnessed to reduce the computational toll. Within the family of multiscale methods, one typically distinguishes between homogenization methods [251] and multiscale finite element methods (MsFEM) [91]. Whereas homogenization methods [29, 108, 355] evaluate an average strain and stress tensor across a locally periodic representational volume element (RVE), the MsFEM, a computational approach, which does not require a full separation of scales or periodicity of the problem, seeks to numerically evaluate a set of micro-scale basis functions (NBFs). The NBFs, which depend on the RVE's topology and material properties, map micro-scale information to a macro-scale mesh, where the governing equations are then solved at reduced computational effort, typically by means of the FEM. Here we utilize the enhanced multiscale finite element method (EMsFEM) [358], which applies FEM principles to map the microscopic response to the macroscopic system response. The central idea is to numerically construct this mapping by locally solving a series of Dirichlet boundary value problems (BVPs). Its predecessor, the multiscale finite element method (MsFEM), was first applied to two-phase flow and transport problems in highly heterogenous porous media [135]. An augmentation thereof, the coupling MsFEM, treated the consolidation of heterogeneous saturated porous media [357]. The further inclusion of Poisson's effect in construction

of the mapping led to its applicability in computational solid mechanics [358] and labelling as EMsFEM. Triantafyllou and Chatzi subsequently proposed the hysteretic multiscale finite element method (HMsFEM) [323], which treats nonlinear static and dynamic analysis of heterogeneous structures within the hysteretic finite element framework [324]. The multi-axial smooth hysteretic model controlling the evolution of plastic strains follows the Bouc-Wen model of hysteresis [55]. This approach was later applied to model validation in reliability analysis and inverse problem formulations [325].

Such inverse problems aim at identifying latent and unknown system parameters by measuring the system response and comparing it to a simulated response, which is typically obtained from a numerical model. The direct solution to the numerical model, i.e. the forward problem, is in practice often infeasible due to incomplete system information. In the presence of measurement data, however, an inverse problem can be formulated to identify the remaining unknown system characteristics. One such problem involves the localization of damage in structures, an application in structural health monitoring (SHM) that has benefited from the advent of low-cost and easily deployable sensor technologies. Damage localization is one part of the SHM process, which comprises the detection of damage, its localization, quantification of severity and extent, and an estimation of a structure's future performance given the accumulation of damage. Heuristic optimization [190] has been shown as a particularly well-suited approach to solving the inverse problem: Such derivative free methods are capable of treating non-convex and non-smooth problems. Localization of cracks was first pioneered by Rabinovich et al. [261, 260] combining XFEM and genetic algorithms (GAs) in 2D static and dynamic problems. Subsequently, generalized flaws where treated in [335, 66]. An adaptive algorithm capable of detecting multiple flaws was first presented in [311]. In [185], a 3-step algorithm for the detection of multiple flaw clusters was proposed. An alternative, yet aligned direction of research lies is the acceleration of such detection schemes. To this end, surrogate models [301, 84], multiscale schemes [325] and component mode synthesis for dynamics [247] have been proposed. Notably absent are computational reduced order modeling (ROM) and reanalysis techniques. Therefore, this direction is further explored.

The adoption of Topology Optimization (TO) into engineering practice stems from the ever-increasing need for the sustainable, economical and accountable use of resources across diverse sectors, e.g., construction, aerospace and automotive. The solution of a computationally expensive forward problem is typically fundamental to TO of continuum structures [44], which aims at defining an optimal structural layout subject to constraints. Originally, Bendsøe and Kikuchi [45] proposed a homogenization based approach. Due to difficulties in evaluating optimal micro-structures, their associated orientation and the absence of a definite length-scale, alternative approaches were sought. The solid isotropic material with penalization (SIMP) approach [43, 362, 203], assumes constant material properties within each element of the domain, which are typically arranged in grids. Filtering techniques, perimeter or gradient constraints must be adopted in order to ensure the existence of solutions, due to the underlying power-law governing the material properties [283]. As opposed to the above approaches, which aim to solve the TO problem using mathematical programming and a continuous description of the design variables, integer-based approaches have been proposed. While dual approaches [35] have been employed for large scale simulations, approaches harnessing global optimization algorithms, e.g., GAs, are considered impractical due to the excessive amount of function evaluations, i.e., forward analyses required. The conventional approach employing a fine grid of design variables, with values of 0 and 1 corresponding to void and solid, respectively, and whose layout remains constant across all iterations, does not reflect the nature of the evolving topology and leads to an excessive computational toll. Several adaptive schemes have been proposed to alleviate this computational burden [337, 134, 273]. In [245] tree-based meshing strategies are explored. Unfortunately, therein the treatment of hanging nodes severely affects the computational efficiency.

Although a mixed SBFEM has been employed for solving TO problems of incompressible materials [168], it follows the conventional fine-grid approach to TO and limits its treatment to linear elements and 2D applications. The SBFEM has proven itself as a remarkably versatile tool in automatic image-based stress analysis [276, 187]. Such hierarchical meshes arising from tree-like image decompositions drastically reduce the amount of DOFs present, which accelerates the solution of the forward problem by alleviating computational effort and memory requirements. Image decomposition techniques, within the context of TO, produce fewer DOFs when material transition zones are eliminated. Hence, bi-directional evolutionary structural optimization (BESO) [138], sequential element rejection and admission (SERA) [21], SIMP combined with grayscale filters [20, 175] and level-set methods [244], for example, represent suitable algorithms. Since image decomposition operates on the design variables to produce analysis-ready meshes at each iteration, this family of techniques only requires interchanging the solver of the forward problem.

Hence, incorporation into existing code bases requires minimal modification. Furthermore, as tree-like image decomposition techniques [47] utilize the uniformity of an element as a criterion for subdivision, multi-material TO [275] may be incorporated through extension to color-aware tree-like decompositions [161].

1.2 Objective and Scope

The objective of this thesis is to accelerate computationally intensive numerical problems harnessing the merits and further extending the capabilities of the SBFEM to a wide class of forward and inverse problems, specifically with applications in computational fracture mechanics, damage localization and topology optimization. The increasing importance of sustainability implies the efficient use of existing resources. In the context of numerical simulations the research objectives are therefore numerous, e.g.:

- Propose efficient schemes to solve large-scale problems on workstation computers previously reserved for compute clusters.
- Empower the analyst by minimizing the computational cost of analysis, such that either treatment of certain problems become tractable again or variant studies may be performed.
- Enhance existing methods and provide efficient means of error estimation.
- Apply enhancements for solving forward problems to the solution of inverse problems.
- Disseminate the results by freely distributing the developed code bases.

The above objectives are pursued through the numerous contribution listed in this thesis. Integral to all schemes in this thesis is the SBFEM. Therefore, reducing the computational toll incurred during such an analysis benefits all. This is approached by seeking to improve the means by which the Hamiltonian eigen-problem is solved. With the aim of exploiting the conventional, powerful algorithm of calculating gSIFs by SBFEM, ways to reverse the computational toll incurred by linearizing the quadratic eigen-problem are sought. Hence, alternative approaches such as employing B-splines to solve the ordinary differential equation (ODE) termed the SBFEM equation in displacements are not considered. Since the gSIFs are of fundamental importance in the LEFM framework, especially as a crack propagation criterion, an accurate error estimator will be developed. Since the gSIFs in SBFEM are derived directly from the singular stress modes, application of the superconvergent patch recovery (SPR) theory is self-evident, thus excluding the investigation into competing methods.

Although SBFEM results in highly efficient simulations, large-scale and real-world problems still pose a substantial computational burden. With the aim of rendering such problems tractable, multiscale methods are investigated, specifically, adoption of the EMsFEM on the coarse scale and SBFEM to incorporate fracture on the fine scale. Since the NBFs, which map the response across scales must only be computed once in an offline phase prior to analysis, they are deemed the method of choice. An additional objective is to ascertain the conventional NBF's ability to accurately capture strong discontinuities on the fine scale, and suggest appropriate modifications to the NBFs construction as required. Further, only a micro and macro scale are considered, since in principle this scheme permits an arbitrary amount of scales. The findings are to be used in the development of a multiscale crack propagation scheme. Since crack propagation is highly dependent on an accurate reconstruction of the stress state in crack tip vicinity, hp-refinement of macro-elements will be investigated.

Having developed highly efficient schemes to accelerate forward problems, these ideas are to be applied towards the solution of inverse problems. Damage localization schemes are a natural choice due to SBFEM's domain specific advantage of efficiently incorporating fracture, i.e., cracks. Since this constitutes a novel application of SBFEM, the investigation is limited to elastostatics and a one-step heuristic approach. Further, a comparison between available global optimization algorithms will be conducted, aiming to determine each individual's merits in minimizing the computational toll. Schemes to accelerate an inverse analysis towards near real-time localization will be explored. To this end, parallel programming principles, precomputation and reanalysis techniques are to be combined. The embarrassingly parallel nature of calculating fitness scores for each individual of a generation should be considered. Precomputation techniques stemming from the adoption of QT meshes will be explored to calculate an undamaged system response, which serves as a baseline for the reanalysis technique. ROM techniques are considered outside the scope of this work. Further, we refrain from incorporating data-drive approaches to damage localization.

TO is routine marred by the excessive computational burden stemming from the repeated solution of an expensive forward problem. Various methods of incorporating adaptivity have been proposed in recent

literature. Due to the pixel-based nature of current TO schemes, inexpensive automatic image compression techniques will be investigated with the aim of arriving at adaptive analysis-ready meshes. The current research limits itself to compliance minimization problems in order to compare with established methods. Further, the merits and potential of this approach will be demonstrated by extending SBFEM-powered TO to 3D problems.

1.3 Outline

This thesis comprises five parts, whose description is provided below:

1. **Introduction:**
   As part of the introduction, the motivation, objectives and scope of this thesis are first outlined. Then the salient theory is provided with emphasis on the use of SBFEM within the LEFM framework. For the case where SBFEM is employed to enhance a broader range of applications within, e.g., EMsFEM, damage localization or TO, generic descriptions of the most commonly employed variants are reproduced. Next, a critical reflection on the current state-of-the-art in discrete and phase field methods for LEFM is provided. This serves as a basis to understand the strengths and weaknesses of the schemes developed in the subsequent parts.

2. **Forward Problem:**
   In this part, schemes which aim at accelerating forward simulations are developed on the basis of SBFEM. One chapter investigates the merits of adopting the Hamiltonian Schur decomposition to reverse the computational burden incurred by linearizing the underlying SBFEM eigen-problem. Further, an efficient and effective error estimator for gSIFs calculated by SBFEM is introduced. It leverages SPR theory, thereby recovering the gSIFs to greater accuracy. Although SBFEM itself is a highly effective numerical method, large problems still pose a significant computational burden. Hence, adoption of the EMsFEM is considered. With the aim of developing a multiscale crack propagation scheme, the effects of discontinuities embedded in RVEs are first examined. Observing insufficient accuracy for select cases in combination with highly coarse meshes, as scheme inherent to SBFEM is developed to locally elevate the approximation space of elements containing crack tips and thereby recovering the gSIFs at significantly improved accuracy. This discussion forms the basis for the developed multiscale crack propagation scheme, where SBFEM incorporates fracture on the fine scale and the EMsFEM is harnessed to construct an associated coarse mesh representation on which the governing equations are solved at a reduced computational toll.

3. **Inverse Problem:**
   Having established and developed effective means of treating forward problems, the gained insights are applied to accelerate large classes of inverse problems, e.g., damage localization and TO. Typically, inverse problems require the repeated solution of an expense forward problem. Within the context of damage localization, automated construction of analysis-ready adaptive meshes coupled with reanalysis and parallel programming techniques are explored to significantly accelerate the localization of cracks and inclusions within solids. Similarly, TO benefits from the introduction a drop-in replacement for the forward problem, which exploits adaptivity and automated image compression techniques. A new and highly intuitive way to interact with TO, i.e., color-encoding analysis information into an input image, is proposed and SBFEM-powered TO is extended to 3D applications.

4. **Conclusion:**
   This thesis concludes with an overview of the merits of each individual contribution and summarizes encountered limitations, which in turn provide the basis for a discussion on future work.

5. **Appendix:**
   The appendix contains additional materials, i.e., the state-of-the-art review of the XFEM and PFM theory, which complements their respective presentations in the introduction.

1.3.1 Origin of Contributions

In this section the original contributions are specifically stated and, where applicable, collaborations and parts contributed by external sources are identified. Although all content presented in this thesis stems from publications, of which I am first author, I would like to acknowledge select sections, which have benefited greatly from my co-author's contributions (see Tbl. 1.1).

Chapter	Title	Source	Collaboration
2.1	The LEFM Problem Statement	[95]	K. Agathos
3	Discrete and Phase Field Methods for LEFM	[95]	U. Pillai, E. Kakouris, S. Triantafyllou, E. Chatzi
7.2.3	3D Topology Optimization	[96]	A. Saputra
A.1	The eXtended/Generalized Finite Element Methods	[95]	K. Agathos
A.2	Phase Field Methods	[95]	S.Triantafyllou, U. Pillai, E. Kakouris

Tbl. 1.1: Sections greatly benefiting from co-author's contributions from selected first author publications.

Further, the chapters listed below (Tbl. 1.2) source material from the following of my publications:

Chapter	Title	Source
1	Introduction	[95], [92], [96], [94], [93]
2	Theory	[95], [92], [96]
3	Discrete and Phase Field Methods for LEFM	[95]
4	Adopting the Hamiltonian Schur Decomposition	[92], [95]
5	Multiscale SBFEM	[94], [93]
7	Topology Optimization	[96]
A	Appendix	[95]

Tbl. 1.2: Chapters containing materials sourced form first author publications.

2 Theory

2.1 The Linear Elastic Fracture Mechanics (LEFM) Problem Statement

To formulate the LEFM problem, we consider the two dimensional cracked domain Ω shown in Fig. 2.1. The boundary Γ consists of the parts Γ_0, where free surface boundary conditions apply, Γ_u, where displacements $\bar{u}$ are prescribed and Γ_t where the surface tractions $\bar{t}$ are applied as Neumann conditions. The domain includes a crack under the assumption of free surface conditions Γ_c. As depicted in Fig. 2.1, the domain boundary is decomposed as $\Gamma = \Gamma_0 \cup \Gamma_u \cup \Gamma_t \cup \Gamma_c$. Then, the elasticity equations with the corresponding boundary conditions apply:

$$\nabla \cdot \{\sigma\} + \{b\} = \{0\} \quad \text{in} \quad \Omega \tag{2.1a}$$

$$\{u\} = \{\bar{u}\} \quad \text{on} \quad \Gamma_u \tag{2.1b}$$

$$\{\sigma\} \cdot \{n\} = \{\bar{t}\} \quad \text{on} \quad \Gamma_t \tag{2.1c}$$

$$\{\sigma\} \cdot \{n\} = \{0\} \quad \text{on} \quad \Gamma_c^0 \tag{2.1d}$$

where $\{\sigma\}$ is the Cauchy stress tensor, $\{n\}$ is the unit outward normal to the boundary, $\{b\}$ is the applied body force per unit volume, $\{u\}$ is the displacement field and ∇ is the gradient operator.

If small deformations are assumed, then the strain field $\{\epsilon\}$ can be described as the symmetric gradient of the displacement field:

$$\{\epsilon\} = \nabla_s \{u\} \tag{2.2}$$

Further, if linear elastic material behavior is assumed, stresses can be obtained from strains through Hooke's law:

$$\{\sigma\} = [D]\{\epsilon\} \tag{2.3}$$

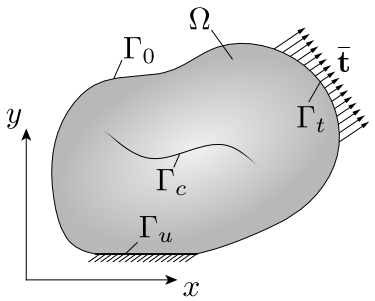

Fig. 2.1: Cracked body and boundary conditions.

where $[D]$ is the elasticity tensor, which in case of two dimensional problems assumes the following form:

$$[D] = \frac{E}{1-\nu^2}\begin{bmatrix} 1 & \nu & 0 \\ \nu & 1 & 0 \\ 0 & 0 & \dfrac{1-\nu}{2} \end{bmatrix}, \quad \text{for plane stress} \tag{2.4a}$$

$$[D] = \frac{E}{(1+\nu)(1-2\nu)}\begin{bmatrix} 1-\nu & \nu & 0 \\ \nu & 1-\nu & 0 \\ 0 & 0 & \dfrac{1-2\nu}{2} \end{bmatrix}, \quad \text{for plane strain} \tag{2.4b}$$

with E and ν denoting the Young's modulus and Poisson's ratio respectively. Eqs. 2.1 combined with Eqs. 2.2 and 2.3 define the strong form.

A decisive quantity in classic fracture mechanics [120, 121] is the energy release rate, defined as:

$$\mathcal{G} = -\frac{\partial \Pi}{\partial a} \tag{2.5}$$

where Π is the total potential energy and a is the crack length for 2D problems. Then, based on the energy release rate criterion, crack propagation will occur when:

$$\mathcal{G} \geq \mathcal{G}_c \tag{2.6}$$

where $\mathcal{G}_c$ is the critical energy release rate or fracture toughness, which can be considered as a material parameter.

For a pure mode I problem, the mode I SIF is related to the energy release rate as follows:

$$\mathcal{G} = \frac{K_I^2}{E'} \tag{2.7}$$

where K_I is the stress intensity factor and E' is the effective Young's modulus:

$$E' = \begin{cases} E & \text{for plane stress} \\ \dfrac{E}{1-\nu^2} & \text{for plane strain} \end{cases} \tag{2.8}$$

Based on this, the critical stress intensity factor is defined as:

$$K_c = \sqrt{E'\mathcal{G}_c} \tag{2.9}$$

The corresponding relation 2.7 for mixed mode planar problems is:

$$\mathcal{G} = \frac{1}{E'}\left(K_I^2 + K_{II}^2\right) \tag{2.10}$$

where K_{II} is the mode II SIF. The square root of the quantity $\left(K_I^2 + K_{II}^2\right)$ can be considered as an equivalent SIF:

$$K_{eq} = \sqrt{K_I^2 + K_{II}^2} \tag{2.11}$$

Then, the energy release rate criterion of Eq. (2.6) can be written in terms of the SIFs as:

$$K_{eq} \geq K_c \tag{2.12}$$

2.2 The Scaled Boundary Finite Element Method (SBFEM) in 2D Elastostatics

The fundamental difference between SBFEM and other numerical methods is the introduction of a scaling center O. In all but a few special cases, this scaling center must be directly visible from any point on the domain boundary. By introducing the scaling center, the Cartesian coordinate system is transformed into one similar to polar coordinates. It is in this process that a radial coordinate ξ and a tangential coordinate η are introduced (Fig. 2.2).

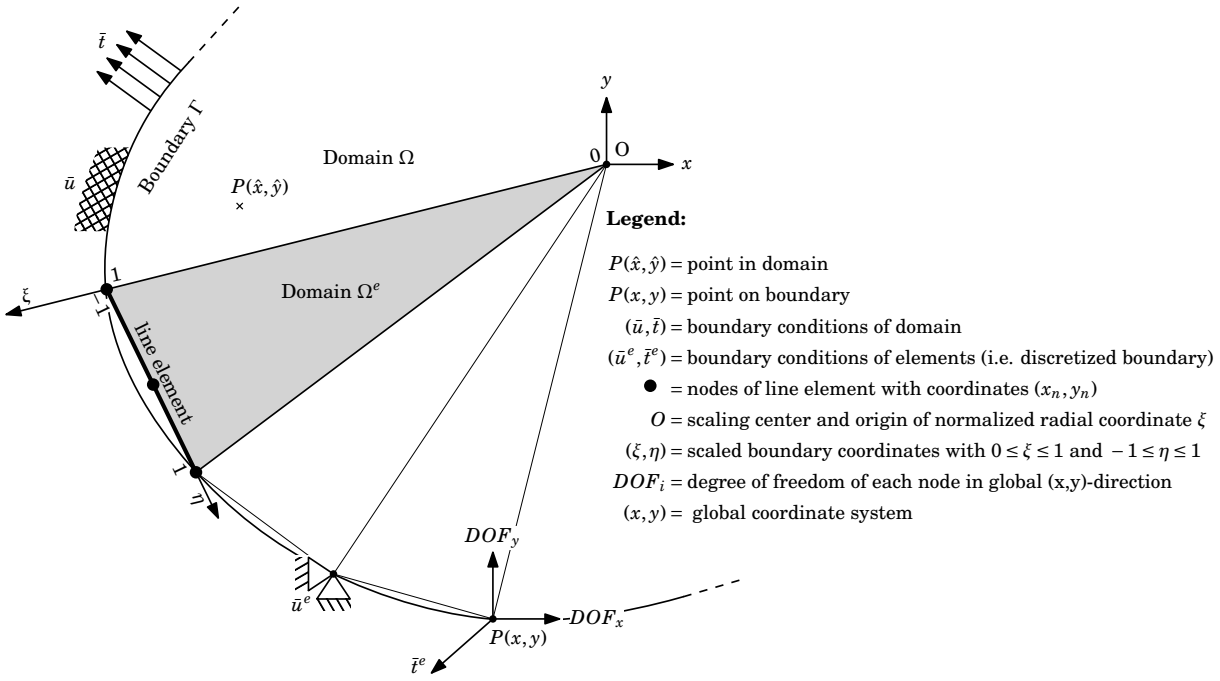

Fig. 2.2: Introduction of SBFEM specific discretization of the bounded domain.

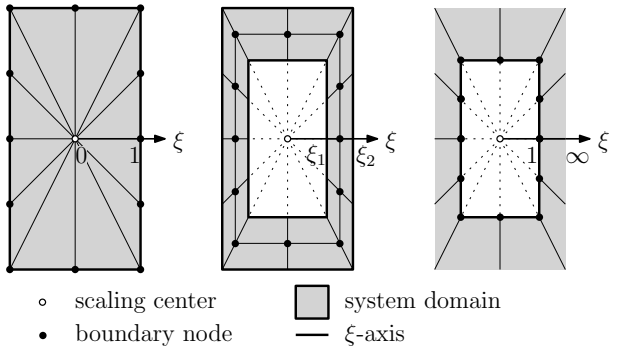

Fig. 2.3: Possible domain types using SBFEM.

Assuming that for SBFEM an analytical solution can be found in radial direction ξ, which is later shown to exist (Eq. 2.40), only the tangential direction η need be discretized in the finite element sense. Depending on the bounds for ξ unbounded domains ($1 \le \xi \le \infty$), bounded domains ($0 \le \xi \le 1$) and bounded domains with similar boundaries ($\xi_1 \le \xi \le \xi_2$) can be accounted for (Fig. 2.3).

By choosing to discretize in radial direction along the boundary, the dimension of the problem is reduced by one. Consequently, the information contained within each element on the boundary encompasses that of the triangular domain spanned by itself and the scaling center (Fig. 2.2).

2.2.1 Derivation Based on the Virtual Work Approach

The theoretical basis of the SBFEM is summarized in [342] and more recently and extensively in [294]. In this thesis, only the fundamental features are discussed. A thorough and more extensive treatment of the latest SBFEM-advancements in the context of LEFM can be found in the recent review paper by Song, Ooi, and Natarajan [295].

The scaled boundary transformation of geometry, wherein Cartesian coordinates (x,y) are mapped to corresponding scaled boundary coordinates (ξ,η) is provided below. It states that any point in the domain

can be equivalently expressed based on the position of the scaling center x_0, some scaling factor in radial direction ξ and an interpolation in tangential direction $x(\eta)$.

$$x(\xi,\eta) = x_O + \xi x(\eta) = x_O + \xi[N(n)]\{x\} \tag{2.13a}$$
$$y(\xi,\eta) = y_O + \xi y(\eta) = y_O + \xi[N(n)]\{y\} \tag{2.13b}$$

where $[N(\eta)]$ corresponds to the finite element interpolation functions $[N_1(\eta), N_2(\eta), ..., N_n(\eta)]$, $\{x\}$ represents the nodal coordinates $\{x_1, x_2, ..., x_n\}^T$ and n is the number of nodes per element on the boundary. The Jacobian $[J]$, its inverse $[J]^{-1}$ and determinant $|J|$, which link the derivatives in Cartesian to scaled boundary coordinates on the boundary are given as:

$$\begin{Bmatrix} \frac{\partial}{\partial\xi} \\ \frac{\partial}{\partial\eta} \end{Bmatrix} = \begin{bmatrix} \frac{\partial x}{\partial\xi} & \frac{\partial y}{\partial\xi} \\ \frac{\partial x}{\partial\eta} & \frac{\partial y}{\partial\eta} \end{bmatrix} \begin{Bmatrix} \frac{\partial}{\partial x} \\ \frac{\partial}{\partial y} \end{Bmatrix} = [J] \begin{Bmatrix} \frac{\partial}{\partial x} \\ \frac{\partial}{\partial y} \end{Bmatrix} \tag{2.14a}$$

$$\begin{Bmatrix} \frac{\partial}{\partial x} \\ \frac{\partial}{\partial y} \end{Bmatrix} = \frac{1}{|J|} \begin{bmatrix} \frac{\partial y}{\partial\eta} & -\frac{\partial y}{\partial\xi} \\ -\frac{\partial x}{\partial\eta} & \frac{\partial x}{\partial\xi} \end{bmatrix} \begin{Bmatrix} \frac{\partial}{\partial\xi} \\ \frac{\partial}{\partial\eta} \end{Bmatrix} = [J]^{-1} \begin{Bmatrix} \frac{\partial}{\partial\xi} \\ \frac{\partial}{\partial\eta} \end{Bmatrix} \tag{2.14b}$$

As a result, the differential volume unit dV is expressed as follows in scaled boundary coordinates:

$$dV = |J|\xi d\xi d\eta \tag{2.15}$$

Subsequently, these derivatives are used to evaluate the linear differential operator $[L]$ in scaled boundary coordinates. Splitting $[L]$ into Cartesian components facilitates the substitution of their scaled boundary equivalents. Factoring into scaled boundary components, this results in:

$$[L] = \begin{bmatrix} 1 & 0 \\ 0 & 0 \\ 0 & 1 \end{bmatrix} \frac{\partial}{\partial x} + \begin{bmatrix} 0 & 0 \\ 0 & 1 \\ 1 & 0 \end{bmatrix} \frac{\partial}{\partial y} = [L^1]\frac{\partial}{\partial x} + [L^2]\frac{\partial}{\partial y} \tag{2.16a}$$
$$= \frac{1}{|J|}\left[[L^1]\left(\frac{\partial y}{\partial\eta}\frac{\partial}{\partial\xi} - \frac{\partial y}{\partial\xi}\frac{\partial}{\partial\eta}\right) + [L^2]\left(\frac{\partial x}{\partial\xi}\frac{\partial}{\partial\xi} - \frac{\partial x}{\partial\eta}\frac{\partial}{\partial\xi}\right)\right] \tag{2.16b}$$
$$= [b^1(\eta)]\frac{\partial}{\partial\xi} + \frac{1}{\xi}[b^2(\eta)]\frac{\partial}{\partial\eta} \tag{2.16c}$$

where $[b^1(\eta)]$ and $[b^2(\eta)]$ represent:

$$[b^1(\eta)] = \frac{1}{|J|}\begin{bmatrix} \frac{\partial y}{\partial\eta} & 0 \\ 0 & -\frac{\partial x}{\partial\eta} \\ -\frac{\partial x}{\partial\eta} & \frac{\partial y}{\partial\eta} \end{bmatrix} \tag{2.17a}$$

$$[b^2(\eta)] = \frac{1}{|J|}\begin{bmatrix} -\frac{\partial y}{\partial\xi} & 0 \\ 0 & \frac{\partial x}{\partial\xi} \\ \frac{\partial x}{\partial\xi} & -\frac{\partial y}{\partial\xi} \end{bmatrix} \tag{2.17b}$$

The displacements $\{u(\xi,\eta)\}$ follow an isoparametric formulation. They too consist of an analytical part in radial direction $\{u(\xi)\}$ and an interpolatory part in tangential direction based on shape functions $[N^u(\eta)]$.

$$\{u(\xi,\eta)\} = [N^u(\eta)]\{u(\xi)\} \tag{2.18}$$

where $[N^u(\eta)]$ represents the shape functions $[N(\eta)]$, which are applied to each DOF of an element separately by means of multiplication with the identity matrix $[I]$:

$$[N^u(\eta)] = [N^1(\eta)I_n, N^2(\eta)I_n, ..., N^n(\eta)I_n] \tag{2.19}$$

As a result, an expression for the strains may be derived by substituting the formulation for the displace-

ments into Eq. 2.2.

$$\{\epsilon(\xi,\eta)\} = [B^1(\eta)]\{u(\xi)\}_{,\xi} + \frac{1}{\xi}[B^2(\eta)]\{u(\xi)\} \tag{2.20}$$

where

$$[B^1(\eta)] = [b^1(\eta)][N^u(\eta)] \tag{2.21a}$$

$$[B^2(\eta)] = [b^2(\eta)][N^u(\eta)]_{,\eta} \tag{2.21b}$$

Substituting Eq. 2.20 into the constitutive relation 2.3 results in the following expression for the stress field.

$$\{\sigma(\xi,\eta)\} = [D]\left([B^1(\eta)]\{u(\xi)\}_{,\xi} + \frac{1}{\xi}[B^2(\eta)]\{u(\xi)\}\right) \tag{2.22}$$

In what follows, the virtual work method is implemented. To this end, the virtual displacements $\{\delta u(\xi,\eta)\}$ and strains $\{\delta\epsilon(\xi,\eta)\}$ are expressed as follows:

$$\{\delta u(\xi,\eta)\} = [N(\eta)]\{\delta u(\xi)\} \tag{2.23a}$$

$$\{\delta\epsilon(\xi,\eta)\} = [L]\{\delta u(\xi,\eta)\} \tag{2.23b}$$

Thus, by equating internal work to external work, the weak form of the scaled boundary finite element method is derived in the following form:

$$\int_V \{\delta\epsilon(\xi,\eta)\}^T\{\sigma(\xi,\eta)\}dV - \int_{\partial\Omega}\{\delta u(\eta)\}^T\{\bar{t}(\eta)\} = 0 \tag{2.24}$$

The second term in Eq. 2.24, gives rise to equivalent nodal loads $\{P\}$, due to applied tractions $\{\bar{t}(\eta)\}$. The corresponding displacements calculated on the boundary are termed $\{u_h\}$. Equating the internal virtual work to the external virtual work results in the complete virtual work equation as stated below and derived subsequently:

$$\begin{aligned}&\{\delta u\}^T\{[E^0]\{u_h\}_{,\xi} + [E^1]^T\{u_h\} - \{P\}\}\\ &\qquad - \int_{xi=0}^{\xi=1}\{\delta u(\xi)\}^T\left\{[E^0]\xi\{u(\xi)\}_{,\xi\xi} + [[E^0] + [E^1]^T - [E^1]]\{u(\xi)\}_{,\xi} - [E^2]\frac{1}{\xi}\{u(\xi)\}\right\}d\xi = \{0\}\end{aligned} \tag{2.25}$$

Considering Eqs. 2.20 and 2.22, the internal work assumes the following form:

$$\begin{aligned}&\int_V \{\delta\epsilon(\xi,\eta)\}^T\{\sigma(\xi,\eta)\}dV\\ &\qquad = \int_V \left[[B^1(\eta)]\{\delta u(\xi)\}_{,\xi} + \frac{1}{\xi}[B^2(\eta)]\{\delta u(\xi)\}\right]^T[D]\left([B^1(\eta)]\{u(\xi)\}_{,\xi} + \frac{1}{\xi}[B^2(\eta)]\{u(\xi)\}\right)dV\\ &= \int_{\partial\Omega}\int_{\xi=0}^{\xi=1}\{\delta u(\xi)\}_{,\xi}^T[B^1(\eta)]^T[D][B^1(\eta)]\xi\{u(\xi)\}_{,\xi}|J|d\xi d\eta + \int_{\partial\Omega}\int_{\xi=0}^{\xi=1}\{\delta u(\xi)\}_{,\xi}^T[B^1(\eta)]^T[D][B^2(\eta)]\{u(\xi)\}|J|d\xi d\eta\\ &+ \int_{\partial\Omega}\int_{\xi=0}^{\xi=1}\{\delta u(\xi)\}^T[B^2(\eta)]^T[D][B^1(\eta)]\{u(\xi)\}_{,\xi}|J|d\xi d\eta + \int_{\partial\Omega}\int_{\xi=0}^{\xi=1}\{\delta u(\xi)\}^T[B^2(\eta)]^T[D][B^2(\eta)]\frac{1}{\xi}\{u(\xi)\}|J|d\xi d\eta\end{aligned} \tag{2.26}$$

Green's theorem leads to the following formulation:

$$\begin{aligned}
&\int_V \{\delta\epsilon(\xi,\eta)\}^T\{\sigma(\xi,\eta)\}dV \\
&= \int_{\partial\Omega} \{\delta u(\xi)\}^T[B^1(\eta)]^T[D][B^1(\eta)]\xi\{u(\xi)\}_{,\xi}|J|d\eta\Big|_{\xi=1} - \int_{\partial\Omega} \{\delta u(\xi)\}^T[B^1(\eta)]^T[D][B^1(\eta)]\times\{\{u(\xi)\}_{\xi}+\{u(\xi)\}_{\xi\xi}\}|J|d\xi d\eta \\
&\quad + \int_{\partial\Omega} \{\delta u(\xi)\}^T[B^1(\eta)]^T[D][B^2(\eta)]\{u(\xi)\}|J|d\eta\Big|_{\xi=1} - \int_{\partial\Omega}\int_{\xi=0}^{\xi=1} \{\delta u(\xi)\}^T[B^1(\eta)]^T[D][B^2(\eta)]\{u(\xi)\}_{,\xi}|J|d\xi d\eta \\
&+ \int_{\partial\Omega}\int_{\xi=0}^{\xi=1} \{\delta u(\xi)\}^T[B^2(\eta)]^T[D][B^1(\eta)]\{u(\xi)\}_{,\xi}|J|d\xi d\eta + \int_{\partial\Omega}\int_{\xi=0}^{\xi=1} \{\delta u(\xi)\}^T[B^2(\eta)]^T[D][B^2(\eta)]\frac{1}{\xi}\{u(\xi)\}|J|d\xi d\eta
\end{aligned} \tag{2.27}$$

In order to simplify the above equation, the following substitutions are introduced:

$$[E^0] = \int_{\partial\Omega} [B^1(\eta)]^T[D][B^1(\eta)]|J|d\eta \tag{2.28a}$$

$$[E^1] = \int_{\partial\Omega} [B^1(\eta)]^T[D][B^2(\eta)]|J|d\eta \tag{2.28b}$$

$$[E^2] = \int_{\partial\Omega} [B^2(\eta)]^T[D][B^2(\eta)]|J|d\eta \tag{2.28c}$$

These simplifications are named "coefficient matrices" and resemble in structure the stiffness matrix of standard FEM schemes. They are calculated element wise and then assembled in the standard FEM sense. Applying boundary conditions on the coefficient matrices is premature, as this will effectively delete parts of the domain corresponding to the space spanned by the DOFs on the boundary and the scaling center. Using the same notation to denote the fully assembled coefficient matrices, the previous equations are rewritten as follows using an abbreviation on the boundary $\{u\}\hat{=}\{u(\xi=1)\}$:

$$\begin{aligned}
&\int_V \{\delta\epsilon(\xi,\eta)\}^T\{\sigma(\xi,\eta)\}dV \\
&= \{\delta u\}^T\{[E^0]\{u\}_{,\xi} + [E^1]^T\{u\}\} - \int_{xi=0}^{\xi=1} \{\delta u(\xi)\}^T\Big\{[E^0]\xi\{u(\xi)\}_{,\xi\xi} + [[E^0]+[E^1]^T-[E^1]]\{u(\xi)\}_{,\xi} - [E^2]\frac{1}{\xi}\{u(\xi)\}\Big\}d\xi
\end{aligned} \tag{2.29}$$

In order for this equation to hold for all ξ, which implies it should be continuously satisfied in radial direction and only compliant in the finite element sense in the tangential direction, the conditions specified by both Eq. 2.30 on the boundary and Eq. 2.31 in the domain, must be satisfied:

$$\{P\} = [E^0]\{u\}_{,\xi} + [E^1]^T\{u\} \tag{2.30}$$

$$[E^0]\xi^2\{u(\xi)\}_{,\xi\xi} + [[E^0]+[E^1]^T-[E^1]]\xi\{u(\xi)\}_{,\xi} - [E^2]\{u(\xi)\} = \{0\} \tag{2.31}$$

The above equation is termed the scaled boundary finite element equation in displacement. Alternatively, one could also formulate the scaled boundary finite element equation in the time or frequency domain by including inertial effects into the virtual work equation. Eq. 2.31 is equivalent to earlier work from Wolf and Song, who first used a mechanically based approach [344] and then a weighted residual method [342]. However, this derivation is more consistent with standard engineering principles and understanding. Eq. 2.31 is characterized as a homogeneous set of Euler-Cauchy differential equations.

2.2.2 Solution Procedure

The general solution to the scaled boundary finite element equation can be written in power series form as:

$$\{u(\xi)\} = c_1\xi^{-\lambda_1}\{\phi_1\} + c_2\xi^{-\lambda_2}\{\phi_2\} + \ldots + c_n\xi^{-\lambda_n}\{\phi_n\} = [\phi]\xi^{\lceil-\lambda\rfloor}\{c\} \tag{2.32}$$

where λ_i and $\{\phi_i\}$ are the corresponding eigenvalues and vectors respectively. The boundary conditions determine the integration constants c_i. As a result, the solution of SBFEM in statics strongly resembles the

mode superposition method of FEM. Hence, the eigenvectors $\{\phi_i\}$ can be interpreted as modal displacement vectors on the boundary with a corresponding scaling factor in the radial direction λ_i (Fig. 2.4).

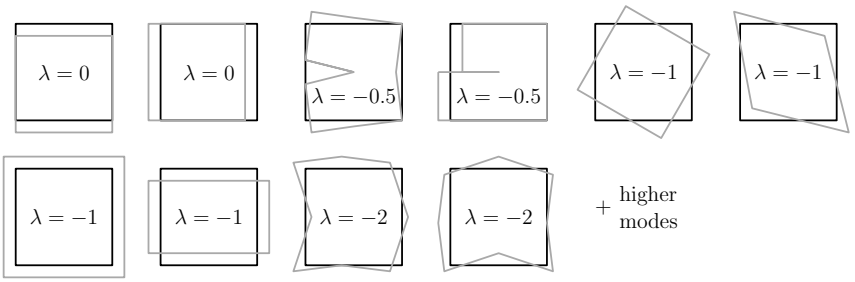

Fig. 2.4: Graphical representation of modes in a square domain with square root singularity. In black the original domain with linear elements and in gray the modes with corresponding values.

A quadratic eigenproblem results from substituting the general solution into the scaled boundary finite element equation in displacements:

$$[\lceil\lambda\rfloor^2[E^0] - \lceil\lambda\rfloor[[E^1]^T - [E^1]] - [E^2]]\{\phi\} = \{0\} \tag{2.33a}$$

$$\{q\} = [[E^1]^T - \lceil\lambda\rfloor[E^0]]\{\phi\} \tag{2.33b}$$

In Eq. 2.33b the boundary forces are expressed in an equivalent modal formulation. Conceptually, they constitute the nodal force modes $\{q\}$, which balance the corresponding displacement modes on the boundary, who are directly dependent on $\{\phi\}$ by definition of the general solution. Linearizing the quadratic eigenproblem has been shown to be beneficial in the context of fracture mechanics [291]. Unfortunately, this means doubling the size of the eigen-problem. This is achieved by rearranging the equivalent nodal forces equation (Eq. 2.33b) to obtain:

$$\lceil\lambda\rfloor\{\phi\} = [E^0]^{-1}[[E^1]^T\{\phi\} - \{q\}] \tag{2.34}$$

which is in turn substituted into the scaled boundary finite element equation (Eq. 2.33a):

$$\lceil\lambda\rfloor[E^0][E^0]^{-1}[[E^1]^T\{\phi\} - \{q\}] - \lceil\lambda\rfloor[E^1]^T\{\phi\} + [E^1][E^0]^{-1}[[E^1]^T\{\phi\} - \{q\} - [E^2]\{\phi\}] = \{0\} \tag{2.35}$$

which is equivalent to:

$$\lceil\lambda\rfloor\{q\} = [E^1][E^0]^{-1}[[E^1]^T\{\phi\} - \{q\} - [E^2]\{\phi\}] \tag{2.36}$$

The linearized, combined form of the quadratic eigen-problem can thus be expressed more compactly in matrix notation as:

$$[Z]\begin{Bmatrix}\phi\\ q\end{Bmatrix} = \lceil\lambda\rfloor\begin{Bmatrix}\phi\\ q\end{Bmatrix} \tag{2.37}$$

with

$$[Z] = \begin{bmatrix}[E^0]^{-1}[E^1]^T & -[E^0]^{-1}\\ [E^1][E^0]^{-1}[E^1]^T - [E^2] & -[E^1][E^0]^{-1}\end{bmatrix} \tag{2.38}$$

where $[Z]$ is a Hamiltonian matrix. This special matrix form mandates symmetry about the real and the imaginary axis for all eigenvalues. As a result, the eigenvalues corresponding to rigid body translational modes can pose significant numerical issues. Machine precision can cause these eigenvalues to arbitrarily alternate in sign.

Since eigenvalues of opposite sign contribute to the response of the system in fundamentally different ways, which will be detailed in the following paragraph, they should be sorted accordingly.

$$[Z]\begin{Bmatrix}\phi\\ q\end{Bmatrix} = \lceil\lambda\rfloor\begin{Bmatrix}\phi\\ q\end{Bmatrix} = \begin{bmatrix}\lceil\lambda_{neg}\rfloor & \\ & \lceil\lambda_{pos}\rfloor\end{bmatrix}\begin{bmatrix}[\phi_1] & [\phi_2]\\ [Q_1] & [Q_2]\end{bmatrix} \tag{2.39}$$

The subscripts “pos" and “neg" refer to positive and negative eigenvalues respectively, which bear the effect of separating the bounded from the unbounded response. For negative eigenvalues the contribution at $\xi = 0$ is bounded and at $\xi = 1$ has a finite value, which represents a solution in agreement with that of

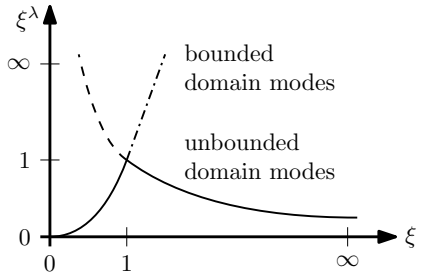

Fig. 2.5: Contributions of the domain modes to the bounded and unbounded domain solutions

the bounded domain, whereas for positive eigenvalues the contribution at $\xi = 1$ is finite and at $\xi = \infty$ is bounded, resembling the solution of an unbounded domain (Fig. 2.5).
Having determined the eigenvalues and eigenvectors, these can be substituted into the general solution (Eq. 2.32) for determining the domain stiffness matrix.

$$\{u(\xi)\} = [\phi_1]\xi^{\lceil -\lambda_{neg} \rfloor}\{c_1\} + [\phi_2]\xi^{\lceil -\lambda_{pos} \rfloor}\{c_2\} \tag{2.40}$$

Considering that only the negative eigenvalues contribute to the response of the bounded domain, the terms associated with the positive eigenvalues of Eq. 2.40 are discarded. Next, in order to evaluate the stiffness matrix, the displacement modes must be linked to the force modes. This is achieved by comparing the displacements on the boundary $\{u(\xi = 1)\}$ with the acting nodal forces $\{P\}$. Enforcing the corresponding boundary conditions, by applying the integration constants to the force modes, results in the following formulation:

$$\{P_{bounded}\} = [Q_1]\{c_1\} \tag{2.41}$$

The integration constants are obtained by evaluating Eq. 2.40 at $\xi = 1$.

$$\{c_1\} = [\Phi_1]^{-1}\{u(\xi = 1)\} \tag{2.42}$$

In a subsequent step, the integration constants are substituted into Eq. 2.33b:

$$\{P_{bounded}\} = [Q_1][\Phi_1]^{-1}\{u(\xi = 1)\} \tag{2.43}$$

Therefore, the stiffness matrix of a bounded domain is found to be:

$$K_{bounded} = +[Q_1][\Phi_1]^{-1} \tag{2.44}$$

The stiffness matrix is symmetric, though fully populated. Hence, the use of higher order elements is not penalized by higher bandwidth as in standard FEM approaches.

Similarly, the stiffness matrix for the unbounded domain may be determined by utilizing the analogous expressions of the unbounded domain:

$$K_{unbounded} = -[Q_2][\Phi_2]^{-1} \tag{2.45}$$

In order to perform the back calculation of strains and stresses, first the integration constants (Eq. 2.42) must be determined, next the general solution (Eq. 2.40) is sought, and only then are the strains (Eq. 2.20) and stresses (Eq. 2.22) derived.

In order to better understand the steps, computational complexity and effort required for an SBFEM analysis the flowcharts in Figs. 2.6 and 3.2 are provided. Restricting discretization along the boundary when using SBFEM comes mainly at the price of the solution of an eigen-problem. Therefore, domains with minimal surface to volume ratio are especially suited for analysis using SBFEM.

Very similarly to standard FE-based approaches, first element-wise coefficient matrices are evaluated and assembled using a standard numerical integration procedure. However, this must be performed for three separate coefficient matrices. As opposed to XFEM though, no additional enrichment terms must be included, and thus the need for integration of singular terms is eliminated. Since in SBFEM all elements

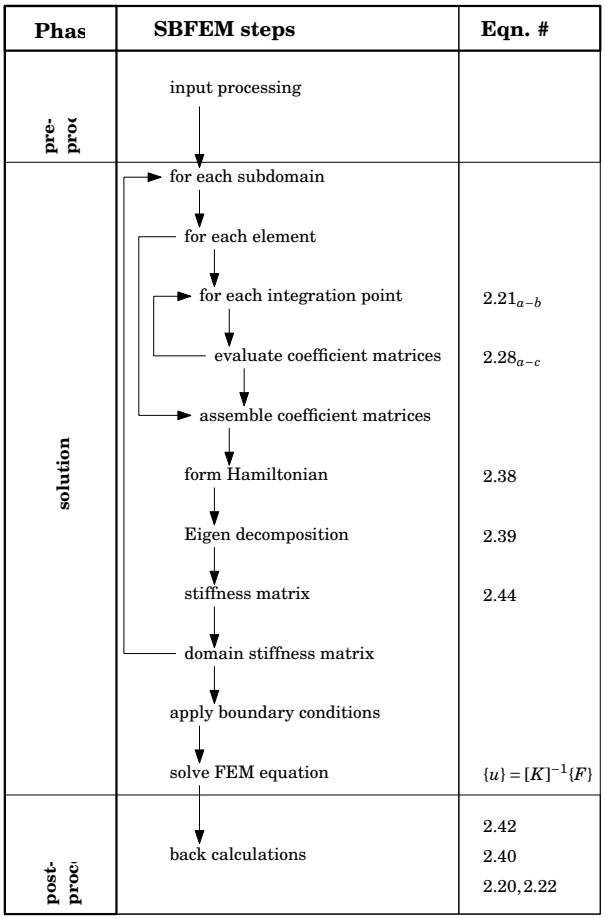

Fig. 2.6: Flowchart of a SBFEM analysis linked to corresponding equations from sec. 2.2.

can be treated equally, many issues pertaining to the condition number of the stiffness matrix can be avoided. Additionally, no further assumptions, for instance pertaining to what type of singularity to include in the crack tip enrichment, are put in place.

In 2D, since the domain is represented by a linked series of bar-type elements, the assembled coefficient matrices are highly sparse and their entries are clustered about the diagonals facilitating the inversion required for constructing the Hamiltonian matrix $[Z]$. The eigen-decomposition is the central core of SBFEM analysis, as it not only is necessary for determining the stiffness matrix, but also delivers the analytical solution for the displacements in radial direction. Once the stiffness matrix is formed, the remaining steps coincide with those of the standard FEM approach. Significant differences may be identified, in the calculation of the SIFs, when compared against the XFEM approach. Not only are the SIF easily identified, efficiently extracted in post-processing, smoothed for further accuracy and used to determine an effective error-estimator in SBFEM (sec. 4.1), but they are additionally exempt from parameter-specific dependencies, such as the radius of integration and enrichment in XFEM. To see how this contributes to reducing computational complexity, approximate flop counts are listed in Tbl. 4.6.

Unfortunately, the calculation of the eigenvalues, λ_i, and eigen-vectors, ϕ_i, by means of eigen-decomposition can result in numerical errors, when near parallel eigen-vector pairs are present [291]. To alleviate this, the block-diagonal Schur decomposition may be adopted [92]. The displacement solution is obtained as a superposition (Fig. 2.4) of the modes, with associated scaling values, and constrained by integration constants c_i, as obtained from the imposed boundary conditions.

$$\{u(\xi)\} = [\Psi^{(u)}]\xi^{-[S]}\{c\} = \sum_{i=1}^{n} \{\Psi_i^{(u)}\}\xi^{-S_i} c_i \tag{2.46}$$

The transformation matrix $[\Psi]$ and block diagonal real Schur form $[S]$ are derived from recasting the

system of first order differential equations as:

$$\xi \begin{Bmatrix} \{u(\xi)\} \\ \{q(\xi)\} \end{Bmatrix}_{,\xi} = -Z \begin{Bmatrix} \{u(\xi)\} \\ \{q(\xi)\} \end{Bmatrix} \tag{2.47}$$

with the Hamiltonian coefficient matrix $[Z]$ defined as in Eq. (2.38) so that Eq. (2.47) is decoupled by the block-diagonal Schur decomposition.

$$[Z][\Psi] = [\Psi][S] \tag{2.48}$$

The columns of the transformation matrix contain the modes, whereas the diagonal blocks of the real Schur form contain the corresponding eigenvalues. However, Eq. (2.47) results in doubling the amount of DOFs present in the solution, which can be shown to contain a bounded response ($0 < \xi < 1$ and negative eigenvalues) and an unbounded response ($1 < \xi < \infty$ and positive eigenvalues). $[S]$ and $[\Psi]$ are sorted in ascending order and partitioned accordingly.

$$[S] = diag([S_{neg}],[S_{pos}]) \tag{2.49}$$

$$[\Psi] = \begin{bmatrix} [\Psi^{(u)}_{neg}] & [\Psi^{(u)}_{pos}] \\ [\Psi^{(q)}_{neg}] & [\Psi^{(q)}_{pos}] \end{bmatrix} \tag{2.50}$$

By expressing the nodal forces on the boundary with enforced integration constants, an expression for the stiffness matrix of the subdomain is obtained and a displacement solution is calculated analogous to FEM:

$$[K_{bounded}] = [\Psi^{(q)}_{pos}][\Psi^{(u)}_{neg}]^{-1} \tag{2.51}$$

Finally, the stresses are obtained by substituting Eq. (2.46) into Eq. (2.22):

$$\{\sigma(\xi,\eta)\} = [\Psi_\sigma(\eta)]\xi^{-[S_{neg}-I]}\{c\} \tag{2.52}$$

where $[\Psi_{\sigma i}(\eta)]$ is the stress mode of the corresponding displacement mode $[\Psi^{(u)}_i]$.

$$[\Psi_\sigma(\eta)] = [D](-[B^1(\eta)][\Psi^{(u)}_{neg}][S_{neg}] + [B^2(\eta)][\Psi^{(u)}_{neg}]) \tag{2.53}$$

The calculation of the stress on the domain boundary ($\xi = 1$) does not require the evaluation of the matrix exponential $\xi^{[S]-[I]}$. This is beneficial when sufficient discretisation of the domain is achieved, e.g. via use of quadtree meshes. However, in case the complete domain is represented by a single large-sized SBFEM cell, the evaluation of displacements and stresses at internal points can become computationally intensive.

2.2.3 Constraints

Several minor constraints are associated with the use of SBFEM as the discretization method.

- Only star-convex domains can be treated.
- Elements containing a crack tip can only incorporate straight crack sides.
- Features in radial direction are analytically captured and cannot be discretized further due to a degenerate Jacobian. Quantities acting along redial direction must therefore be incorporated into the scaled boundary equation in displacements.
- The translational modes obtained from the eigen-decomposition must be overwritten.

The first three constraints are easily overcome by subdividing the domain. Treatment of the translational modes is more invasive, yet still simple. Since the associated eigen-values with value zero are subject to machine precision errors, the sorting procedure is error prone. Therefore, directly after completion of the eigen-decomposition, the two corresponding eigen-modes are overwritten with rigid body modes corresponding to translation, while the eigenvalues are prescribed equal to zero. This procedure consists of rectifying machine precision issues by enforcing physical knowledge of the system.

2.2.4 Generalized Stress Intensity Factors (gSIFs)

Since the general solution to the SBFEM equation is extracted as a power series, the singular modes are readily identified: By inspection of S_i any $-1 < \texttt{real}(\lambda) < 0$ will result in a singularity at $\xi = 0$. Placement of the scaling center at a crack tip may be exploited to calculate the generalized SIFs (Fig. 2.7a). By including

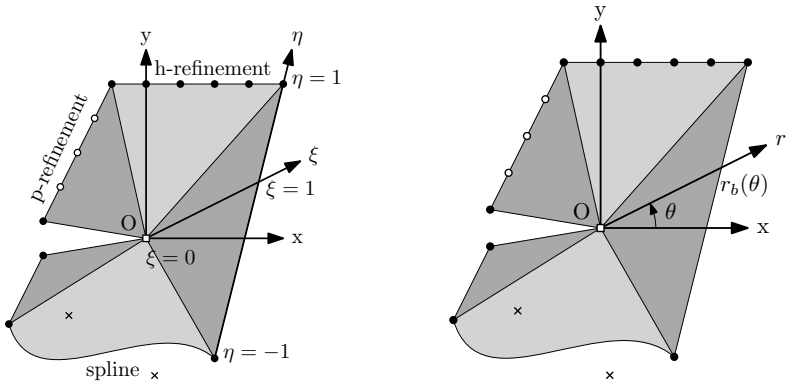

(a) Polygon domain with scaled boundary coordinates

(b) Transformation to polar coordinates of singular stress field around crack tip

Fig. 2.7: Domain discretisation, scaling center O and introduction of scaled boundary coordinated

a double node at the crack mouth, two additional modes, the singular modes, arise (Fig. 2.4), whose eigenvectors resemble the mode I and mode II fracture cases. The singular stress field is extracted from the general solution (Eq. (2.52)), where the superscript $^{(s)}$ denotes the singular quantities:

$$\{\sigma^{(s)}(\xi,\eta)\} = [\Psi^{(s)}_{\sigma}(\eta)]\xi^{-[S^{(s)}-I]}\{c^{(s)}\} \tag{2.54}$$

For consistency with other numerical methods and experimental reporting, a characteristic length L is introduced and a transformation to polar coordinates is sought (Fig. 2.7b):

$$\xi = \frac{r}{r_b(\theta)} = \frac{L}{r_b(\theta)} \times \frac{r}{L} \tag{2.55}$$

The singular stress field is equivalently expressed in polar coordinates as:

$$\{\sigma^{(s)}(r,\theta)\} = [\Psi^{(s)}_{L}(\theta)]\left(\frac{r}{L}\right)^{-[S^{(s)}-I]}\{c^{(s)}\} \tag{2.56}$$

implying the corresponding stress modes $[\Psi^{(s)}_{L}(\theta)]$ given by:

$$[\Psi^{(s)}_{L}(\theta)] = [\Psi^{(s)}_{\sigma}(\eta(\theta))]\left(\frac{L}{r_b(\theta)}\right)^{-[S^{(s)}-I]} \tag{2.57}$$

For the case of 2D elastostatics, two singular stress modes exist. Hence, $[S^{(s)}]$ and $[\Psi^{(s)}_{L}(\theta)]$ reduce to matrices $\in \mathbb{R}^{2\times 2}$, while both $\{c^{(s)}\}$ and $\{\sigma^{(s)}(r,\theta)\}$ form vectors $\in \mathbb{R}^2$. More specifically, only the components of $\{\sigma^{(s)}(r,\theta)\} = (\sigma^{(s)}_{\theta}(r,\theta), \tau^{(s)}_{r\theta}(r,\theta))^T$ are retained, which correspond to mode I and II cracks, for which the formal definition of the gSIFs at angle θ is given as [296]:

$$\begin{Bmatrix} \sigma^{(s)}_{\theta}(r,\theta) \\ \tau^{(s)}_{r\theta}(r,\theta) \end{Bmatrix} = \frac{1}{\sqrt{2\pi L}}\left(\frac{r}{L}\right)^{-[\tilde{S}^{(s)}(\theta)]} \begin{Bmatrix} K_I(\theta) \\ K_{II}(\theta) \end{Bmatrix} \tag{2.58}$$

The *matrix of orders of singularity* $[\tilde{S}^{(s)}(\theta)]$ is introduced such that:

$$[\tilde{S}^{(s)}(\theta)] = [\Psi_L^{(s)}(\theta)]([S^{(s)} + I])[\Psi_L^{(s)}(\theta)]^{-1} \tag{2.59}$$

$$\begin{Bmatrix} \sigma_\theta^{(s)}(r,\theta) \\ \tau_{r\theta}^{(s)}(r,\theta) \end{Bmatrix} = \left(\frac{r}{L}\right)^{-[\tilde{S}^{(s)}(\theta)]} [\Psi_L^{(s)}(\theta)]\{c^{(s)}\} \tag{2.60}$$

Comparing Eq. (2.58) with Eq. (2.60) permits the evaluation of the gSIFs as:

$$\begin{Bmatrix} K_I(\theta) \\ K_{II}(\theta) \end{Bmatrix} = \sqrt{2\pi L}[\Psi_L^{(s)}(\theta)][c^{(s)}] \tag{2.61}$$

The use of the matrix order of singularity automatically accounts for special cases in material interfaces. This is achieved by its off-diagonal terms [296]. Consequently, the SBFEM does not pose any a priori assumption on the type of singularity, which greatly facilitates the simulation of crack propagation through heterogeneous media.

Since the SIFs are directly evaluated using singular stress modes, standard recovery techniques may be applied, in order to improve on the solution during post-processing. Two pertinent methods are the SPR theory [367, 368, 83] and curve fitting by splines [239]. In the former, an improved estimation of the singular stresses is obtained by smoothing the singular stress modes by means of SPR theory (sec. 4.1). The main benefit originates in the availability of error estimators [92] and the theoretical underpinning of the method. The latter is highly pragmatic and empirically offers comparable accuracy at reduced computational cost. Differing from the SPR method, the singular stresses computed at the Gauss points are fitted using a spline.

2.2.5 Hierarchical Meshes

Early efforts in SBFEM were limited due to the lack of specialized meshers. With the advent of polygon and virtual finite element methods ([334],[312],[317]), this was partially remedied, allowing for treatment of more involved and practical numerical examples. Specifically the use of the quadtree decomposition [238] has established itself as the predominant mesh choice ([235],[241],[67]), since it elegantly complements SBFEM's polygon underpinnings. By restricting the differences in cell sizes between neighbors to a ratio of 2:1, i.e., by enforcing balanced quadtrees (Fig. 2.8b), it suffices to precompute only 16 realizations of SBFEM subdomains, while issues commonly associated with hanging nodes are alleviated.

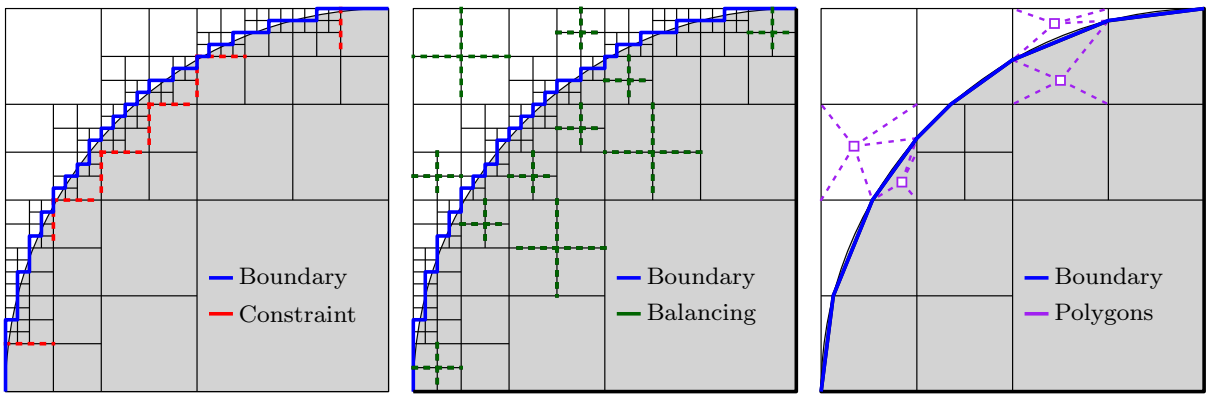

(a) Conventional QT decomposition. (b) Balanced QT decomposition. (c) Hybrid-polygon QT decomposition.

Fig. 2.8: Polygon clipping operating on a balanced quadtree decomposition enables accurate geometry representation with coarser meshes.

Features which do not align with the square grid of the quadtree decomposition require special treatment. In the standard FEM, this is achieved by mans of refinement near boundaries, until the lower threshold to a user-specified block size is reached. Generally, this results in step-like boundaries (Fig. 2.8a) and excessively fine meshes. This is mitigated in SBFEM by employing polygon clipping. Consequently, the mesh consists of a) standard square cells and b) clipped polygon cells (Fig. 2.8c). So-called hybrid

quadtree meshes combine both types of cells, with the benefit of improved approximation of the geometry, at coarser discretisation levels. Standard FEM quadtree decompositions are nonetheless also adopted in SBFEM analyses, mostly in the context of automated image-based stress analysis [276], where the input data (pixel information) is inherently jagged by nature. In conclusion, balanced quadtree meshes are economical to construct, automatically provide a certain degree of adaptivity around changing domain features and permit efficient analysis using the SBFEM by exploiting precomputation.

The schemes proposed in this thesis exploit the balanced hybrid-polygon quadtree decomposition as a mesh for SBFEM analysis. The quadtree decomposition is termed after the method by which it subdivides heterogeneous domains: A parent cell is bisected both horizontally and vertically, thus resulting in and being replaced by four equally sized new cells, which are referred to as its children. If this procedure is performed often enough, the resulting graphical representation (Fig. 2.9a) resembles that of a tree. The criterion, which dictates how and when to subdivide is dependent on the variant of quadtree decomposition used. Typically, a distinction is made between image and feature based SBFEM analysis. Image based analysis appraises the gray-scale values contained within the parent cell. If the difference between the minimum and maximum values is larger than a user specified tolerance, the cell is subdivided. For feature based analysis, the criterion for subdivision is based on the points comprising the polygon, which describes the problem geometry: If more points are detected within a cell than permitted according to user input, then the cell is subdivided. A typical resulting quadtree decomposition is depicted in Fig. 2.9b. Characteristic is the excessive refinement about boundaries, while these are still represented coarsely, in a step-like fashion. Many different element realizations (orientation, size, neighbor configurations, transitions, etc.) arise, rendering the resulting decomposition highly irregular. A polygon based FEM variant such as SBFEM can directly employ the quadtree decomposition as its mesh, however, from a computational expenses perspective, this would mandate treating each cell individually. Upon balancing the quadtree, i.e., enforcing all neighbouring cells to exhibit at most a 2:1: ratio in size difference, the irregularities are minimized as at most 16 different realizations of cells arise. Quantities associated with these cells can be trivially precomputed and stored for later retrieval, rendering this approach highly computationally efficient. Further, the transitions in element sizes across the decomposition domain are smoothed (Figs. 2.10a and 2.10b). Yet, the issue of coarse resolution on boundaries still remains, necessitating excessive mesh refinement to minimize errors in geometry representation. Since the SBFEM permits the treatment of star convex, polygonal domains, a complementary approach arises, which simultaneously alleviates excessive mesh refinement and enables an improved treatment of the boundary representation: The hybrid-polygon quadtree decomposition. All generic quadtree cells along the boundaries are additionally subjected to polygon clipping, thus generating polygon cells. The benefits of fusing these two types of cells within a mesh, comes at the price of having to treat each of these newly clipped cells individually. Fortunately, this permits the usage of coarser quadtree decompositions and thus meshes, which offset the computational toll introduced by clipping the boundaries. Though polygon clipping can in principal be performed on any type of quadtree decomposition, for computational efficiency reasons during SBFEM analysis the balanced variant is preferred, resulting in the balanced hybrid-polygon quadtree decomposition.

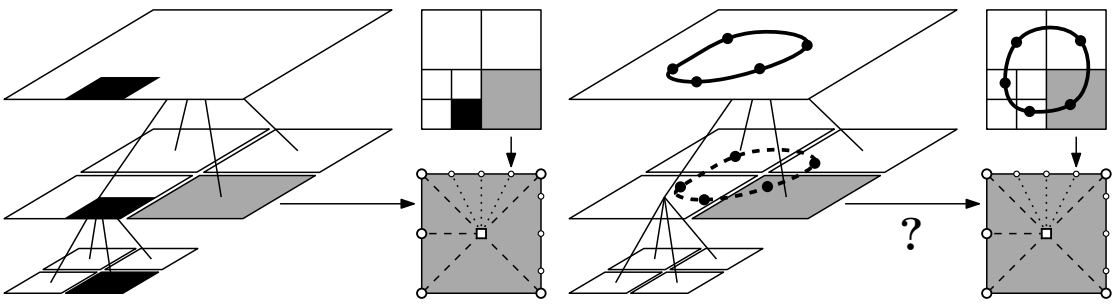

(a) Image-based quadtree decomposition. (b) Feature-based quadtree decomposition.

Fig. 2.9: Example of image decomposition by quadtree algorithm with sample SBFEM polytope element in gray.

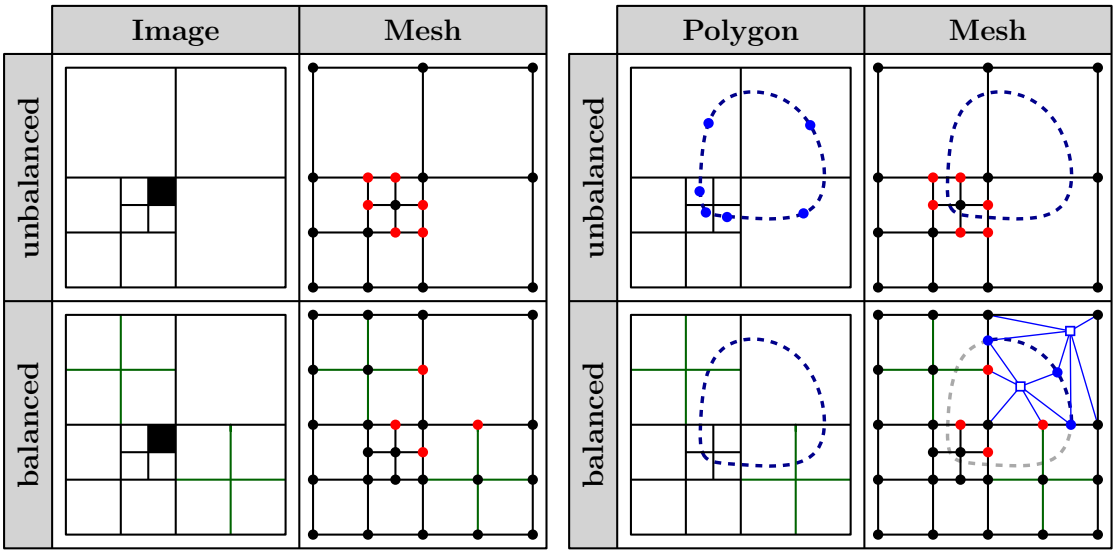

(a) Image-based quadtree decomposition.

(b) Feature-based quadtree decomposition.

Fig. 2.10: Segmentation of input with resulting mesh for unbalanced and balanced quadtree decompositions. Hanging nodes in red and additional elements introduced due to balancing in green.

2.2.6 Crack Propagation on Hierarchical Meshes

Cracks are introduced into the hybrid balanced quadtree mesh by polygon clipping [238]. Traversed blocks are split into two parts, by introducing a double node. Blocks containing a crack tip are augmented with an additional node, where the crack enters, and the scaling center is placed to coincide with the crack tip (Fig. 2.11a). Discretisation of the crack tip segment is not required, since its solution is included in the radial and therefore analytic portion of the SBFEM solution. Specifically, discretisation of the crack tip segment is not permitted, due to the Jacobian of the respective element equalling zero.

In the case of crack propagation, the SIFs have to be calculated with sufficient accuracy. Since a simply cracked block does not permit sufficient resolution of the singular stress field or its radial distribution, a region surrounding the crack tip is homogenized (Figs. 2.11b and 2.11c). The crack is then propagated by imposing a suitable criterion, e.g., Eq. (5.5), with which the new crack tip is then projected (Fig. 2.11d).

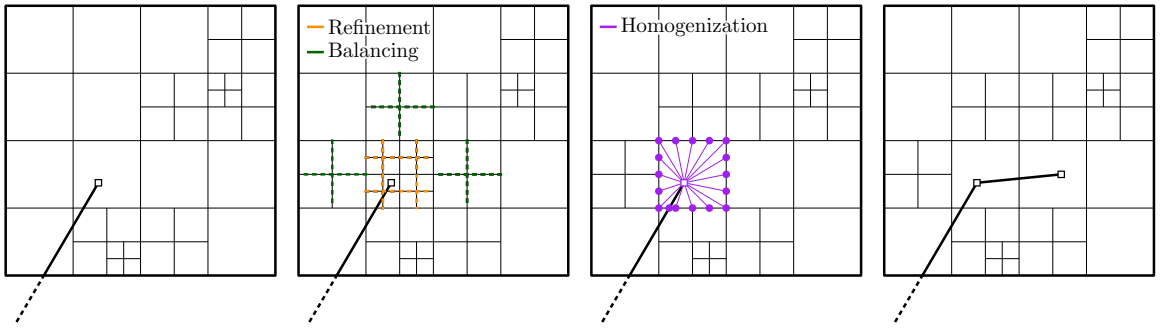

(a) Crack entering existing balanced quadtree region.

(b) Refinement and balancing around crack tip.

(c) Unifying cells into SBFEM macro element around crack tip

(d) New crack tip projected by gSIFs and Δa.

Fig. 2.11: Main steps in SBFEM crack propagation scheme.

2.3 The Hamiltonian Schur Decomposition (HSchur)

The SBFEM solution process benefits from the adoption of the Hamiltonian Schur decomposition (HSchur) in multiple ways:

- It eliminates the need for an arbitrary stabilizing parameter ϵ, traditionally given by $[E^2] = [E^2] + \epsilon[I]$.
- By respecting Hamiltonian symmetry of the eigenvalues, regular and steeper convergence rates can be achieved.
- The doubling of the problem size when linearizing the quadratic eigenvalue problem is reversed and thus computational complexity is significantly reduced.
- It still benefits from a Schur form, which allows to quantify general SIFs for bi-material interfaces.

The following is an abridged treatment of the theory first presented in [193] with emphasis placed on the parts integral to SBFEM. To alleviate visual clutter, all quantities are considered as matrices unless explicitly stated otherwise.

A matrix $H \in \mathbb{R}^{2n \times 2n}$ is Hamiltonian iff:

$$H_{start} = \begin{bmatrix} A & G \\ C & -A^T \end{bmatrix} \tag{2.62}$$

Additionally, $G^T = G$ and $C^T = C$, which holds for the case of SBFEM (Eq. 2.38).

Matrix H is said to be in Hamiltonian real Schur form if

$$H_{final} = \begin{bmatrix} T & G \\ 0 & -T^T \end{bmatrix}. \tag{2.63}$$

where T is quasitriangular. Any eigenvalue $+\lambda$ found in T has a corresponding eigenvalue $-\lambda$ in $-T^T$. For most applications it makes sense to group eigenvalues with same sign into T and $-T^T$ respectively.

In order to arrive at H_{final} from H_{start}, a series of orthogonal symplectic similarity transformations are performed:

$$H_{i+1} \leftarrow \hat{Q}^T H_i \hat{Q} \tag{2.64}$$

Every step is accompanied by the corresponding update, for which the starting values of Q_0 is chosen as I_{2n}:

$$Q_{i+1} \leftarrow Q_i \hat{Q} \tag{2.65}$$

In algorithmically formulating this process of arriving at the Hamiltonian real Schur form, first a symplectic URV decomposition of H is performed. The SLICOT library [232] provides the necessary backwards stable routines:

$$H = UR_1V^T \text{with } R_1 = \begin{bmatrix} S & G \\ 0 & T^T \end{bmatrix} \tag{2.66}$$

$T \in \mathbb{R}^{n \times n}$ is upper-triangular, $S \in \mathbb{R}^{n \times n}$ is quasitriangular and $G \in \mathbb{R}^{n \times n}$. It is at this point that the eigenvalues of H can be determined as they are equal to the square roots of the eigenvalues of the quasitriangular matrix $-ST$.

Next, the eigenvalues of $-ST$, which correspond to the eigenvalues of H^2 are partitioned into blocks. Many clustering algorithms exist, however here we choose an open ball with radius:

$$r = 10 \times ||S||_F ||T||_F \times \kappa \times \epsilon \tag{2.67}$$

$||\bullet||_F$ denotes the Frobenius norm, κ is the condition number of the eigenvalue, ϵ is machine precision and the factor 10 is included to arrive at a conservative estimate as originally proposed in [193]. Eigenvalues of overlapping balls are placed in the same block. Complex conjugates are then added to the block if they exist as well. In a last operation for this step, the eigenvalues of the URV decomposition are ordered to match their blocks. The new structure of the matrix $-ST$ is given as follows:

$$-ST = B = \begin{bmatrix} B_{11} & \dots & B_{1s} \\ & \ddots & \vdots \\ 0 & & B_{ss} \end{bmatrix} \tag{2.68}$$

The spectrum of B_{ii} is given by eigenvalues Λ_i of block $1 < i < s$. At this point, the first orthogonal symplectic update is performed using the sorted output of the URV decomposition:

$$H \leftarrow U^T H U \tag{2.69}$$

Henceforth, each block will be considered separately. The general procedure will be illustrated based on the first block B_{11} with size k. First, a QR decomposition is performed on:

$$[E_k \, HE_k] = QR \tag{2.70}$$

$E_k \in \mathbb{R}^{2n \times k}$ is the submatrix of I_{2n} constructed from the first k columns. Next, a Schur decomposition is performed:

$$G = Q^T H Q \xrightarrow{Schur} \widetilde{Q}\widetilde{T}\widetilde{Q}^T \tag{2.71}$$

The eigenvalues of $\widetilde{Q}$ are subsequently sorted into left- ($\widetilde{Q}_1$) and right ($\widetilde{Q}_2$) half plane respectively:

$$\widetilde{Q} = [\widetilde{Q}_1, \widetilde{Q}_1] \tag{2.72}$$

In order to construct an orthonormal basis for the invariant subspace of H, a matrix X is introduced as follows:

$$X = Q\widetilde{Q}_1 \tag{2.73}$$

The main task lies in transforming X into E_k and thus to achieve a deflation. This is carried out by means of finding an orthogonal symplectic S such that $S^T X = E_k$, which will be subsequently used to perform an update on $H \leftarrow S^T H S$. To this end, first X is partitioned to conform to the block sizes:

$$X = \left[\begin{array}{c} X_1 \\ \vdots \\ X_s \\ \hline X_{s+1} \\ \vdots \\ X_{2s} \end{array}\right] \tag{2.74}$$

S can be found as:

$$S = \begin{bmatrix} \hat{S} & 0 \\ 0 & \hat{S} \end{bmatrix} \quad \text{with} \quad \hat{S} = diag\{\check{S}, I\} \quad \text{and} \quad \check{S} = Q\widetilde{F} \tag{2.75}$$

$\widetilde{F}$ is a flip vector obtained from reversing the column order of the identity matrix $[I]$, Q results from the QR decomposition of the submatrix of X corresponding to $[X_{s+1}; X_{s+2}]$. After carrying out the updates $X \leftarrow \widetilde{S}^T X$ and $H \leftarrow \widetilde{S}^T H \widetilde{S}$, the vector X assumes the following form:

$$X = \left[\begin{array}{c} X_1 \\ \vdots \\ X_s \\ \hline 0 \\ X_{s+2} \\ \vdots \\ X_{2s} \end{array}\right] \tag{2.76}$$

Subsequent iterations on the lower blocks of X, introduce further blocks of zeros eventually resulting in:

$$X = \left[\begin{array}{c} X_1 \\ \vdots \\ X_s \\ \hline 0 \\ \vdots \\ 0 \\ X_{2s} \end{array}\right] \tag{2.77}$$

For the last block a slightly modified procedure must be applied as there is no successive block, which could be used to install a further block of zeros. For the last block the actions are modified, by considering the submatrix $[X_s; X_{2s}]$. Based on the QR decomposition of the aforementioned submatrix, from which $\breve{Q}$ results, the required updates $X \leftarrow \widetilde{Q}^T X$ and $H \leftarrow \widetilde{Q}^T H \widetilde{Q}$ are constructed:

$$\begin{bmatrix} X_s \\ X_{2s} \end{bmatrix} = \begin{bmatrix} \breve{Q}_1 \\ \breve{Q}_2 \end{bmatrix} R \tag{2.78}$$

and

$$\widetilde{Q} = \begin{bmatrix} \widetilde{Q}_1 & -\widetilde{Q}_2 \\ \widetilde{Q}_2 & \widetilde{Q}_1 \end{bmatrix} \quad \text{and } \widetilde{Q}_1 = diag\{I, \breve{Q}_1\};\ \widetilde{Q}_2 = diag\{I, \breve{Q}_2\} \tag{2.79}$$

This results in the entire lower portion of X running from blocks $s+1 < k < 2s$ to be filled with zeros.

In a next step, an analogous procedure for the block $1 < k < s$ will be applied. S can be found as:

$$S = \begin{bmatrix} \hat{S} & 0 \\ 0 & \hat{S} \end{bmatrix} \quad \text{with} \quad \hat{S} = diag\{\breve{S}, I\} \quad \text{and} \quad \breve{S} = Q \tag{2.80}$$

Q results from the QR decomposition of the submatrix of X corresponding to $[X_{s-1}; X_s]$. Again a block of zeros is inserted into X:

$$X = \left[\begin{array}{c} X_1 \\ \vdots \\ X_{s-1} 0 \\ \hline 0 \\ \vdots \\ 0 \end{array}\right] \tag{2.81}$$

This procedure is continued until only one block remains. After $2s-1$ updates of $X \leftarrow \widetilde{S}^T X$ and $H \leftarrow \widetilde{S}^T H \widetilde{S}$ the desired deflation is nearly achieved. At this point, the Hamiltonian matrix H is of the form:

$$H = \left[\begin{array}{cc|cc} A_{11} & A_{12} & G_{11} & G_{12} \\ 0 & A_{22} & G_{21} & G_{22} \\ \hline 0 & 0 & -A_{11}^T & 0 \\ 0 & C_{22} & -A_{11}^T & -A_{22}^T \end{array}\right] \tag{2.82}$$

It is now admissible to deflate the problem. Subsequent operations are performed on the following Hamiltonian submatrix:

$$H = \begin{bmatrix} A_{22} & G_{22} \\ C_{22} & -A_{22}^T \end{bmatrix} \tag{2.83}$$

This deflation is repeated for each block until the real Hamiltonian Schur form is reached:

$$H = \begin{bmatrix} A & G \\ 0 & -A^T \end{bmatrix} \tag{2.84}$$

Q contains the orthonormal basis for the stable invariant subspace. In a last step, a sorting of the eigenvalues and vectors spanning the stable invariant subspace is performed, in order to retain only negative eigenvalues. Such routines are also available in the Slicot library [232].

It therefore becomes evident that application of the HSchur decomposition in the solution process of SBFEM as proposed, will increase accuracy, while reducing complexity.

2.4 The Enhanced Multiscale Finite Element Method (EMsFEM)

Computational multiscale methods, in principle, aim to project dominant system behavior from a fine scale (micro) mesh onto a significantly coarser scale (macro) mesh, where the governing equations are solved at reduced computational cost. In contrast to homogenization methods, the EMsFEM follows a numerical approach to construct NBFs, which map the response between scales. The generality of this approach permits the treatment of an arbitrary number of scales as well as the construction of h-adaptive elements on the coarse scale mesh.

Implementing EMsFEM comprises four steps. Quantities inherent to the first two may be calculated prior to analysis, during the offline phase. Those associated with while the latter two must be computed during analysis, in the online phase.

1. Numerically construct the basis functions (Fig. 2.12)
2. Evaluate the equivalent coarse element stiffness matrix
3. Solve the governing equations on the macro-scale
4. Downscaling of the macro-scale solution to micro-scale

Here we first illustrate the overall procedure by means of linear boundary conditions and one specific BVP. Subsequently the general construction procedure of coarse element stiffness matrices is considered. Then, different types of boundary conditions and associated formulations are treated. Regions from which coarse scale representations are obtained, are termed RVEs.

The NBFs, which provide the mapping between scales (Fig. 2.12) are constructed numerically by solving a Dirichlet BVP on a RVE. We implement linear boundary conditions. These are constructed sequentially and independently of each other, permitting the use of parallel computing techniques. Example boundary displacements are illustrated in Fig. 2.12: A unit displacement is imposed at node 1 in x-direction. Displacements in x-direction vary linearly, analogous to bilinear shape functions, along the boundaries 12 and 14. The whole domain is constrained in y-direction. Additionally, boundaries 23 and 34 are further constrained in x-direction.

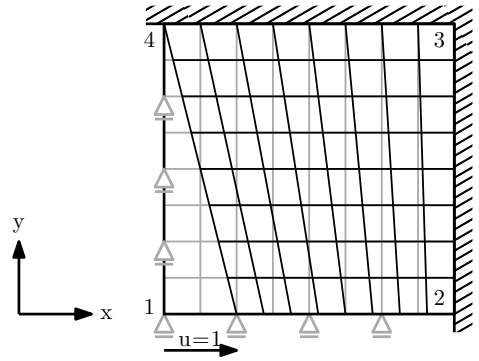

Fig. 2.12: Construction the linear NBFs by solving the associated Dirichlet BVP.

The resulting displacement solution comprises a column entry of the basis function mapping the effect of a unit displacement of the coarse scale to the response on the fine scale. Completing the procedure for all coarse DOF, by appropriately adapting the unit displacement and associated prescribed displacements on the boundary, results in:

$$\{u_e\} = [N]\{u_E\} \tag{2.85}$$

where $\{u_e\}$ contains the displacements of the fine scale mesh, $\{u_E\}$ is the displacement vector of the coarse mesh and [N] the basis function matrix. Here, [N] is a nDOF x 8 matrix for a RVE of 4 coarse nodes and 2 DOF per node, with columns obtained by solving the Dirichlet boundary value problem associated with the corresponding DOF. The method does not impose a limit on the amount of coarse nodes permitted per RVE.

Hence coarse element representing RVEs are abbreviated as CMX, where “CM” refers to coarse multiscale elements and “X” is the amount of coarse nodes (see sec. 5.1).

The equivalent stiffness matrix of a coarse element is obtained by energy equivalence. To this end, the strain energy of the fine scale is mapped to the coarse scale by means of Eq. 2.85.

$$\Pi_e = \frac{1}{2}\{u_e\}^T[K_e]\{u_e\} = \frac{1}{2}\{u_E\}^T[N]^T[K_e][N]\{u_E\} \tag{2.86}$$

with the equivalent stiffness matrix of the RVE therefore given as $[K_{RVE}] = [N]^T[K_e][N]$. $[K_e]$ is the RVE stiffness matrix on the micro-scale.

The macro-scale computations are then performed in the standard FEM sense. Upon solution of the governing equations on the coarse mesh, downscaling operations are necessary to evaluate the fine scale response. Through reverse mapping of the macro-scale displacements to the micro-scale (Eq. 2.85) the displacements are provided for each element on the fine scale and the standard procedures for strain and stress evaluation are available. The EMsFEM therefore permits the extension of any numerical method capable of solving Dirichlet BVPs to handle multiscale calculations. However, excessive over-constraining and thus overestimation of an RVE’s stiffness associated with the use of linear boundary conditions can limit the accuracy of the method. Periodic boundary conditions as well as oversampling techniques have been proposed to overcome such issues. For periodic boundary conditions, the restrained boundaries are exchanged with tie constraints, whereby opposite points are enforced to move in unison (Fig. 2.14). The prescribed displacement δx takes on a value of 1 at and in direction of its associated DOF and varies linearly until it vanishes at its neighboring coarse nodes. In essence it resembles the procedure to construct linear boundary conditions with the addition of multi-point constraints, which are enforced by Lagrange multipliers. Further, the use of periodic boundary conditions mandates the existence of opposite points (e.g., A^+ and A^- in Fig. 2.14) and implies a continuous strain field.

Although these linear and periodic boundary conditions have been employed in numerous studies, certain issues still remain: The exact fraction of δx to apply to each node, is based purely on geometric considerations (Fig. 2.15, top row), i.e., distance of a node to the application of unit displacement, thereby neglecting material properties. Oversampling is introduced to overcome this issue (Fig. 2.15, bottom row). By sampling a larger region on which a surrogate Dirichlet BVP is solved, the geometric constants can be replaced by ones incorporating knowledge of the RVEs material properties: The values of the calculated displacement constants are then applied as prescribed displacements on the original Dirichlet BVP. Hence, oversampling can be combined with both linear and periodic boundary conditions.

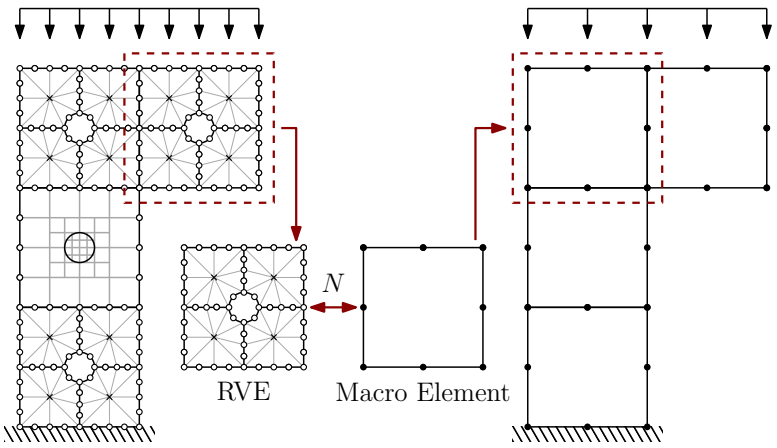

Fig. 2.13: Micro (left) and macro (right) scale representation of the problem domain with NBFs mapping RVE quantities to the corresponding macro element.

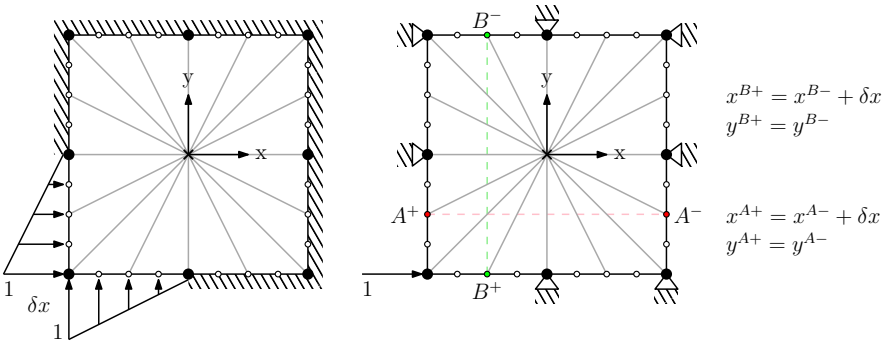

Fig. 2.14: Construction the NBF by solving the associated Dirichlet BVP. Left, application of linear boundary conditions for the CM8 element. Right, application of periodic boundary conditions. Quantities denoted by $\cdot^-$ and $\cdot^+$ form a tie-constraint. The use of periodic boundary conditions mandates the existence of opposite point pairs to tie-constrain.

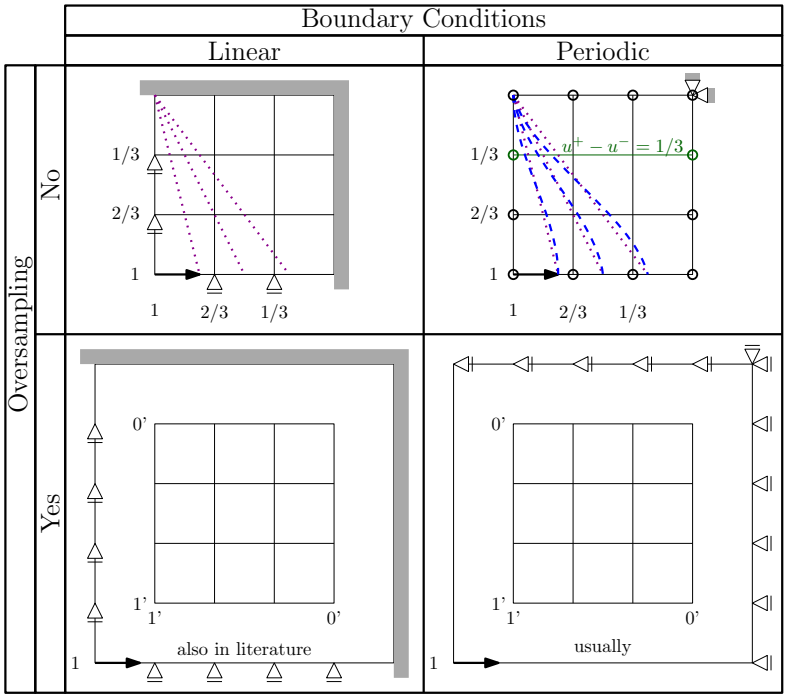

Fig. 2.15: Techniques of constructing boundary conditions for EMsFEM.

2.5 Damage Localization

2.5.1 The Inverse Problem

Inverse problems aim at identifying latent and unknown system parameters, based on measurement of the system response. Typically, though not necessarily, they are accompanied by an associated numerical model, as is the case in this study. The solution to the numerical model, i.e., the forward problem, is in practice often infeasible due to incomplete system information. In the presence of supplementary information, however, such as the measured system response, an inverse problem can be formulated to identify the remaining unknown system characteristics of the forward problem. This thesis treats parametrized structural flaws, in the form of strong (cracks) and weak (holes) discontinuities, as the aforementioned unknowns. A solution is sought by recasting to a minimization problem of several design parameters θ, which define the flaw's geometry. These include number, location, shape, size and orientation. The aim is to minimize the difference between measured system response (^{m}) and candidate response (^{h}). The latter is obtained by repeated forward analysis with iteratively improved design variables characterizing the flaw.

The measured response of structural systems typically comprises strains on specimen surfaces, though in principle displacements, velocities and accelerations suffice as well given appropriate excitation and measurement apparatus. Commonly, strains are calculated at and compared to the corresponding data at the measurement points. Should too few sensors exist, be positioned too far away from the flaw or not sensitive enough to adequately register their presence, the problem is said to be ill-posed and possibly without unique solution. The way in which the objective function $F(\theta_i)$, which must be minimized, is defined, greatly affects the well-posedness of the inverse problem. Typically, it relates the relative error between the actual measured response to the simulated response in the form of the L_2 norm. The inverse problem is therefore summarized as the following optimization problem:

$$\text{Find } \theta_i \text{ such that } F(\theta_i) \rightarrow \texttt{min} \quad i = 1, \ldots, n_{par} \tag{2.87}$$

where

$$F(\theta_i) = \frac{||\{\epsilon^m\} - \{\epsilon^h(\theta_i)\}||}{||\{\epsilon^m\}||} \tag{2.88}$$

The numerically computed strains at the sensor locations, due to the candidate flaw with specific realization parameters θ_i are consolidated into $\{\epsilon^h(\theta_i)\}$. The measured strains at the same locations are denoted by $\{\epsilon^m\}$. Depending on the measurement setup, the strains can contain up to three components for a 2D plane stress analysis.

2.5.2 Global Optimization Algorithms

Global algorithms are suitable for solving the optimization problem stated in Eq. 2.87. Since an evaluation of the objective function equates to performing a FEM analysis of the problem structure, computational efficiency concerns arise. Hence, the algorithm of choice should fulfill certain conflicting requirements, so to reduce the amount of necessary function evaluations: An algorithm must be both exploratory and exploitative. Exploratory behavior a) ensures that all regions of the response surface are explored, b) is the mechanism by which local minima are escaped and c) prohibits revisiting of already evaluated sections. The exploitative behavior of the algorithm determines how efficiently a local minimum is determined. Any algorithm capable of exploiting the physicality of the problem will exhibit favorable behavior.

The inherent non-convexity of such problems renders the use of efficient gradient-based algorithms unsuitable, since the line search component cannot escape a local minimum (Fig. 2.16, from `peaks` command in Matlab). The adoption of heuristic global optimization algorithms remedies this short-coming by exploiting its exploratory component at the cost of additional function evaluations, i.e., sampling and evaluating the fitness function for more varied combinations of θ_i. The way in which θ_i is sampled is specific to the flavor of global optimization algorithm utilized. Although several are employed throughout this thesis (see sec. 6.2), here the GA is presented for brevity: Its intuitive and simple structure permits a concise treatment, while covering most of the salient features characterizing global optimization algorithms.

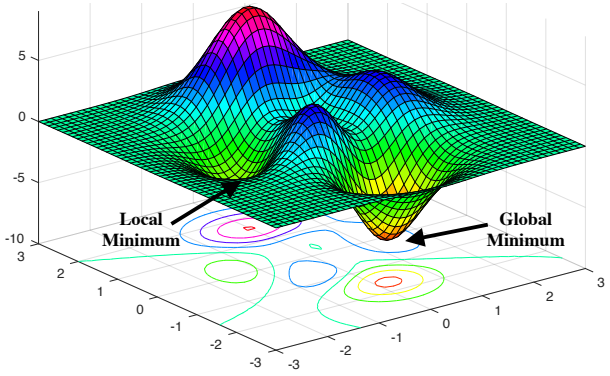

Fig. 2.16: Example of a surface with both local and global minimum.

The GA attempts to mimic natural selection to arrive at the best estimate for the design parameters. This process is based on selection, crossover, and mutation of populations across generations (Fig. 2.17). In a first step an initial population, i.e., a user-specified number of design variable combinations are sampled.

To this end, a Latin hyper-cube sampling of the design variables is often selected. Next, the fitness score of each individual of the current generation is determined by forward analysis. If any so obtained fitness score falls below a predetermined threshold, the termination criterion is met and the best overall individual is returned. Otherwise the individuals with the best fitness score become the parents, i.e., form the basis, for subsequent generations. A user-specified amount of elite design variable combinations are kept, the rest are discarded. By means of crossover, i.e., the process of creating new individuals by recombining subsets of the parent's design variables, and mutation, i.e., a random seed operating on each individual separately, unique individuals are constructed until the generation limit is met. This newly constructed generation with design variables updated with last generations elite performers, is then again evaluated for fitness, closing the loop. It should be noted that the exploratory behavior of the GA is attributed primarily to the mutation phase, while the crossover phase enhances the exploitative capabilities.

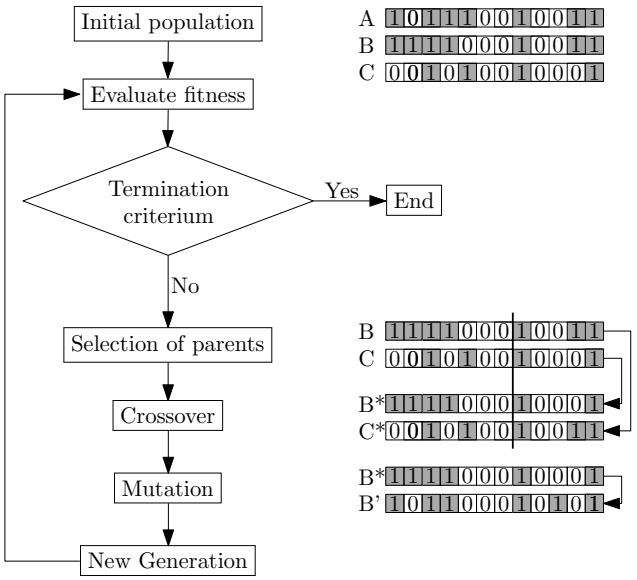

Fig. 2.17: Flowchart of the GA approach, demonstrating the steps using a binary representation of the design variables for specific realizations thereof (A-C).

2.5.3 The Conventional Approach

In a first step, the design variables are identified. Typically, each crack is characterized in 2D applications by four numbers (either crack tip locations or center, length and angle), and circular inclusions by three (center and radius). Further GA specific parameters are set, e.g., amount of generations, individuals per generation, selection-, crossover- and mutation rates, to name a few. Each of these parameters is provided with a lower and upper bound. This is a critical step ensuring solutions fall within a feasible and meaningful space. Next a translation layer is required when passing the individual design variable realizations to the forward solver, since the design variables constitute encoded crack and inclusion information.

Since global optimization algorithms have not been proven to arrive at global minima, albeit routinely do so in practice, the results upon analysis completion must be checked. To this end, the convergence plots of the fittest individual per generation may be considered. If the plot has not plateaued prior to analysis completion, the simulation should be rerun with an increased generation limit. It is prudent to plot a handful of the best individual of the last generation in order to check if small changes in the fitness score significantly alters the design variables, since select problems may suffer from, e.g., symmetry issues. In any case, secondary runs with different random seeds are advisable, to check that the obtained results are independent of the initial population choice.

2.6 Topology Optimization

In this thesis, an effective means to accelerate TO is proposed (sec. 7). This is achieved though a drop-in replacement for calculating the displacement field. Seeing how the underlying scheme of TO remains unchanged in the process, this section only concerns a generic TO formulation, i.e., minimum compliance optimization, solid isotropic material with penalization (SIMP), optimality criterion (OC) and a convolution based filtering technique.

We consider TO with focus on compliance minimization when subjected to a volume constraint, i.e., maximizing the structural stiffness when only a fraction of the original volume is available [44]:

$$\begin{aligned} \min_{\{x\}} &: c(\{x\}) = \{F\}^T\{u\} = \{u\}^T[K]\{u\} = \sum_{e=1}^{N} g(x_e)\{u_e\}^T[k_0]\{u_e\} = \sum_{e=1}^{N} E_e(x_e)\{u_e\}^T[k_0]\{u_e\} \\ \text{subject to} &: V(\{x\})/V_0 = f \\ &: [K]\{u\} = \{F\} \\ &: \{0\} < x_{min} < \{x\} \leq \{1\} \end{aligned} \tag{2.89}$$

where the set of N design variables $\{x\}$ spans the design domain and specifies the material distribution. Three conditions are imposed, constraining the optimal solution. First, each element of $\{x\}$, denoted by x_e, must fall within limit values of x_{min} and 1, which correspond to void and solid regions respectively. Typically, x_{min} is chosen as a small number, 10^{-3}, to avoid numerical singularities. Second, a user prescribed volume fraction f follows as the ratio of current volume $V(\{x\})$ to initial volume V_0. Third, the displacement field $\{u\}$, required to compute the compliance c, follows from the solution of the forward problem in elastostatics. $[K]$ denotes the corresponding stiffness matrix and $\{F\}$ the load vector respectively. The compliance can either be calculated globally or locally, as a summation of element contributions. The elemental nodal displacements are denoted by $\{u_e\}$ and the corresponding stiffness matrix, calculated with Young's modulus equal to one, i.e., a solid element, is given as $[k_0]$. $g(x_e)$ is a function, which typically scales $[k_0]$ according to the specific realization of its design variable x_e to account for intermediate material properties, i.e., Young's modulus. In the modified SIMP approach an element's Young's modulus is thus given as follows, whereby intermediate material densities are penalized:

$$E_e(x_e) = E_{min} + x_e^p(E_0 - E_{min}) \tag{2.90}$$

E_0 is the materials initial stiffness, E_{min} a small stiffness denoting void, typically 10^{-9} assigned to mitigate a singular stiffness matrix and p the penalization power, whose value is traditionally set as $p = 3$.

The conventional OC method is invoked to solve the optimization problem of Eq. 2.89. To this end, the following heuristic updating scheme is adopted [20]:

$$x_e^{new} = \begin{Bmatrix} \max(0, x_e - m), & \text{if } x_e B_e^{\eta} \leq max(0, x_e - m) \\ \min(1, x_e + m), & \text{if } x_e B_e^{\eta} \geq min(1, x_e - m) \\ x_e B_e^{\eta}, & \text{otherwise} \end{Bmatrix} \tag{2.91}$$

where m and $\eta = 1/2$ are the positive move limit and numerical damping coefficient, respectively. B_e follows from the necessary condition of optimality, which invokes Lagrange multipliers λ to satisfy the constraints of Eq. 2.89:

$$B_e = \frac{-\frac{\partial c}{\partial x_e}}{\lambda \frac{\partial V}{\partial x_e}} \tag{2.92}$$

where λ is determined by, e.g., bisection algorithm, such that the volume constraint is satisfied. Assuming each element is of unit volume, the change in volume with respect to any element x_e is $\partial V/\partial x_e = 1$. To evaluate the sensitivity of the objective function c with respect to an element density x_e, the compliance is augmented by a zero function, pre-multiplied by an arbitrary real displacement vector $\bar{\mathbf{U}}$:

$$c(\{x\}) = \{F\}^T\{u\} - \{\bar{u}\}^T([K]\{u\} - \{F\}) \tag{2.93}$$

After rearrangement the sensitivities follow as:

$$\frac{\partial c}{\partial x_e} = (\{F\}^T - \{\bar{u}\}^T[K])\frac{\partial\{u\}}{\partial x_e} - \{\bar{U}\}^T\frac{\partial[K]}{\partial x_e}\{u\} = -\{\bar{u}\}^T\frac{\partial[K]}{\partial x_e}\{u\} \quad \text{since} \quad (\{F\}^T - \{\bar{u}\}^T[K]) = 0 \tag{2.94}$$

given that $\{\bar{u}\}$ satisfies the adjoint problem, i.e., is obtained by solving the forward problem, e.g., by FEM. It follows by inspection of the system stiffness matrix that Eq. 2.94 may be equivalently formulated on the element level as:

$$\frac{\partial c}{\partial x_e} = -px_e^{p-1}(E_0 - E_{min})\{u_e\}^T[k_0]\{u_e\} \tag{2.95}$$

Filtering techniques are employed to ensure the existence of a solution to Eq. 2.89. Their application prior to the heuristic updating scheme combats checker-boarding and has empirically been shown to produce mesh-independent designs:

$$\frac{\partial \hat{c}}{\partial x_e} = \frac{1}{\max(\gamma, x_e)\sum\limits_{i\in N_e} H_{ei}}\sum_{i\in N_e} H_{ei}x_i\frac{\partial c}{\partial x_i} \tag{2.96}$$

where N_i comprises the elements i within a specified filter radius r_{min} of the current element e. Typically, a linear decay for the weight factor H_{ei} is assumed such that $H_{ei} = \max(0, r_{min} - \texttt{dist}(e,i))$. For numerical stability reasons, $\gamma = 10^{-3}$ is introduced.

The above procedure is summarized in Fig. 2.18. A TO analysis starts with an initial guess for the material distribution. Typically, the volume fraction is assigned uniformly to the domain, i.e., a fine grid of unit sized elements. After solution of the forward problem, the compliance for this initial iteration is computed. Then the sensitivities are evaluated for each element. Filtering is subsequently applied to avoid mesh-dependent results and the formation of checker-boarding. Next, the optimization algorithm of choice selects the appropriate elements to either demote/promote towards void/solid respectively. This marks the end of an iteration. If the change in calculated compliance varies less than a user specified amount across iterations, convergence is assumed. Ultimately, the analysis is concluded and the resulting topological layout is visualized.

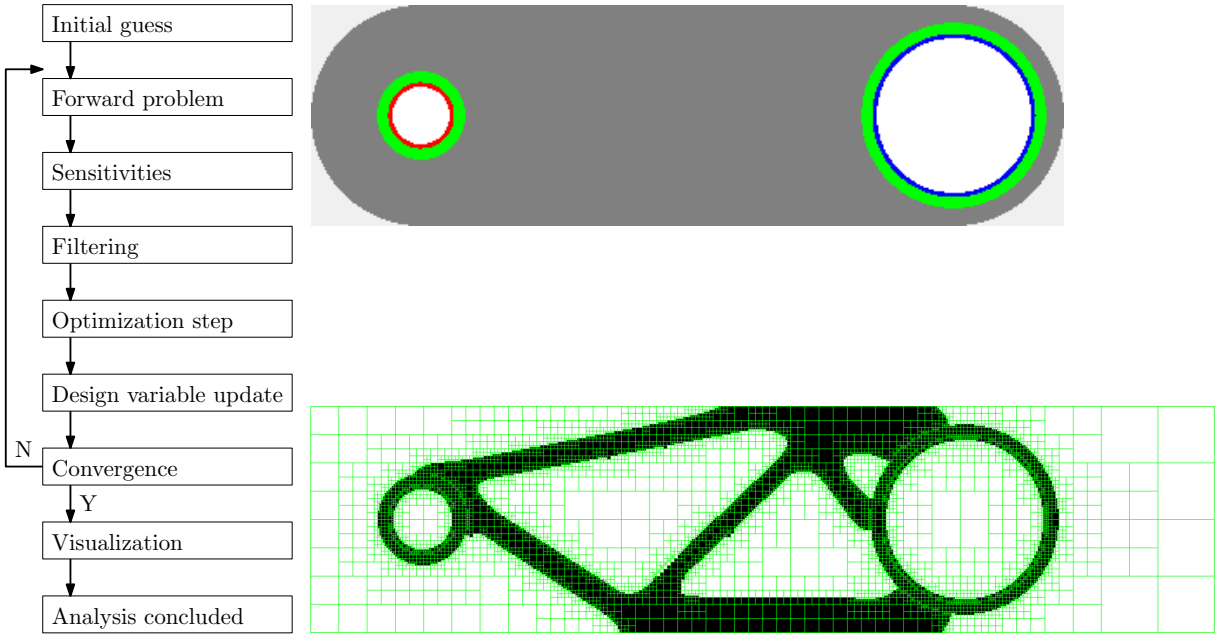

Fig. 2.18: Flowchart of a typical TO analysis.

For several of these steps, alternative methods have been proposed. The following are select examples thereof. BESO, SERA and level-set based approaches have been reported as alternatives to the SIMP, mathematical programming techniques such as the method of moving asymptotes (MMA) and the convex linearization method (CONLIN) as powerful replacements for the OC method, and heavy-side, partial differential equation (PDE) and gray-scale filters as substitutes for the convolution based filters. Further

one can differentiate so-called hard vs. soft kill variants. The latter is presented in this section. There defining characteristic comprises the inclusion of void material during analysis by severely reducing such an element's stiffness. This can incur severe conditioning issues accompanied by slow convergence when employing iterative methods for the solution of the forward problem. Hard kill variants disregard void elements during solution. Hence, the size of the stiffness matrix is varies for each iteration. Although this may be computationally favorable, it induces issues pertaining to unconstrained substructures.

3 Discrete and Phase Field Methods for LEFM

Over the past 20 years, the XFEM, the SBFEM and most recently the Phase Field method (PFM) have emerged as distinct methodologies with the common objective of resolving fracture propagation. In this chapter, we provide a comparative platform for these methodologies pertinent to both the mathematical treatment of damage evolution and the corresponding algorithmic implications within the framework of LEFM.

LEFM methods describe damage initiation and propagation within the remit of brittle and quasi-brittle material response. LEFM has been traditionally treated within two distinct methodological frameworks, i.e., computational fracture mechanics [see, e.g., 18] and continuum damage mechanics [see, e.g., 216]. In the former, damage is explicitly defined as a discrete, i.e., topological discontinuity. In the latter, damage is effectively homogenised over a representative volume. Diffuse crack approaches effectively lie in the boundary of the two aforementioned methods. The need to predict damage related phenomena precisely, accurately, and economically within the context of LEFM has spurred research into an extensive suite of alternative methodologies.

The FEM, a representative of the discrete methods class, has reached a mature development status, effectively becoming the industry standard in numerical methods. Yet, challenges remain when characterizing singularities or propagation due to discrete cracks. This is a direct consequence of the following, select FEM shortcomings. The first four challenges primarily originate from the discretization method itself, while the remaining two pertain to difficulties associated with integration of LEFM into the discretization process:

1. A conforming mesh topology is required to represent the associated crack.
2. The typical polynomial-based interpolation functions cannot reproduce the singular stress field.
3. Tracking crack paths and incorporating branching and merging behaviour is algorithmically challenging.
4. Mesh dependant projection errors arise within the context of nonlinear and dynamic analyses.
5. Nucleation, branching and merging of cracks cannot be treated in a uniform and theoretically sound manner.
6. Calculation of the SIFs requires additional post-processing methods.

A number of techniques have been developed to tackle the aforementioned issues. First, sophisticated remeshing algorithms [48, 56, 24] and tools [25, 112] have been introduced to model the singular stress field. The utilization of special element types or the introduction of a fine mesh around crack tips contribute to tackling this challenge. Second, specially developed quarter-point elements [32], which are placed around the crack tip, to accurately capture the crack tip singularity. Third, diverse techniques have been proposed to determine the fracture parameters, such as the SIFs. This includes path-independent integrals [210, 116, 78, 150], the virtual crack closure technique [271, 262, 154], the hybrid-element approach [146], and the Irwin's crack closure integral [339]. The computational toll for such analyses is significant, with the majority of the effort stemming from the remeshing algorithm and the need for a fine mesh in the vicinity of the crack tip. Due to these limitations several novel numerical methods treating discrete cracks, such as meshless methods (MM), material point methods (MPM), BEM, the extended/generalized finite element method (XFEM/GFEM), and the SBFEM have been applied, all distancing themselves from FEM in the way they define their support.

MM [41, 40, 184] were conceived with the aim of eliminating difficulties associated with the reliance on a mesh. Hence, the interpolation in MMs is solely based on a set of distributed nodes, thus eliminating FEM issues commonly associated with mesh distortion and remeshing. Crack path extensions are effortlessly accounted for by introducing additional nodes. However, certain drawbacks remain. The MM shape

functions require higher order integration and the treatment of essential boundary conditions is intricate, since the shape functions do not satisfy the Kronecker delta property. Generally, the computational toll of MMs results higher to that of the FEM [229].

MPM [310] is an extension to Particle-In-Cell methods [76], which efficiently treat history-dependent variables. In MPM, the continuum is represented by a set of material points that are moving within a non-deformable (Eulerian) computational grid where, contrary to MM, solution of the governing equations is performed. Treatment of discrete cracks is accounted for by the introduction of multiple velocity fields [218] or more recently phase fields [349, 143, 213]. MPM has been found to offer significant computational advantages when compared to purely meshless methods since it does not require time-consuming neighbour searching.

The BEM [192] solves initial value problems described as boundary integral equations hence reducing dimensionality by one. This significantly reduces the complexity of mesh generation, since only the boundary and the crack front need be discretised. Further, compared to the FEM, BEM can often achieve greater accuracy, due to the nature of integrals used in the problem description. However, this is simultaneously the source of disadvantages. This formulation results in fully populated, dense matrices necessitating tailored numerical methods [269, 126] to efficiently solve the resulting discrete equations. The introduction of IGA [139, 228] suggests profound implications on practical engineering design. The key concept entails employing NURBS not only for the geometric representation, but also for the discretization employed in the subsequent analysis. NURBS substitute standard FEM shape functions with the solution obtained on their support. A hybrid isogeometric boundary element method has been proposed [171, 288, 279] coupling many of the advantages of its parent methods. The direct adoption of the geometry representation as given by CAD software, greatly facilitates the integration of design and analysis, since no volume parametrization is required for crack propagation. Additionally, when applied to fracture [225, 253], the delivered higher-continuity can increase the accuracy of the stress field around the crack tip.

An effective means of tackling the issues of mesh dependency and treatment of singularities, is provided by the XFEM/GFEM [205, 304], whose use is wide spread both in academia and industry. The most characteristic trait of this method is the use of partition of unity (PU) enrichment [27, 28, 194], to incorporate known features of the solution in the finite element approximation space through appropriate enrichment functions. For fracture mechanics problems, discontinuous and singular enrichment functions are employed locally, i.e., in the vicinity of the crack, to allow the representation of discrete cracks independently of the underlying mesh. This in turn significantly decreases or even removes the remeshing burden, while also increasing the accuracy with which asymptotic fields are represented. Alternatively, the SBFEM [343] naturally incorporates the singular stress field, providing an elegant extraction of the gSIFs in post-processing at negligible additional computational cost [296]. This is a consequence of SBFEM retaining an analytical solution in the radial direction, while only requiring discretization along the tangential boundary in the standard FEM sense. However, double nodes are introduced to accommodate strong discontinuities. This is partially mitigated due to the polytope nature of SBFEM, which only imposes the condition of star-convexity on elements. Exploiting balanced quadtrees as hierachial meshes in conjunction with polygon clipping the majority of meshing effort is circumvented [238].

Alternative discrete fracture methods based on cohesive theories have been utilized to overcome stress singularities in LEFM and to consider the nonlinear separation phenomena [18]. [31] originally introduced the cohesive zone method (CZM) to model fracture in brittle materials. Later, [90] extended the CZM to study yielding and plastic zone around the crack tips and [131] proposed a linear decohesion relation between the fracture energy and the tensile strength of concrete. In cohesive fracture theory, the material is not considered perfectly brittle as in Griffith's theory. Rather, there is a small zone in front of the crack that can exhibit some ductility. The fracture energy is gradually released at the crack tip based on crack opening and equals the critical fracture energy at full crack opening. If the cohesive zone is sufficiently small, the ductility zone becomes unimportant and the theory of LEFM can be applied. In finite element-based methods, the CZM introduces cohesive elements at the finite element interfaces. These cohesive elements do not have any physical meaning. Rather, cohesive traction forces occur when the material interfaces are separated. The degradation along a discrete crack is a function of these traction forces. The traction forces are based on the relative displacements (crack opening) at the finite element interface. Crack paths can only evolve along the element interfaces, hence limiting the possible crack patterns that the method can account for or necessitating the use of a very fine mesh discretization. The cohesive elements can either be defined at the area of interest if the crack path is known a priori, e.g. from experimental observations, or at all element interfaces. In the latter case, the computational costs are dramatically increased. Examples of

the CZM with FEM can be found in [351] for dynamic crack propagation problems where it was shown that crack branching emerged normally without any ad hoc branching criteria. Furthermore, [68] introduced a cohesive zone finite element-based method for modelling of hydraulic fracture. Apart from these, cohesive theories has also been applied to other mesh-based method e.g. the BEM for the crack growth analysis in concrete [274]. The main disadvantage of these procedures is that the crack paths always align with the structure mesh, rendering the resulting solution mesh dependent. A possible solution to overcome that issue is with remeshing techniques [141, 62]. Another way to overcome this issue is with the partition of unity methods (PUMs) introduced by [28]. A third and natural way to overcome the sensitivity of the mesh is with particle methods. Cohesive theories with particle methods has been studies by [224] with smooth particle hydrodynamics, [153] with reproducing kernel particle method and [300] with the element-free Galerkin method.

Another popular PUM and a reasonable extension of CZM is the cohesive segments method (CSM) introduced by [266], using the XFEM approach solution procedure. As mentioned earlier, CZM uses cohesive interface elements aligned with the finite element mesh, leading to mesh dependence during crack propagation. CSM overcomes this limitation by introducing arbitrary cohesive segments into the finite elements that act as discontinuities in the displacement field with the PUM. The cracks are modelled as a set of overlapping cohesive segments where their support nodes are enriched with jump and tip enrichment functions similar to XFEM. A combination of overlapping crack cohesive segments results in a continuous crack. [266] originally applied the CSM in quasi-static brittle fracture problems mainly focused on mode I separation problems. Later, [267] extended the CSM in simulating dynamic crack propagation problems where they demonstrated that the method can efficiently deal with multiple and branched cracks. Following the concept of CSM, various PUM with cohesive theories have been successfully introduced with meshless methods. For instance, [30] introduced a meshless CSM for crack initiation and propagation in composites, utilizing the reproducing kernel particle method. Similarly, a meshfree method based on the local partition of unity for cohesive cracks was proposed by [259], using the element free Galerkin Method.

Rather than attempting to model the actual, discrete crack topology, either as a strong discontinuity in the displacement field (e.g. XFEM) or an explicitly defined boundary (e.g. SBFEM), diffuse approximations of cracks incorporate the effects associated with the crack formation, e.g., the stress release or the stiffness degradation into the constitutive model [214]. Such approaches initiated with the pioneering work of Rashid [264], who defined a cracking criterion for pre-stressed concrete pressure vessels on the basis of loss of material stiffness in the direction normal to a crack as this evolves. During the past 10 years, several methodologies pertinent to diffuse crack models emerged, such as gradient enhanced damage methods [252, 287], Thick Level Set methods [208], and Phase field methods [58]. In the taxonomy of damage theories, diffuse crack approximations fall within the family of Continuum Damage Mechanics, where however particular treatment of strain localisation is implicitly performed. Borst and Verhoosel [54], Mandal, Nguyen, and Heidarpour [see, also, 188] highlighted the similarities between gradient enhanced damage methods and phase field methods. An insightful discussion on the similarities and differences between thick level sets and phase fields is provided in [63].

PFMs for brittle fracture arose from the pioneering work of Francfort and Marigo [101], who treated elastic fracture as an energy minimization problem within a robust variational setting. Bourdin, Francfort, and Marigo [58] used the Mumford-Shah potential [16] to provide a regularization of this variational formulation. In this, brittle fracture is numerically treated as a coupled, i.e., displacement and phase field problem; the latter accounts for the crack interface geometry. To this point, finite element based phase field formulations have been introduced to treat brittle/fatigue [9, 212, 10], ductile [15, 53], and hydraulic fracture [340, 199, 129, 97, 256]. Very recently, the phase field method has been introduced within an MPM [143, 144] and a Virtual element framework [9]. .

This thesis delivers a critical comparison among numerical methods relying on discretisation, namely XFEM/GFEM and SBFEM, and the PFM, which belongs in the class of diffuse methods. The latter has as of late garnered much attention, not only limited to the field of LEFM. Specifically, we compare the potential of these methods in accurately and efficiently predicting crack propagation, paths and arrest. Additionally, we remark on the overall computational effort involved in the analysis and the inherent capabilities/limitations of each method within the LEFM context.

3.1 Comparison and Discussion

This section initiates by detailing the steps involved in a crack propagation analysis, attempted by each of the described methods. Emphasis is placed on identifying sources of computational effort, while illustrative flowcharts are provided for each method. This visual representation of the methods then serves as a basis for the discussion on the merits and drawbacks of each individual method within the context of LEFM.

3.1.1 Crack Propagation by XFEM/GFEM

A conceptual representation of the steps involved in a typical crack propagation analysis with the XFEM/GFEM is provided in Fig. 3.1. As should be obvious based on sec. A.1, enriched finite element methods are essentially discretisation schemes and, as such, require coupling to appropriate criteria in order to model crack propagation. In the present case these are provided by the LEFM framework. The flowchart of Fig. 3.1 involves elastic solution steps followed by the evaluation of a crack propagation criterion. This is common for most LEFM schemes relying on discretizstion, such as for instance FEM or SBFEM. The coupling to further schemes for crack propagation, such as the cohesive zone model, is also possible, in which case the steps of Fig. 3.1 would have to be modified.

The enriched finite element schemes contained within the XFEM/GFEM family of numerical methods permit the treatment of discontinuities and singularities independently of the mesh, while preserving the convergence rates of the underlying FE method. Hence, conventional meshers are employed, yet enriched node and element sets need to be specified and their contributions to the equilibrium equations need to be assembled. This, apart from introducing additional DOFs associated with the enrichment functions (Eq. (A.6)) and potential conditioning problems, requires the use of more involved numerical integration schemes leading to an increased computational toll. Nevertheless, these operations are only performed on a small part of the domain, thus minimizing this additional cost. As mentioned in sec. A.1, several techniques are available that allow to perform the required tasks in a robust and automated manner.

For the calculation of the SIFs, elements within the interaction integral domain are identified and their contributions are assembled. A suitable crack propagation criterion is applied in order to evaluate the propagation direction, and together with a user-specified crack propagation increment Δa determine the new crack tip location. Since implicit crack representation has become an almost integral part of enriched finite element methods, the next step would involve the update of this representation. This task might introduce additional challenges, however, significant work has been carried out in this direction, with several methods available for tackling this issue in a simplified manner.

3.1.2 Crack Propagation by SBFEM

The crack propagation process by SBFEM, enhanced via hybrid balanced quadtree polygon meshes, requires the polygon representation of domain features as input, including the crack. The points comprising the polygons constitute the subdivision criterion for the quadtree decomposition. If more than a user-specified number of points fall within a quadrant, this is subdivided. Together with the balancing operation, these steps entail minimal computational effort. The explicit neighbours of each cell do not need to be calculated, but simply the size of its neighbour. This is efficiently achieved by querying the center of each element, offsetting them by the element size in all four cardinal directions, passing them through the tree structure, and finally returning the size of the final cell. Assuming a balanced mesh, all possible element realizations are precomputable. When the domain features, such as the boundary and strong & weak discontinuities do not align with the Cartesian axes, polygon clipping algorithms are required. Although efficient algorithms exist for polygon clipping, the resulting polygonal elements are no longer precomputable and must therefore be calculated individually. In order to construct the stiffness matrix of an SBFEM element, a Hamiltonian eigen-problem must be solved. This entails a real Schur decomposition, sorting of the eigenvalue blocks and subsequent block-diagonalization, as well as the inversion of the matrix $[E^0]$ and the evaluation of a matrix exponential, if quantities of interest inside the SBFEM element need be determined. For smaller elements, commonly employed on quadtree meshes, this additional step when compared to the standard FEM procedure, does not generate a significant computational overhead. Specifically, Ooi et al. [238] report a reduction of computational effort close to 50% on typical analysis domains, when employing precomputable alongside clipped elements. When larger domains are investigated by using a single SBFEM element for the whole domain and hp-refinement is employed, determining the

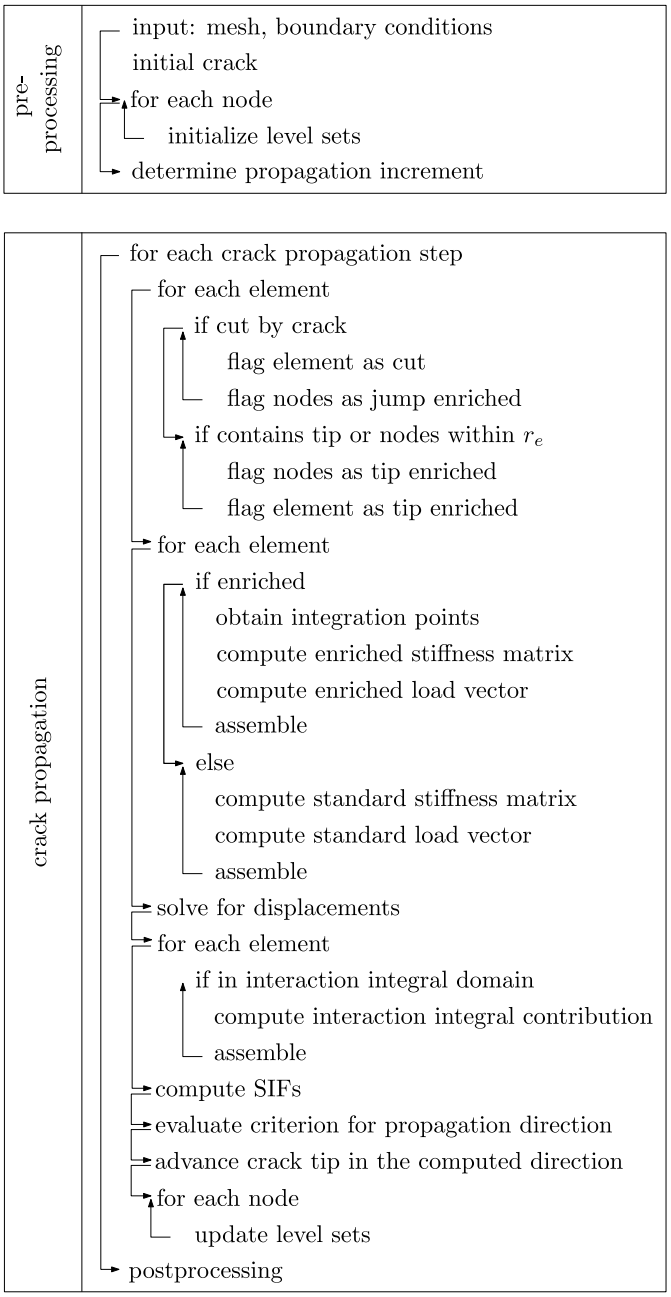

Fig. 3.1: Steps comprising an XFEM/GFEM crack propagation analysis

stiffness matrix dominates the computational effort of the analysis. Unfortunately, the stiffness matrix is fully populated, yet symmetric. Hence, this type of analysis is best suited for problems with small boundary to domain ratios. Determining the gSIFs entails post-processing calculations localized to the element containing the crack tip. The singular modes are identified according to Eq. (2.54) and the gSIFs are calculated by evaluating the components of the stress tensor $\sigma^{(s)}$ in crack extension direction (Fig. 2.7b). The crack propagation angle is selected based on a suitable criterion (Eq. (5.5)), while the crack propagation increment Δa is user specified. After definition of the updated crack tip location, the crack path polyline is updated accordingly and provided as input to the meshing phase of the next iteration. The steps to a standard SBFEM analysis are summarized in Fig. 3.2.

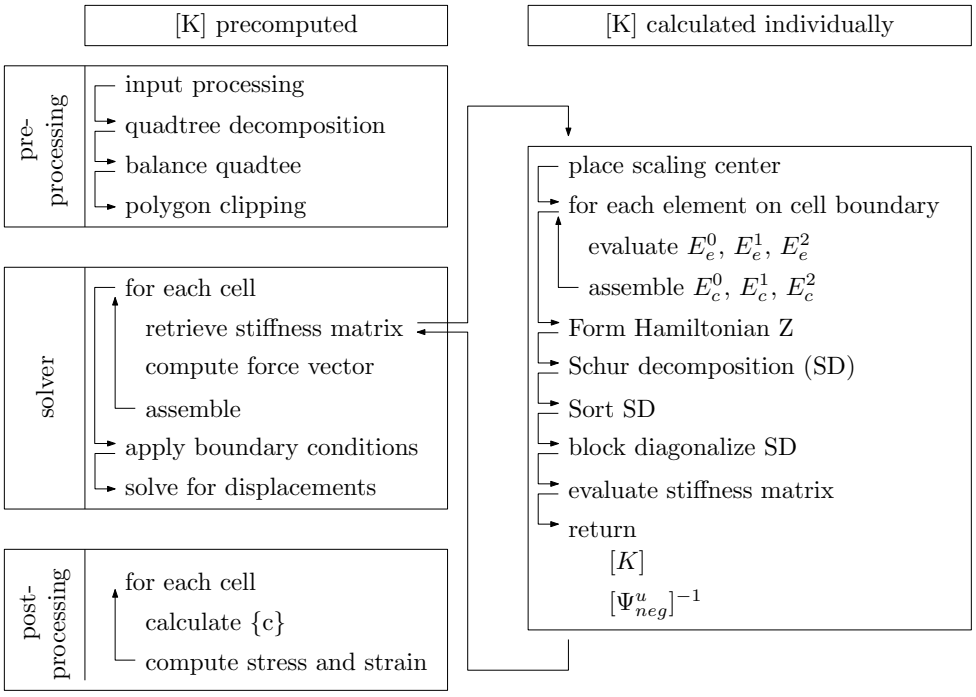

Fig. 3.2: Steps comprising SBFEM analysis

3.1.3 Crack Propagation by PFM

In PFM fracture is not introduced as an explicit or implicit discontinuity in the displacement field. Rather, it is associated with the evolution of a continuous field, i.e., the phase field. The governing equations of the crack propagation problem emerge through the minimization of the total potential energy established in Eq. (A.33), see, e.g., [58]. This gives rise to the coupled system of equilibrium and phase field governing equations established in Eqs. (A.34) and (A.35). The crack is not explicitly represented but derived from the solution of the coupled system as the region where $c = 0$ (typically values of $c < 10e-3$). Within the setting of an incremental solution procedure, the phase field is updated at each time step and with it the crack topology. Nucleation, merging, branching and arrest of cracks as well as the associated crack propagation increment is a natural byproduct of the phase field evolution. The mechanical/ phase field coupling is enforced by introducing a material degradation function that is dependent on the phase field. The evolution of fracture follows through the solution of this coupled strong form. Existing discontinuities may be introduced into the domain by providing initial values to the phase field. Mesh density is contingent on sufficient resolution of the fracture process zone, mandating a highly refined mesh in its vicinity. The combination of length scale and level of mesh refinement interact and affect the estimation of the fracture energy hence necessitating the scaling of the critical energy release rate. The numerical solution of the PFM-coupled governing equations is performed using either monolithic or staggered solvers. Monolithic solvers are typically based on the Newton-Raphson solution procedure and have been proven to provide accurate fracture paths. However, they have been shown to suffer from poor convergence due to the non-convex nature of the underlying energy functional [348]. Yet, the accuracy provided by monolithic solvers renders them a favourable solution, especially in the case of dynamic fracture problems and several attempts have been suggested in the literature to improve the robustness of monolithic procedures [see, e.g. 109, 130, 289]. In staggered methods the displacement and phase field equations are decoupled and solved separately within each load increment. In principle, a staggered algorithm for coupled field problems is based on freezing one field variable at a constant value, solving for the other until convergence is achieved. The staggered approach (also known as alternate minimization approach) provides better convergence rates than the monolithic due to the convexity of the energy functional (Eq. (A.33)) with respect to the two unknown fields $\{u\}$,$\{\phi\}$ separately. However, its accuracy is dependent on the incremental step unless staggered iterations are performed; these however increase the computational burden of the analysis. Very recent developments aim towards providing more robust staggered solvers, [see, e.g., 60]. The

steps to a typical PFM solution procedure with a staggered solution scheme are summarized in Fig. 3.3.

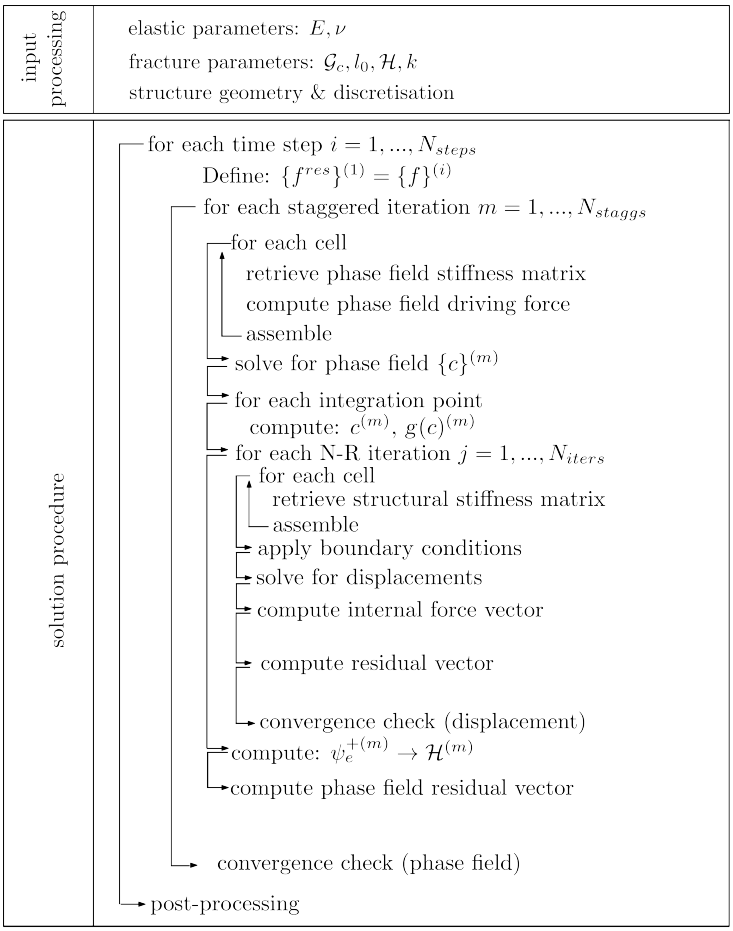

Fig. 3.3: Steps comprising Phase field analysis

3.1.4 Contrasting Discrete and PFM Crack Representation Approaches

The merits of each method within the LEFM setting are discussed by contrasting key features and analysis steps. For the discrete methods, the representation of the crack is typically available in explicit form. Crack propagation analysis yields a polyline description of the crack topology. Since SBFEM employs polygon clipping, it does not require further information. XFEM, if chosen to employ an implicit enrichment representation, models the crack additionally by associated level sets. Crack path extraction is not necessary, since it is already given as a polyline. A crack consisting of a one-segment polyline is usually provided as input. For the PFM, the crack is represented by a scalar phase-field, with the phase-field variable directly embedded into the constitutive equations. The crack is represented as the region of fully degraded material with $c = 0$. Hence, no explicit crack representation is required during the analysis, albeit readily available in post-processing, if required. Initial defects are introduced in the system by specifying sets of points with corresponding phase field values.

Meshing requirements for analysis by XFEM are largely decoupled due to the level set representation, yet substituted by more involved numerical integration procedures. This permits the use of a constant mesh during crack propagation analysis. This is contrary to analysis by SBFEM, where the initial quadtree decomposition, i.e., the mesh, is updated during each step incrementally. Discontinuities introduced by polygon clipping result in double nodes, such that the nDOF of the system increase gradually as the analysis proceeds. Further, in select cases, clipping can result in non star-convex elements, which the method cannot treat. Delaunay triangulation of the element is required in such instances. Further, due to clipping, elements with poor aspect ratios, in the conventional FEM sense, may arise. Empirically, this does not seem to be as severe an issue manifesting itself in erroneous numerical integration results,

when employing SBFEM. In order to adequately represent the fracture process zone, the PFM requires a highly refined mesh in the regions of expected crack propagation as well as at the crack tip, rendering the phase-field method computationally expensive for solving large-scale problems, especially when compared to discrete fracture approaches. However, this computational burden is effectively addressed using parallel solvers, adaptive mesh refinement [52, 217], multiscale computation techniques [249] also within a local/global solution context [111].

The methods further differ in the hyper-parameters that ought to be specified by the analyst. XFEM requires the specification of crack tip enrichment type and radius, as well as the region where the interaction integral is to be calculated. Special care must be taken to exclude blending elements from the calculation of the SIFs, which may affect final results. SBFEM similarly requires the analyst to specify the homogenization region about the crack tip. In the PFM the specification of the length scale regulates the response, imposing guidelines on mesh discretization and scaling of the critical fracture energy.

The solution process for both XFEM and SBFEM involves a single elastic solution step. The PFM, as previously described in sec. 3.1.3, comprises either monolithic or staggered approaches within an iterative solution scheme. In the quasi-static regime, displacement or generalised control solution procedures are typically employed. This however necessitates that either the Eqs. (A.34)-(A.35) must be solved with very small time-increments (typically 10^{-5}-10^{-6}), or staggered iterations must be performed between both equations to ensure energy convergence. Often both of these options lead to high computational cost.

Therefore, the corresponding load-deflection curve follows from the solution at every time step. In such quasi-static analyses, displacement controlled analysis automatically yields the load-deflection curve along with the softening branch. The discrete crack methods derive the load deflection curve in back-calculation. To this end, an arbitrary loading, e.g., force or displacement based, is applied. The resulting equivalent SIF is compared to the critical stress intensity factor. Hence, a scaling factor is derived for the loads and displacements at which crack propagation is initiated. This implies that recovery of the linear branch is a one-step process. Recovering an explicit linear elastic branch with the PFM requires either a linear phase field approximation as in sec. A.2.0.4 or cubic degradation functions [53]. Absence of these approaches will yield deviations from the linear elastic behaviour contingent on the evolution of material degradation in the process zone. Since the overall system stiffness is underestimated, the associated displacements are overestimated accordingly.

In the PFM a crack is never explicitly propagated, but associated with the evolution of the phase field that emerges from the solution of the phase field governing equation. This is driven by the definition of the crack driving force as discussed in sec. A.2.0.1. Depending on the PFM formulation employed, the crack driving force can be established on the basis of either energy or limit-stress criteria. The discrete crack methods, within the LEFM framework, require the calculation of the crack propagation angle and some crack propagation increment. Examples of the later are either user specified or provided by Paris' equation. The crack is assumed to propagate in a straight line, originating from the crack tip determined in the previous analysis step. Hence, the history variables required are none other than the polyline for SBFEM, while XFEM propagates the associated level sets as well. PFM require updating the scalar phase field and specific realization of the PFM require further history variables to impose the crack-irreversibility condition, preventing the crack from healing during cyclic loading.

The fact that the solution of the phase field governing equations emerge from an energy minimization problem, opposite to discrete fracture approaches, enables the resolution of crack initiation without the requirement for a crack path to be defined a priori. Furthermore, crack nucleation, growth and coalescence happen automatically; this results in a robust method with enormous flexibility to model complex cracking patterns including the simulation of curvillinear cracks, crack merging, and crack branching without the need for ad-hoc crack tracking methods. Finally, the method is naturally extended to 3D [52], considering also the case of fracture under multi-physics scenaria, e.g., temperature induced fracture [201, 156] and hydraulic fracturing [230, 97, 199, 340, 363]. These advantages, render the phase-field approach a robust crack prediction method. Compared to discrete fracture approaches, the variational structure upon which the phase field theory emerges, equips it with significant capabilities for modelling diverse and complex fracture problems in a unified and consistent manner.

The major advantage of the diffuse crack methods and the PFM specifically lies in their generality. Extending the discrete crack methods to exhibit similar capabilities involves significant algorithmic changes, as these codes are custom and not readily extendable to further types of analysis. Furthermore, extension to 3D problems is not straightforward, in addition, the definition of crack propagation increment in 3D is difficult to specify. Further, judging if a crack arrests or the method simply does not permit continuation

across obstacles, requires expert knowledge.

3.2 Numerical Examples

In this section, four numerical examples are presented, allowing for a comparison in terms of the modeling capabilities of the investigated methods. The first two examples consider a square plate, first under tension, then under shear loading, with both setups having been studied extensively in existing literature. Although analytical solutions for these two setups do not exists, the geometry can be modelled by one SBFEM subdomain and therefore a high-fidelity reference solution can be constructed for the peak load and displacements following the first crack increment. For the last two examples, the notched plate with hole and L-shaped panel, respectively, there exist experimentally obtained crack paths to compare against. Further, the test setups closely mimic crack propagation scenarios under real world conditions. For the former numerical example, modelling the complete crack path by discrete crack methods is particularly challenging, since they do not provide the capability to nucleate cracks. The later numerical example presents a similar issue, however, modelling by discrete crack methods is achieved by placing the crack tip at the re-entrant corner, effectively circumventing the nucleation issue manually. To this end, we first outline the implementation details adopted for each numerical method, then proceed to the numerical examples.

3.2.1 Implemented Variants

For the numerical examples presented in this section, the standard XFEM with shifted enrichment functions is employed. The enrichment radius assumes a value equal to $r_e = 3.5h$, with h denoting the element size, while the radius used for the interaction integral is $r_d = 1.5h$. Element partitioning and almost polar integration are employed for the integration of jump and tip enriched elements respectively. Finally, levels sets are updated using the $\phi\psi r\theta$ method from the work of Duflot [89].

The specific realization of SBFEM employed in the presented examples is based on balanced hybrid-polygon quadtrees, unless otherwise explicitly stated, and thus discretises the boundary with linear line elements. The Gauss-Lobotto integration scheme is employed, to offset computational effort for the numerical examples where hp-refinement is introduced (sec. 3.2.2). Decoupling of the linear system of ordinary differential equations (Eq. (2.47)) is performed by block diagonal Schur decomposition. The gSIFs are estimated by means of the spline fitting approach. For the case of the tension test, the domain is approximated via use of a single subdomain with hp-refinement on the boundary to produce gSIFs of highest possible accuracy. Results obtained by this variant are termed SBFEM hi-fi, acknowledging the high fidelity solutions they produce [74].

For the PF-FEM case, 4-noded quadrilateral plane strain/stress elements with bilinear basis functions and based on a full integration technique have been adopted for the presented analysis. A displacement-controlled nonlinear static analysis scheme is utilized with constant displacement increments. Displacement is monitored and controlled at any single node on the loading edge, to which all other nodes on the edge are kinematically coupled in the direction of loading. Unless explicitly stated, the solution is implemented within a stagger phase-field solution algorithm with a single prediction step ($N_{staggs} = 1$) and $tol_u = 10^{-5}$.

3.2.2 Single Edge–notched Tension Test

This example considers mode-I fracture behavior of a square panel, with geometric description of the domain, boundary conditions and material parameters as defined in Fig. 3.4. A state of plane strain is assumed, the specimen thickness is $t = 1$ mm. The Young's modulus, Poisson's ratio, length scale, fracture energy density and crack propagation length are chosen as $E = 210$ kN/mm^2, $\upsilon = 0.30$, $l_0 = 0.0075$ mm, $\mathscr{G}_c = 0.0027$ kN/mm and $a = 0.02$ mm, where applicable. The bottom edge of the specimen is clamped in both x and y directions, such that $u_x = 0; u_y = 0$. The loading and constraining of the top edge by discrete and PFM is enforced differently, yet with equivalent outcome: For XFEM and SBFEM a prescribed displacement of $u = u_y \geq 0$ is imposed on the top edge, while for PFM, a quasi-static displacement control analysis procedure is implemented considering a concentrated load applied at point C and kinematic coupling of the vertical displacement DOF along the top edge, such that $u = u_y \geq 0$ is obtained.

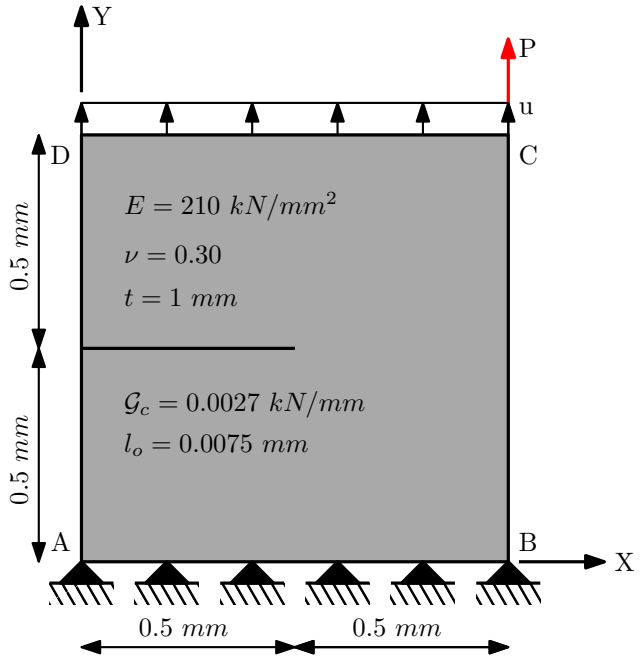

Fig. 3.4: Tension test geometry, material parameters, loading and boundary conditions.

The analysis procedures for each approach as described in sec. 3.2.1 apply. Two different solution procedures based on standard and cohesive phase field approaches, as described in secs. A.2.0.7 and A.2.0.8 respectively, are studied within this example.

The nucleation and propagation of the crack at successive time-increments is shown in Fig. 3.5. The nucleation of the crack automatically occurs at the notch-tip, and then this propagates linearly in the direction perpendicular to the applied load. It is known that the value of the length scale parameter l_o not only controls the width of the phase field diffusion zone, but also affects the peak fracture force values. This is illustrated in Fig. 3.6 and Fig. 3.8, where a decreasing the value of l_o leads to sharper crack topologies and higher peak fracture forces, thus showcasing a more brittle-like fracture behaviour. It can be inferred from Fig. 3.8 that if l_o is chosen sufficiently small, i.e., in the limit $l_o \to 0$, the force-displacement curves converge towards Griffith's description of brittle fracture; a property well-known as Γ-convergence of regularized phase field fractures. However, an important point to note is that a formal proof of Γ-convergence of anisotropic strain-energy splits (detailed in [198] and [17]) towards Griffith's theory isn't available yet, as also stated in [348].

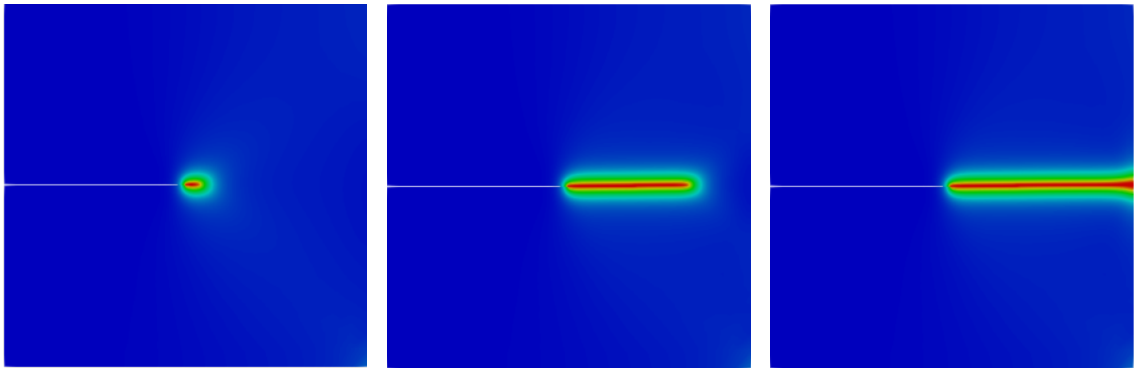

Fig. 3.5: Tension test phase field evolution for u=0.0057 mm (left), u=0.00585 mm (center) and u=0.00595 mm (right), with displacement increment $\Delta u = 1e^{-6}$ mm.

It is evident from Fig. 3.7 that both discrete crack methods, i.e., XFEM/SBFEM, predict similar fracture characteristics, whereas the critical fracture force obtained from phase-field method is slightly overestimated when the actual value of $G_c^{actual} = 0.0027$ kN/mm is used. Considering $h = 0.005$ mm and $l_0 = 0.0075$

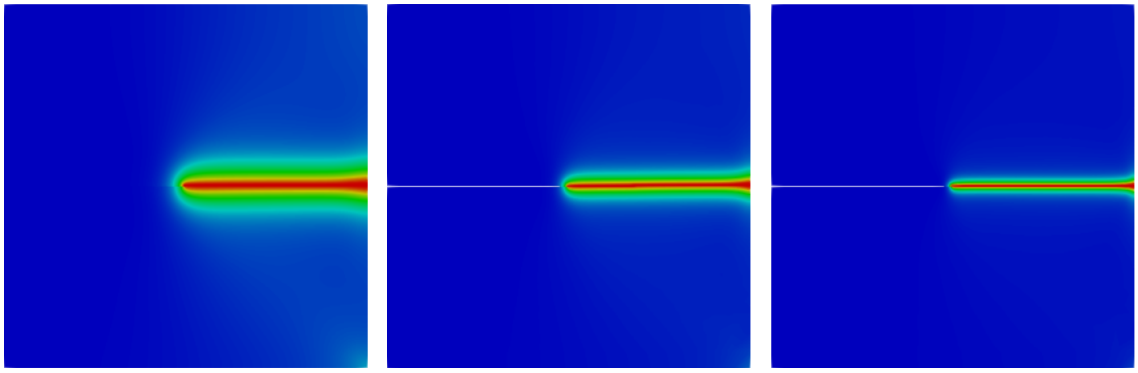

Fig. 3.6: Tension test comparison of phase field diffusion widths employing l_o=0.015mm (right), l_o=0.0075mm (center), l_o=0.00375mm (left).

mm which have been used for the current analysis, an effective fracture energy $G_c^{eff} = 0.00231$ kN/mm can be calculated based on Eq. (A.48). The critical fracture load thus obtained using G_c^{eff} shows very good agreement with those predicted by discrete methods XFEM/SBFEM. The difference in the elastic stiffness of the material between XFEM/SBFEM and PF-FEM cases is due the fact that in conventional PF-FEM formulations, as in [58], the phase-field variable evolution and consequently stress degradation start as soon as the material is loaded and hence, prevents recovery of a pure linear elastic limit. The crack paths, however, coalign as expected, although for the PF-FEM the resulting displacements are over-estimated as the fracture must initiate at the same critical load for a given value of $\mathscr{G}_c$. An alternate approach, which is highly effective in determining accurate gSIFs [74], may be applied when the domain is star convex with regards to the crack tip, and is introduced here as a high fidelity reference solution (SBFEM hi-fi). Although by hp-refinement on the boundary, the gSIFs are accurately determined utilizing only few DOFs, and thus minimal computational resources, this approach is only applicable to crack propagation in select few cases, such as in this symmetric tension test, where the crack path remains straight. Fig. 3.7 demonstrates that the standard SBFEM and XFEM implementations match the deflections and peak load, while the phase field method with G_c^{eff} approximates only the peak load closely. The SIFs obtained by discrete crack methods coincide to the fourth significant figure.

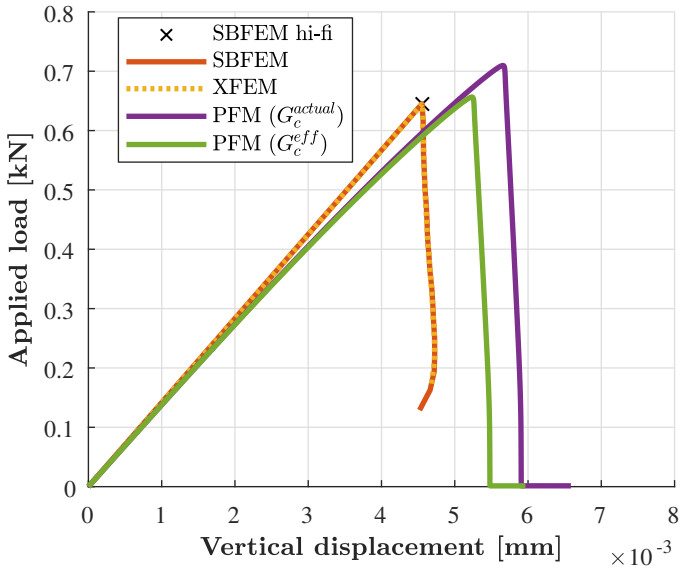

Fig. 3.7: Tension test load-deflection curves.

For comparison, the tension test is also performed using the cohesive phase field method shown in Eq. (A.55). The fracture response in this case depends on the shape parameter p, which controls the shape

of cohesive stress-crack opening curve. Increasing the value of p enables faster degradation of stresses as soon as the critical stress limit is reached, however, too large p may lead to poor convergence. Fig. 3.9 shows the dependence of load-displacement responses and critical loads on the choice of shape parameter p. A cohesive phase-field model is highly useful when the size of fracture process zone (FPZ) is large enough, and the Griffith's description of purely brittle fracture becomes inadequate [107]. In such cases, the numerical phase-field model can be calibrated with the specific material responses by making an optimal choice for the parameter p.

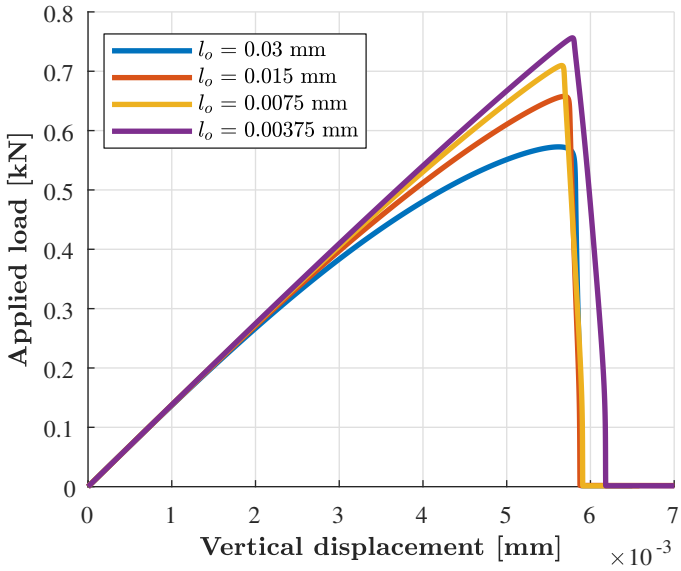

Fig. 3.8: Tension test effect of length-scale parameter variation on load displacement curves.

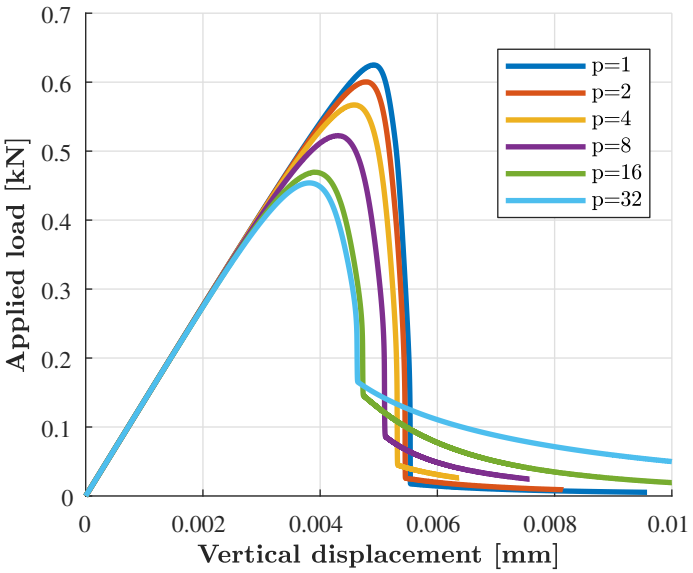

Fig. 3.9: Tension test with cohesive phase field formulation studying effect of shape parameter p on the peak fracture loads, while $l_0 = 0.0075$ mm is kept constant.

3.2.3 Single Edge–notched Shear Test

In the present example, mode-II fracture behavior of a square panel is examined, with geometric description of the domain and boundary conditions as shown in Fig. 3.10a. This is a standard benchmark test to

evaluate damage characteristics under shear loads, and has been analyzed extensively in the literature, see for e.g., [198, 52]. The specimen thickness is $t = 1$ mm and a state of plane-strain is assumed. The material parameters are chosen as $E = 210$ kN/mm^2, $\upsilon = 0.30$, $l_0 = 0.0075$ mm, $\mathcal{G}_c = 0.0027$ kN/mm and $a = 0.02$ mm, in accordance with [198]. Zero y-displacement boundary conditions are enforced ($u_y = 0$, Fig. 3.10a) on all outer edges of the plate. Furthermore, the bottom edge of the specimen is retrained in the horizontal direction ($u_x = 0$). For the discrete crack methods, a horizontal displacement $u = u_x \geq 0$ is imposed on the top edge of the specimen, while the PFM applies a concentrated load P at point C, kinematically couples the horizontal DOF on the top edge and solves enforcing quasi static displacement control. The second order quadratic phase field formulation described in sec. A.2.0.2 is employed in this example. The analysis procedures for each approach are as described in sec. 3.2.1.

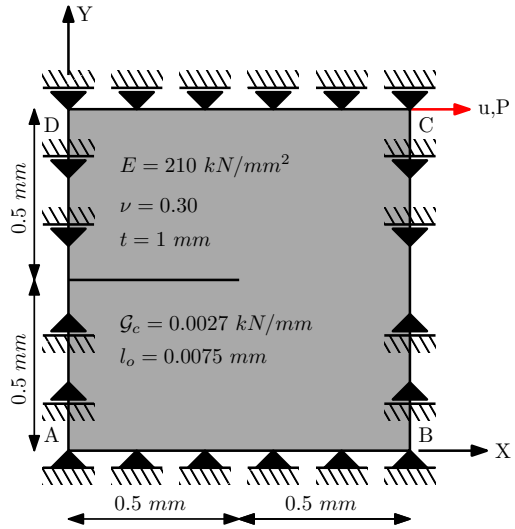

(a) Shear test geometry, material parameters, loading and boundary conditions.

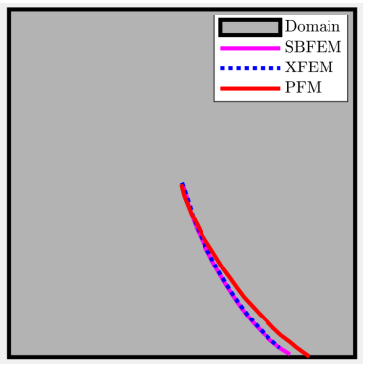

(b) Shear test crack-paths obtained from SBFEM, XFEM and PFM based crack propagation analysis.

Fig. 3.10: Shear test description and resulting crack paths.

The shear test results in a biaxial stress state developed at the notch-tip which leads to an inclined crack propagation at an angle 45^o to the horizontal. Fig. 3.11 depicts various stages of evolution of the phase field variable for the shear fracture case.

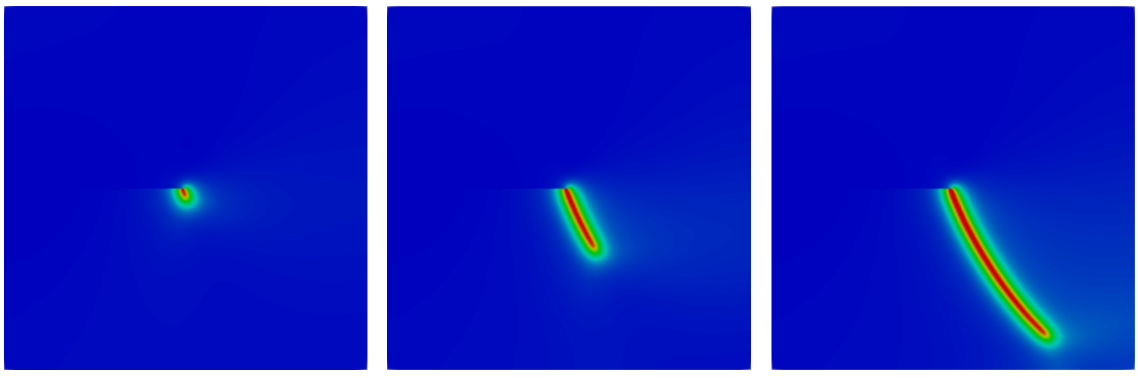

Fig. 3.11: Shear test phase field evolution at $u = 0.009$ mm (left), $u = 0.011$ mm (center) and $u = 0.013$mm (right), with displacement increment $\Delta u = 1e^{-6}$ mm.

The crack paths are closely aligned (Fig. 3.10b), however, the origin of the discontinuity differs slightly between the PFM and the discrete crack methods, resulting in a slight differentiation of the crack paths upon crack propagation. Such behavior is a consequence of the discrete crack methods mandating the crack propagate starting from the proceeding crack tip, whereas the PFM permits the evolution along the notch.

Further discrepancy is also observed in the significantly differentiated behavior of the associated load-deflection curve. The higher peak load obtained by discrete crack methods and the snap back behavior is not mirrored in the PFM result. Contrary to the discrete methods where equilibrium path is derived from sequential linear solutions, PFM relies on incremental iterative solvers; hence the snap back response would not be captured with a displacement control nonlinear analysis procedure; rather, a generalized, e.g., arc-length, analysis is required. Even though the PFM results shown in Fig. 3.10b are identical to the results provided in the literature [see, e.g., 198, 13], the 8% difference in the peak load compared to discrete methods highlights the importance of the length scale parameter on the solution. The effect of the length scale l_0 on the crack topology and the peak fracture loads is shown in Figs. 3.12 and 3.13b, respectively. It can be noted that the shear crack paths and load-displacement curves show a similar trend as already seen in sec. 3.2.2, wherein decreasing l_0 leads to sharper and more brittle cracks with higher peak fracture forces which converge to the discrete fracture solution.

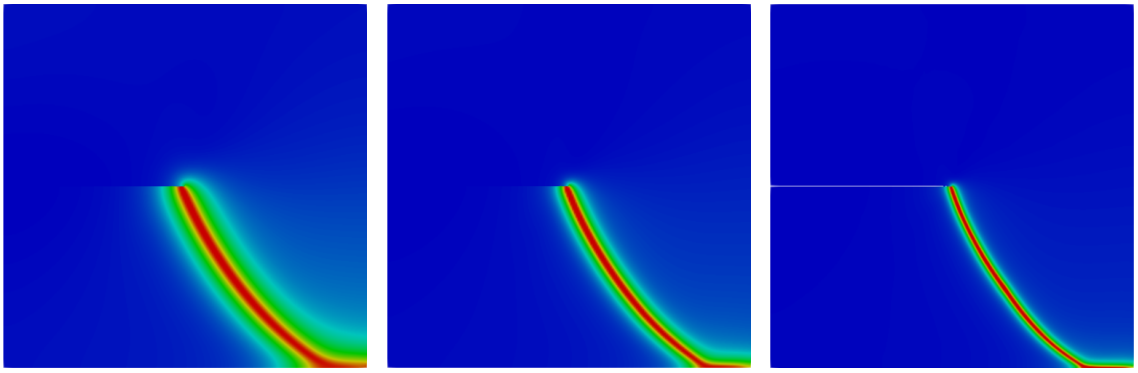

Fig. 3.12: Shear test comparison of phase field diffusion widths with respect to decreasing l_o, where l_o=0.015mm (left), l_o=0.0075mm (center) and l_o=0.00375mm (right).

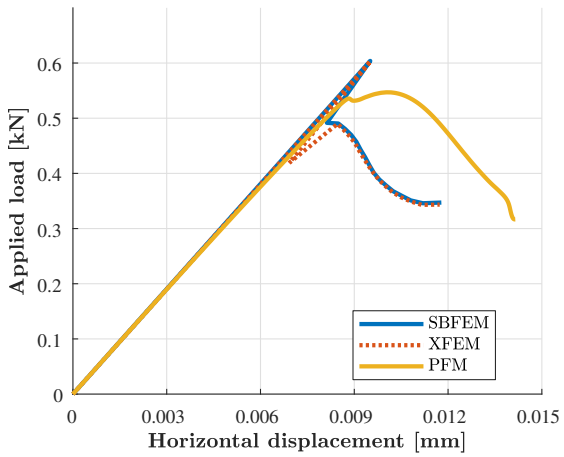

(a) Load-deflection curves of the shear test.

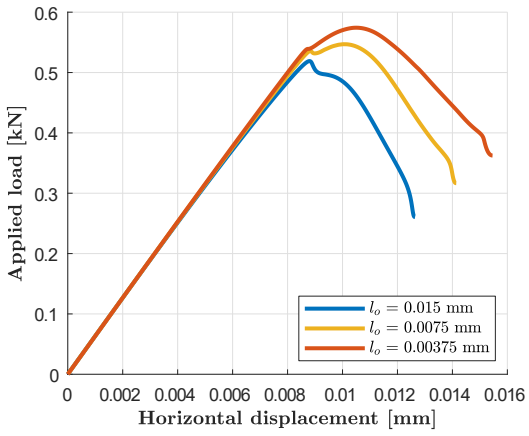

(b) Shear test effect of length-scale parameter l_o variation on load displacement curves.

Fig. 3.13: Shear test load deflection curves.

3.2.4 Notched Plate with Hole (NPwH)

A notched plate containing a hole is considered with geometric description of the domain, boundary conditions and material parameters as defined in Fig. 3.14. In [14, 143], a similar example has been analyzed previously. The specimen thickness is $t = 15$ mm and a state of plane-stress is treated. The Young's modulus, Poisson's ratio, length scale, fracture energy density and crack propagation length are chosen as $E = 5.98$ kN/mm^2, $\upsilon = 0.221$, $l_0 = 0.35$ mm, $\mathscr{G}_c = 0.00228$ kN/mm and $a = 2$ mm, where applicable. A zero

displacement boundary condition ($u_x = 0; u_y = 0$) is enforced on the bottom pin, whereas a vertical displacement $u = u_y \geq 0$ is imposed on the top pin. The analysis procedures for each approach as described in sec. 3.2.1 apply. The numerically predicted crack path is compared with the experimental results presented in [13].

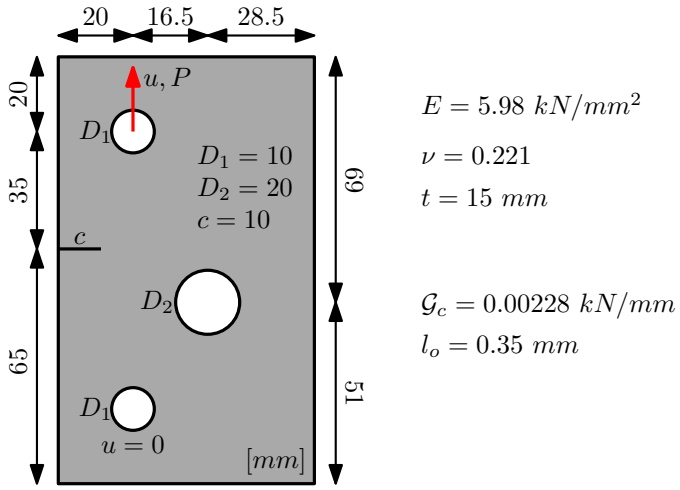

Fig. 3.14: NPwH geometry, material parameters, loading and boundary conditions.

For the PF-FEM case, a comparison is made (see also [143]) for the influence of the number of staggered phase field iterations on the accuracy of the predicted peak fracture loads. Four different cases with constant displacement increments $\Delta u = 10^{-2}$, $\Delta u = 5 \cdot 10^{-3}$ mm, $\Delta u = 10^{-3}$ mm and $\Delta u = 5 \cdot 10^{-4}$ mm are considered in Fig. 3.15 (left). In all cases, the phase-field solution is predicted with a single staggered iteration step $N_{staggs} = 1$ and a tolerance of $tol_u = 10^{-5}$ is maintained. It can be seen that solution accuracy improves when the size of displacement increments Δu is sufficiently small, and convergence is achieved for $\Delta u = 1 \cdot 10^{-3}$mm. Further reduction of Δu marginally affects the results at the cost of increased number of calculations, with $\Delta u = 5 \cdot 10^{-4}$ mm and $\Delta u = 1 \cdot 10^{-3}$mm yielding almost similar load-displacement curves.

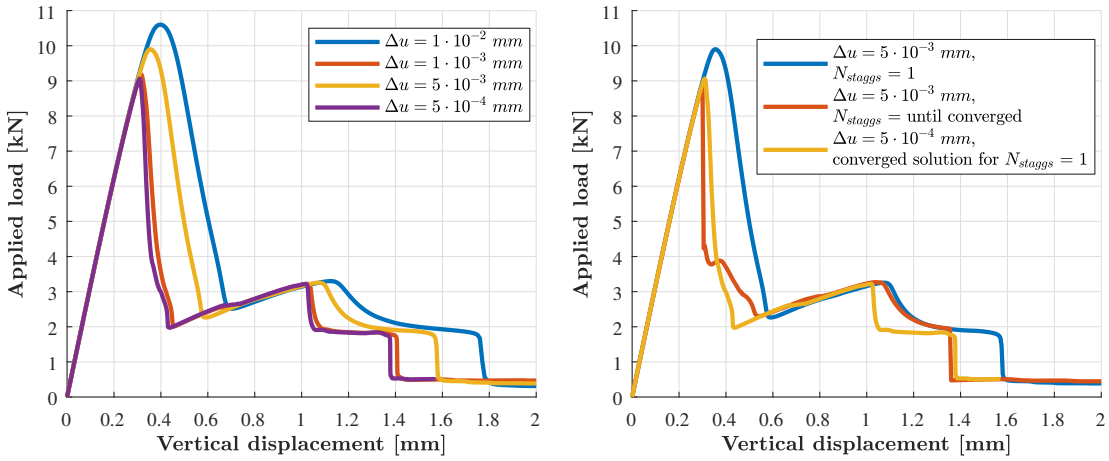

Fig. 3.15: NPwH PFM force displacement response illustrating the dependence of peak fracture force on Δu for Nstaggs=1 (left) with further investigation of the Δu=5e-3mm case subject to Nstaggs=1 and staggered iterations until convergence (right).

Fig. 3.15 (right) compares the converged solution of Fig. 3.15 (left) with the $\Delta u = 5 \cdot 10^{-3}$mm case based on a) single staggered iteration $N_{staggs} = 1$ and, b) staggered iteration performed until the phase field solution converges. It is evident that the peak fracture loads obtained in converged staggered iteration case is lower as compared to the $N_{staggs} = 1$ case, and are actually closer to the converged solution shown

in Fig. 3.15 (left). Fig. 3.16 represent the evolution of phase field at successive displacements u = 0.35 mm, u = 0.96 mm and u = 1.20 mm respectively, obtained using single staggered iteration $N_{staggs} = 1$ and constant displacement increment $\Delta u = 10^{-3}$ mm. The crack paths obtained from phase field calculations (Fig. 3.17) show good agreement with the experimental fracture results presented from [13]. Comparing PFM to discrete crack methods, the obtained peak load is similar (Fig. 3.18), however, the crack paths differ significantly (Figs. 3.19 and 3.20). Since the discrete methods do not possess an intrinsic method to nucleate cracks, once the crack tip has propagated into the hole, the algorithm terminates. This is apparent, since both XFEM and SBFEM report a final vertical displacement of approximately 0.33 mm. Due to this inherent limitation, expert judgment is required to interpret crack propagation results stemming from discrete crack methods as their termination is indistinguishable from crack arrest, when inspecting conventional results. The phase field methods circumvent these issues resulting in a highly flexible and generalized method, at the cost of significantly increased computational effort.

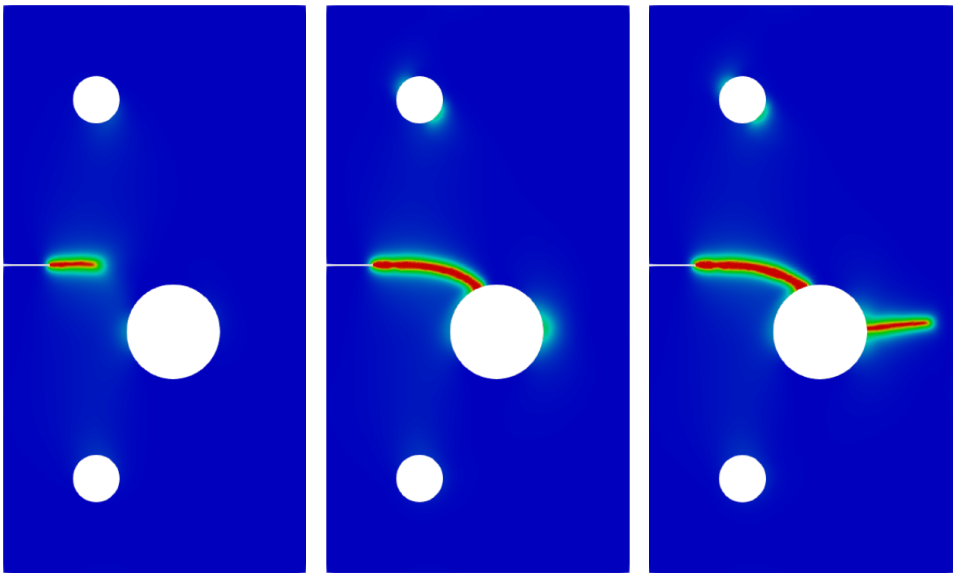

Fig. 3.16: NPwH phase field analysis for time step u=0.35 mm, u=0.96 mm and u=1.20 mm (left to right), with displacement increment $\Delta u = 1e^{-3}$ mm and 1 stagger iteration.

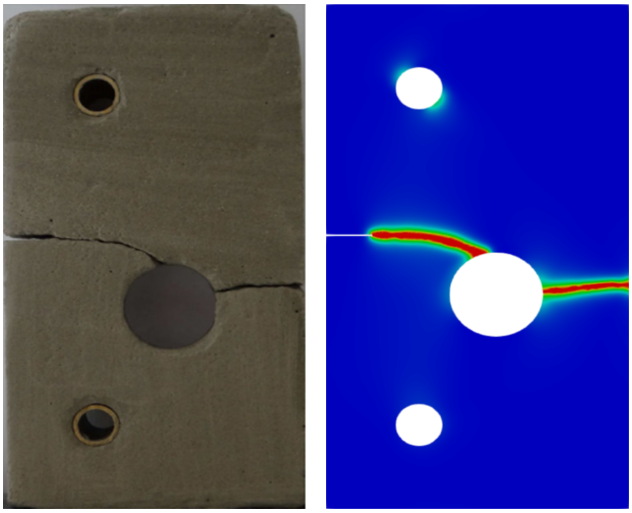

Fig. 3.17: NPwH comparison of crack topologies depicting experiments from [14] on the left vs. phase field simulations on the right.

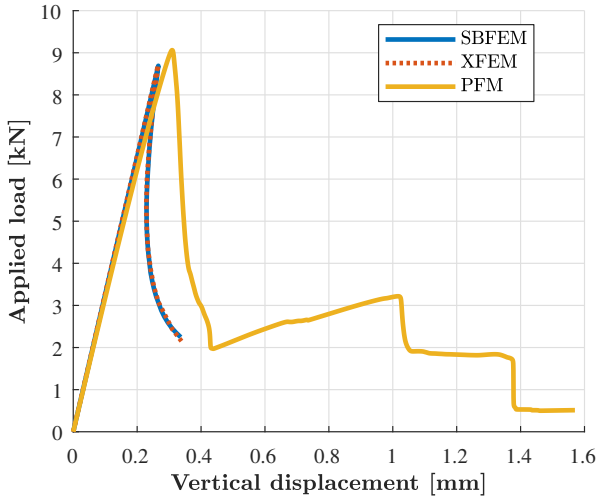

Fig. 3.18: NPwH load-deflection curves.

Furthermore, the analysis has been conducted using two different anisotropic strain energy splits widely used within the phase field literature (Fig. 3.21):

1. Spectral decomposition of strains proposed in [198]
2. Volumetric Deviatoric strain split proposed in [17]

The crack path predicted via the spectral strain decomposition [198] appears closer to the experimentally observed crack than the volumetric-deviatoric strain split [17] (Fig. 3.21 (a)-(b)). These minor differences are also reflected to the equilibrium paths shown in Fig. 3.21c. Since, contrary to the spectral strain decomposition split, the volumetric-deviatoric split only partially prohibits degradation due to purely compressive stresses, a higher amount of material is overall degraded in the latter case; hence the peak force is indeed expected to be lower. However, the spectral strain decomposition leads to a highly nonlinear formulation and therefore increased computational costs - see also [13] for a hybrid procedure to alleviate these. This highlights the significance of choosing the appropriate split and hence the level of expert judgment required when employing PFM for LEFM.

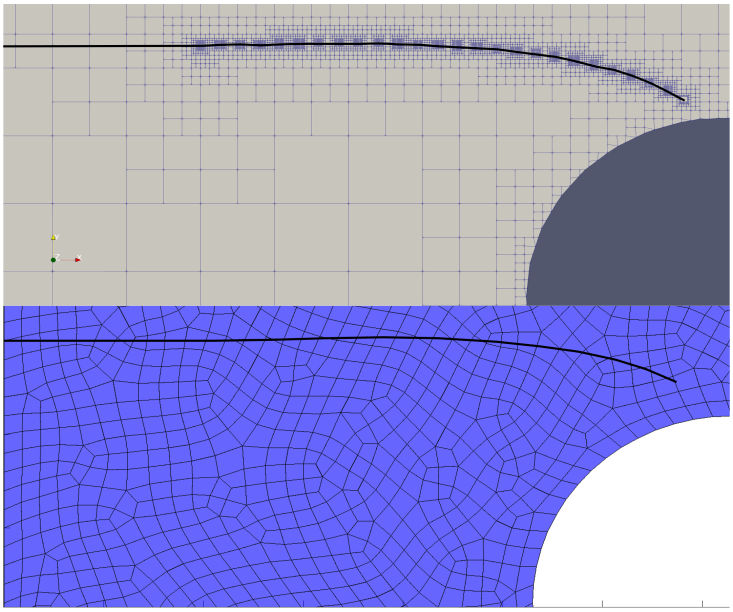

Fig. 3.19: NPwH meshes for SBFEM (top) and XFEM (bottom), with focus on crack path region.

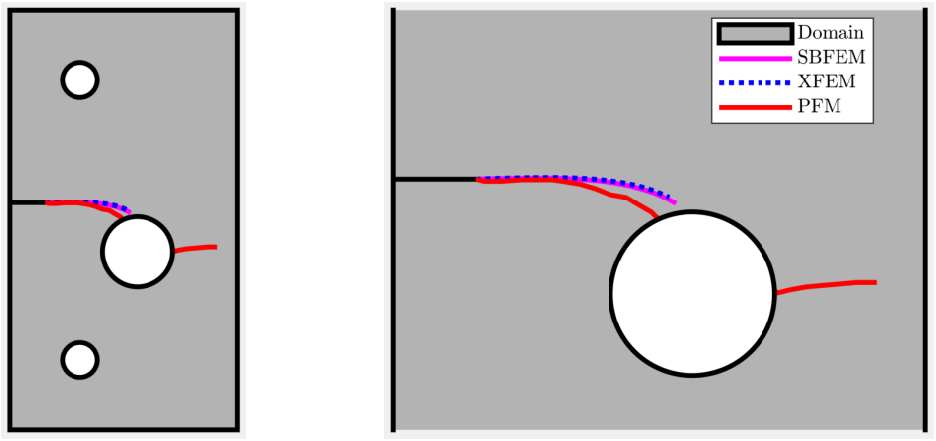

Fig. 3.20: NPwH crack-paths obtained from SBFEM, XFEM and PFM based crack propagation analysis.

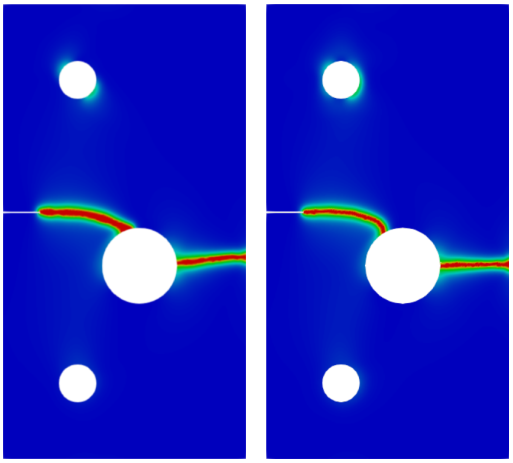

(a) Crack path from analysis implementing the anisotropic split proposed in [198].

(b) Crack path from analysis implementing the anisotropic split proposed [17]

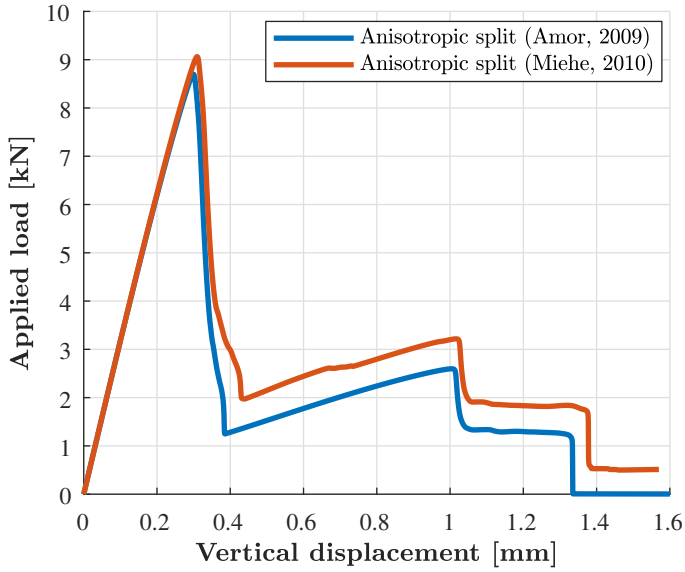

(c) Force-displacement response comparison between the anisotropic phase field models.

Fig. 3.21: NPwH comparison between anisotropic phase field models with strain energy splits proposed in [198] and [17].

3.2.5 L-shaped Panel (LSP) Test with Crack at Re-entrant Corner

Fig. 3.22 (left) depicts the geometric description of the domain, boundary conditions and material parameters for an L-shaped panel. A state of plane stress is considered with specimen thickness $t = 100$ mm. The Young's modulus, Poisson's ratio, length scale, fracture energy density and crack propagation length are chosen as $E = 5.98$ kN/mm^2, $v = 0.2$, $l_0 = 2.5$ mm, $\mathcal{G}_c = 0.0089$ kN/mm and $a = 10$ mm, where applicable. A zero displacement boundary condition ($u_x = 0; u_y = 0$) is enforced on the bottom side, while a cyclic imposed displacement envelope is considered at a distance $d_l = 30$ mm from the rightmost edge of the panel with a constant displacement increment $\Delta u = 10^{-3}$ mm and the load history as shown in Fig. 3.22 (left).

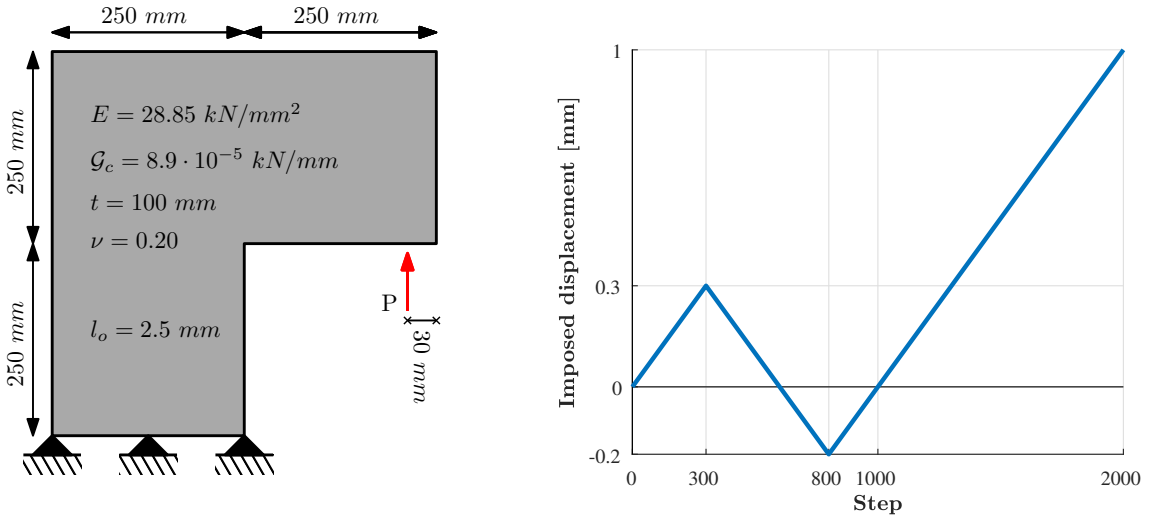

Fig. 3.22: LSP geometry, material parameters, loading and boundary conditions (left) with corresponding loading scheme (right).

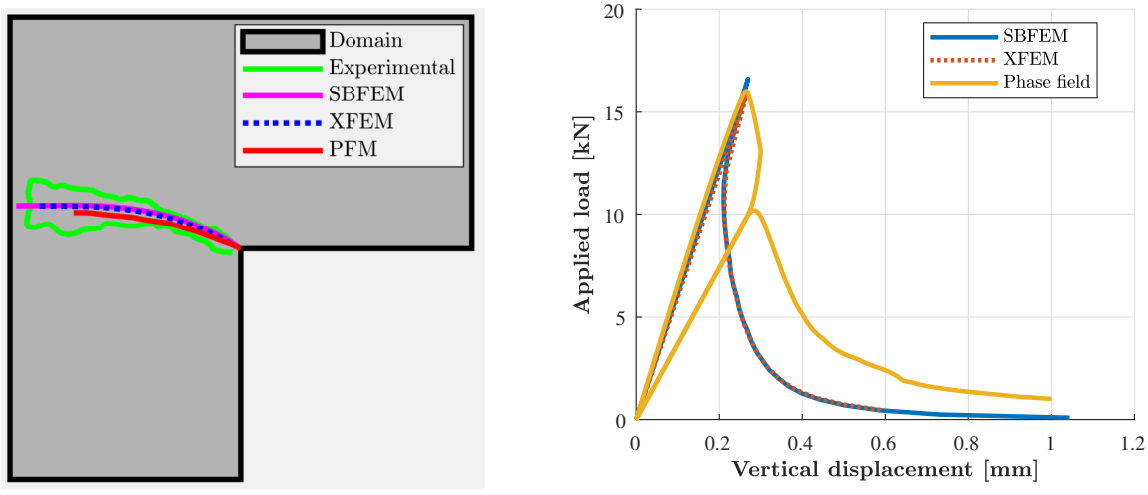

(a) LSP crack paths for SBFEM, XFEM and PFM.

(b) LSP load-deflection curves.

Fig. 3.23: LSP crack paths with corresponding load-deflection curves.

The analysis procedures described in sec. 3.2.1 for each method apply. Through this application, we simulate the experimental program undertaken in [341] which has also been investigated in previous publications pertinent to computational fracture mechanics (see, e.g., [13]). Since the discrete crack methods do not intrinsically posses the capability to avoid crack over-closure and interpenetration, without intro-

ducing contact, the numerical simulations employing XFEM and SBFEM follow a modified loading path (3.22 right) starting from time step 1000.

The crack path obtained in Fig. 3.24 coincides with the experimentally observed crack in [341], where all methods remain within the envelope of the experimental results (Fig. 3.23a). Moreover, the load-displacement curve and the peak fracture force (Fig. 3.23b) is in accordance with existing literature [13] (See also [143]) and all methods report similar results. For the case of SBFEM, the crack tip does not coincide with the re-entrant corner, since the implementation requires the crack tip to reside within the domain and not on the boundary. Hence, the crack tip was perturbed by a small value and thus the peak load is slightly overestimated. Furthermore, a comparison is drawn between the load-displacement curves obtained using spectral strain decomposition in [198] and the constrained hybrid phase field model proposed in [13]. From Fig. 3.25c it is noted that the anisotropic spectral split [198] naturally avoids crack face overlapping during crack closure when cyclic loads are considered. On the other hand, the hybrid phase-field model in [13] requires an additional constraint to prohibit interpenetration of crack faces during compression phases.

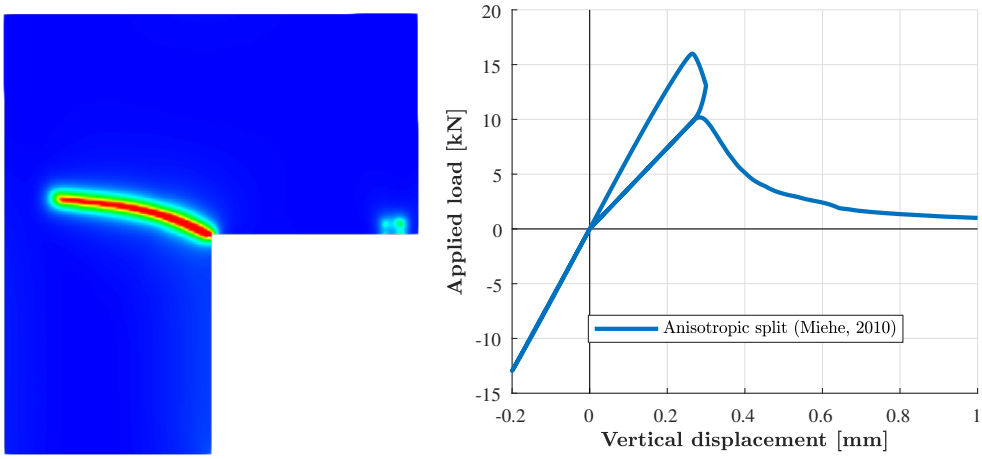

Fig. 3.24: LSP crack topology and constitutive force-displacement response under cyclic loading defined in Fig. 3.22 (right).

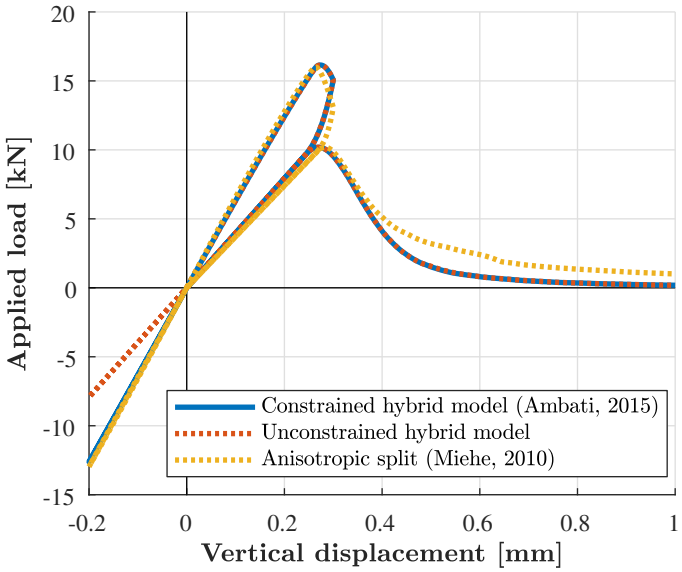

Fig. 3.25: LSP comparison of load-displacement curves implementing the anisotropic spectral split vs. hybrid phase field models.

3.2.6 Plate with Two Holes and Edge Cracks (PwHC)

The case of the plate shown in Fig. 3.26 is considered here. This numerical example is studied, since it poses challenges for both diffuse and discrete methods as discussed in [348]. The boundary conditions and material parameters are also shown in Fig. 3.26 according to [56].

A state of plane strain is considered. The Young's modulus, Poisson's ratio, length scale, fracture energy density and crack propagation length are $E = 210$ kN/mm^2, $v = 0.3$, $l_0 = 0.1$ mm, $\mathcal{G}_c = 1.0$ N/mm, $h_{PFM} \approx 0.06$ mm, and $\Delta a \leq 1$ mm, where applicable. Furthermore, for the phase-field analysis, a volumetric-deviatoric strain decomposition (similar to Amor, Marigo, and Maurini [17]) is employed. The bottom edge of the plate is clamped, while on the top edge a prescribed displacement is applied in the vertical direction and displacements in the horizontal direction are prohibited ($u_x = 0; u_y > 0$). The specimen thickness is $t = 1$ mm.

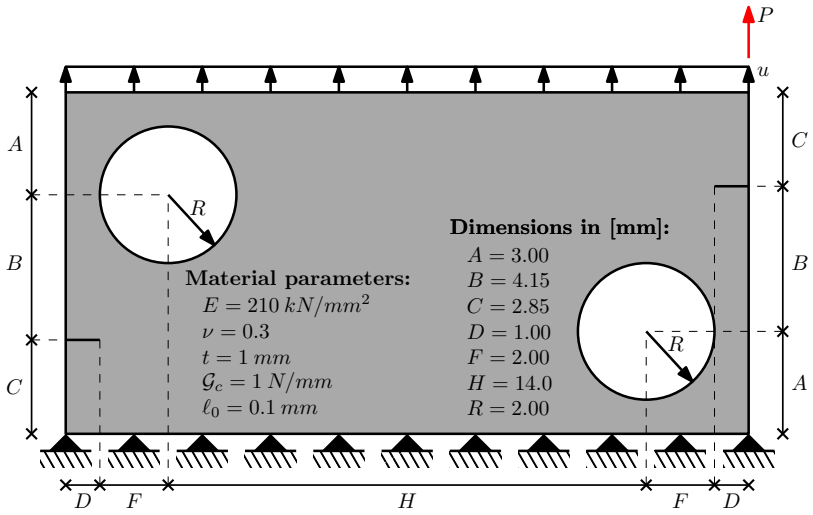

Fig. 3.26: PwHC geometry, material parameters, loading and boundary conditions.

In the presence of multiple cracks inside a domain, methods employing discrete crack representations typically implement a stability analysis [61] to ascertain the propagating cracks at each step. However, in this specific case, this involved procedure can be circumvented, due to the symmetric test setup. Nevertheless, the naive approach of simply running the analysis will result in an undesirable outcome, since slight numerical imbalances can result in asymmetric and erroneous results. To counteract these effects, symmetric meshes are employed in the XFEM analysis, while the SBFEM analysis enforces symmetric gSIFs about the diagonal. An average of the gSIFs is calculated to determine the crack propagation angle.

Solving this example using the PFM produces interesting characteristics with respect to the crack initiation location and crack-paths. It is observed that when there is no restriction imposed on the crack from initiating near the holes, the phase-field variable (or crack) initiates simultaneously and symmetrically at the top and bottom hole edges and propagates almost horizontally as if no notches were present in the structure (Fig. 3.27). However, when the crack evolution is restricted near the hole boundary (by imposing a very high G_c in the surrounding region), the crack initiates at both notch tips and propagates towards the hole edges simultaneously (Fig. 3.28a). Further loading leads to evolution of multiple cracks initiating at the edges of holes which ultimately merge in the centre of the structure (Fig. 3.28c). This observation is similar to what has been previously reported in [348]. However in the absence of experimental results for this problem, it is currently difficult to deduce which method predicts a realistic crack pattern. Hence, we refrain from reporting the typical load-deflection curves and focus only on the crack paths.

Since the crack paths derived from XFEM/SBFEM have been shown to coincide very well when employing similar discretization levels and crack propagation increments, modified mesh discretizations and crack propagation increments are sampled (Fig. 3.29). The crack paths for all three variants align very well for the initial portion, while separating slightly as they approach the holes due to the crack propagation increment and mesh density variations.

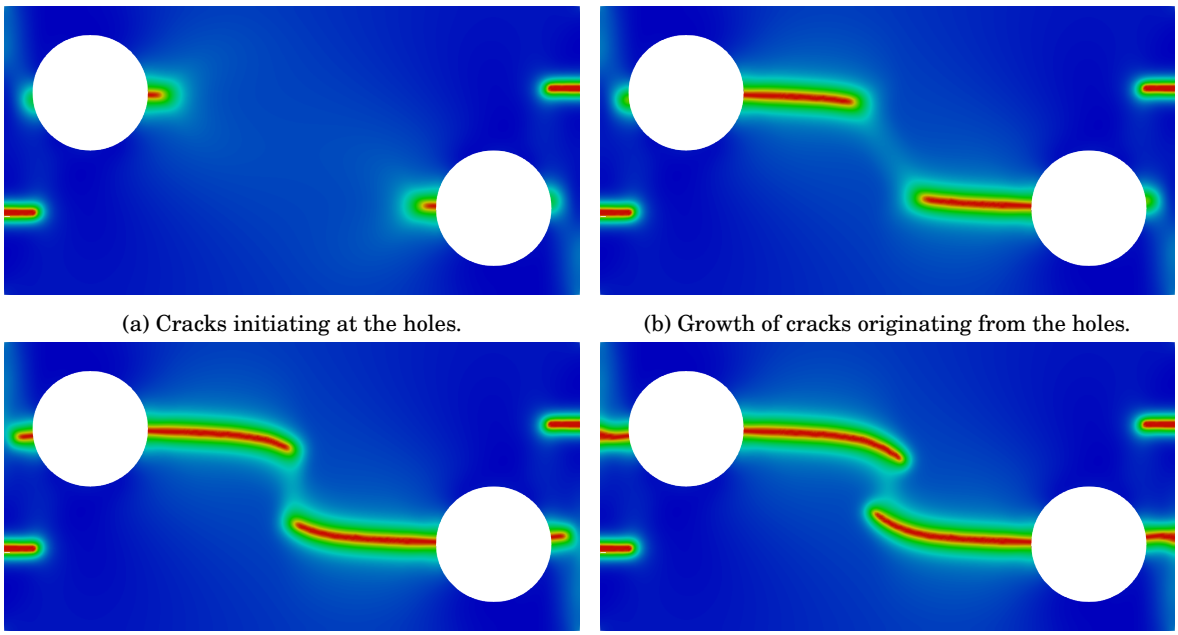

(a) Cracks initiating at the holes.

(b) Growth of cracks originating from the holes.

(c) Additional cracks nucleate at the holes.

(d) Nucleated cracks reach the domain boundary.

Fig. 3.27: PFM crack path without restricting nucleation at the holes.

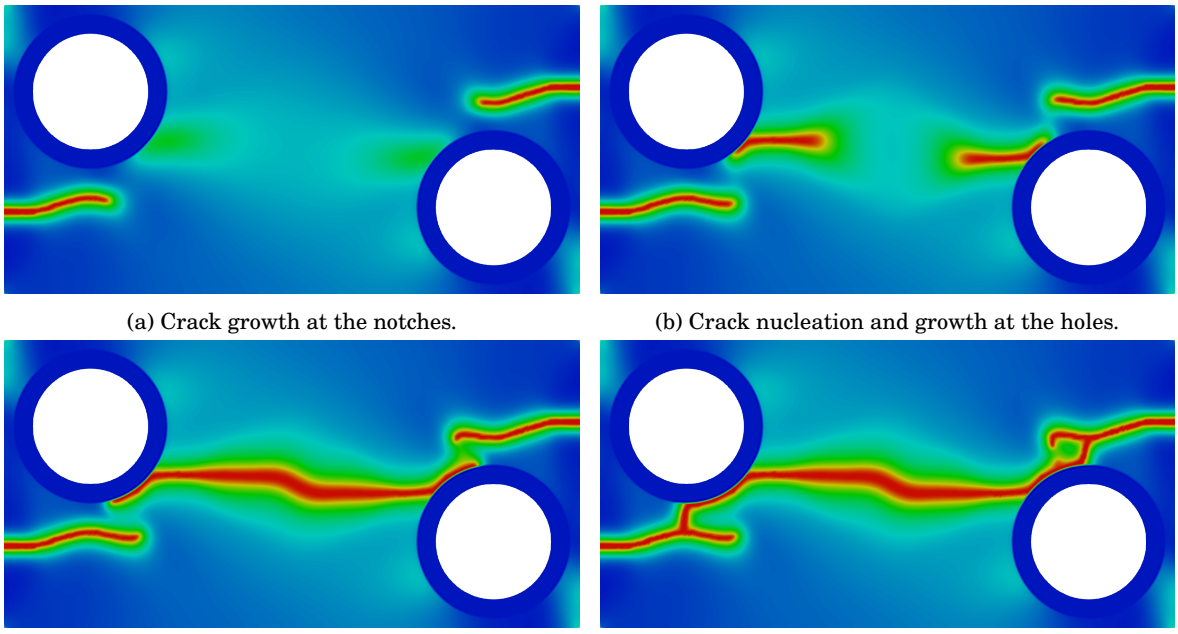

(a) Crack growth at the notches.

(b) Crack nucleation and growth at the holes.

(c) Joining of nucleated cracks at the holes.

(d) Merging of notch and hole cracks.

Fig. 3.28: PFM crack path when restricting the nucleation at the holes.

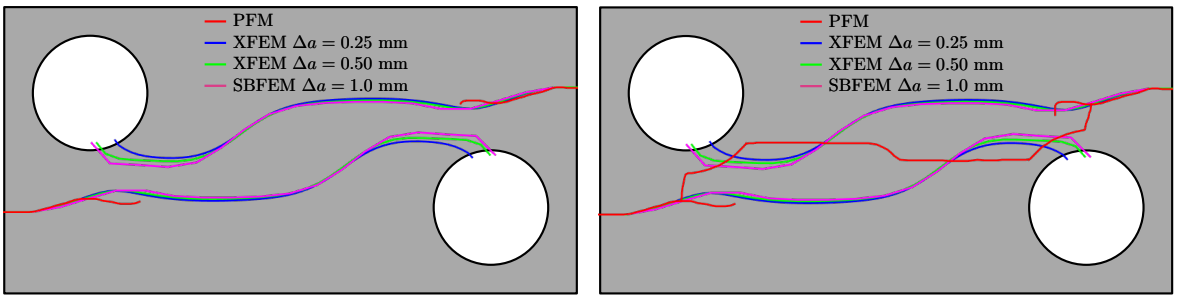

(a) Prior to crack nucleation at the holes.

(b) After crack merging.

Fig. 3.29: Crack path overlay for three variants: XFEM employing a fine mesh with $\Delta a = 0.25$ mm (pink), a coarse mesh with $\Delta a = 0.50$ mm (green) and SBFEM employing an adaptive mesh with $\Delta a = 1.00$ mm (orange).

Part II

Accelerating the Forward Problem

4 Adopting the Hamiltonian Schur Decomposition

A blocked Hamiltonian Schur decomposition is herein proposed for the solution process of the SBFEM, which is demonstrated to comprise a robust simulation tool for LEFM problems. By maintaining Hamiltonian symmetry increased accuracy is achieved, resulting in higher rates of convergence and reduced computational toll, while the former need for adoption of a stabilizing parameter and, inevitably user-supervision, is alleviated.

The method is further enhanced via adoption of superconvergent patch recovery theory in the formulation of the stress intensity factors. It is shown that in doing so, superconvergence, and in select cases ultraconvergence, is succeeded in the SIFs calculation. Based on these findings, a novel error estimator for the stress intensity factors within the context of SBFEM is proposed.

To investigate and assess the performance of SBFEM in the context of linear elastic fracture mechanics, the method is contrasted against the FEM and the XFEM variants. The comparison, carried out in terms of computational toll and accuracy for a number of applications, reveals SBFEM as a highly performant method.

The two conventional approaches to solving the SBFEM's underlying eigen-rpoblem are the eigen-decomposition and the Schur decomposition. In the case of the eigen-decomposition, early strategies to compensate for the numerical issues arising from its use include:

1. Minimizing the condition number by
   - Preconditioning coefficient matrices [169]
   - Normalizing domain properties [344]
2. Addition of a mesh and platform dependent stabilizing parameter ϵ to $[E^2]$. The optimal value of this parameter is unknown a priori ([344], [180]). This corresponds to physically adding small springs to the boundary.

However, these are demonstrated to be insufficient. Employing a Schur decomposition effectively alleviates numerical issues. Unfortunately, due to the linearization of the underlying quadratic eigen-problem, one still must solve a system with double as many unknowns than DOF. With the adoption of the HSchur, which exploits symmetry during the solution process, this doubling is reversed.

4.1 Stress Recovery to Enhance the gSIFs and Introduce an Error Estimator

What sets SBFEM apart from other numerical methods is how elegantly highly accurate SIFs may be obtained. The standard solution procedure by default accommodates cracks. Values for the SIFs can easily be extracted during post-processing of the stresses with only negligible additional computational effort. This is a consequence of the analytical solution in radial direction. If the scaling center is placed at the crack tip, an analytical solution for the strains and therefore additionally the stresses in radial direction may be computed. The SIFs can be determined by evaluating the limit of the stresses as $\xi \to 0$. After substituting the general solution for displacements into the definition of the stresses (Eq. 2.22), the stresses for any particular element can be obtained as a superposition of stress modes:

$$\sigma(\xi,\eta) = \sum_{i=1}^{n} c_i \xi^{-\lambda_i - 1} \Gamma_i \tag{4.1}$$

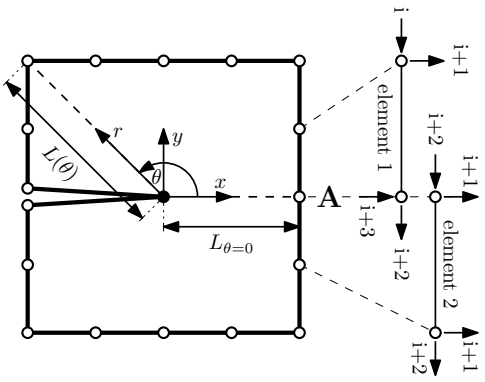

Fig. 4.1: Cracked SBFEM domain with crack tip location coinciding with scaling center. Additionally, the DOFs of the two element used to compute the SIFs are identified.

with Γ_i representing the associated stress modes.

$$\Gamma_i = \begin{Bmatrix} \Gamma_{xx} \\ \Gamma_{yy} \\ \Gamma_{xy} \end{Bmatrix}_i = [D](-\lambda_i[B^1(\eta)] + [B^2(\eta)])\{\Phi_i\} \tag{4.2}$$

The contribution of each mode to the stress response is illustrated in Fig. 4.2. Only the modes corresponding to eigenvalues within the range $-1 < \lambda < 0$ contribute to the singular response at the crack tip ($\xi = 0$). Consequently, for the purpose of determining the SIFs, all other modes can be discarded. In 2D elastostatics, only two eigenvalues and thus modes in the aforementioned range exist. As each element contains these singular modes, theoretically the SIFs could be extracted from any element in the domain. Here, the elements lying directly along the crack path extension (Fig. 4.1, point A) are chosen. Once the singular modes have been identified, corresponding stresses can be theoretically computed using values from anywhere within the bounded domain $0 < \xi < 1$. Due to numerical concerns, the singular stresses are evaluated at the boundary ($\xi = 1$) and consequently the power expression for ξ in Eq. 4.1 is reduced to 1.

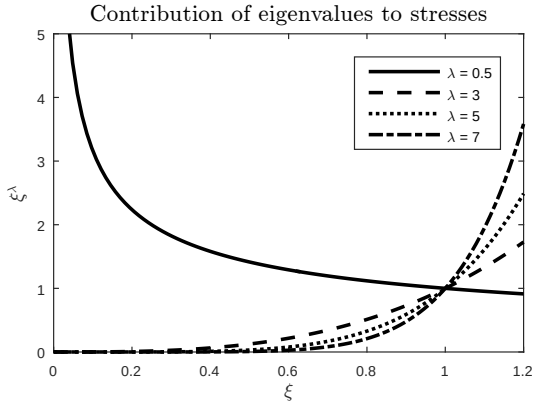

Fig. 4.2: Contribution of eigenvalues to the stress solution, reaffirming that $-1 < \lambda < 0$ leads to singularities as $\xi \to 0$.

Since the singular components of the stresses can be derived analytically, these can be matched directly to the definition of the SIFs. The integration constants c_i correct for the boundary conditions. L_0 is then defined as the distance from the crack tip to the location of the evaluated stresses. Thus, the mode I and mode II SIFs assume the following form:

$$\begin{Bmatrix} K_I \\ K_{II} \end{Bmatrix} = \sqrt{2\pi L_0} \begin{Bmatrix} \sum_{i=I,II} c_i \Gamma_{yy}(\eta = \eta_A)_i \\ \sum_{i=I,II} c_i \Gamma_{xy}(\eta = \eta_A)_i \end{Bmatrix} \tag{4.3}$$

The stress modes Γ_i need only be evaluated at one specific point ($-1 < \eta = \eta_A < 1$) along the element. In order to accomplish this, the correct submatrix ϕ_i must be identified. This consists in finding the eigenvector linked to the singular eigenvalue, as well as identifying the rows representing the DOFs of the corresponding element on the boundary. Their intersection (Fig. 4.3) marks the relevant data for the calculation of the SIF modes. Consequently, the calculation of the SIFs requires only minimal computational effort.

$$[\phi] = \begin{bmatrix} & & \lambda^1_{0.5} & \\ \phi_{1,1} & \cdots & \phi_{1,j} & \cdots \phi_{1,n} \\ \vdots & \ddots & \vdots & \ddots \vdots \\ \phi_{i,1} & \cdots & \phi_{i,j} & \cdots \phi_{i,n} \\ \vdots & \ddots & \vdots & \ddots \vdots \\ \phi_{i+5,1} & \cdots & \phi_{i+5,j} & \cdots \phi_{i+5,n} \\ \vdots & \ddots & \vdots & \ddots \vdots \\ \phi_{n,1} & \cdots & \phi_{n,j} & \cdots \phi_{n,n} \end{bmatrix} \quad DOF_{[i,i+5]}$$

Fig. 4.3: Singular displacement modes as columns and associated DOFs in rows of a representative element on the boundary. The dark gray intersection signifies the submatrix ϕ_i required in order to compute the SIFs.

Since the SIFs are determined solely on the basis of calculated stresses, they can be easily inferred. Should the crack extension fall directly between two elements, different stresses are calculated for each element at the respective node A (Fig. 4.4). Trivial averaging of the stresses is an option, but not necessarily the best one. Thus, in this work, a novel application of SPR theory to SIFs is proposed, resulting in superconvergent and in select cases ultraconvergent convergence rates for the SIFs. This extends previous work by Deeks [83].

Recovered stresses are gained by least squares fit of the raw stresses sampled at the Gauss integration points over a patch of two elements. For the case of enhancing SIFs, the two elements are proposed to coincide with those in the direction of crack extension. Based on [83] and [342] the fitted recovered stresses are calculated as:

$$\sigma^{rec}(\eta) = \{P\}\{a\} \tag{4.4}$$

where $-1 < \eta < 3$ (Fig. 4.4) and for this specific application $\eta = 1$, i.e., point A. $\{P\}$ is a vector of powers of η and $\{a\}$ is a vector of undetermined coefficients a_i. The vector of raw stresses computed at the Gauss integration points is denoted by $\{\sigma^{raw}\}$.

$$\{P\} = \begin{Bmatrix} \eta^0 \\ \eta^1 \\ \vdots \\ \eta^i \\ \vdots \\ \eta^n \end{Bmatrix}^T, \{a\} = \begin{Bmatrix} a_1 \\ a_2 \\ \vdots \\ a_i \\ \vdots \\ a_n \end{Bmatrix}, \{\sigma^{raw}\} = \begin{Bmatrix} \sigma^{raw}_1 \\ \sigma^{raw}_2 \\ \vdots \\ \sigma^{raw}_i \\ \vdots \\ \sigma^{raw}_n \end{Bmatrix} \tag{4.5}$$

where n denotes the amount of Gauss integration points present in the patch. The vector of unknown coefficients $\{a\}$ can be determined by evaluating vector $\{P\}$ at each Gauss integration point, and adding its contribution to matrix $[\bar{P}]$.

$$[\bar{P}] = \begin{bmatrix} \eta^0_1 & \eta^2_1 & \dots & \eta^i_1 & \dots & \eta^n_1 \\ \eta^0_2 & \eta^2_2 & \dots & \eta^i_2 & \dots & \eta^n_2 \\ \vdots & \vdots & \ddots & \vdots & \ddots & \vdots \\ \eta^0_i & \eta^2_i & \dots & \eta^i_i & \dots & \eta^n_i \\ \vdots & \vdots & \ddots & \vdots & \ddots & \vdots \\ \eta^0_n & \eta^2_n & \dots & \eta^i_n & \dots & \eta^n_n \end{bmatrix} \tag{4.6}$$

The least squares problem can then be formulated as:

$$[\bar{P}](\{\sigma^{raw}\} - [\bar{P}]\{a\}) = 0 \tag{4.7}$$

Subsequently, the vector of unknown coefficients is determined as:

$$\{a\} = ([\bar{P}]^T[\bar{P}])^{-1}[\bar{P}]^T\{\sigma^{raw}\} \tag{4.8}$$

Thus, recovered stresses in the direction of crack extension are determined by substituting $\eta = \eta_A$ (Fig. 4.4, point A) into Eq. 4.4. These stresses are indirectly recovered, by smoothing the stress modes Γ_i (Eq. 4.2), which in turn rely on the displacement modes $[\Phi_i]$. Since only two displacement modes contribute to the singular response, only a small subset of the eigenmodes resulting from the SBFEM solution must be smoothed. This is the first means used to reduce the computational effort for determining the SIFs. Further, since only one patch in direction of crack extension is considered, recovery over only two elements, again a small subset of the whole domain, is necessary. It is assumed that this trade off in potential accuracy is offset by the gain in computational speed. This is later demonstrated to hold true in sec. 4.2. Consequently, Eq. 4.1 may be rewritten as:

$$\sigma^s(\xi,\eta) = \sum_{i=1}^{2} c_i \xi^{-\lambda_i - 1}\Gamma_p^s \tag{4.9}$$

in which superscript s denotes the singular modes and subscript p corresponds to the stress modes smoothed on the patch in direction of crack extension. Since the stresses are evaluated at the boundary, $\xi = 1$ and Eq. 4.9 simplifies to the extent that the SIFs can now be formulated as:

$$\begin{Bmatrix} K_I^{rec} \\ K_{II}^{rec} \end{Bmatrix} = \sqrt{2\pi L_0} \begin{Bmatrix} \sum_{i=1}^{2} c_i \Gamma_{p,yy}^s(\eta = \eta_A) \\ \sum_{i=1}^{2} c_i \Gamma_{p,xy}^s(\eta = \eta_A) \end{Bmatrix} \tag{4.10}$$

Finally, it stands by virtue of the SPR theory, that the so-recovered SIFs should be at least superconvergent.

Based on the difference in raw and recovered stresses, a novel error estimator accompanying the proposed recovery scheme for SIFs can be deduced.

$$\{e_\sigma^*(\xi,\eta)\} = \{\sigma^*(\xi,\eta)\} - \{\sigma_h(\xi,\eta)\} \tag{4.11}$$

where superscript * denotes the recovered value and subscript h denotes the raw value of the stress calculated in direction of crack extension. By consequence, obtaining the error estimator is rendered computationally inexpensive.

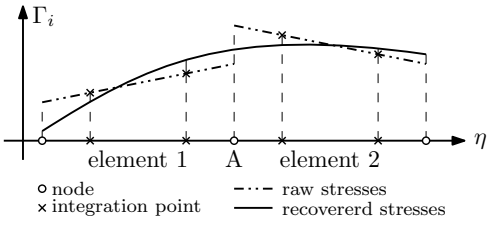

Fig. 4.4: Stress recovery based on SPR. A least square fit is constructed for the stresses in point A, based on values computed at the Gaussian integration points.

4.2 Numerical Examples

The first numerical example illustrates the benefits to the overall robustness of the proposed SBFEM solution, incorporating the HSchur decomposition, versus the established eigen and standard Schur decomposition. This novel contribution alleviates the need for an architecture-dependent stabilizing parameter ϵ. The second numerical example demonstrates the consequently improved convergence behavior of the

L_2 displacement and stress norms. Additionally, an efficient procedure is proposed to enhance the accuracy of the calculated SIFs. According to the latter, only local stress recovery over select few elements is performed on the boundary instead of over the whole domain, simultaneously resulting in significantly reduced computational effort. Further, it is established that the SIFs calculated by the proposed method are superconvergent for even-noded elements or even ultraconvergent for some odd-noded cases. This forms the basis for a novel error estimator for SIFs. As part of the third numerical example, the computational effort for an SBFEM solution is contrasted to that of FEM, based on an approximate flop count, which is demonstrated for the first time herein. Additionally, the enhancement in accuracy for the proposed local recovery of the stresses compared to adoption of trivial averaging of raw stresses at nodes is demonstrated. Next, SBFEM is directly contrasted to XFEM and the FE-based commercial software Abaqus in terms of SIF reconstruction and conditioning of the stiffness matrix. To the authors knowledge, this is the first occurrence of a direct comparison between standard SBFEM and XFEM in literature. As XFEM represents a major competing method to SBFEM within the context of LEFM, the fourth numerical example primarily considers this comparison. Furthermore, the computational time required for various parts of the SBFEM procedure are shown, illustrating the computational gains achieved by the proposed HSchur decomposition and smoothing processes.

Calculations were performed on an Intel Core i5 6600K and an Intel Xeon E3-1225 v3. SBFEM and XFEM where implemented in Matlab 2015b. In Abaqus 6.14-1 the contour integral method was used to determine the SIFs.

4.2.1 Edge-cracked Square Plate Under Bending

A square, homogeneous domain with an edge crack as depicted in Fig. 4.5 is considered, with length $L = 2$ units and crack length $a = L/2$. The domain boundary is uniformly discretized. For this special case of pure bending, an analytical solution exists for the SIFs [100]. The application of point boundary restraints in SBFEM is similarly problematic as would be in the standard FEM case, as these must be applied for eliminating rigid body motion. Since in this numerical example restraints have to be positioned along the direction of crack extension, they may induce restraining forces precisely at the position used to calculate the SIFs. This complicates the accurate determination of the SIFs, though it may be mitigated to an extent for this special test case by scaling the problem domain uniformly. This is admissible since the SIF for an edge cracked square plate under bending only depends on the ratio of side length to crack length [100].

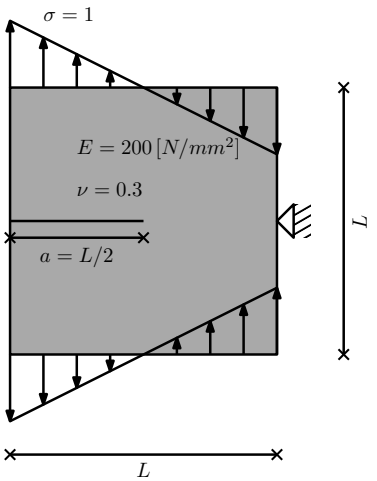

Fig. 4.5: Edge-cracked square plate subject to bending. The problem statement for the first numerical example.

Numerical difficulties arise in the solution process of SBFEM due to the occurrence of rigid body modes. In 2D elastostatics, a 4x4 block of zero eigenvalues exists. Two are associated with the response of the bounded domain, whereas the other two contribute to the response of the unbounded domain (Fig. 2.5). Numerical issues may perturb eigenvalues, resulting in signs, which may alternate arbitrarily. A subsequent reordering of eigenvalues into left half plane and right half plane may thus result in an eigenvalue

intended for the unbounded domain to falsely contribute to the bounded domain. Since the stiffness matrix is constructed from the corresponding eigenvectors, this effect leads to erroneous results. As an example, it is possible that the rigid body mode of horizontal displacement is considered twice, whereas the rigid body mode of vertical displacement is not considered at all and vice versa (Fig. 2.4).

Since one is not able to predict the outcome of the sorting a priori, a stabilizing parameter ϵ is typically introduced in existing literature [344], with the intent of shifting the eigenvalues of the rigid body modes off of the imaginary axis. This is achieved by modifying the input to the Hamiltonian Matrix $[Z]$ (Eq. 2.38) as follows, which physically bears the effect of introducing springs on the boundary:

$$[E^2] = [E^2] + \epsilon[I] \tag{4.12}$$

Tbl. 4.1 summarizes the solution quality of SBFEM for various values of epsilon. According to [344], the typical values for epsilon range from $10^{-6} < \epsilon < 10^{-12}$. Below, the eigen decomposition is considered, though similar effects may also be observed for the standard Schur decomposition. It is evident, that values of ϵ exist, where incorrect solutions are obtained. Further, there exist regions for which the choice of ϵ does not bear significant influence on the solution. Remarkable is the fact that on different CPUs, the values for epsilon, which result in solution errors due to incorrect separation of eigenvalues, differ. Consequently, the correct choice of epsilon cannot be determined prior to the analysis. In order to ensure robust results, multiple runs with different values for epsilon are necessary and usually require user intervention, which reduces the computational advantage of SBFEM. This significantly complicates modeling of crack propagation and effectively bars SBFEM from being used for problems, where successive function evaluations are required, such as optimization problems using heuristic methods.

Tbl. 4.1: Correct solutions obtained as a function of the stabilizing parameter ϵ for various CPU architectures. Discretized with 3-noded elements and 6 elements per side.

$\boldsymbol{\epsilon = 10^{-()}}$	6	6.5	7	7.5	8	8.5	9	9.5	10	10.5	11	11.5	12	12.5	13	13.5	14	14.5	15
Core i5	✓	✓	X	X	X	X	✓	✓	✓	✓	X	X	✓	✓	✓	✓	✓	X	✓
Xeon E3	✓	X	✓	✓	X	X	✓	✓	X	X	X	✓	✓	✓	✓	✓	✓	✓	✓

The main advantage of the HSchur decomposition stems from the fact that it accounts for the special structure of the Hamiltonian Matrix $[Z]$, which dictates symmetry about the real and imaginary axis for all eigenvalues. Taking advantage of symmetry by only considering the left half plane associated with the negative eigenvalues, the eigenvalues are always separated properly, and the need for a stabilizing parameter is removed by default. Thus, this novel approach enables a robust, parameter independent solution process for SBFEM.

This symmetry may be observed in Fig. 4.6, where the eigenvalues for the square plate are plotted. The HSchur decomposition better respects symmetry in comparison to the corresponding eigen and Schur decompositions. For the Schur decomposition, the block diagonalization seems to weaken symmetry. The eigen-decomposition approach does not require this step, resulting in improved symmetry. However, the issues pertaining to the sorting of the rigid body modes remains. Slight variation of the stabilizing parameter induces variation in the eigenvalues, resulting in modified eigenvectors. As a result, the stiffness matrix loses its symmetry (Fig. 4.7), which results in solution errors.

A large value for the stabilizing parameter epsilon results in loss of solution accuracy, as introducing springs on the boundary effectively results in a different structural system. On the other hand, too small values for epsilon may result in incorrect solutions due to improper separation of eigenvalues. Fig. 4.7 visualizes, that there is a region for ϵ, where the solution is better behaved. For this purpose, the values in the stiffness matrix ($K_{i,j}$) are compared to the averaged sum ($K_{ave} = (1/2) * (K_{i,j} + K_{j,i})$). According to Brenner and Kressner [46] this difficulty of computing the zero and negative eigenvalues of a Hamiltonian matrix is well known for QR and Arnoldi based decompositions, leading to loss of symmetry due to round-off errors. It is further well-known that accuracy is compromised, when computing eigenvalues of a matrix whose elements differ by several orders of magnitude [320]. Since this is the case for the entries of the Hamiltonian matrix $[Z]$, due to the contribution of the inverse of $[E^0]$, this further compounds numerical errors. Normalizing the contributions of the coefficient matrices [344] or applying a preconditioner [169] mitigate this effect partially, however the issues discussed in [46] still remain.

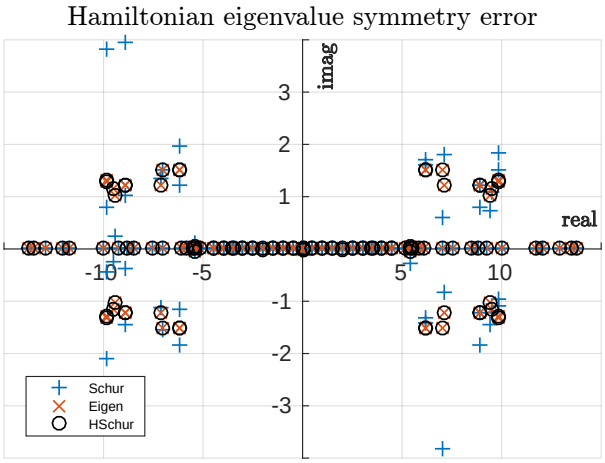

Fig. 4.6: Symmetry of eigenvalues for eigen, Schur and HSchur decomposition. Discretized with 2-noded elements and 4 elements per side.

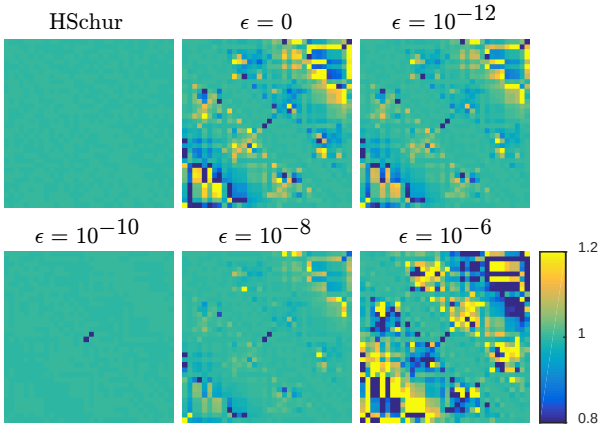

Fig. 4.7: Symmetry of stiffness matrix for various choices of ϵ compared to HSchur decomposition. Discretized with 2-noded elements and 4 elements per side.

Further, the condition number of the stiffness matrix varies, depending on different choices of stabilizing parameter. Fig. 4.8 depicts the evolution of the condition number for the eigen-decomposition with $\epsilon = 10^{-12.5}$ compared to the HSchur decomposition. However, since the condition number additionally varies as a function of ϵ for the standard eigen-decomposition case, box plots are further provided, indication variation for the range of $10^{-6} < \epsilon < 10^{-15}$. The observed spread in condition number may pose unpredictable, numerical challenges. This spread is not present for the proposed HSchur decomposition. The same is observed for matrix $[\Phi]$ (Eq. 2.44), whose inversion is required for the formation of the stiffness matrix and the evaluation of the vector of coefficients $\{c\}$ (Eq. 2.42).

Since the HSchur decomposition results in a robust and predictable solution for SBFEM, the calculated SIFs result independently of the stabilizing parameter epsilon. Fig. 4.9 demonstrates the fluctuation in computed SIFs by eigen-decomposition, contrasted to the estimates of the HSchur decomposition. It is observed that the error in calculated SIFs via eigen-decomposition with a variable ϵ may outweigh the inherent accuracy of the method itself. Additionally, as is later demonstrated in the next numerical example, the L_2 displacement error for lower order elements also fluctuates significantly with variation in ϵ (Fig. 4.15). This is not the case when employing the HSchur decomposition (Fig. 4.16).

In [100] an exact value for K_I is provided for the edge cracked plate subjected to pure bending. In Figs. 4.10 and 4.11 respectively, the SIF K_I computed using raw stress and recovered stress is depicted. Stress recovery is performed only on the two element patch in the direction of crack extension (Fig. 4.1), and not on the entire domain. Tbl. 4.2 indicates that for the proposed case of local recovery the computational effort is drastically reduced, while achieving similar accuracy to full domain recovery. This is important,

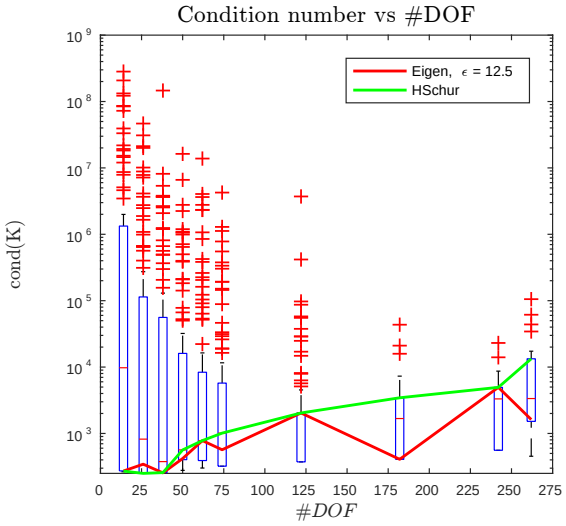

Fig. 4.8: Evolution of the condition number for eigen and HSchur decomposition. Discretized with 2-noded elements.

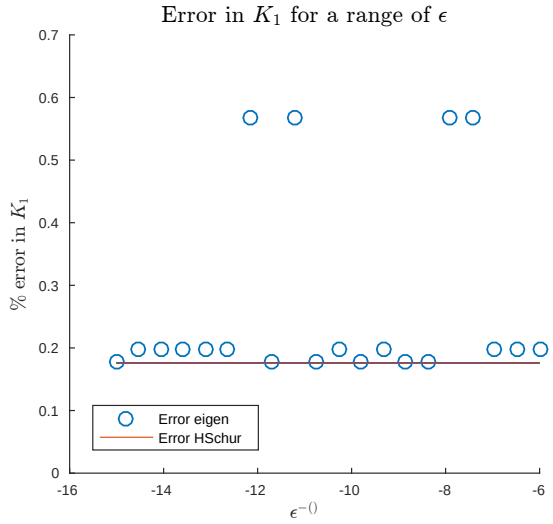

Fig. 4.9: Error in SIF K_I computed by eigen-decomposition as a function of ϵ, contrasted to the HSchur decomposition. Discretized with 3-noded elements and 6 elements per side.

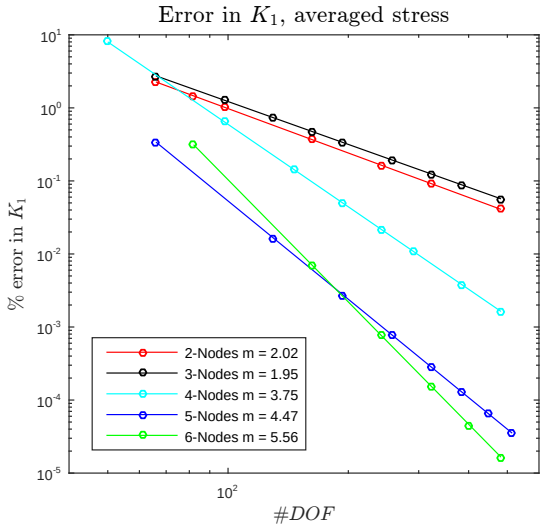

Fig. 4.10: Error in SIF K_I computed using raw averaged stress.

since stress recovery in SBFEM occupies a significant portion of the total execution time (Tbl. 4.5). The formulation of an error estimator for SIFs based on the difference of the raw and recovered stresses, as proposed herein, may be exploited to greatly facilitate the SBFEM post-processing procedure. In Fig. 4.12 the computed error estimator is contrasted to the exact error for the SIF, where good agreement is noted. The proposed procedure allows for inherent checking of the accuracy of the computed SIFs, within a single analysis and with minimal computational effort.

Tbl. 4.2: Percent of total analysis time spent on calculating K_I based on full or local domain stress recovery. Discretized with 3-noded elements and 3 elements per side, 4-noded elements and 4 elements per side and 5-noded elements and 5 elements per side respectively.

$\#DOF$	full domain		local domain	
	% total time	% error K_I	% total time	% error K_I
98	36.03	0.128	0.24	0.131
198	30.63	0.019	0.10	0.020
322	26.11	0.001	0.02	0.001

4.2.2 Edge-cracked Square Plate with Forced SIFs

The square, homogeneous domain with an edge crack, as depicted in Fig. 4.13 is considered, with length $L = 2$ units and crack length $a = L/2$. The boundary is uniformly discretized. An analytical solution for displacements, stresses and SIFs is given in [99]. The expressions linking the displacements, stresses and SIFs are given in Tbl. 4.3.

For this example, the mode I and mode II SIFs are chosen as $K_I = 0$ and $K_{II} = 1$. The coinciding exact displacements on the boundary are then enforced as boundary conditions at each node. The improvements in convergence properties when using the novel approach based on the HSchur decomposition are investigated. To this end, first the L_2 error in displacements norm is considered, followed by the L_2 error in stress norm. Figs. 4.15 and 4.16 demonstrate the L_2 error in displacements norm for the eigen and HSchur decomposition respectively. Since the boundary conditions are applied to all nodes, the error norm is calculated based on chosen displacements post-processed at 10 equally spaced points along ξ, as denoted by crosses in Fig. 4.14. The same procedure was carried out in the case of the stresses.

A significant improvement in the regularity and rate of convergence is observed between the proposed HSchur decomposition (Fig. 4.16) and the standard eigen-decomposition (Fig. 4.15), as optimal convergence

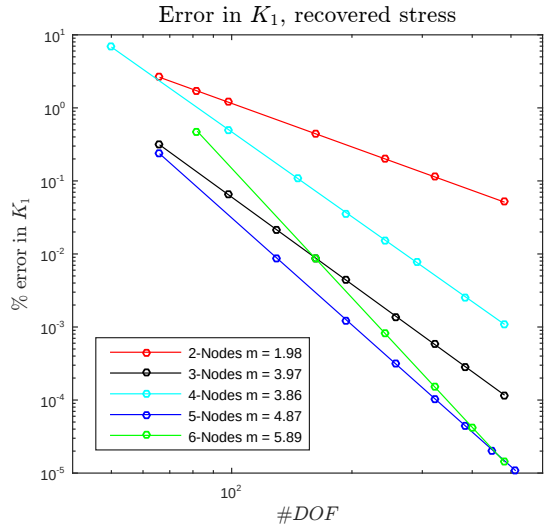

Fig. 4.11: Error in SIF K_I computed using recovered stress.

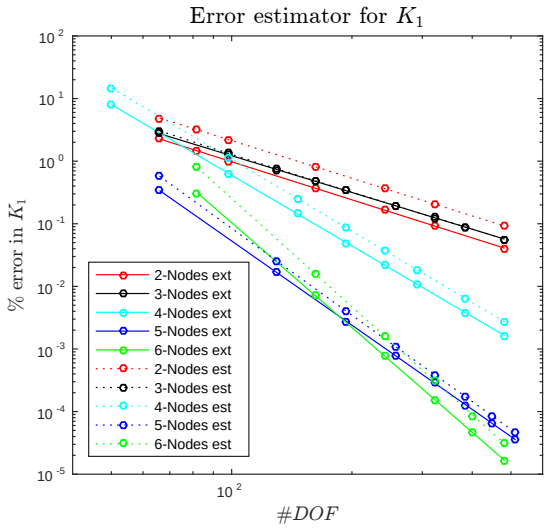

Fig. 4.12: Proposed error estimator for SIFs contrasted to exact error.

Tbl. 4.3: Analytical solution for edge cracked plate under forced K_{II}

Component	**Exact solution**
u_1:	$\frac{K_2}{2*\mu}\sqrt{\frac{r}{2\pi}}\sin(\theta/2)(\kappa+1+2\cos^2(\theta/2))$
u_2:	$-\frac{K_2}{2*\mu}\sqrt{\frac{r}{2\pi}}\cos(\theta/2)(\kappa-1-2\sin^2(\theta/2))$
σ_{11}:	$-K_2/\sqrt{2\pi r}\sin(\theta/2)(2+2\cos(\theta/2)\cos(3\theta/2))$
σ_{22}:	$K_2/\sqrt{2\pi r}\sin(\theta/2)\cos(\theta/2)\cos(3\theta/2)$
σ_{12}:	$K_2/\sqrt{2\pi r}\cos(\theta/2)(1-2\sin(\theta/2)\sin(3\theta/2))$

is almost achieved. Since the proposed HSchur decomposition is independent of a stabilizing parameter, its convergence properties do not exhibit oscillations, as is observed for the standard eigen-decomposition. For the eigen-decomposition, these oscillations may be amended, by appropriate variation of ϵ, a task, which

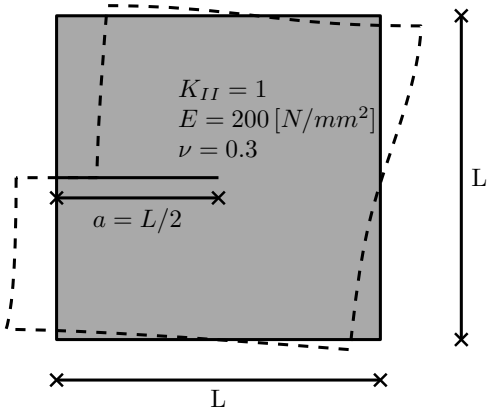

Fig. 4.13: Edge-cracked square plate problem domain subject to $K_{II} = 1$ as boundary conditions. The problem statement for the second numerical example.

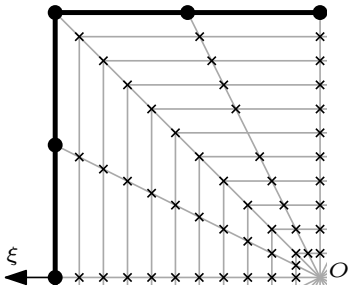

Fig. 4.14: Points at which the L_2 norms are calculated, denoted by crosses. The upper left quarter of the domain is depicted.

however is not straightforward. This further implies that an increase of the employed number of DOFs does not guarantee higher accuracy in the eigen-decomposition case. Furthermore, the convergence rates m of this newly proposed method, better approximate the values predicted by established FEM theory. Optimal values m^{opt} are equal to the order of the interpolation function. For SBFEM, this is equal to the amount of nodes present in each element.

Next, the performance of i) the Schur decomposition as provided in Matlab, ii) the Hamiltonian Schur decomposition of [75], and iii) the proposed new blocked Hamiltonian Schur decomposition, HSchur, is further investigated via the following residual metric [75]:

$$\text{Residual}_{Schur} = \frac{||\{U\}^T[H]\{U\} - [\hat{H}]||_2}{||[\hat{H}]||_2} \tag{4.13}$$

where $[\hat{H}]$ represents the computed Hamiltonian Schur form and $[H]$ denotes the original Hamiltonian Matrix. The residual of the current Matlab implementation of the Schur decomposition, does not vary significantly with changing values of ϵ. In Tbl. 4.4 the residual for all three methods is provided for different levels of discretization. The newly proposed HSchur decomposition clearly outperforms the competing methods, which results in improved convergence rates and elimination of the oscillations of the standard eigen-decomposition (Fig. 4.15). It should be noted that the Hamiltonian Schur method (CSchur) proposed by Chu et al. [75], which is the precursor to the currently proposed method, has previously been shown to exhibit increased residuals when clusters of tightly grouped eigenvalues are present.

Clustering of eigenvalues is generally the case for SBFEM, which is demonstrated in Fig. 4.6 for few DOFs and Fig. 4.17 for a typical amount of DOFs necessary for such an analysis. Naturally, as the amount of DOFs increases the clustering issues further propagate, and the residual of CSchur tends to accordingly increase. The block of zero eigenvalues [193] still poses a computational challenge for the proposed HSchur

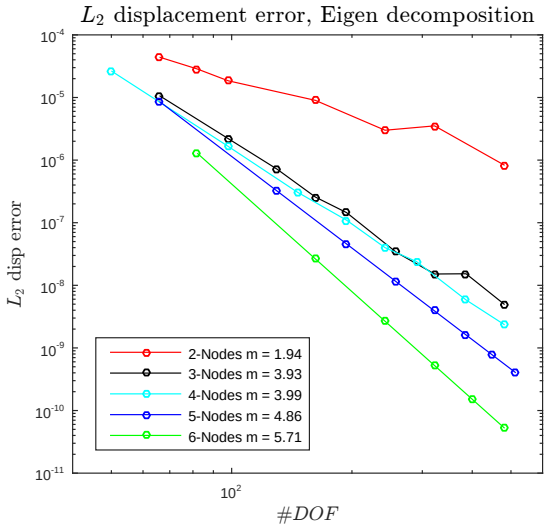

Fig. 4.15: Convergence results of the L_2 displacement error based on the eigen-decomposition.

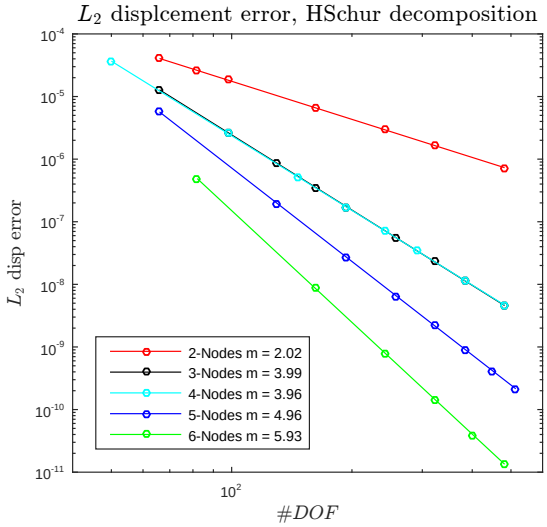

Fig. 4.16: Convergence results of the L_2 displacement error based on the HSchur decomposition.

Tbl. 4.4: Residuals for each decomposition type. Discretized with 3-noded elements.

# DOF	**Schur**	**CSchur**	**HSchur**
160	$5.4 * 10^{-1}$	$8.1 * 10^{-5}$	$9.1 * 10^{-11}$
226	$6.3 * 10^{-1}$	$6.2 * 10^{-5}$	$7.5 * 10^{-12}$
280	$2.7 * 10^{-1}$	$9.0 * 10^{-3}$	$6.3 * 10^{-9}$
360	$3.5 * 10^{-2}$	$1.3 * 10^{-2}$	$5.2 * 10^{-9}$
448	$7.7 * 10^{-2}$	$2.6 * 10^{-2}$	$2.8 * 10^{-12}$

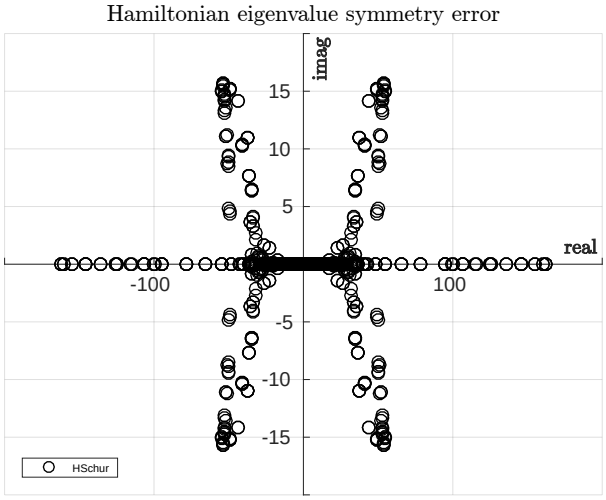

Fig. 4.17: Eigenvalue clustering for domains with higher levels of discretization. Discretized with 5-noded elements and 10 elements per side.

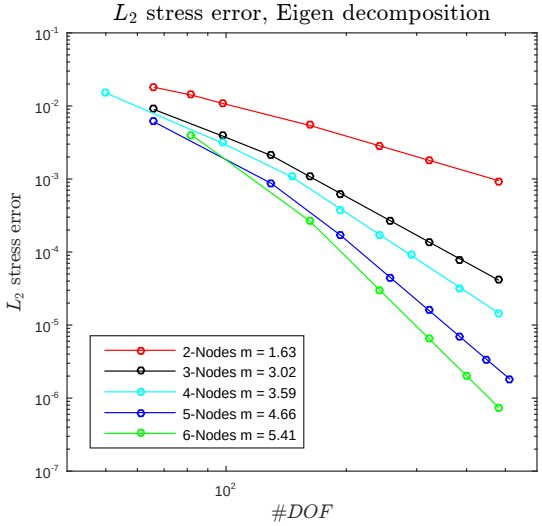

Fig. 4.18: Convergence results of the L_2 stress error based on the eigen-decomposition.

method. The presence of purely imaginary eigenvalues results in failure to find an invariant, isotropic subspace to working precision. By relaxing the isotropy checks, a near real Schur form is nonetheless obtained, thereby forfeiting numerical accuracy. The is observed for residual values greater than machine precision ($eps = 2.22 * 10^{-16}$).

Figs. 4.18 and 4.19 plot the L_2 norm of the stress error vs DOFs. To this end, the stresses are first computed, and then recovered using SPR theory. The von Mises stress is adopted for this comparison. Again, the proposed HSchur decomposition outperforms the standard eigen-decomposition scheme. However, certain features cannot be overcome. A change in convergence rate is observed, when few element are used to model a side of the domain. As stress recovery techniques require at least two elements to form a recovery patch, they are not applicable when one element is used to discretize a side. The lack of stress recovery options leads to a decreased rate of convergence. It is therefore proposed to discretize each side by at least two elements, in order to harness the benefits of SPR theory. Furthermore, a coarse discretization significantly limits the resolution of the mode shapes comprising part of the SBFEM solution.

Since the stress variation in the tangential direction is not smooth around corners, special consideration must be taken for these cases. In order to avoid errors, an automated procedure is proposed, based on the

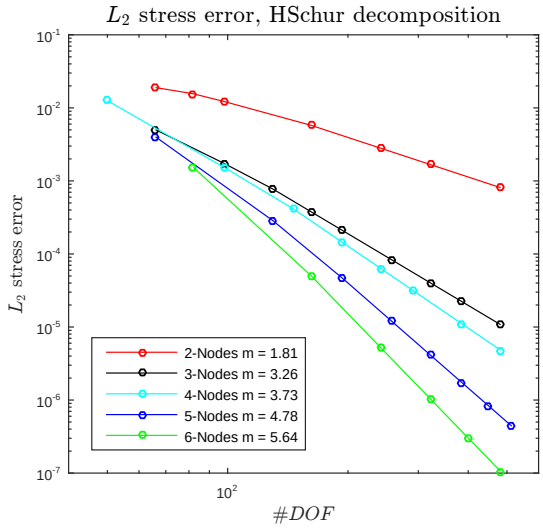

Fig. 4.19: Convergence results of the L_2 stress error based on the HSchur decomposition.

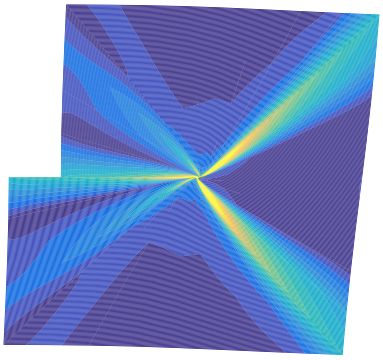

Fig. 4.20: Qualitative location of errors in von Mises stress (yellow), by comparing the SBFEM solution to the analytical ones provided in Tbl. 4.3. Discretized with 3-noded elements and 4 elements per side.

orientation of adjacent elements. As long as the normal vectors of two adjacent elements point along the same direction, i.e., the cosine of the angle spanned between them approaches the value of 1, then the adjacent element is added to the patch. Such a process may not be put in place for the case of corner points, an issue, which is elaborated upon in the fourth numerical example.

Fig. 4.20 contrasts the von Mises stresses computed with only few DOF by SBFEM with the exact stresses obtained from Tbl. 4.3. The largest discrepancy on the domain results around abrupt changes in boundary orientation for the reason hinted at earlier. Hence, it it shown that optimal superconvergence cannot be obtained due to this limitation. Apart from this exception, the HSchur decomposition succeeds in improving the convergence behavior.

For the current numerical example, the stresses along the boundary in the direction of crack extension are recoverable and thus the SIFs are accurately and efficiently calculated, as observed in Fig. 4.21. The error is determined based on the exact values for the SIFs, imposed originally through the boundary conditions. The improvement over the case with only trivial averaging of stresses at nodes (Fig. 4.22) is recognizable. The convergence rates m are observed as superconvergent, i.e., the stresses converge at the same rate as the displacements.

Since one of the aims is to determine the potential of SBFEM for readily determining the SIFs, the

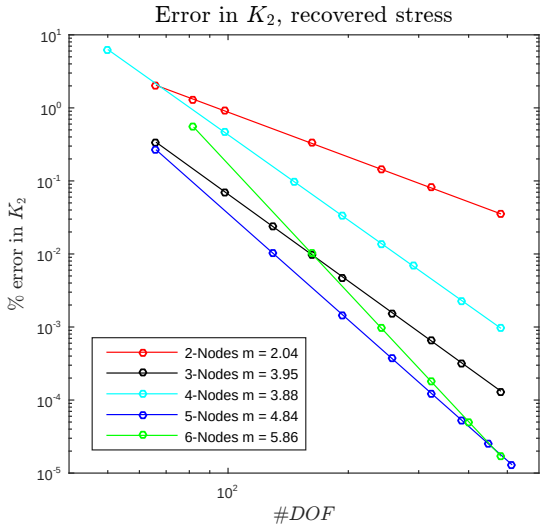

Fig. 4.21: Percent error in K_2 calculated using recovered stress.

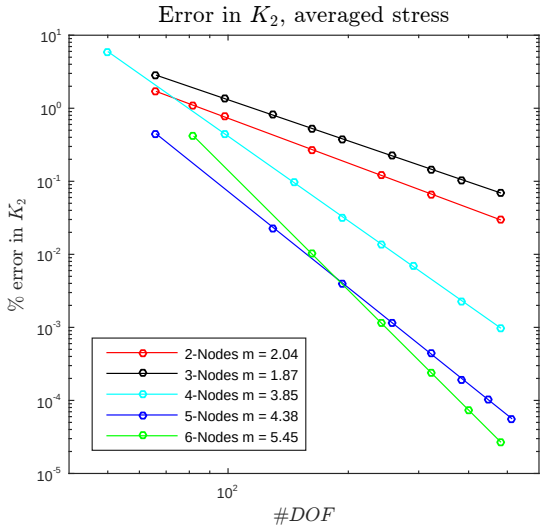

Fig. 4.22: Percent error in K_2 calculated using averaged stress.

error in K_2 is plotted against wall clock time for each analysis (Fig. 4.23). It is apparent, that SBFEM can compute the SIFs with sub-percent accuracy in well under a second on current generation computers. Further, it seems that the odd-noded elements outperform their even-noded counter parts.

Tbl. 4.5 summarizes the computational time required for completing the various tasks in SBFEM. Striking is the fact that for the current implementation of SBFEM, recovery of the stresses over the entire domain significantly extends the required computational time. In contrast, calculation of SIFs by the proposed local stress recovery scheme does not add any significant computational toll.

The associated error estimator for the SIFs is plotted in Fig. 4.24. Moreover, for this example, the a posteriori error estimator is highly effective and may be easily determined. In contrast to other SIF error estimators ([246],[115]), solving for a second right hand side is not necessary. The absolute difference between estimated and exact error estimator is seen to decrease for all elements and is generally in the order of percent fractions (Fig. 4.24).

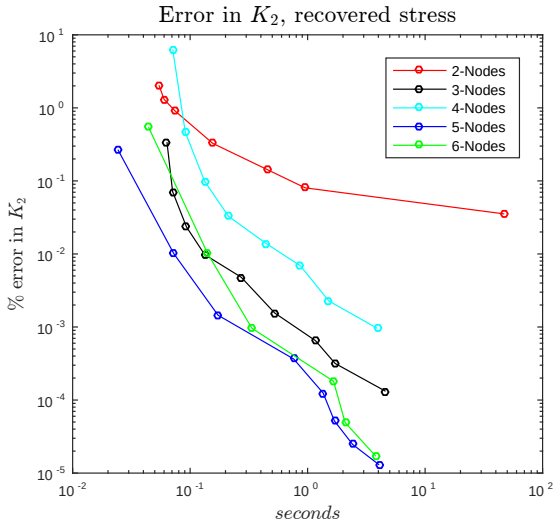

Fig. 4.23: Percent error in K_2 calculated using averaged stresses vs wall clock time. The calculations were performed on an Intel Xeon E3-1225 v3.

Tbl. 4.5: Percentage of computational time spent on various tasks for the solution of SBFEM. Discretized with 3-noded elements and 3 elements perside, 4-nodd elements and 4 elements per side and 5-noded elements and 5 elements per side respectively.

Task	**98 DOF**	**198 DOF**	**322 DOF**
invert $[E^0]$	0.53	0.63	0.43
HSchur	52.26	64.03	70.18
form $[K]$	0.38	0.30	0.25
invert $[K]$	6.87	3.88	2.64
form $\{c\}$	3.69	0.43	0.37
stress recovery	36.03	30.63	26.11
SIF	0.24	0.10	0.02

4.2.3 Double Edge-cracked Plate Under Tension

A double edge-cracked plate under tension as depicted in Fig. 4.25 is considered, with length $L = 1$ units and crack length $a = L/4$. The boundary is uniformly discretized. For this numerical example, SBFEM is compared to XFEM and the commercial FEM software Abaqus. Three primary metrics for a solution, i.e., accuracy of calculated SIFs, floating point operations (flops) and number of DOFs are considered. Since the motivation for employing SBFEM to model fracture is accelerating simulations, analysis time is included as a secondary metric.

The flops required for the solution of each method are based on simplified assumptions. Steps exist, such as the inversion of matrices and the solution of the eigen-problem, which dominate the computational toll of an analysis. For XFEM and the standard FEM, this toll is assumed to stem primarily from the inversion of the structures stiffness matrix. In SBFEM however, multiple computationally intensive steps exist, summarized in Tbl. 4.6. The variables n and m denote the DOFs present in SBFEM and XFEM respectively, whereas b represents the half-bandwidth of the matrix $[E^0]$. The solution process in SBFEM is constrained by the computational demands of the Schur decomposition. The newly proposed HSchur decomposition reduces this burden by exploiting the symmetry conditions of the Hamiltonian matrix $[Z]$. Considering flops alone, the HSchur decomposition is clearly more performant. Since the method is currently implemented as proof-of-concept code written in Matlab, execution times are similar to the generic Schur decomposition. Once this novel method is assimilated into high performance libraries, calculation

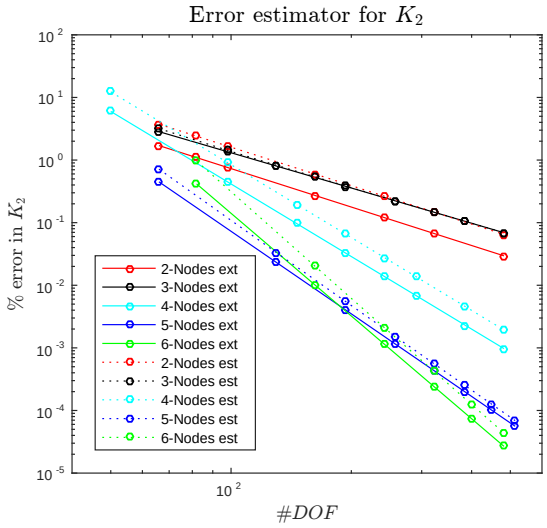

Fig. 4.24: Error estimator for K_2 based on difference between raw and recovered stress.

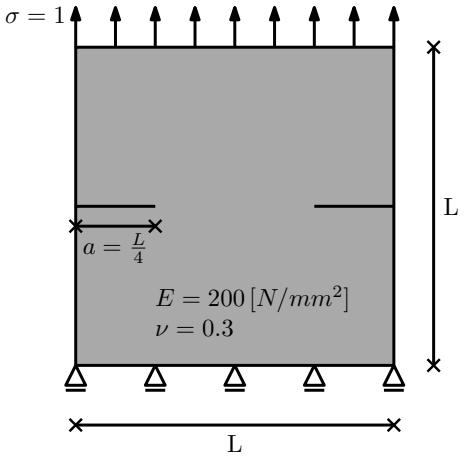

Fig. 4.25: Double edge cracked plate under tension. Problem statement for the third numerical example.

times are expected to improve considerably.

In Abaqus, quadratic elements are used with the mid-side nodes set at the quarter points and the element sides are collapsed into a single node, in order to emulate singular elements capable of representing a square root singularity. The SIFs are calculated by a contour integral with four contours. In XFEM, linear elements are employed. The radius of enrichment is kept constant at $r_e = 0.2$ units, while the radius of integration is fixed at $r_i = 2.55$ times the element size. The SIFs are calculated by interaction integral. In SBFEM, the use of higher order elements does not significantly alter the computational effort. Since the stiffness matrix is fully populated, higher order elements do not affect the bandwidth other than in the formulation of $[E^0]^{-1}$ (Eq. 2.38). This operation constitutes a minor part of the overall computational complexity (Tbl. 4.6). Subsequently, the worst case is assumed and the half-bandwidth is chosen to be maximal. The computational burden due to fully populated matrices is offset by symmetry and the fact that only the boundary need be discretized.

Fig. 4.26 depicts the theoretical flop count required for analysis as a function of DOFs. A comparison focused simply on flop count favors the XFEM and FEM-based implementations. The proposed HSchur decomposition performs favorably, compared to the current standard Schur, requiring roughly an order of magnitude less flops for the same solution. However, in a direct comparison to XFEM, it still requires substantially higher computational effort at an equal level of discretization.

Tbl. 4.6: Rough flop counts for two SBFEM variants and (X)FEM

Step	**SBFEM**		**(X)FEM**
	Schur	HSchur	
Coefficient Matrices	bn^2	bn^2	0
Decomposition.	$25*(2n)^3$	$40n^3+205n^2$	0
Sort	$3n^3$	$3n^3$	0
Diagonalize	$2n^3$	$2n^3$	0
Stiffness Matrix	$2/3n^3$	$2/3n^3$	0
$\{u\}=[K]^{-1}\{F\}$	$1/3n^3$	$1/3n^3$	$1/3m^3$
Integration Constants	$1/3n^3$	$1/3n^3$	0
Total	$\frac{619}{3}n^3+bn^2$	$\frac{139}{3}n^3+(205+b)n^2$	$(1/3)m^3$

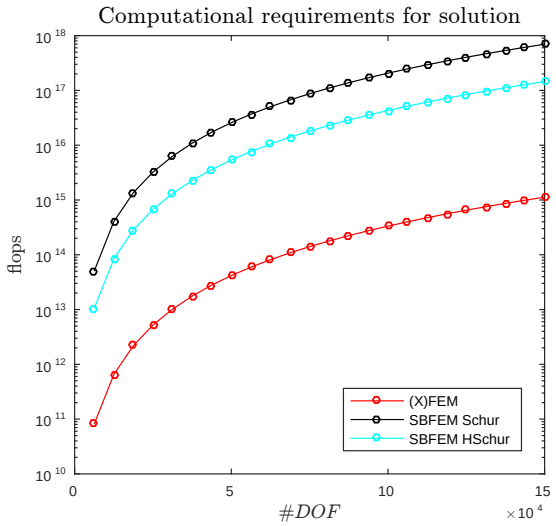

Fig. 4.26: Computational requirements for solution for (X)FEM, SBFEM using the conventional Schur decomposition and the newly proposed HSchur decomposition.

In order to offer a more meaningful comparison, Fig. 4.27 provides the corresponding accuracy of the calculated SIFs plotted against the DOFs. To this end, a reference solution obtained from a fine mesh in Abaqus of approximately half a million DOFs is used. SBFEM evidently outperforms the competing methods, as fewer DOFs are required in order to approach the reference solution. Significantly higher rates of convergence are obtained by SBFEM by employing higher order elements. Noteworthy are the linear, two noded elements, which outperform XFEM and the standard FEM approach with a slope of $m=2$, calculated using recovered stresses.

Fig. 4.28 depicts the error in calculated SIF as a function of the flops required for analysis. At lower flop counts, all methods perform comparably. A slight edge goes to the FEM implementation. Since in Abaqus the integration domain is specified manually, the amount of DOFs present in the system is not uniformly distributed at coarser discretizations. Consequently, the FEM plot exhibits a plateau. Once this plateau is passed, the rate of convergence stabilizes to $m_{FEM}=0.88$. The rate of convergence for XFEM is higher at $m_{XFEM}=1.06$. At higher flop counts, SBFEM begins to separate itself from the competing methods, due to higher rates of convergence.

Fig. 4.29 indicates the error in computed SIFs as a function of wall clock time. For Abaqus, analysis times are extracted from the log file. For XFEM and SBFEM, the stopwatch timer in Matlab is employed. Results for this numerical example are obtained on an Intel i5-6600K @ 3.9 GHz. As observed in Fig. 4.29, the current implementation of SBFEM, based on the newly adopted HSchur, outperforms XFEM

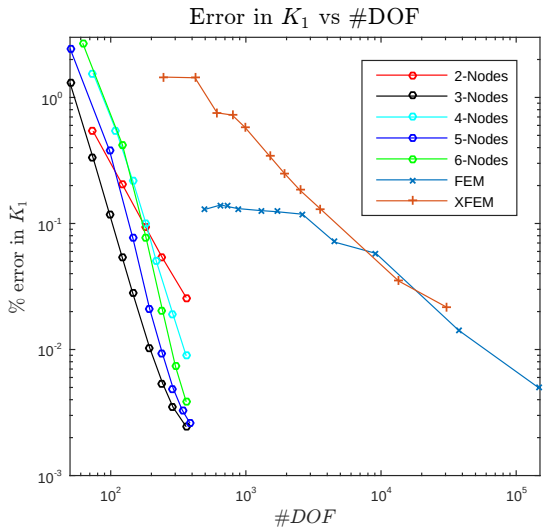

Fig. 4.27: Accuracy of K_I as a function of DOFs for SBFEM, XFEM and FEM for the double edge crack problem. For SBFEM the proposed HSchur decomposition is utilized.

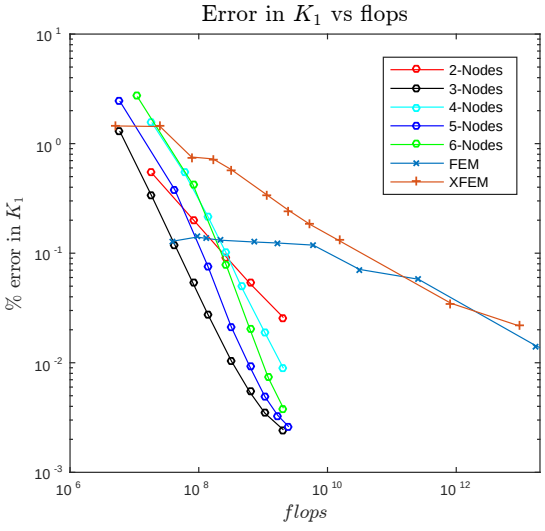

Fig. 4.28: Accuracy of K_I as a function of the flops required to obtain the solution for the double edge crack problem. For SBFEM the proposed HSchur decomposition is utilized.

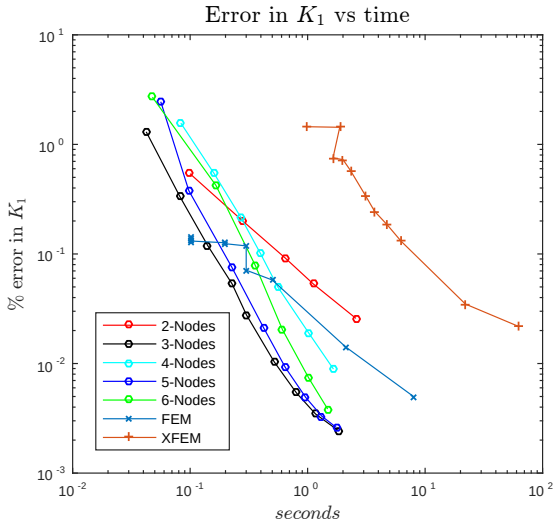

Fig. 4.29: Accuracy of K_I as a function of analysis wall clock time for the double edge crack problem. For SBFEM the proposed HSchur decomposition is utilized.

by approximately an order of magnitude. This quantification must be treated with caution, since both the SBFEM and XFEM implementations have yet to undergo optimization. This discrepancy between analysis time and computation complexity (Fig. 4.28) is attributed to operations specific to XFEM, not incorporated in the theoretical flop count, and language related performance limitations. Examples for the former are operations associated with the integration of the enrichment terms and the post-processing of the SIFs. Employing loops in scripting languages, such as Matlab, is known to significantly impact run time. The number of loops performed during analysis is dependant on the amount of elements and integration points, which is significantly larger for the case of XFEM than SBFEM. These considerations are equally applicable to the fourth numerical example.

Compared to the optimized code of the commercial software Abaqus, which utilizes highly optimized numerical routines, SBFEM compares favorably. Similar accuracy in the calculated SIFs is observed at comparable analysis times. Further, for the higher noded elements, SBFEM with the adopted HSchur decomposition manages to outperform commercial software.

Fig. 4.30 compares the accuracy of the calculated SIFs to the computational effort by proxy of flop count. The computational advantage of the HSchur decomposition over the generic Schur decomposition is demonstrated to approach an order of magnitude, with the analysis time expected to decrease with further refinement of the code.

A last comparison between XFEM and SBFEM considers the evolution of the condition number of the stiffness matrix for an increasing number of DOFs. Fig. 4.31 demonstrates the numerical difficulties associated with standard XFEM. Typically, the condition number of the stiffness matrix increases rapidly, mandating preconditioning, which constitutes a computational burden. This is not the case in SBFEM since the method naturally extends to encompass fracture related phenomena. Consequently, no terms are added, which affect the condition number adversely. However, it is evident that higher order elements do increase the condition number steadily.

4.2.4 Slant Crack in Square Plate

A slant crack as depicted in Fig. 4.32 is considered, with length $L = 1$ unit, crack length $a = L/2$ and crack inclination angle equal to $\pi/4$. The boundary is evenly discretized. A crack inclination angle of $\pi/4$ is purposely chosen, since the largest errors in computed stresses appear at corner points (Fig. 4.20). The aim of this numerical example is to ascertain, how SBFEM performs in a worst case scenario, when compared against alternatives. XFEM and the standard FE-based approach are considered in the following comparisons. For XFEM, the enrichment radius is kept constant at $r_e = 0.2$ units, while the radius of integration is fixed at $r_i = 2.55$ times the element size. For Abaqus, the same quadratic elements where

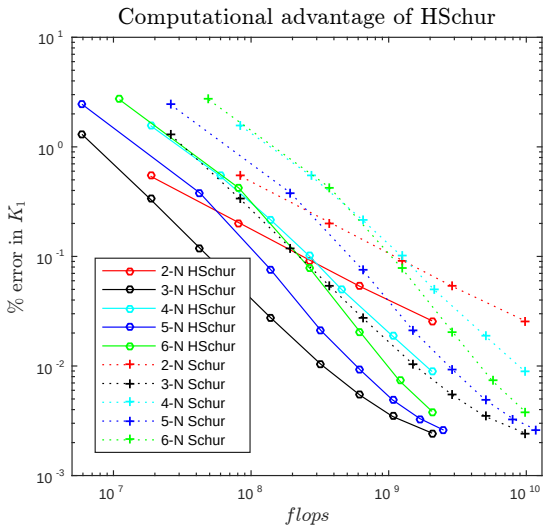

Fig. 4.30: Accuracy of K_I comparing the proposed HSchur and standard Schur decomposition, based solely on theoretical flop counts.

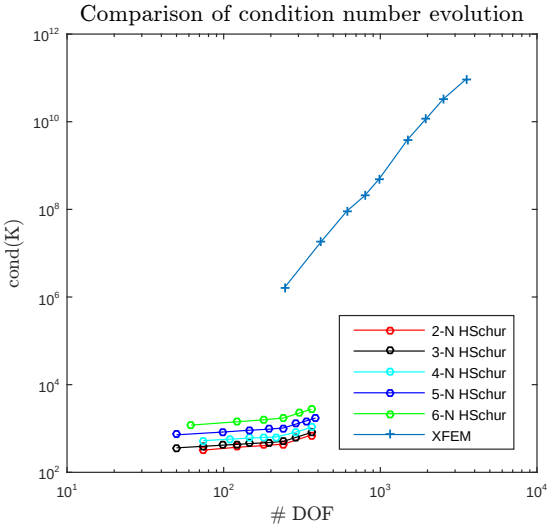

Fig. 4.31: Evolution of the condition number of the stiffness matrix as a function of DOFs for the double edge crack problem.

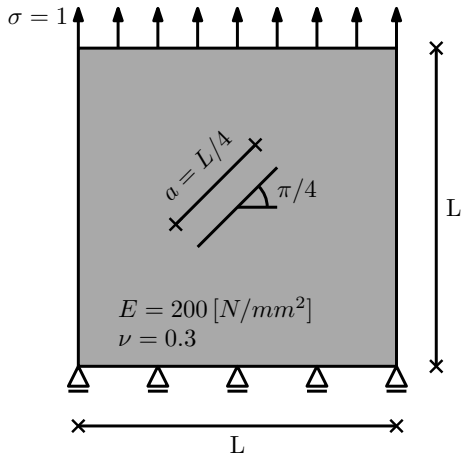

Fig. 4.32: Slant crack in square plate under tension. The problem statement for the fourth numerical example.

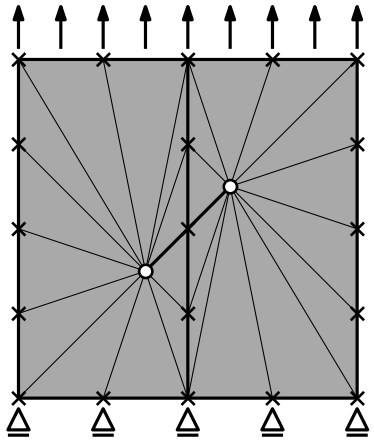

Fig. 4.33: Sample discretization scheme for modeling a slant crack with SBFEM. It can be seen, that in order to accommodate different crack inclination angles, simply the scaling centers (circles) must be moved, which may be done independently of the mesh (crosses).

chosen as in the previous example. Modeling the slant crack problem with SBFEM entails separating the domain into two parts. Each is inscribed its own scaling center, placed at the crack tip (Fig. 4.33). The results reported, correspond to the SIFs calculated at the upper right sided crack tip.

Fig. 4.34 illustrates the accuracy of computed K_2 as a function of DOFs. To this end, a finely meshed reference solution in Abaqus was employed. The FEM-based calculation of the SIFs by Abaqus, the XFEM implementation as well as the 2-noded elements of SBFEM are observed to converge at a comparable rate, although XFEM has a slightly higher rate of convergence. Admitting higher order elements, SBFEM outperforms the other numerical methods. The odd-noded elements outperform their even-noded counterparts. Since the computational effort per DOF for SBFEM is greater than for the two contrasted numerical methods, Fig. 4.35 plots the accuracy of K_2 as a function of flops. SBFEM compares favorably to the FE-based approach and the XFEM implementation, even in this worst-case scenario. It would seem that the calculation of SIFs at a crack inclination angle of $\pi/4$ is also a challenging task for other FE-based numerical methods.

Fig. 4.36 provides the analysis times for calculating the SIFs based on all three compared methods. Calculations were performed on an Intel Xeon E3-1225 v3. Oscillatory behavior for the first few points is attributed to the method of reporting in Abaqus. Values are reported at discrete 0.1 second intervals. Since for systems with small amounts of DOFs the I/O overhead dominates the overall computational

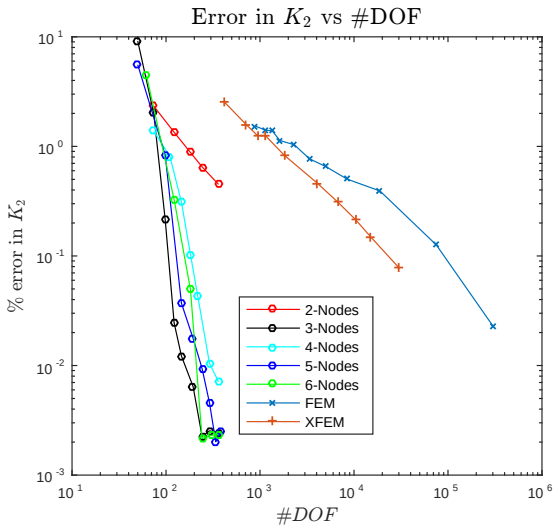

Fig. 4.34: Accuracy of K_2 as a function of DOFs for the slant crack problem. For SBFEM the proposed HSchur decomposition is utilized.

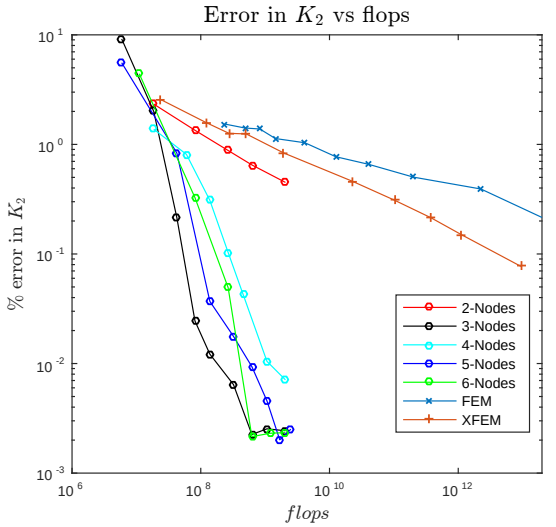

Fig. 4.35: Accuracy of K_2 as a function of flops required for solution of the slant crack problem. For SBFEM the proposed HSchur decomposition is utilized.

time, oscillatory values of 0.2 and 0.3 seconds were obtained. SBFEM is demonstrated to perform on par with current commercial software in terms of efficiently and accurately calculating the SIFs. Further, for problems with simple crack geometries, it outperforms a similarly implemented XFEM by approximately an order of magnitude at equivalent accuracy. This is attributed to the ease with which higher order elements may be employed. However, considering only linear elements, the advantage of SBFEM over XFEM is marginal.

Fig. 4.37 plots K_2 calculated based on raw stresses and the standard eigen-decomposition as a function of analysis time. Especially the lower noded elements suffer from this transition. While the XFEM implementation outperforms the 2-noded elements, the commercial software Abaqus performs similarly to the 3-noded elements. SBFEM is only observed to maintain its competitive advantage, when employing elements with four or more nodes.

In Fig. 4.38 the condition number of an SBFEM solution is contrasted to that of XFEM as a function of

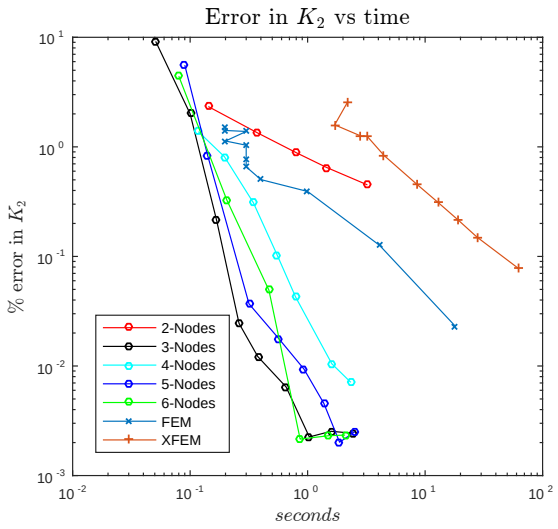

Fig. 4.36: Accuracy of K_2 as a function of analysis wall clock time for the slant crack problem. For SBFEM the proposed HSchur decomposition is utilized.

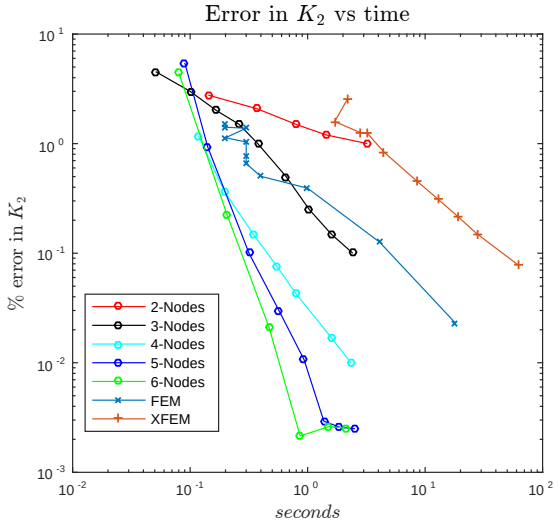

Fig. 4.37: Accuracy of K_2 as a function of analysis wall clock time for the slant crack problem. For SBFEM the eigen-decomposition combined with raw stresses for the calculation of K_2 is utilized.

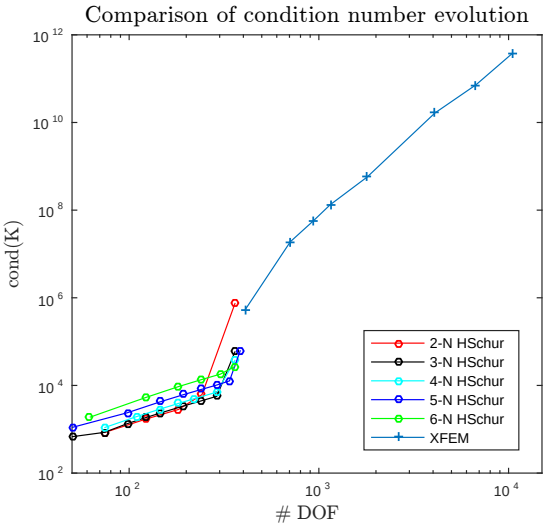

Fig. 4.38: Evolution of the condition number of the stiffness matrix as a function of DOFs for the slant crack problem.

increasing DOFs. The condition numbers are not clearly separated. For finer domain discretizations, the condition number of SBFEM approaches that of XFEM. However, at that level of discretization, SBFEM is fully converged as opposed to XFEM. This escalation in condition number is dependent on the angle spanned between an element on the boundary and the scaling center. The smaller the angle, the more numerical difficulties occur due to the degeneration of the Jacobian. With a higher boundary discretization, these angles tend to further decrease. Should severe numerical issues be encountered, a splitting of the domain perpendicular to the crack line is advised, distributing the angles spanned by the boundary elements and the scaling center more evenly.

One of the strengths of SBFEM is exploited to perform a study of variants. Modeling of varying crack inclination angles becomes trivial, as only the scaling centers must be repositioned. As a result, a procedure is proposed, which accommodates the application of SPR theory to the SIFs.

1. The direction of crack extension is determined.
2. The intersection point between the boundary and the crack extension line is calculated. The nearest node is calculated and the corresponding intersection element is found.
3. The stresses are recovered over a patch of two elements, as described in sec. 4.1, with the addition of a check, ensuring the chosen patch does not entail corners. This process is automated by applying the orientation checking procedure as detailed in sec. 4.2.2.
4. The SIFs are calculated based on the locally recovered stresses, which are rotated by the crack inclination angle.

In Tbl. 4.7 the SIF K_I is tabulated for various discretization levels and crack inclination angles. A reference solution is obtained from a fine meshed Abaqus analysis. In order to investigate the stability of SBFEM for various crack inclination angles, the values for K_I are normalized with respect to the reference solution. As observed in Tbl. 4.7, K_I behaves independently of the crack inclination angle. All three methods, SBFEM, XFEM and FEM provide comparable results, with deviations lower than 1%. Tbl. 4.8 summarizes the results for the case of K_2. It is verified that the SIFs computed by SBFEM are independent of the crack inclination angle. However, as the crack inclination angle is increased, numerical issues arise due to the introduction of small angles spanned by the elements on the boundary and the scaling center. These angles approach the values of zero as the crack inclination angle approaches 90° (Fig. 4.33).

Tbl. 4.7: Values of computed K_I as a function of the crack inclination angle ranging from 10° to 80°. For SBFEM, 3-noded elements were chosen with 1 to 4 elements discretizing each side. For Abaqus and XFEM, K_I was calculated using fine meshes. The normed values correspond to the ratio of SBFEM K_I solution to the Abaqus reference solution.

Type	10°	20°	30°	40°	50°	60°	70°	80°
36 DOFs	1.09394	1.03033	0.87814	0.69875	0.50031	0.31072	0.15275	0.05671
50 DOFs	1.09307	1.02125	0.87838	0.69869	0.50038	0.31028	0.15225	0.04827
74 DOFs	1.09390	1.01546	0.87856	0.69873	0.50042	0.31006	0.15200	0.04691
98 DOFs	1.09486	1.01544	0.87871	0.69865	0.50046	0.31001	0.15189	0.04682
Normed	1.00475	1.00444	1.00581	1.00735	1.00538	1.00515	0.99140	0.99272
Abaqus ref.	1.08968	1.01094	0.87364	0.69355	0.49778	0.30843	0.15321	0.04716
XFEM	1.09278	1.01336	0.87647	0.69119	0.50215	0.30976	0.15172	0.04707

Tbl. 4.8: Values of computed K_2 as a function of the crack inclination angle ranging from 10° to 80° using the same methodology as in Tbl. 4.7.

Type	10°	20°	30°	40°	50°	60°	70°	80°
36 DOFs	0.13061	0.29445	0.41963	0.49134	0.50066	0.44532	0.33312	0.17540
50 DOFs	0.13018	0.29185	0.41719	0.49132	0.50072	0.44541	0.33329	0.17823
74 DOFs	0.12990	0.29034	0.41713	0.49123	0.50073	0.44569	0.33344	0.17862
98 DOFs	0.12935	0.28989	0.41703	0.49126	0.50073	0.44572	0.33348	0.17862
Normed	0.99768	1.00279	1.00322	1.00338	1.00190	1.00051	0.99779	0.99700
Abaqus ref.	0.12965	0.28908	0.41569	0.48961	0.49978	0.44550	0.33422	0.17915
XFEM	0.12946	0.28948	0.41683	0.49037	0.49991	0.44586	0.33454	0.17923

4.3 Conclusion

In this work, the adoption of a blocked Hamiltonian Schur decomposition is proposed, which proves highly beneficial when substituted into the solution process of SBFEM. By preserving Hamiltonian symmetry, i.e., the symmetry of the eigenvalues about the real and the imaginary axis, enhanced accuracy is achieved leading in improved, near optimal, convergence rates. Further, only half of the analysis domain need be considered, which alleviates the additional computational toll incurred in linearizing the quadratic eigenvalue problem. An additional benefit stems from the fact that the eigenvalues are automatically partitioned based on sign. Thus, errors incurred due to improper sorting, resulting in an erroneous stiffness matrix are eliminated along with the prior need for a stabilizing parameter ϵ. By consequence, the adopted HSchur decomposition is demonstrated to significantly improve the regularity of the method.

The convergence rates of SBFEM are investigated in a benchmark example, featuring an analytical solution. The L_2 error in displacements, stresses as well as the error in computed stress intensity factors are recovered. Implementation of SPR theory allows for superconvergent recovery of stresses, and in select cases ultracovergent behavior. This property is exploited to significantly improve the accuracy and convergence behavior of the calculated SIFs. It is further demonstrated that stress recovery need not be carried out for the entire domain, since similar accuracy is achieved when only considering the patch in direction of crack extension, at reduced computational cost. A local error estimator is proposed, which arises as a natural extension of the stress recovery scheme, and is highly accurate as well as computationally inexpensive.

Finally, SBFEM is explicitly contrasted against other numerical methods within the context of LEFM in terms of rough flop count, and wall clock time (albeit for unoptimized Matlab implementations for the SBFEM and XFEM variants). It is demonstrated that for simple crack geometries, a higher order SBFEM consistently outperforms frequently adopted alternatives.

5 Multiscale SBFEM

Modeling of structures comprising features across multiple length scales can, in principle, be achieved by utilizing the conventional FEM. However, excessive discretization required to account for micro-structural heterogeneity can render such an approach intractable from both a compute and storage perspective. Since the complexity to solve large finite element problems is roughly of order $O(n_z^{3/2})$, where n_z denotes the nDOF, such schemes are typically limited to small scale numerical experiments focusing on RVEs. Multiscale methods have been proposed to circumvent this issue, by projecting the fine scale information onto a coarse mesh, where the governing equations are then solved at reduced computational cost. Due to its generality, the family of MsFEMs, which constitute computational approaches to constructing mapping functions between scales, are adopted. First, fusion of the EMsFEM with SBFEM, which treats fracture on the fine scale, is investigated. Then a method of enhancing the SBFEM's ability to accurately calculate the gSIFs on coarse meshes is proposed. This is subsequently exploited in a multiscale SBFEM crack propagation scheme, to further reduce the computational toll.

5.1 The Multiscale Scaled Boundary Finite Element Method (MSBFEM)

Accounting for damage related phenomena via use of the SBFEM significantly accelerates computation, however, full scale problems still pose a challenge: Problems which are inherently multi-scale in nature constitute a significant computational burden. Multiscale methods [2] are therefore introduced in order to mitigate such issues. A novel multiscale scheme is proposed, which harnesses the SBFEM benefits on the microscale for modeling fracture, and employs the EMsFEM [3] for defining a coarse mesh on the macro scale, where the governing equations of the problem are solved, greatly reducing the computational toll and analysis time. The different scales are linked by mapping functions, which are only computed once, prior to analysis.

Four numerical examples are presented. In in the first two, an RVE with embedded crack is represented by two subdomains, each containing a crack tip. For the latter two, the image based quadtree decomposition is employed to automatically create an analysis-ready adaptive mesh of a masonry RVE.

5.1.1 Homogeneous RVE with Embedded Slant Crack Under Tension

A rectangular plate as depicted in Fig. 5.1 is considered. A state of plane stress is assumed. The Young's modulus, Poisson ratio, side length, crack angle, crack length and tension force are given as $E = 200$ [N/mm^2], $\nu = 0.3$, $L = 1$ [mm], $\alpha = 30°$, $a =$ variable and $t = 0.1$ [N/mm]. The quantities of interest are the global displacement field as well as the gSIFs K_I & K_{II} at the right crack tip. The domain is modeled as a single RVE employing CM4-16 elements, with coarse nodes as given in Fig. 5.2. Both linear and periodic boundary conditions are studied. Inspection of the displacement fields obtained from simulations employing CM4-12 elements (Fig. 5.3), with $a/L = 0.5$ indicates that already CM8 elements manage to accurately capture the RVE's behavior for this load case and crack orientation. The CM4 element cannot accurately account for the curvature displayed in the displacement field at the top edge, due to the linear interpolation between coarse nodes.

Typical accuracy targets for harnessing the computed gSIFs for subsequent applications, mandate errors smaller than 1%. A reference solution for the gSIFs is constructed using the commercial software Abaqus and seen to match the values obtained from using SBFEM. Hence, the accuracy of the gSIFs obtained from the multiscale analysis is compared to those obtained from SBFEM across $0.1 \leq a/L \leq 0.9$. In addition to the CM4-16 elements constructed by both linear (L) and periodic (P) boundary conditions, quadratic (Q) boundary conditions are investigated for the CM8 element (Fig. 5.4). Due to the amount of

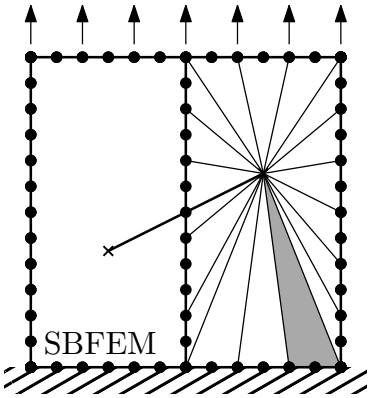

Fig. 5.1: Problem geometry of homogeneous RVE with embedded slant crack under tension.

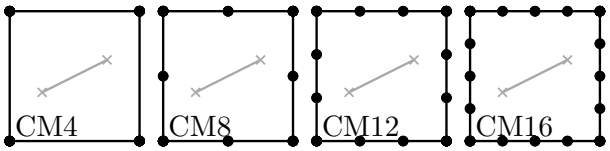

Fig. 5.2: Coarse node placement of CM4-16 elements.

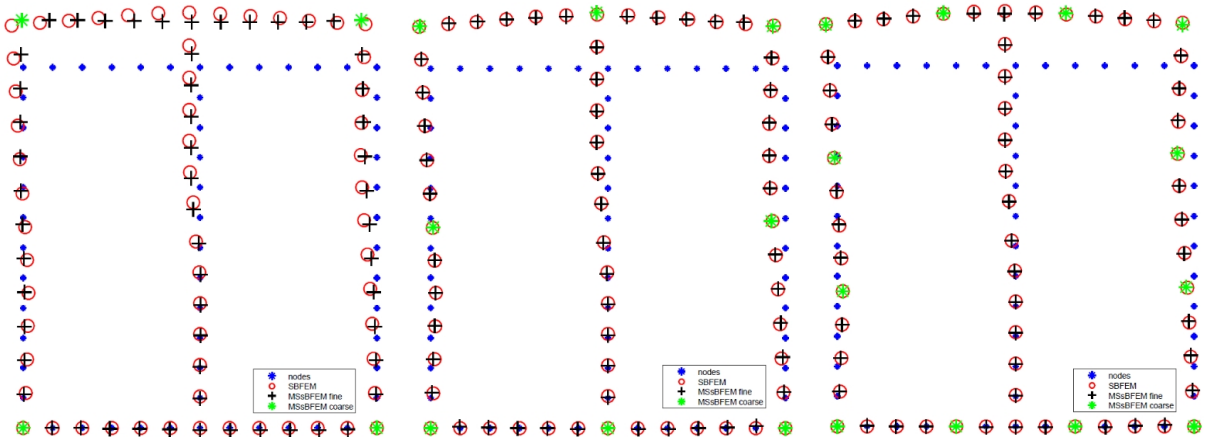

Fig. 5.3: Comparison of displacement field obtained by multiscale methods to SBFEM reference solution. Node positions in blue, SBFEM solution in red, MSBFEM solution in black with green denoting the coarse node locations. From left to right; CM4, CM8 and CM12 elements are employed.

data, results are color-coded (see the scale in Fig. 5.4 at the bottom). Since the quadratic boundary conditions do not offer an improvement in performance, they are discarded from subsequent reporting. If the accurate calculation of gSIFs is required within a multiscale context, CM4 elements should not be utilized. Improvements for the case of linear NBFs seem to track well with increased amounts of coarse nodes: While CM8 elements manage to accurately capture $a/L \leq 0.2$, CM12 and CM16 can handle upto $a/L \leq 0.3$ and $a/L \leq 0.4$ respectively. For the case of periodic NBFs only the CM16 element can capture the gSIFs to desired accuracy levels.

5.1.2 Plate with Multiple Slant Cracks Under Tension

A rectangular plate comprising a grid of 5x5 RVEs, as depicted in Fig. 5.5, is considered. Both cracked and undamaged RVEs exist in this analysis. The cracked RVEs (Fig. 5.5, numbered 1-5) are placed so that specific conditions may be evaluated: Performance when affected by displacement boundary conditions, traction boundary conditions, interaction of two cracked RVEs and the exclusion of interaction is evaluated by considering the RVEs 1, 5, 3 & 4, and 2 respectively.

a/L	SIF	SBFEM	CM4L	CM8L	CM8LQ	CM12L	CM16L	CM4P	CM8P	CM8PQ	CM12P	CM16P
0.1	K_I	0.0281	0.53	0.66	1.21	0.26	0.04	0.79	0.47	0.66	0.06	0.07
	K_{II}	0.0168	9.17	0.29	1.36	0.31	0.18	8.25	1.39	2.88	1.14	0.38
0.2	K_I	0.0441	1.92	0.31	0.21	0.13	0.14	1.64	0.35	0.34	0.44	0.15
	K_{II}	0.0241	10.49	0.06	1.35	0.15	0.22	10.00	1.70	2.77	1.11	0.47
0.3	K_I	0.0573	5.21	2.35	1.82	0.80	0.50	3.74	0.10	0.31	0.95	0.28
	K_{II}	0.0309	12.39	0.29	1.37	0.11	0.33	12.62	2.12	2.61	1.13	0.63
0.4	K_I	0.0716	9.51	5.41	4.79	1.65	1.04	6.44	0.96	1.31	1.51	0.50
	K_{II}	0.0370	14.38	0.61	1.34	0.35	0.59	15.43	2.43	2.32	1.28	0.82
0.5	K_I	0.0881	14.19	9.51	8.60	2.62	1.77	9.27	2.23	2.48	1.99	0.82
	K_{II}	0.0427	16.29	0.47	0.96	0.31	1.23	17.67	2.39	1.88	1.78	1.06
0.6	K_I	0.1080	18.84	14.57	13.09	3.82	2.62	11.88	3.92	3.69	2.38	1.18
	K_{II}	0.0484	18.03	0.93	0.32	0.58	2.70	18.08	1.75	1.48	3.07	1.32
0.7	K_I	0.1327	23.31	20.23	18.08	5.96	3.27	14.31	6.19	5.13	3.20	1.51
	K_{II}	0.0545	19.76	4.59	3.17	3.33	5.33	15.20	0.27	1.59	5.78	1.48
0.8	K_I	0.1649	27.93	25.65	23.34	10.68	3.16	17.17	9.28	7.62	5.88	1.68
	K_{II}	0.0613	21.96	10.98	8.04	8.80	7.94	8.29	2.35	2.41	10.02	1.65
0.9	K_I	0.2102	33.67	29.75	28.54	20.12	2.87	21.64	13.26	12.25	12.30	2.12
	K_{II}	0.0672	26.02	19.26	15.11	15.20	4.40	1.24	6.28	3.04	13.46	4.29

Error % linear **Error % periodic**

< 1	1-2	2-5	5-10	> 10

Fig. 5.4: Percentage error across various ratios of a/L in calculated gSIFs when employing a multiscale representation of the domain. The Suffixes L, P and Q denote linear, periodic and quadratic NBFs respectively.

A state of plane stress is assumed. The Young's modulus, Poisson ratio, side length, crack angle, crack length and tension force are given as $E = 200$ [N/mm^2], $\nu = 0.3$, $L = 5$ [mm], $\alpha = 30°$, a = variable and $t = 0.1$ [N/mm].

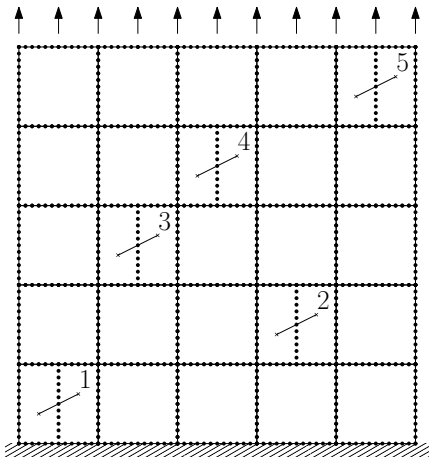

Fig. 5.5: 5x5 grid of RVEs comprising the square plate under tension with cracked RVEs 1-5.

The errors in gSIFs are reported in Fig. 5.6 for RVEs 1 and 5. By inspection, elements with eight coarse nodes or less tend to perform poorly and do not comply with the desired accuracy threshold. They are therefore excluded from subsequent discussions. Employing CM12-16 elements permits accurate computation of the gSIFs for $a/L \leq 0.5$. Fig. 5.7 depicts the results for RVEs 2-4. An interesting trend presents itself: Coarse elements constructed using linear NBFs outperform their periodic counterparts. While for the linear case the desired accuracy is obtained for $a/L \leq 0.6$, in the periodic case $a/L \leq 0.3$ is barely reached.

This can be attributed to the underlying physics of the original assumptions with which the NBFs are constructed. Periodic NBFs assume a constant strain state across the domain, which does not hold in the presence of discontinuities such as cracks. Hence, the linear NBF, which prevent movement of opposite nodes and attribute the full influence of an imposed unit displacement to the affected side, better represent the discontinuous physical behavior in the presence of cracks. Since linear boundary conditions excel at representing cracks, while periodic boundary conditions do so for undamaged media, we investigate an empirical hybrid boundary condition approach. If opposite nodes are interrupted by the presence of a crack, linear boundary conditions are enforced, else periodic ones are applied for that node pair (Fig. 5.8). As a result, an improved representation of the displacements and overall strain within the domain is achieved, coupled with a more consistent characterization of the SIFs (Fig. 5.9). Benefits of employing periodic boundary conditions are obtained, where applicable, while considering physical crack behavior. This balanced behavior, unburdens the analyst from guessing prior to analysis which type of boundary conditions might prove to be most suitable.

Crack 1, linear

a/L	CM4 K_I	CM4 K_{II}	CM8 K_I	CM8 K_{II}	CM12 K_I	CM12 K_{II}	CM16 K_I	CM16 K_{II}
0.9	23.8	25.4	10.6	16.4	5.4	3.2	0.1	4.3
0.8	17.8	19.5	8.2	8.7	2.4	2.3	0.6	3.3
0.7	13.4	15.9	5.9	3.7	1.4	0.8	1.0	1.7
0.6	9.7	13.3	3.6	0.7	1.2	0.0	1.0	0.6
0.5	6.4	11.3	1.6	1.0	1.2	0.3	0.8	0.1
0.4	3.5	9.5	0.1	1.8	1.0	0.2	0.6	0.1
0.3	1.0	7.9	1.4	2.1	0.8	0.0	0.4	0.1
0.2	0.8	6.7	2.4	2.4	0.5	0.2	0.2	0.2
0.1	1.4	5.9	3.0	2.5	0.3	0.4	0.1	0.2

Crack 5, linear

a/L	CM4 K_I	CM4 K_{II}	CM8 K_I	CM8 K_{II}	CM12 K_I	CM12 K_{II}	CM16 K_I	CM16 K_{II}
0.9	33.0	26.8	15.3	31.3	14.6	3.9	0.1	7.5
0.8	28.4	22.6	13.4	22.9	7.8	2.4	1.6	8.5
0.7	24.6	19.8	8.8	16.0	4.5	0.2	2.4	5.8
0.6	20.7	16.9	2.9	11.4	3.2	1.5	2.1	3.3
0.5	16.4	13.8	3.0	9.2	2.5	1.8	1.5	1.8
0.4	11.9	10.3	8.4	9.0	1.8	1.4	0.9	1.0
0.3	7.4	6.6	12.8	10.2	1.1	0.9	0.5	0.6
0.2	3.5	3.2	16.0	12.7	0.5	0.4	0.2	0.3
0.1	1.0	0.8	16.3	16.1	0.1	0.1	0.0	0.1

Crack 1, periodic

a/L	CM4 K_I	CM4 K_{II}	CM8 K_I	CM8 K_{II}	CM12 K_I	CM12 K_{II}	CM16 K_I	CM16 K_{II}
0.9	21.4	5.1	5.1	8.2	5.7	0.9	1.6	5.8
0.8	12.7	2.8	6.4	5.2	4.8	3.0	2.0	6.7
0.7	7.3	8.7	5.9	3.0	3.8	3.0	2.0	5.5
0.6	4.1	11.4	4.5	2.0	2.5	2.4	1.7	3.8
0.5	1.9	11.3	3.0	1.8	1.3	1.9	1.2	2.5
0.4	0.4	9.8	1.7	1.7	0.5	1.5	0.7	1.7
0.3	0.7	8.0	0.6	1.4	0.0	1.1	0.3	1.1
0.2	1.5	6.4	0.2	1.0	0.4	0.9	0.1	0.8
0.1	1.5	5.6	0.6	0.7	0.4	0.7	0.2	0.5

Crack 5, periodic

a/L	CM4 K_I	CM4 K_{II}	CM8 K_I	CM8 K_{II}	CM12 K_I	CM12 K_{II}	CM16 K_I	CM16 K_{II}
0.9	19.7	8.5	1.6	10.1	4.1	4.3	1.3	1.2
0.8	16.8	13.4	0.6	5.9	0.0	4.3	0.9	1.0
0.7	14.6	17.2	0.2	3.2	1.0	2.1	0.6	0.4
0.6	12.5	18.0	0.5	1.5	0.7	0.4	0.5	0.1
0.5	10.1	16.1	0.6	0.5	0.1	0.3	0.4	0.0
0.4	7.3	12.3	0.6	0.1	0.2	0.5	0.4	0.0
0.3	4.5	7.9	0.4	0.1	0.2	0.4	0.3	0.0
0.2	2.1	3.8	0.3	0.0	0.1	0.2	0.2	0.1
0.1	0.6	0.9	0.1	0.0	0.0	0.1	0.1	0.1

Fig. 5.6: Percentage Error in gSIFs for cracks 1 and 5 of Fig. 5.5

Crack 2, linear

a/L	CM4 K_I	CM4 K_{II}	CM8 K_I	CM8 K_{II}	CM12 K_I	CM12 K_{II}	CM16 K_I	CM16 K_{II}
0.9	19.7	30.0	7.8	21.2	3.6	1.6	1.2	5.4
0.8	15.4	24.6	7.0	14.3	1.1	0.0	0.4	3.8
0.7	12.1	20.8	6.0	9.8	0.3	0.2	0.1	2.2
0.6	9.3	17.4	5.0	7.3	0.3	0.6	0.3	1.0
0.5	6.6	14.1	4.2	6.4	0.3	0.8	0.2	0.4
0.4	3.9	10.7	3.5	6.5	0.3	0.7	0.1	0.1
0.3	1.4	7.5	3.0	7.3	0.1	0.4	0.0	0.0
0.2	0.6	4.7	2.6	8.4	0.0	0.1	0.1	0.1
0.1	1.6	2.9	2.7	9.6	0.1	0.0	0.2	0.1

Crack 3, linear

a/L	CM4 K_I	CM4 K_{II}	CM8 K_I	CM8 K_{II}	CM12 K_I	CM12 K_{II}	CM16 K_I	CM16 K_{II}
0.9	29.0	32.7	8.3	24.2	4.5	1.8	0.6	5.1
0.8	23.1	27.5	5.0	16.4	1.6	0.2	0.0	3.7
0.7	18.5	23.2	2.1	10.9	0.7	0.4	0.5	2.1
0.6	14.5	19.0	0.4	7.5	0.6	0.8	0.6	1.1
0.5	10.9	14.7	2.5	5.8	0.6	0.8	0.4	0.5
0.4	7.6	10.4	4.2	5.4	0.5	0.7	0.3	0.3
0.3	4.5	6.4	5.4	6.0	0.4	0.5	0.2	0.2
0.2	2.0	3.1	6.2	7.2	0.2	0.2	0.1	0.1
0.1	0.4	0.8	5.7	8.9	0.0	0.1	0.0	0.0

Crack 4, linear

a/L	CM4 K_I	CM4 K_{II}	CM8 K_I	CM8 K_{II}	CM12 K_I	CM12 K_{II}	CM16 K_I	CM16 K_{II}
0.9	25.2	28.0	3.6	20.8	3.7	0.6	0.8	5.0
0.8	20.5	23.6	1.7	14.3	1.3	0.3	0.0	3.6
0.7	16.8	20.1	0.3	10.2	0.6	0.3	0.6	2.1
0.6	13.6	16.7	2.4	8.1	0.6	0.7	0.6	1.1
0.5	10.4	13.1	4.2	7.5	0.6	0.8	0.5	0.5
0.4	7.4	9.4	5.8	8.2	0.5	0.7	0.3	0.3
0.3	4.5	5.7	7.2	9.9	0.4	0.5	0.2	0.1
0.2	2.0	2.5	8.0	12.2	0.2	0.2	0.1	0.1
0.1	0.4	0.3	7.3	15.2	0.0	0.0	0.0	0.0

Crack 2, periodic

a/L	CM4 K_I	CM4 K_{II}	CM8 K_I	CM8 K_{II}	CM12 K_I	CM12 K_{II}	CM16 K_I	CM16 K_{II}
0.9	13.7	11.7	11.3	2.1	9.4	1.0	3.9	1.9
0.8	7.9	14.5	13.1	2.2	9.1	1.3	4.5	3.3
0.7	4.2	17.4	12.3	1.4	8.1	1.3	4.5	2.8
0.6	1.9	18.2	10.1	0.9	6.3	0.8	3.9	2.0
0.5	0.3	16.4	7.5	0.9	4.4	0.5	2.9	1.3
0.4	0.8	13.0	4.9	1.0	2.7	0.4	2.0	1.0
0.3	1.6	9.0	2.6	0.9	1.3	0.5	1.1	0.8
0.2	2.2	5.4	0.9	0.8	0.3	0.6	0.4	0.6
0.1	2.2	2.9	0.2	0.6	0.3	0.6	0.0	0.5

Crack 3, periodic

a/L	CM4 K_I	CM4 K_{II}	CM8 K_I	CM8 K_{II}	CM12 K_I	CM12 K_{II}	CM16 K_I	CM16 K_{II}
0.9	20.6	15.2	10.2	1.6	8.8	0.9	4.1	3.0
0.8	13.9	17.8	12.8	1.7	8.9	0.9	4.8	3.7
0.7	9.4	19.6	12.3	0.7	8.0	0.7	4.7	2.8
0.6	6.5	19.2	10.2	0.2	6.3	0.1	4.0	1.7
0.5	4.4	16.4	7.5	0.1	4.4	0.2	3.0	0.9
0.4	2.8	12.2	5.0	0.2	2.7	0.3	2.0	0.5
0.3	1.5	7.6	2.8	0.2	1.5	0.3	1.2	0.2
0.2	0.5	3.6	1.1	0.1	0.5	0.2	0.5	0.0
0.1	0.0	1.0	0.1	0.1	0.0	0.1	0.1	0.1

Crack 4, periodic

a/L	CM4 s	CM4 K_{II}	CM8 K_I	CM8 K_{II}	CM12 K_I	CM12 K_{II}	CM16 K_I	CM16 K_{II}
0.9	17.1	12.1	15.0	2.3	12.2	1.6	5.2	2.2
0.8	11.7	15.2	15.9	2.2	11.1	0.7	5.4	3.4
0.7	8.2	17.6	14.3	1.1	9.3	0.7	5.1	2.7
0.6	5.9	17.6	11.4	0.5	7.1	0.2	4.3	1.7
0.5	4.2	15.2	8.3	0.4	5.0	0.0	3.2	1.0
0.4	2.8	11.3	5.5	0.5	3.2	0.1	2.2	0.5
0.3	1.6	6.9	3.2	0.3	1.8	0.2	1.3	0.3
0.2	0.6	3.0	1.4	0.1	0.7	0.2	0.6	0.1
0.1	0.0	0.3	0.3	0.1	0.1	0.2	0.1	0.1

Fig. 5.7: Percentage Error in gSIFs for cracks 2, 3 and 4 of Fig. 5.5

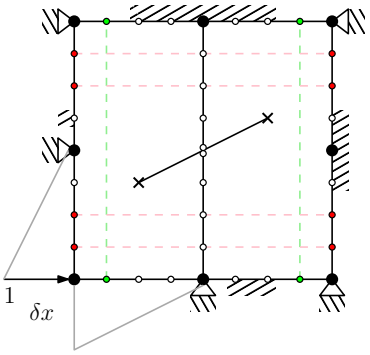

Fig. 5.8: The proposed hybrid NBFs. In color, node pairs for which tie constraints are applied, incorporating periodic information. All other nodes are restrained in accordance with linear NBFs.

	CM4						CM8					
	Linear		Periodic		Hybrid		Linear		Periodic		Hybrid	
a/L	K_I	K_{II}	K_I	K_{II}	K_I	K_{II}	K_I	K_{II}	K_I	K_{II}	K_I	K_{II}
0.45	29.00	32.66	20.57	15.24	21.83	17.85	8.27	24.17	10.24	1.56	8.57	4.95
0.40	23.10	27.54	13.93	17.78	15.31	19.24	5.03	16.35	12.76	1.66	6.19	3.86
0.35	18.46	23.19	9.43	19.62	10.79	20.16	2.13	10.89	12.29	0.75	3.66	2.27
0.30	14.50	18.96	6.48	19.21	7.68	18.99	0.41	7.45	10.16	0.18	1.87	1.27
0.25	10.91	14.67	4.39	16.44	5.37	14.94	2.51	5.76	7.52	0.12	3.26	0.96
0.20	7.55	10.42	2.76	12.22	3.48	10.69	4.17	5.38	4.99	0.21	4.29	0.99
0.15	4.51	6.43	1.47	7.65	1.92	6.61	5.43	5.96	2.82	0.21	3.21	1.07
0.10	2.03	3.06	0.53	3.63	0.76	3.15	6.20	7.19	1.14	0.09	1.90	1.15
0.05	0.42	0.85	0.02	0.96	0.08	0.87	5.72	8.91	0.09	0.05	0.94	1.38

	CM12						CM16					
	Linear		Periodic		Hybrid		Linear		Periodic		Hybrid	
a/L	K_I	K_{II}	K_I	K_{II}	K_I	K_{II}	K_I	K_{II}	K_I	K_{II}	K_I	K_{II}
0.45	4.50	1.82	8.77	0.89	5.14	1.03	0.60	5.07	4.09	3.03	1.12	3.34
0.40	1.63	0.21	8.92	0.93	2.72	0.32	0.05	3.66	4.79	3.75	0.76	3.67
0.35	0.73	0.42	8.01	0.69	1.82	0.46	0.54	2.15	4.75	2.85	1.17	2.25
0.30	0.63	0.75	6.26	0.08	1.47	0.18	0.58	1.10	4.02	1.70	1.10	1.19
0.25	0.63	0.84	4.36	0.24	1.19	0.33	0.44	0.54	3.03	0.91	0.83	0.60
0.20	0.54	0.73	2.73	0.30	0.87	0.36	0.28	0.28	2.04	0.47	0.55	0.31
0.15	0.36	0.49	1.45	0.25	0.52	0.29	0.16	0.15	1.17	0.21	0.31	0.16
0.10	0.17	0.25	0.53	0.18	0.23	0.19	0.07	0.08	0.49	0.04	0.13	0.05
0.05	0.04	0.07	0.03	0.12	0.03	0.07	0.01	0.04	0.05	0.07	0.02	0.04

Fig. 5.9: Percentage error in gSIFs including the proposed hybrid NBFs.

5.1.3 Masonry RVE with Embedded Crack Under Tension

Transitioning to RVEs comprising quadtree meshes, a square masonry domain consisting of both mortar and brick (Fig. 5.10) is considered. At the base the RVE is clamped, while at the top surface both shear and tension tractions with magnitude $q = 0.1$ are applied. Plane stress conditions are imposed. The side length is given as $L = 512$, while the Young's modulus for brick and mortar are 11 and 7 respectively. The Poisson ratio is set for both materials to 0.25. A reference solution for the displacement field and the gSIFs is obtained from the commercial software Abaqus. The SIFs are computed via contour integral and quadratic, singular, quarter-point elements. The error in displacement norm is calculated according to Eq. 5.1, which contrasts the numerically obtained displacements (see Fig. 5.11), $\{u_h\}$, to those obtained from the Abaqus reference solution $\{u_{ref}\}$, with results given in Tbl. 5.1:

$$\frac{||\{u_h\} - \{u_{ref}\}||_2}{||\{u_{ref}\}||_2} \tag{5.1}$$

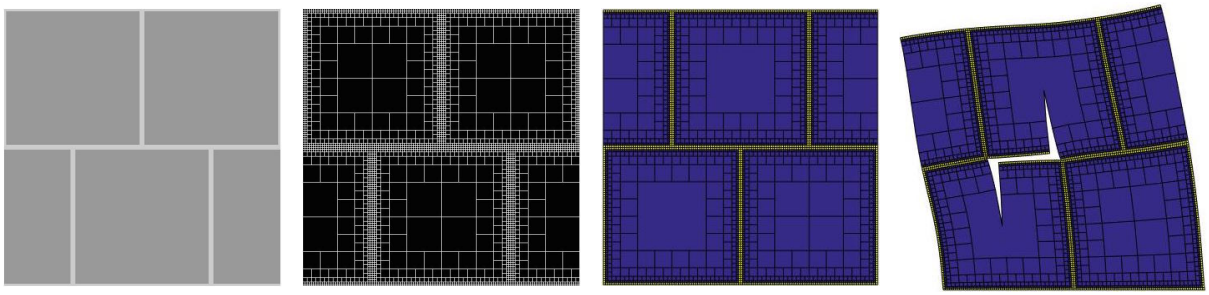

Fig. 5.10: Masonry RVE with embedded crack under tension. Definition of the RVE can be as simple as processing an image. Then the domain is partitioned into blocks by quadtree decomposition. Each block represents an SBFEM polygon element and is assembled in the finite element sense. Double nodes are then inserted to create the crack seams. Blocks are merged to position the crack tip.

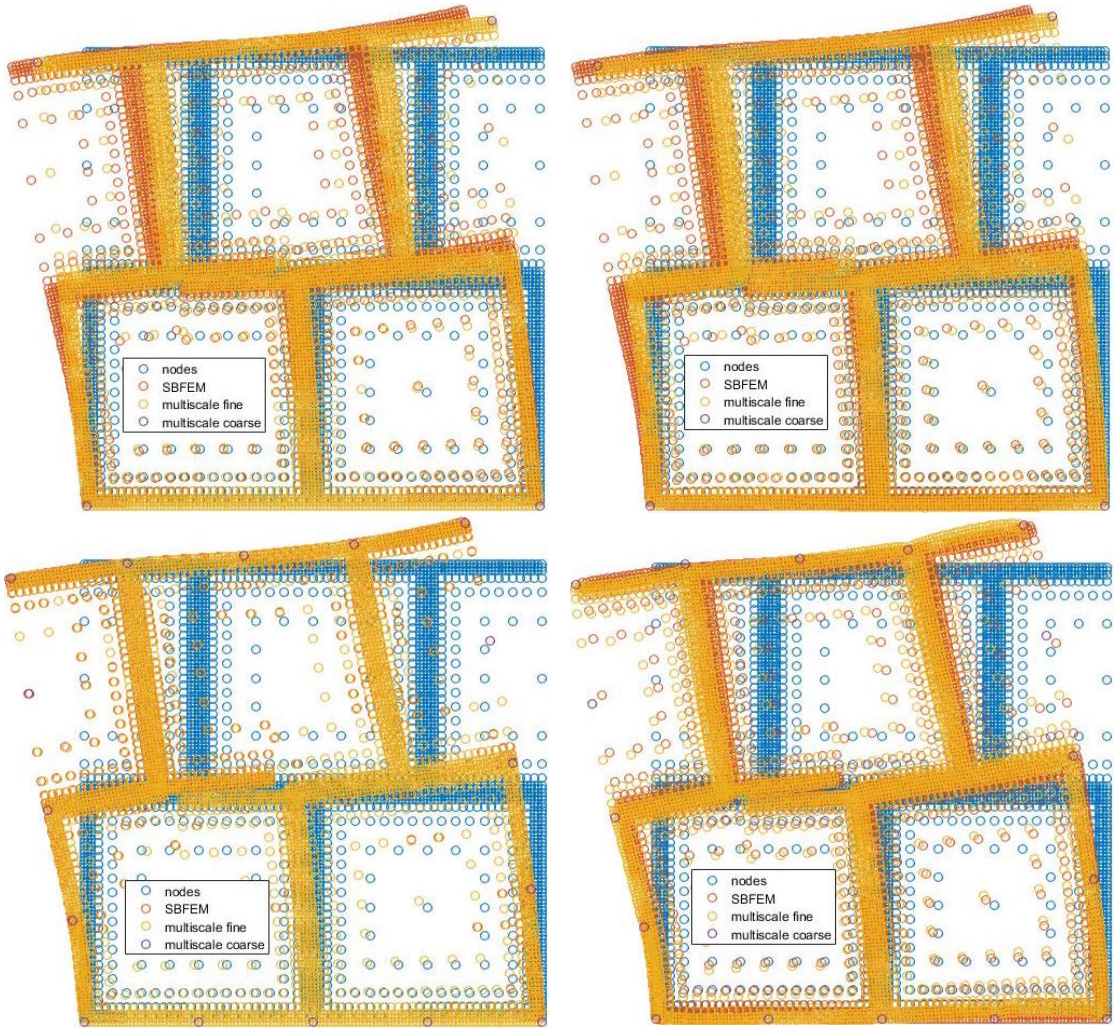

Fig. 5.11: Masonry RVE with embedded crack under tension. Comparison of displacement solution using a multiscale representation to the SBFEM baseline. Mesh nodes in blue, SBFEM reference solution in red and multiscale solution in yellow. Purple points denote CMX nodes. CM4 elements on top row and CM16 nodes on bottom row. On the left, linear NBFs and on the right periodic NBFs.

While the error for linear NBFs decreases as the amount of coarse nodes is increased, demonstrating expected behavior, the same does not hold for the periodic NBFs. This is indicative of spurious oscillatory

behavior, which violates the clamped boundary condition at the base between coarse nodes, as observed in Fig. 5.11 for the CM16 element. Further, in the presence of discontinuities, periodic NBFs do not accurately represent the underlying physics and thereby incur an accuracy penalty.

Tbl. 5.1: Error in L_2 displacement norm.

	Linear	**Periodic**
CM4	$3.31 \cdot 10^{-4}$	$3.24 \cdot 10^{-4}$
CM8	$1.18 \cdot 10^{-4}$	$1.02 \cdot 10^{-4}$
CM12	$0.38 \cdot 10^{-4}$	$1.70 \cdot 10^{-4}$
CM16	$0.16 \cdot 10^{-4}$	$1.92 \cdot 10^{-4}$
SBFEM	$4.28 \cdot 10^{-6}$	-

	Linear				Periodic				
2-N	K_I	%Err	K_{II}	%Err	**2-N**	K_I	%Err	K_{II}	%Err
CM4	0.925	55.7	1.716	51.9	**CM4**	0.971	53.5	2.245	37.1
CM8	1.296	37.9	2.605	27.0	**CM8**	1.584	24.1	2.518	29.4
CM12	1.692	19.0	3.251	8.9	**CM12**	1.762	15.6	3.284	8.0
CM16	1.864	10.7	3.281	8.1	**CM16**	1.830	12.4	3.336	6.5
SBFEM	1.982	5.1	3.356	6.0					
Abaqus	2.088	-	3.569	-					

	Linear				Periodic				
3-N	K_I	%Err	K_{II}	%Err	**3-N**	K_I	%Err	K_{II}	%Err
CM4	0.956	54.2	1.803	49.5	**CM4**	1.008	51.7	2.364	33.7
CM8	1.345	35.6	2.735	23.4	**CM8**	1.649	21.0	2.655	25.6
CM12	1.760	15.7	3.424	4.1	**CM12**	1.837	12.0	3.464	2.9
CM16	1.944	6.9	3.456	3.2	**CM16**	1.907	8.7	3.518	1.4
SBFEM	2.069	0.9	3.539	0.9					

(a) gSIFs computed at top crack tip.

	Linear				Periodic				
2-N	K_I	%Err	K_{II}	%Err	**2-N**	K_I	%Err	K_{II}	%Err
CM4	1.271	8.0	2.059	26.4	**CM4**	0.898	35.0	2.037	27.2
CM8	1.383	-0.1	1.941	30.6	**CM8**	0.745	46.1	2.461	12.0
CM12	1.149	16.9	2.334	16.6	**CM12**	0.623	54.9	2.848	-1.8
CM16	1.288	6.8	2.547	9.0	**CM16**	0.886	35.9	2.840	-1.5
SBFEM	1.306	5.5	2.633	5.9					
Abaqus	1.382	-	2.797	-					

	Linear				Periodic				
3-N	K_I	%Err	K_{II}	%Err	**3-N**	K_I	%Err	K_{II}	%Err
CM4	1.327	4.0	2.153	23.0	**CM4**	0.941	31.9	2.145	23.3
CM8	1.456	-5.3	2.037	27.2	**CM8**	0.783	43.3	2.594	7.2
CM12	1.204	12.8	2.455	12.2	**CM12**	0.649	53.0	3.005	-7.4
CM16	1.352	2.1	2.682	4.1	**CM16**	0.927	33.0	2.997	-7.2
SBFEM	1.370	0.9	2.776	0.8					

(b) gSIFs computed at top crack tip.

Fig. 5.12: Percentage error in the calculated gSIFs by multiscale method, compared to Abaqus reference solution and SBFEM baseline. Direcretization of the SBFEM element containing the crack tip with eigher linear (2-N) or quadratic (3-N) elements.

Considering the gSIFs, we investigate the influence of replacing the linear elements of the fine mesh comprising the cracked element with cubic ones. In Fig. 5.12a the Abaqus reference solution is provided for the top crack tip. The gSIFs obtained by pure SBFEM analysis employing linear elements underestimate K_1 and K_{II} by 5.1% and 6.0% respectively. The SBFEM analysis employing cubic elements only underes-

timates K_1 and K_{II} by 0.9% and 0.9% respectively. Employing higher order elements locally on the fine mesh reduces the error in gSIFs calculated by multiscale approach across all CMX elements. The same is observed for the lower crack tip as well (Fig. 5.12b). However, the choice of periodic NBFs results in larger errors in calculated K_I, when contrasted to those obtained by linear NBFs. Nevertheless, all gSIFs calculated by multiscale approach differ from the SBFEM reference solution by more than 1% and do therefore not meet the accuracy threshold.

5.1.4 Masonry Wall Under Shear

As depicted in Fig. 5.13, a masonry wall comprising a grid of 5x6 undamaged masonry RVEs, with properties previously detailed in sec. 5.1.3, is considered. The base is clamped and on the top edge, displacements in vertical direction are prohibited ($u_y = 0$). A shear traction $q = 0.1$ is applied on the top edge. Plane stress conditions are imposed. The displacement field and the von Mises stress are considered. The SBFEM reference solution of the displacement field (the maginitude of u) is depicted in Fig. 5.14. Visual inspection affirms that all CMX-based discretizations replicate the reference solution to sufficient accuracy, when utilizing linear NBFs. However, this is not the case for the von Mises stress plots. The SBFEM reference solution (Fig. 5.15) is accurately reconstructed using CM12-16 elements, sufficiently captured using CM8 elements and conceptually discernible when employing CM4 elements. Characteristic of insufficiently fine discretization on the coarse scale is the discontinuity of the stresses across elements, which mimics conventional FEM behavior.

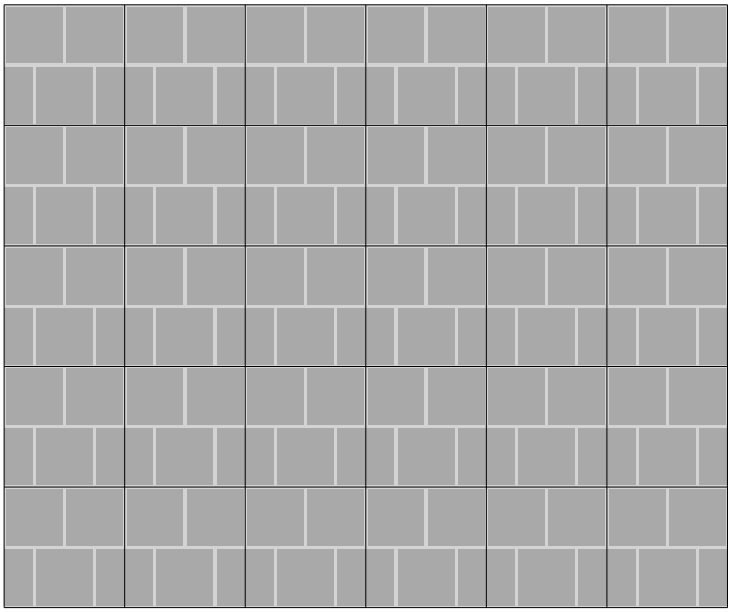

Fig. 5.13: Masonry wall constructed by assembling RVEs in a 5x6 grid.

Fig. 5.16 contrasts the computational effort of conventional vs. multiscale analysis. It is observed that sufficient levels of accuracy can be achieved using several orders of magnitude fewer DOF. This in turn accelerates the analysis time significantly. For this specific example and code, the time required to construct the NBFs exceeds the pure SBFEM simulation. This is due to a naive approach being employed: High performance implementations would only decompose the stiffness matrix of the fine scale once and then exploit the embarrassingly parallel nature of the problem. In any case, the NBFs are only dependent on the geometry and material properties of the domain and therefore invariant. This necessitates them to only be computed once prior to analysis and then stored for later retrieval as required.

5.1.5 Conclusions

In this section the SBFEM is successfully extended to multiscale problems by fusion with the EMsFEM. Further, cracks have been incorporated on the micro-scale, such that the gSIFs are accurately reconstructed using information stemming from the coarse scale solution. In the process, CM4-16 elements are evaluated

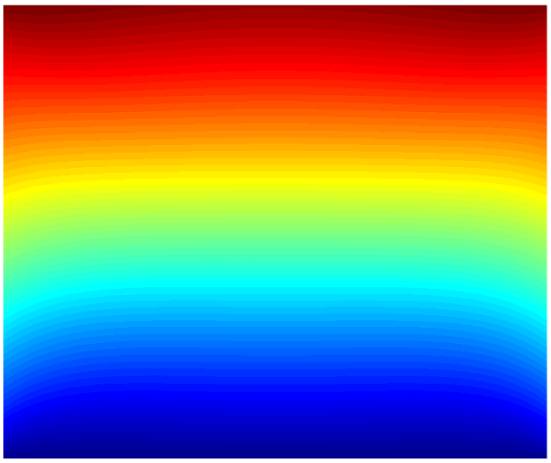

(a) SBFEM reference solution for displacement magnitude.

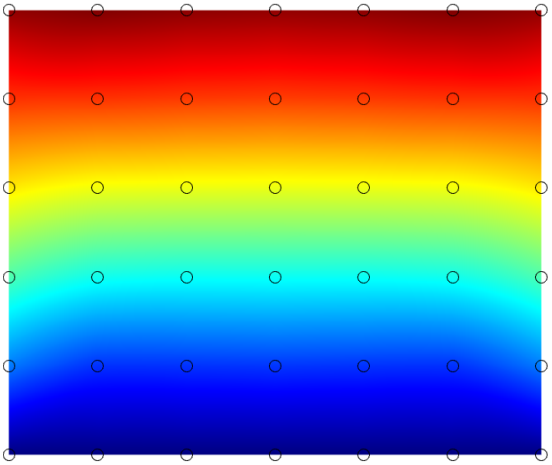

(b) Displacement field calculated employing CM4 elements, with coarse nodes in black.

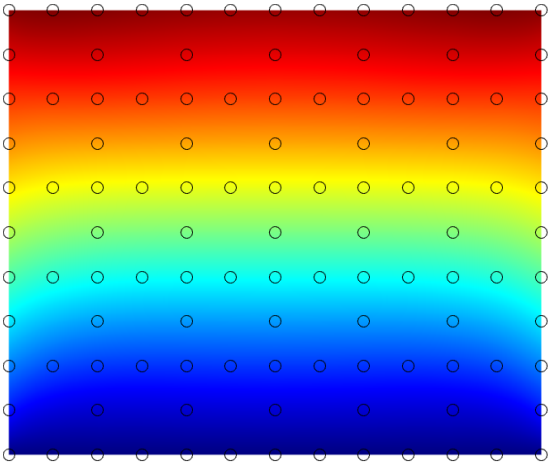

(c) Displacement field calculated employing CM8 elements, with coarse nodes in black.

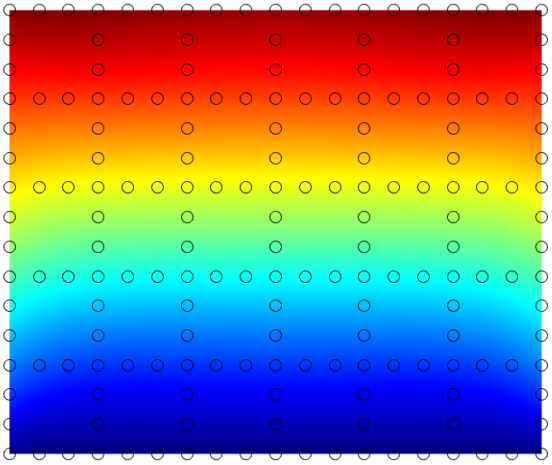

(d) Displacement field calculated employing CM12 elements, with coarse nodes in black.

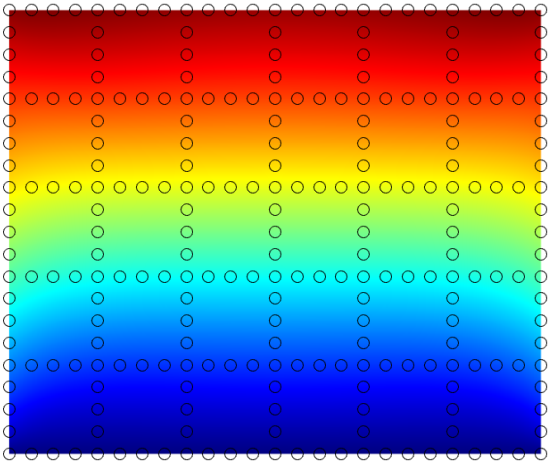

(e) Displacement field calculated employing CM16 elements, with coarse nodes in black.

Fig. 5.14: Undamaged masonry wall comprise 5x6 grid of undamaged RVEs. Plots comparing the magnitude of the displacement field calculated by CMX elements to a SBFEM reference solution.

utilizing both linear and periodic NBFs. Use of CM4-8 elements is not recommended, when crack are present of the fine scale. Further, quadratic NBFs have been shown to offer no benefit, when compared

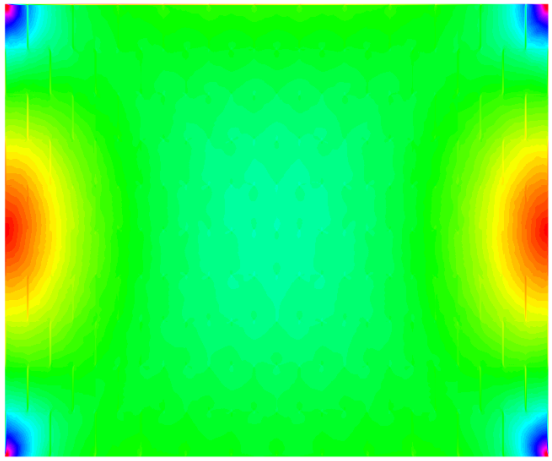

(a) SBFEM reference solution for von Mises stress.

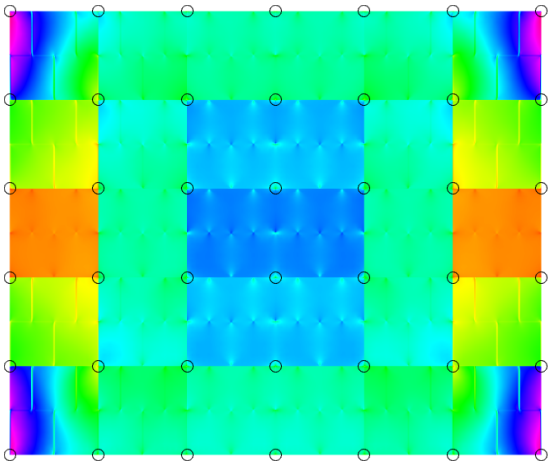

(b) Von Mises stress field calculated employing CM4 elements, with coarse nodes in black.

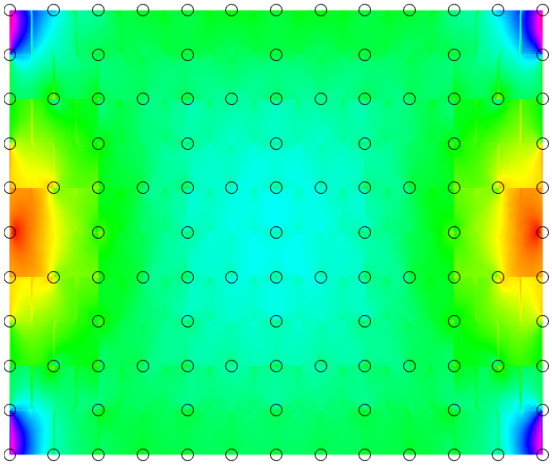

(c) Von Mises stress field calculated employing CM8 elements, with coarse nodes in black.

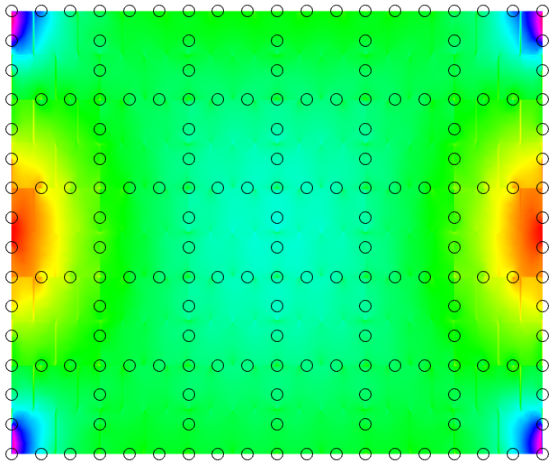

(d) Von Mises stress field calculated employing CM12 elements, with coarse nodes in black.

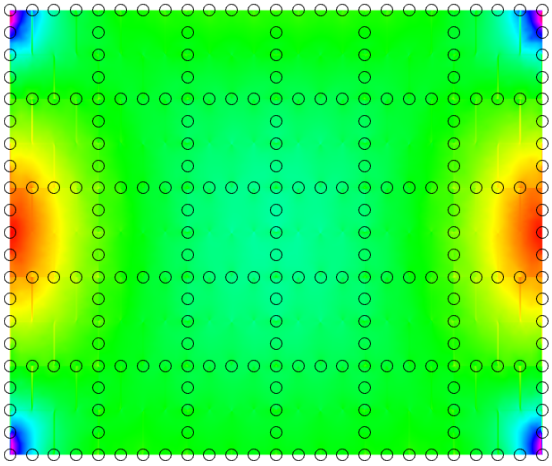

(e) Von Mises stress field calculated employing CM16 elements, with coarse nodes in black.

Fig. 5.15: Undamaged masonry wall comprise 5x6 grid of undamaged RVEs. Plots comparing the von Mises stress field calculated by CMX elements to a SBFEM reference solution.

to their linear and periodic counterparts. Overall, CM12-16 elements deliver the best performance and can accurately capture the gSIFs to within 1% accuracy for ratios of $a/L \leq 0.5$. For larger ratios, the

	CM4		CM8		CM12		CM16		
	L	P	L	P	L	P	L	P	Units
DOF SBFEM	96189		96189		96189		96189		-
DOF MSBFEM	84		226		368		510		-
Ratio	11451		4256		2614		1886		x
Time SBFEM	0.6247		0.6247		0.6247		0.6247		[s]
Time MSBFEM	0.0008		0.0026		0.0028		0.0048		[s]
Ratio	762		243		227		131		x
Time NBF	0.667	0.700	1.027	1.325	1.537	1.894	1.862	2.534	[s]
Displ. Norm	34.54	28.83	3.65	65.06	1.86	46.57	1.31	43.37	[1e-4]

Fig. 5.16: Masonry wall constructed by assembling RVEs in a 5x6 grid.

boundary effects are difficult to capture with just 12 or 16 coarse nodes and the conventional choice of NBFs. Hence hybrid NBFs are introduced, which borrow from both linear and periodic variants to provide more predictable performance and unburden the analyst having to chose the most suitable NBFs prior to analysis.

5.2 Asymptotic Tip Enrichment

In this contribution, the unique properties of the SBFEM are exploited to improve the accuracy of computed gSIFs on hybrid balanced quadtree-polygon (QT) meshes. The gSIFs are extracted by harnessing the semi-analytical solution in radial direction. This is achieved by placing the scaling center of the element containing the crack at the crack tip. Taking an analytic limit of this element's stress field as it approaches the crack tip, delivers an expression for the singular stress field. By applying the problem specific boundary conditions, the geometry correction factor is obtained and the gSIFs are then evaluated based on their formal definition.

Computation of the gSIFs by SBFEM permits exceptional accuracy, however, when combined with QT meshes employing linear elements, this does not always hold. Nevertheless, it has been shown that crack propagation schemes are highly effective even given very coarse discretizations, utilizing criteria than only rely on the ratio of mode I to mode II gSIFs. The absolute values of the gSIFs may still be subject to undesirable errors. Hence, we propose a post-processing scheme, which minimizes the error resulting from the approximation space of the cracked element. Thus, the errors in the calculation of the gSIFs is only limited to the discretization error of the quadtree mesh. This is achieved by h- and/or p-refinement of the cracked element, which elevates the amount of modes present in the solution. The resulting numerical description of the element is highly accurate, with the main error source now stemming from its boundary displacement solution. Numerical examples show, that this post-processing procedure can significantly improve the accuracy of the computed gSIFs with negligible computational cost even on coarse meshes resulting from QT decompositions.

5.2.1 The Proposed Method

By inspecting the expression of the singular stresses (Eq. 2.54), the accuracy of the gSIFs (Eq. 2.61) can be improved in two ways:

1. Finding a better approximation for the integration constants $\{c\}$ stemming from the displacement solution of the domain.
2. Enhancing the displacement and thus stress field approximation $[\Psi]$ and $[S]$ within the cracked element by escalating the amount of DOFs present.

The contribution of the first source can be adjusted by h- or p-refinement on the mesh, either locally or globally. However, this is a costly procedure due to, e.g., remeshing, reassembly followed by solution, in the understanding that a significant amount of DOFs are newly introduced. Considering the convergence rate of the linear elements employed, this is deemed a sub-optimal approach from a computational resources standpoint. The second source allows for enhancement directly in post-processing and permits certain insight into how close we might be to the exact solution, by contrasting the gSIFs calculated using the traditional approach to those using the improved scheme.

The steps comprising the improved scheme are (Fig. 5.17):

1. **Perform analysis**
   A displacement solution for the given mesh is sought.
2. **Create a high order cracked element**
   The existing cracked element is replaced by one elevated by h- and/or p-refinement. New nodes, lying in-between existing QT mesh nodes, are introduced in the process.
3. **Impose linearly interpolated displacements on all DOFs**
   To guarantee compatibility with the surrounding QT mesh, linear displacements are enforced between its nodes, on the boundary of the elevated cracked element.
4. **Back calculate $\{c\}$ for cracked element**
   Since the cracked element comprises one subdomain, with all DOFs situated on the boundary, where the prescribed displacements are imposed, the calculation of the stiffness matrix is not necessary. Only the block-diagonal Schur decomposition is required. The integration constants are obtained as $\{c\} = [\Psi^{(u)}_{neg}]^{-1}\{u\}$ [294]. Typically, refined crack elements comprising 100 DOFs have sufficiently converged. Since the original already contains 10-30 DOFs, this does not noticeably impact computation time.
5. **Extract singular stress modes**
   The identification and extraction of the singular stress modes remains unchanged.
6. **Calculate gSIFs**
   The gSIFs are calculated given Eq. 2.61, however, now based on the quantities originating from the elevated cracked element.
7. **Contrast original with improved gSIFs**
   By contrasting the values for the gSIFs calculated by both methods, we can gauge the quality of the original analysis. If the discrepancy in gSIFs is deemed too large, refinement of the original mesh may be warranted.

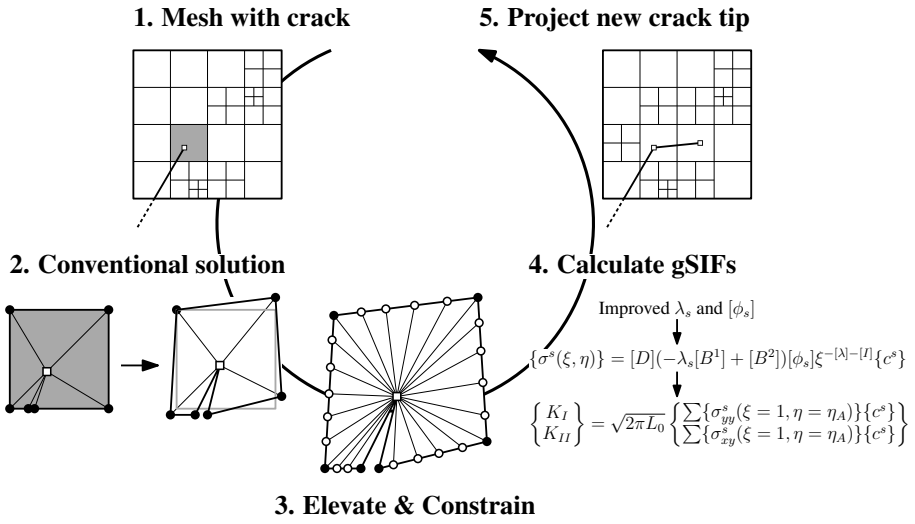

Fig. 5.17: Steps comprising the improved scheme.

5.2.2 Numerical Examples

5.2.2.1 Edge Cracked Square Plate in Mode II

An edge cracked square plate subjected to a plane stress state is examined (Fig. 7.1). Along the boundary, the analytic solution [142] of the near-tip crack field is prescribed given $K_{II} = 1$ (Tbl. 5.2), imposing pure mode II loading. The material properties are $E = 200$ [N/mm^2], $\upsilon = 0.3$ and the side length is $L = 1$ [mm].

Three cracked element discretizations are considered, as they arise typically on QT meshes, prior to the refinement and homogenization steps (Fig. 2.11c). The exact solution is applied to the QT mesh nodes identified in Fig. 5.19. The remaining nodes resulting from internal element refinement are restricted to move as a linear combination of their neighbouring QT mesh nodes, thereby enforcing compatibility.

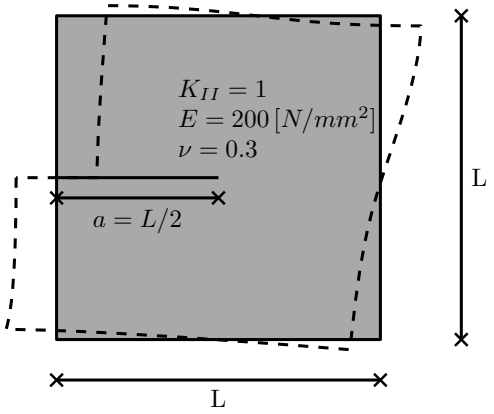

Fig. 5.18: Experimental setup for numerical example A.

Tbl. 5.2: Analytic solution of the near-tip crack field.

	Exact displacement solution for mode II fracture
u_x	$\frac{K_{II}}{2\mu}\sqrt{r/(2\pi)}sin\frac{\theta}{2}\left(\kappa+1+2cos^2\frac{\theta}{2}\right)$
u_y	$-\frac{K_{II}}{2\mu}\sqrt{r/(2\pi)}cos\frac{\theta}{2}\left(\kappa-1-2sin^2\frac{\theta}{2}\right)$

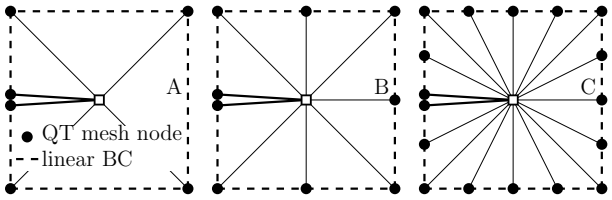

Fig. 5.19: Typical element types A-C arising from QT meshes.

The convergence behaviour is investigated in Fig. 5.20. Due to the over-constraining of the boundary, deviation in convergence behaviour is expected, i.e., by enforcing linearly dependant displacement boundary conditions between QT mesh nodes, an effective stress state is imposed that differs mildly from the exact solution. In this example, the gSIFs are therefore slightly overestimated, which is evident in the asymptotic behaviour on all three meshes. Nevertheless, the error in K_{II} is significantly reduced for all QT meshes, as can be seen in Tbl. 5.3. The diverging results for the case of 2-noded elements is explained by the examination of the absolute values. While the higher order elements approach the asymptotic solution from the high end, the two-noded elements approach from the lower end, thus crossing the imposed $K_{II} = 1$ in the process. The obtainable accuracy is naturally limited by the artificially imposed boundary conditions. Therefore, the expected convergence behaviour is disrupted accordingly. In this specific example, the convergence behaviour of even-noded elements was observed to behave predictably, while the odd-noded elements exhibited slight oscillatory behaviour.

It can be observed that the computed values for K_{II} remain practically stable when more than 100 DOFs are employed within the cracked element. Preference should be given to higher order elements due to their enhanced convergence properties. On a contemporary laptop employing unoptimized Matlab code, this entails calculations completing in less than 0.1s. Tbl. 5.3 provides the results for K_{II} calculated on the original QT meshes and contrasts them to the asymptotic solutions for the refined crack elements, given a high fidelity SBFEM solution.

Assuming a user-specified accuracy tolerance, the improved method of calculating the gSIFs facilitates a decision criterion on whether global mesh refinement is required. The difference in achieved accuracy for each QT mesh is primarily attributed to the manner in which the enforced displacements on the boundary conform to the exact field solution. Deviations therein are reflected in the integration constants $\{c\}$ (Eq. 2.42) and comprise the remaining error in the asymptotic solution. In a practical application of this method, the displacement solution on the QT mesh nodes results from the FEM solution of the global QT

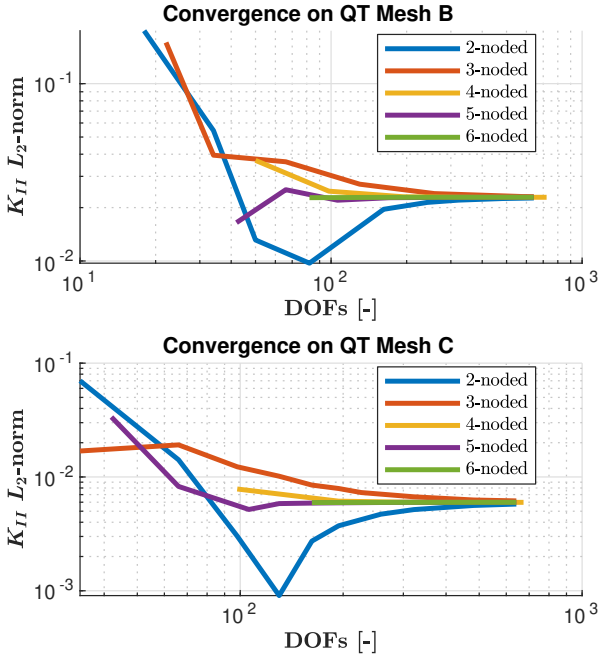

Fig. 5.20: Convergence behaviour of K_{II} on QT meshes employing n-noded elements as boundary discretization.

mesh. Since the method proposed to improve the calculation of gSIFs does not increase the amount of global DOFs, the overall analysis does not differ. Solely on the cracked element that is refined, "virtual" nodes are introduced that, however, never manifest in calculation of system displacements as their values are predetermined due to the linearized BCs. In principle, a more accurate representation of the displacement modes and eigenvalues is achieved inside the cracked element, while the boundary constraints remain unchanged. This explains the counter intuitive results of the asymptotic error for QT mesh type A for which smaller errors are observed than for the QT mesh type B: For this specific loading, i.e., mode II excitation, on average, the enforced displacement field on the boundary results in a closer approximation of the exact stress field. If mode I excitation where, however, considered, for which the right boundary of the cracked element exhibits concave behaviour, QT mesh Type A results in a 15% error, since it is not able to reproduce such displacement behaviour. Between QT meshes type B and C we observe convergence as expected, as QT mesh C can represent all displacement modes of QT mesh B, while also introducing additional ones.

Tbl. 5.3: Convergence of gSIFs to imposed solution.

Method		K_{II}	**error [-]**	**error [%]**
imposed		1	-	-
(v) hi-fi		1.00000000524414	≈ 0	≈ 0
(iii) QT mesh	A	1.01547261490198	0.0155	1.55
	B	0.80116357970950	0.1988	19.88
	C	0.92998436271287	0.0700	7.00
(iv) asympt.	A	1.01124862611779	0.0113	1.12
	B	1.02286467268900	0.0287	2.29
	C	1.00598223218854	0.0060	0.60

5.2.2.2 Edge Cracked Square Plate in Mode I

An edge cracked square plate subject to a plane stress state is examined (Fig. 7.4). The bottom edge of the plate is fully clamped, while on the top edge forced displacements $u_y = 1$ and $u_x = 0$ are applied. The Young's modulus, Poisson's ratio, fracture energy, crack propagation increment and side length are given as $E = 200$ [N/mm^2], $v = 0.3$, $G_c = 2.7$ [N/mm^2], $\Delta a = 0.025$ [mm] and $L = 1$ [mm] respectively.

First, the load-deflection curves obtained from several methods are compared: (i) XFEM, (ii) traditional QT SBFEM, (iii) SBFEM on QT mesh types A-C, (iv) the newly proposed SBFEM method and (v) a high fidelity SBFEM solution comprising one subdomain with h- and p-refinement. The load-deflection curves (Fig. 5.22) are constructed using the following procedure:

1. Calculate the critical stress intensity factor K_c from the E-modulus and the critical energy release rate G_c:
$$K_c = \sqrt{EG_c} \quad \text{for plane stress} \tag{5.2}$$
2. Formulate the equivalent stress intensity factor K_{eq}:
$$K_{eq} = \sqrt{K_I^2 + K_{II}^2} \tag{5.3}$$
This implies that the crack propagates as soon as $K_{eq} \leq K_c$. Hence, the gSIFs and the sum of the reaction forces are stored at each iteration.
3. Determine the load factor such that crack propagation initiates, i.e., as the ratio $K_c/K_{eq} = 1$. The effective displacements and loads at each crack increment step are calculated by scaling the initially imposed values by the load factor.
4. Employ the minimum strain energy density criterion (or equivalent) to calculate the crack propagation angle [285]:
$$\theta_c = 2\tan^{-1}\left[\frac{-2K_I/K_{II}}{1+\sqrt{1+8(K_I/K_{II})^2}}\right] \tag{5.4}$$

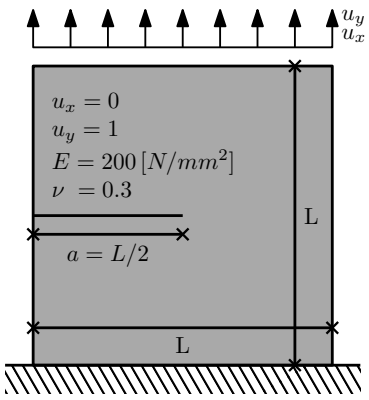

Fig. 5.21: Experimental setup for numerical example A.

For this simple example, the crack paths for all methods coincide, i.e., they propagate in direct extension of the imposed crack. Investigating the load-deflection behaviour (Fig. 5.22), two reference solutions are constructed: a high fidelity SBFEM solution (v) employing 568 DOFs and an XFEM solution (i) employing a domain discretization of 161x161 element (52'488 DOFs). As expected, the traditional approach (ii) utilizing 1024 DOFs mirrors the reference XFEM solution. Similarly, the correct load-deflection response is obtained by the novel approach (iv), however, employing only 880 DOFs, i.e., on the same mesh as the deficient method (iii). The difference in DOFs is attributed to the balancing operation following refinement around the crack tip, which propagates across the domain.

Given this specific geometry, an exact solution for the crack tip singularity is available, i.e., a square root singularity, which we exploit for benchmarking purposes. By inspection of Eq. 2.59, this is the case when all eigenvalues contained in $[S^{(s)}]$ are equal to 0.5. Since the singular eigenvalues depend only on the boundary discretization, a SBFEs ability to reproduce the exact solution is purely a reflection of its

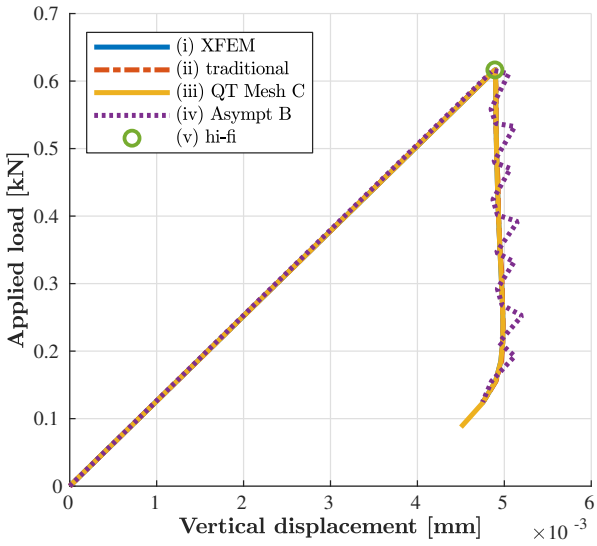

Fig. 5.22: Load deflection curves for methods (i) - (v).

approximation space. Hence, by leveraging hp-elements, the error in calculated gSIFs, due to the choice of approximation space, can be minimized so that the remaining error stems only from the surrounding mesh discretization. Tbl. 5.4 summarizes the results for the SBFEM based methods given different levels of refinement. As expected, the hi-fi (v) solution is able to approximate the exact solution to nearly machine

Tbl. 5.4: Convergence of eigenvalues to square root singularity.

Method		**DOFs**	λ_1	λ_2
exact		-	0.5	0.5
(ii) trad.	2	34	0.502106496308655	0.502106496308665
	3	66	0.500547555626861	0.500547555626900
	6	162	0.500088619101087	0.500088619101087
	12	322	0.500022191325667	0.500022191325716
(iii) QT mesh	A	12	0.543331260622274	0.487073508787698
	B	18	0.506300843546734	0.506300843547260
	C	34	0.501432879576478	0.501432879577241
(iv) asympt.	3n	66	0.499993111156218	0.499991972174270
	3n	98	0.499998547338467	0.499998547338467
	3n	130	0.499999524753473	0.499999524753473
	5n	42	0.500958236174165	0.500555777249317
	5n	68	0.500001822342609	0.500001760606780
	5n	106	0.500000389900685	0.500000214938575
(v) hi-fi		578	0.499999999998063	0.500000000000369

precision even with very few DOFs. Both the proposed method (iv) and traditional (ii) approaches deliver approximations accurate to several significant figures. For method (iv) 3- and 5-noded elements, denoted by 3n and 5n respectively are considered. For method (ii), studies were conducted using either {2,3,6,12} linear elements per long side of the cracked domain. It can be observed that the proposed method (iv) significantly outperforms the traditional (ii) approach at similar internal discretization levels. The elements, as they are employed in method (iii), perform poorly and report significantly fewer accurate digits.

We compare K_I obtained by our proposed method (iv) and method (iii) to the hi-fi reference solution (v) (Tbl. 5.5). Since both methods employ the same mesh, we isolate the gains of the proposed method (iv). Indeed, for mesh types A and B we observe an improvement in accuracy of the calculated gSIFs by approxi-

mately and order of magnitude. For mesh C, however, we approach a limit given by the discretization error of the underlying mesh and therefore the error cannot be reduced to such a degrees as with the previous meshes. Nevertheless, accuracy < 1% is readily achieved, indicating a sufficiently accurate solution for most SIF-based applications.

Tbl. 5.5: Convergence of gSIFs to high-fidelity solution.

Method		K_I	**error [-]**	**error [%]**
(iii) QT mesh	A	18.824826991544300	3.4427	22.38
	B	17.144699325716516	1.7626	11.46
	C	15.767196554450349	0.3851	2.50
(iv) asympt.	A	15.714940415023673	0.3328	2.16
	B	15.629945166079814	0.2478	1.61
	C	15.457607616329554	0.0755	0.49
(v) hi-fi		15.382113483624098	-	-

5.2.3 Conclusions

This contribution demonstrates that the accuracy of gSIFs calculated on hierarchical meshes can be significantly enhanced by implementing local refinement of the cracked element, while constraining the boundary displacements to conform with the surrounding mesh. The error stemming from the element's ability to accurately represent the singular stress field is alleviated and the remaining deviation is attributed to the discretization error introduced by the mesh. The proposed method permits the use of significantly coarse discretizations of the domain without the need for artificial refinement about the crack tip to obtain comparable accuracy of the gSIFs. This benefit is compounded, since the balancing operation employed on the hierarchical mesh, to arrive at a finite number of precomputable element realizations, is eliminated. Numerical examples have demonstrated that the use of higher order elements and approximately 100 DOFs in the refined element produce accurate results, while retaining high computational efficiency. The limitations of this approach stem from the linear boundary discretization, imposing artificial constraints on the solution. The use of higher order elements, such as cubic line elements on hierarchical meshes could minimize this issue and require the development of targeted implementations for more involved domain geometries.

5.3 The Multiscale Crack Propagation Scheme

In this contribution, we fuse the SBFEM on balanced hybrid quadtree-polygon meshes with EMsFEM to accelerate crack propagation simulations. This scaled boundary multiscale approach to crack propagation employs SBFEM in a fully resolved region immediately surrounding the crack tip and coarse elements, i.e., EMsFEM unit cells, in the remaining domain. As the crack propagates across the domain, unit cells within the immediate crack path are resolved. Once the crack completely transitions a resolved unit cell it is replaced by two newly constructed, coarse unit cells. This approach limits computational effort to the crack tip region, primarily replacing the fine mesh on the domain by a coarse one, on which the governing equations are solved. Early results indicate that this method results in a reduction of required DOFs by at least an order of magnitude for simple domains. Further the techniques introduced in the previous section are exploited to enrich the crack tip element and further reduce the amount of refinement necessary about the crack tip. The latter traditionally negatively affects the QT mesh due to the balancing operation. Via fusion of these two techniques, the amount of DOFs during simulations of crack propagation remains tractable.

5.3.1 The Proposed Method

The proposed method is split into two distinct phases: online and offline calculations. The offline phase comprises the identification and precomputation of the coarse elements. The computational burden associated with the repeated solution of the Dirichlet boundary value problem is minimized by first condensing

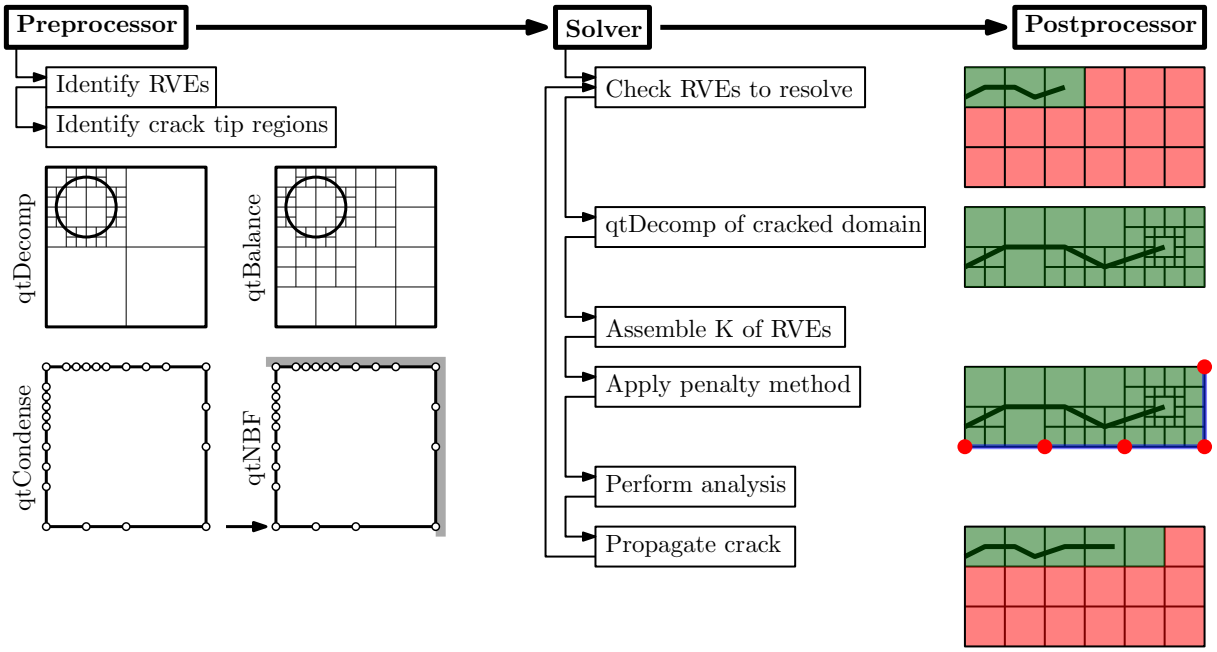

Fig. 5.23: Scaled boundary multiscale approach to crack propagation (MSBFEM).

the internal DOF and then constructing $[N]$, or by decomposing the stiffness matrix by direct methods. The online phase comprises the crack propagation scheme. To this end, the unit cells in vicinity of the crack tip are fully resolved, meshed and their elements assembled in the finite element sense. In parallel, the coarse elements comprising the remaining domain are also assembled and the coarse and fine meshes are tied together by penalty method (Fig. 5.23, blue lines), to not introduce further DOF in the process. The linear boundary conditions employed during construction of the unit cells imply linear displacements between coarse nodes (Fig. 5.23, red dots), defining the tie constraint behaviour. The system is then solved for and the crack is propagated according to a prescribed crack increment Δa and computed crack propagation angle [285]:

$$\theta_c = 2\tan^{-1}\left[\frac{-2K_I/K_{II}}{1+\sqrt{1+8(K_I/K_{II})^2}}\right] \tag{5.5}$$

The accurate calculation of the gSIFs is paramount. However, sufficient angular resolution of the singular stress field is required. Typically, this is achieved by homogenizing a region around the crack tip (Fig. 2.11c) at the expense of introducing a significant number of DOF due to the balancing requirement.

5.3.2 Numerical Examples

5.3.2.1 Variant of Plate with Two Holes and Edge Cracks

We consider a variant of the plate with two holes and edge cracks (PwHC) (Fig. 5.24). Notches of length $A = 1$ [mm] are introduced at a distance $L = 4$ [mm] from the top and bottom respectively. Displacements are prescribed on both sides such that $[u_x, u_y] = [0, \pm 0.1]$. The material properties are $E = 200$ [N/mm^2], $\upsilon = 0.3$, $K_{Ic} = 1500$ [N/mm$^{3/2}$]. The height and width of the plate are $H = 10$ [mm] and $W = 20$ [mm] respectively. Plane stress conditions are assumed. In a first step, we consider the conventional approach to SBFEM crack propagation [239]. Fig. 5.25 depicts four snapshots of such an analysis. For this numerical example, we exploit symmetry, by first averaging the gSIFs and then projecting the new crack tips simultaneously. This circumvents the necessity for a stability analysis in the presence of multiple propagating cracks. Due to legibility concerns a significantly coarser representative mesh is presented than is employed for the actual MSBFEM simulation. Even at this level of discretization it is immediately apparent that:

1. The crack does not interact equally strongly with all regions.
2. Large regions exist, whose properties and topology remain unchanged during analysis.

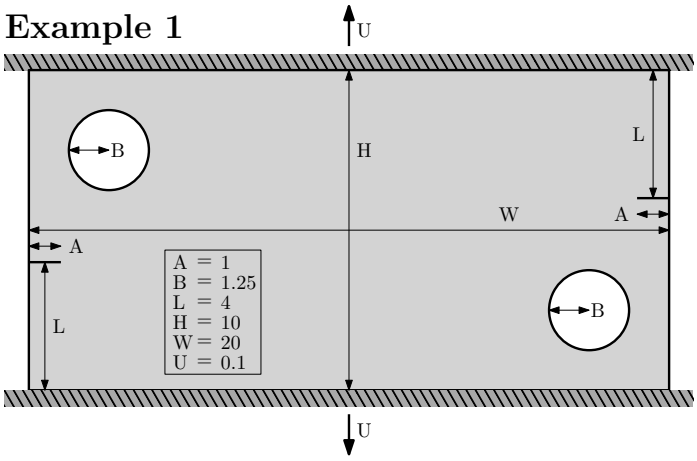

Fig. 5.24: Experimental setup for numerical example 1.

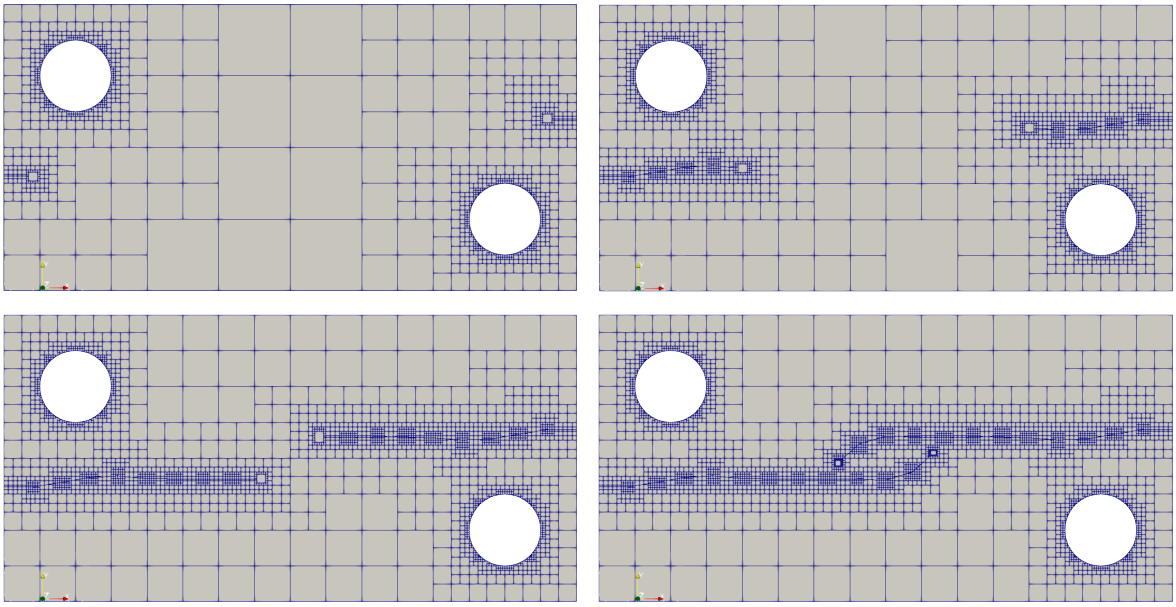

Fig. 5.25: Conventional approach to crack propagation employing SBFEM. (Matlab code courtesy of C. Song at UNSW)

3. Incorporating specific geometric features such as circles and crack paths greatly increase the amount of DOF present.
4. Homogenizing large regions at the crack tip with subsequent balancing of the quadtree significantly increases the amount of DOF present.

Therefore, the MSBFEM approach to crack propagation aims at reducing the computational effort required to perform a crack propagation analysis by:

1. exploiting the unchanged and repetitive portions of the mesh.
2. excepting a slight decrease in accuracy in the predicted crack propagation path in favor of significantly accelerating the analysis.

To this end, several possible levels of discretization by CMX elements are investigated (Fig. 5.26). In a first approach a grid of 4x8 possible conventional CM4 elements was considered. Only two unique coarse elements have to be constructed, denoted by 1 and 2 respectively in Fig. 5.26. The inclusion can be treated by rotating the stiffness matrix of coarse element 1 using conventional approaches. However, this discretization does not result in an accurate reconstruction of the crack path, as is evident by inspection

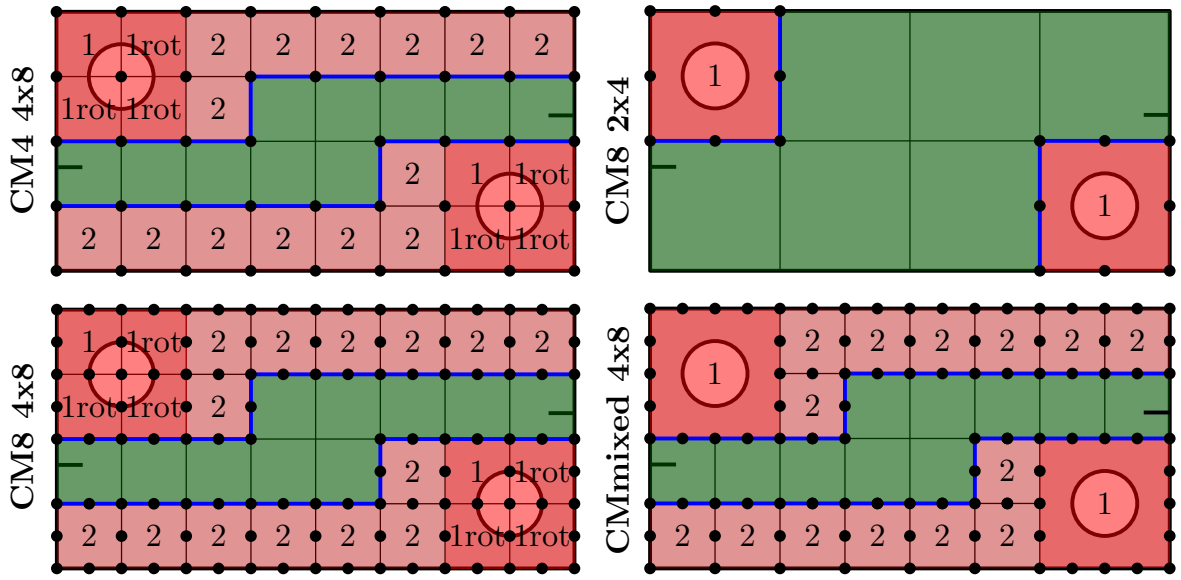

Fig. 5.26: Several possible domain discretizations employing CMX elements (red), the fine grid (green), tie-constraints (blue) and coarse nodes (black dots). All NBFs are constructed subject to linear boundary conditions. The final crack propagation snapshot is depicted.

of Fig. 5.27. The stress field in crack propagation direction is heavily influenced by the surrounding CM4 element, which enforce a linear displacement field on their boundaries. Relaxing this requirement at similar coarse discretization levels is the second approach employing a 2x4 grid of CM8 elements. Since CMX elements are replaced with their fine grid as they are approached by the crack tip, larger elements do permit more accurate crack path prediction, however, at the cost of significantly greater DOF. Although a crack path affine to the conventional SBFEM approach is observed, the CM8 element containing the inclusion impacts the accuracy of the stress field during early iterations and therefore prompts the crack path to deviate. Two further discretization levels were considered: 4x8 grids of CM8 and mixed CM8 & CM16 coarse elements. Effectively, the amount of coarse nodes was doubled with respect to the two previous variants. Both variants manage to accurately reproduce the conventional SBFEM crack path, while only resolving a narrow band of the domain. The mixed variant is preferred due to the following reasons and will therefore be further discussed in the subsequent numerical example:

- It accurately captures the inclusion with a CM16 element, without having to exploit rotation symmetry. Further, it could also treat the inclusion if it where not centered with respect to the element.
- Given that the MSBFEM could be employed across an arbitrary number of scales, we demonstrate here that the CMX elements can be employed to treat hanging nodes in an adaptive setting.
- Additionally, the CMX elements are not constrained to rectangular geometries. The ability to construct polygonal coarse elements is highly beneficial in complex meshing applications.

5.3.2.2 Notched Perforated Plate

A perforated plate as depicted in Fig. 7.4 is considered. A notch of length $A = 1$ [mm] is introduced at a distance $L = 18$ [mm] from the bottom right corner. Displacements are prescribed on both sides such that $[u_x, u_y] = [\pm 0.1, 0]$. The material properties are $E = 200$ [N/mm^2], $\upsilon = 0.3$, $K_{Ic} = 1500$ [N/mm$^{3/2}$]. The height and width of the perforated plate are $H = 24$ [mm] and $W = 60$ [mm] respectively. Plane stress conditions are assumed.

Fig. 5.29 depicts various snapshots of the various crack propagation phases. During phase 1, the initial discretization is employed, i.e., a fine mesh (green) immediately surrounding the crack front (orange), encased by CM8 and CM16 homogenized elements (red) and tied together by penalty method along the interface (blue). While the conventional SBFEM requires approx. 52'000 DOF, the scaled boundary multiscale approach (MSBFEM) employs 2268 DOF, reducing the amount of DOF by a factor of 22, without perceivable altering the crack path (Fig. 5.30). Once the crack tip falls within a user specified distance to

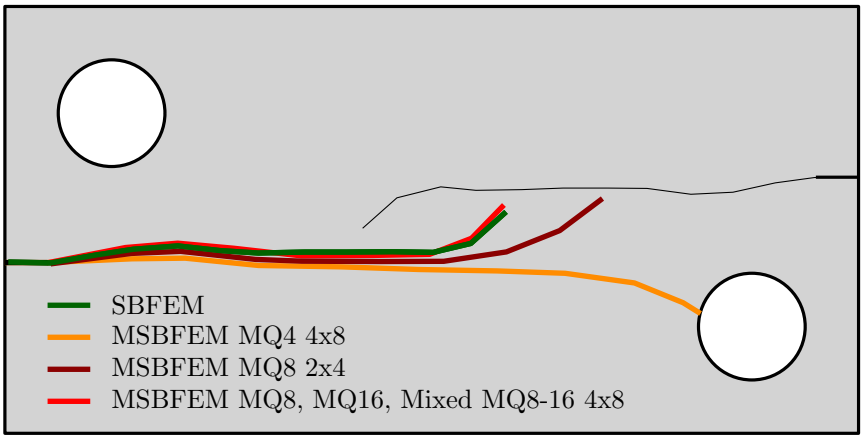

Fig. 5.27: Crack paths resulting from discretization levels depicted in Fig. 5.26 contrasted to the conventional SBFEM approach to crack propagation.

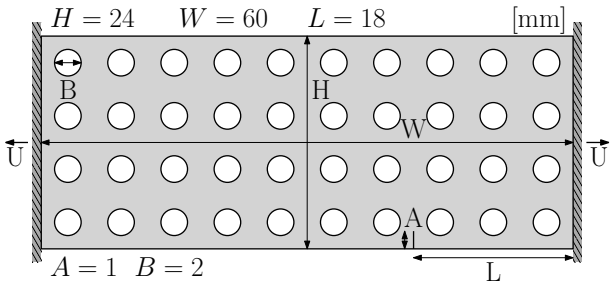

Fig. 5.28: Experimental setup for numerical example 2.

the adjacent CMX elements, here chosen as one fifth of a CM8 element side length, these are fully resolved as well, resulting in phase 2 (Fig. 5.29). Analysis by conventional SBFEM results in approx. 58'000 DOF, while MSBFEM employs 4318 DOF, a reduction by a factor of 13. However, the crack paths calculated by the two methods starts to deviate slightly. This is the effect of the linearized boundary conditions, which result from the method with which the multiscale NBF are computed, prescribed on the fully resolved region (green). The imposed linear boundary conditions artificially over-constrain the unit cell, resulting in a stiffer response on the coarse scale, thus impacting the accuracy of the calculated stress field on the fine scale.

In phase 3 (Fig. 5.29) the crack has transitioned all fully resolved blocks from phase 2. Hence, this region can be replaced by corresponding CMX elements (purple) without incurring a loss in accuracy. To this end, the crack path is smoothed into linear segments joined by the CMX coarse nodes. The computational effort expended in constructing these CMX (purple) elements online is expected to be recuperated over few subsequent crack propagation steps. Indeed, while SBFEM requires approx. 65'000 DOF for analysis, the proposed MSBFEM scheme makes due with 2436 DOF, a reduction by a factor of 26. If the online phase where to be forgone, the MSBFEM approach would require 6386 DOF and only result in a reduction by a factor of 10. The crack paths do continue to diverge slightly with the effects becoming more visible. First, small deviations are compounded across all crack propagation steps. Second, linearized boundary conditions in the narrow, fully resolved band (phase 3, green) affect the stress state to a greater degree than in the previous phases. By inspection of the two crack paths it seems as if the MSBFEM approach is more resistant to local stress concentrations influencing the gSIFs and thus the crack path incorporates fewer sharp changes in direction as seen in points A, B and C in Fig. 5.30.

5.3.3 Conclusions

MSBFEM is an effective scheme to focus the computational burden of crack propagation analysis on select regions. This is achieved by substituting regions characterized by weak interaction with coarse elements constructed by EMsFEM. To this end, the amount of DOF present is reduced by more than an order of

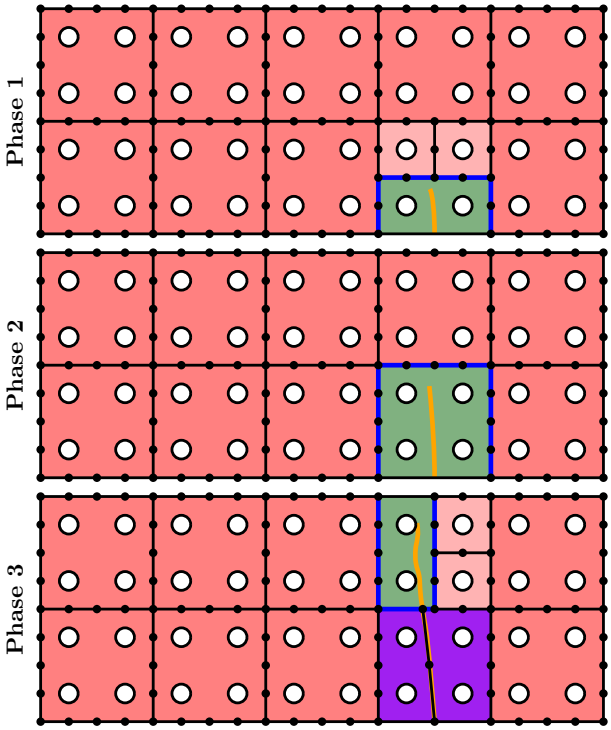

Fig. 5.29: Crack propagation phases 1-3.

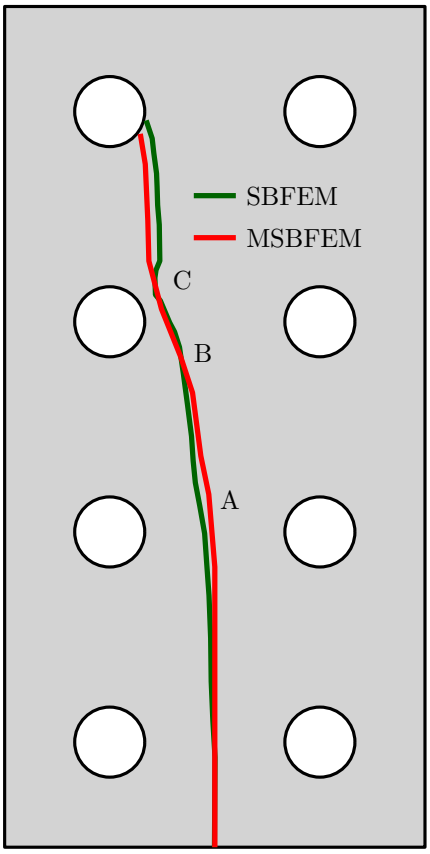

Fig. 5.30: Crack paths for SBFEM and MSBFEM inside the affected subdomain.

magnitude as demonstrated by the crack propagation analysis of a notched, perforated plate. Further, exploiting SBFEM's unique feature set to enhance the quality of calculated gSIFs in post-processing is shown to further reduce the required number of DOFs for standard crack propagation analysis in the fully resolved region. This reduction in the set of active DOFs does not hinder accuracy; the resulting MSBFEM crack path closely resembles the SBFEM reference case.

Part III

Accelerating the Inverse Problem

6 Damage Localization

The solution to the inverse problem as stated in sec. 2.5.1 is achieved by minimizing a fitness function using global optimization algorithms. This process entails the repeated evaluation of the forward problem for different realizations of the design variables, e.g., number of flaws, shapes, sizes and locations, each resulting in a fitness score. Hence, the method by which the forward problem is solved must be parametric, robust and preferably computationally efficient. The present work marks the first time that SBFEM is harnessed to solve the associated forward LEFM problem. It is especially suited for this task, among others, due to the simplified meshing, precomputation potential and the ability to naturally capture singularities, with each detailed in the following subsections.

6.1 The Damage Localization Scheme

In this thesis, an accelerated optimization scheme is proposed, which is largely independent of the chosen global optimization algorithm. In the forward problem, precomputation and reanalysis are exploited, whereas in the inverse problem, techniques to parameterize and constrain the inverse problem are treated.

6.1.1 Precomputation

The introduction of a flaw in the analysis domain only affects select cells of the quadtree (Fig. 6.1, red). The properties of unaffected cells as well as the imposed boundary conditions and loading remain unchanged. Owing to the hierarchical nature of the quadtree decomposition, any alterations resulting from the introduction of a flaw can be condensed out to the original configuration. Hence, only the treatment of a much smaller problem is necessary. To this end, a forward analysis of the undamaged system is performed prior to the global optimization loop, establishing the structures stiffness matrix, load vector and displacement solution. Further, this serves as a baseline for the strain readings. The affected cells are treated in the standard SBFEM sense by modifying the quadtree, balancing it, introducing polygonal elements as required and finally computing the associated element properties. A condensation step applied to the modified cells reduces the problem statement to the original mesh, however, with rank one updates corresponding to the DOF of each updated cell. The treatment of rank one updates in linear static analysis is well researched and commonly classified as reanalysis techniques.

6.1.2 Reanalysis Technique

In this work, the reanalysis techniques described in [151] are implemented and stated here for completeness. Such techniques are commonly employed to accelerate iterative simulations on marginally varying structures. They derive their expedience by considering the effect of an introduced stiffness perturbation on the resulting displacement field. If the perturbation effects are highly localized, the associated computational effort is marginal. The incremental stiffness matrix $[\Delta K]$ containing the perturbed quantities is compressed by pre- and post multiplying by boolean matrix $[b]$, resulting in the reduced incremental stiffness matrix $[K_R]$ of size equal to the rows and columns affected by the perturbation.

$$[\Delta K] = [b]^T [\Delta K_R][b] \tag{6.1}$$

Hence, by exploiting the Woodbury matrix identity, the inversion of the stiffness matrix $[K]$ subject to a perturbation $[\Delta K]$, is stated as:

$$[K]^{-1} = ([K_0] + [b]^T [\Delta K_R][b])^{-1} = [K_0]^{-1} - [K_0]^{-1}[b]^T([I] + [\Delta K_R][b][K_0]^{-1}[b]^T)^{-1}[\Delta K_R][b][K_0]^{-1} \tag{6.2}$$

where $[I]$ is the identity matrix of size($[\Delta K_R]$) and $[K_0]$ the initial stiffness matrix available as $[K_0] = [U_0]^T[U_0]$, e.g., from a previous Cholesky decomposition, with $[U_0]$ an upper triangular matrix. The resulting displacements follow as the superposition of the initial displacements $\{r_0\}$ and the displacement increments $\{\Delta r\}$:

$$\{r\} = \{r_0\} + \{\Delta r\} \tag{6.3}$$

Post multiplying Eq. 6.2 by $\{F_0\}$, the initial force vector, substituting the initial equilibrium equation $[K_0]\{r_0\} = [F_0]$ results in:

$$\{\Delta r\} = -[K_0]^{-1}[b]^T([I] + [\Delta K_R][b][K_0]^{-1}[b]^T)^{-1}[\Delta K_R][b]\{r_0\} \tag{6.4}$$

Therefore, the computational toll of updating the displacement field is primarily attributed to the inversion of the reduced unsymmetrical matrix $([I] + [\Delta K_R][b][K_0]^{-1}[b]^T)^{-1}$. Two substitutions are performed to permit a positive-definite expression. To this end, the symmetric influence matrix of unit changes $[Q]$ and an associated rectangular matrix $[Z]$ are introduced:

$$[Q] = [b][K_0]^{-1}[b]^T = [b][U_0]^{-1}([U_0]^T)^{-1}[b]^T = [Z]^T[Z] \tag{6.5}$$

resulting in the final expression for the update of the displacement field:

$$\{\Delta r\} = -[U_0]^{-1}[Z][Q]^{-1}([Q]^{-1} + [\Delta K_R])^{-1}[\Delta K_R][b]\{r_0\} \tag{6.6}$$

6.1.3 Design of Experiment

The convergence behaviour and rate of the selected global optimization algorithm is highly dependent of the choice of fitness function. Ideally, a fitness function should exhibit the following criteria:

- Permit a simple evaluation with physically interpretable results
- Result in a smooth response surface, not too shallow or too steep as to become ill-posed.
- Feature as few local minima as possible

The strategy with which the corresponding response surface is explored, depends on the global algorithm of choice. As is demonstrated in sec. 6.2 different families of global optimization algorithms can obtain convergence with significantly fewer function evaluations. Similarly, it is apparent that by increasing the number of function evaluations, any global optimization algorithm is empirically capable of converging.

In select cases, commonly associated with an irregular analysis domains, candidate flaws must be rejected. Accepted procedure for such instances entails assigning a penalty factor, which leads to a loss of information. First, all design variables comprising the candidate flaw are rejected, though the rejection might have only been triggered by a subgroup of design variables. Second, it is highly likely that the admissible design variables were selected to improve the flaw's localization. However, these will not be evaluated. Third, some implementations of global optimization algorithms do not resample a candidate flaw once one has been rejected via penalty. Hence, especially for algorithms where few candidates are spawned for each iteration, a significant portion of information is lost. Further, a resampling when candidates were previously selected to be as independent as possible, may not yield new insight. In order to avoid most issues presented above, and thus accelerate the convergence and analysis, special care is given to the parametrization of the introduced flaw. Using the example of straight cracks, two approaches arise. In the first approach the x-/y-coordinates of the two crack tips constitute the design variables.

The second approach requires the specification of the crack center, the crack angle and the crack length. Both approaches require the optimization of four design variables. The first approach, however, dictates a symmetric solution, since the same crack is introduced regardless of crack tip order. Hence, the solution space contains two global and twice the amount of local minima, which encumbers the optimization process. The second approach requires special treatment when transitioning from edge to embedded cracks. Since the information provided by the design variables is not sufficient to prevent unphysical cracks or splitting of the analysis domain, an increased amount of candidate flaws must be rejected. Identical for both methods is the difficulty and computational toll to treat an arbitrary amount of flaws. Typically, a handful of cracks are introduced and de-/activated as required. Provided the analysis concludes with the maximum amount of cracks active then further analysis must be conducted with a higher upper limit. Since locating the

global minimum by global optimization algorithms is not guaranteed, it is advised to perform multiple detection runs to avoid reporting local minima instead.

Within a structural health monitoring context, localization of flaws to within extreme accuracy is usually not necessary: Identifying the correct component or part as well as general flaw location and orientation is sufficient in order to target subsequent inspections effectively. Owing to this relaxation of requirements, a discrete representation of the design variables (e.g., crack center, length and angle) is introduced to substantially reduce the search space. The dis-/advantages are discussed by means of the GA-bitstring variant (sec. 6.2). Ideally, the user-specified mapping between discrete variables defined by a set of bits and corresponding physical representation:

- minimizes the amount of rejected candidate flaws.
- uniquely discretizes the search space of each physical design variable (e.g., number and stepping of possible realizations) subject to upper and lower bounds.
- permits de-/activation of flaws

However, issues arise, since the global optimization algorithm is not aware and therefore cannot take full advantage of the user-specified mapping:

- Mapping adds an additional transformation between bitstring input and the physical representation of the design variable, which impedes the development of efficient exploratory and exploitative behaviour.
- Cyclic design variables, e.g., crack angle, encounter wrap-around issues, which can limit their realization to either the upper or lower bound.

Although most of the described issues only complicate analysis and implementation, some issues remain: Behaviour associated with crack overclosure can result in unphysical symmetry conditions. Favoring an expedient analysis, such behaviour is permitted and left for the engineer to catch during the interpretation of results.

6.1.4 The Implemented Steps

The proposed scheme focuses on the forward problem to accelerate the optimization, the effects of which can be quantified prior to analysis and have been shown to increase computational efficiency. The most suited fitness function definition, parametrization and constraining of the design variables is rarely known in advance, owing to its problem dependency. Hence, these effects are studied in sec. 6.2 for fracture mechanics problems.

The proposed scheme incorporates four steps (Fig. 6.1):

1. **Precompute uncracked domain**
   In the first step, the system is analyzed in its undamaged state. This entails the quadtree decomposition, polygon clipping and the assembly of the system-level quantities followed by one linear solution step to obtain the displacements.
2. **Update crack region**
   With the second step, the global optimization algorithm commences. A flaw is introduced into the domain. The blocks containing the crack are located. Only these effect the computational toll. If refinement is necessary (each block can only contain one crack tip), it is performed accordingly. The stiffness matrices for the crack tip elements are updated. Split blocks receive similar treatment.
3. **Solution**
   Changes to precomputed blocks are condensed out so that only the DOF and blocks of the original, undamaged state remain. Modifications in the stiffness properties of those blocks affected by the introduced crack are gathered and form the basis for the reanalysis technique introduced in sec. 6.1.2.
4. **Post-processing**
   Once the updated displacements are obtained, the strains are back-calculated at the sensor locations, permitting the evaluation of the fitness score.

As a reference and to better understand the reporting in the numerical examples section, an early variant of the acceleration scheme is described in Fig. 6.2. In it, reanalysis techniques are not leveraged yet. Instead of condensing out the changes due to the presence of the crack, thus potentially working

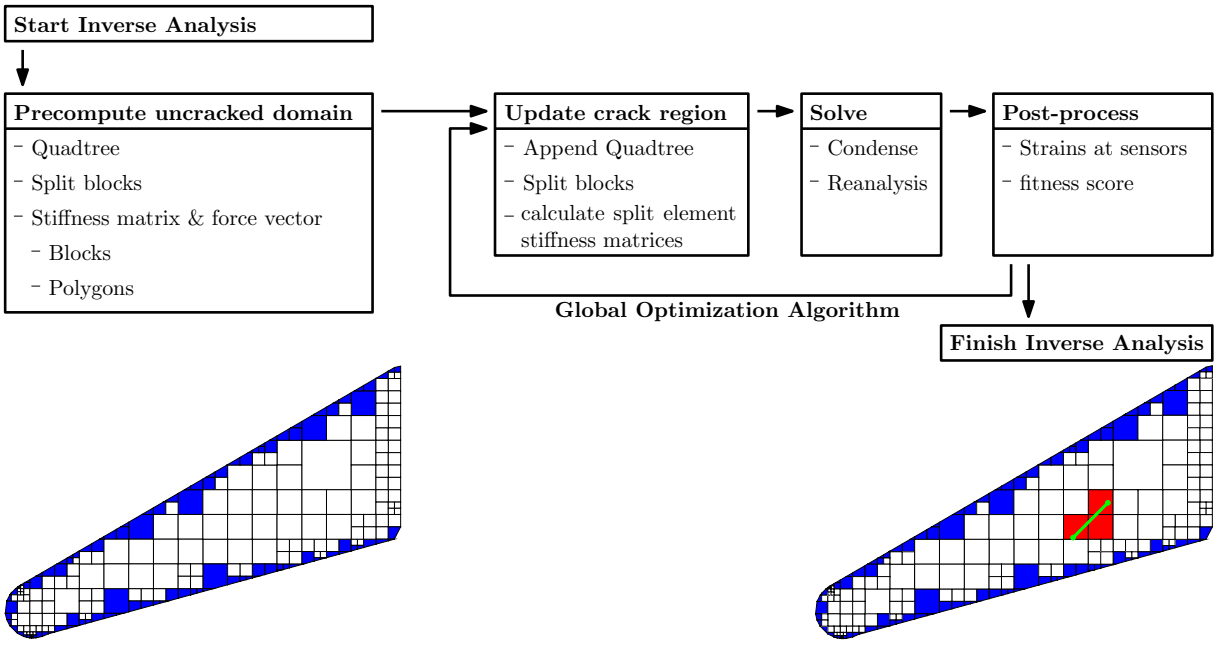

Fig. 6.1: Proposed accelerated damage localization scheme leveraging reanalysis. System comprising recomputed quantities on the right with split quadtree blocks in blue. System with region affected by crack in red and identified crack in green. For the proposed acceleration scheme only the DOF of the red blocks contribute to the overall computational effort.

with a small subdomain, the few pertinent positions of the precomputed sparse matrix assembly vectors are overwritten and appended where necessary. Hence, large portions of a conventional FEM analysis are omitted. However, the full system must still be assembled, have the appropriate boundary conditions applied to it and then be solved.

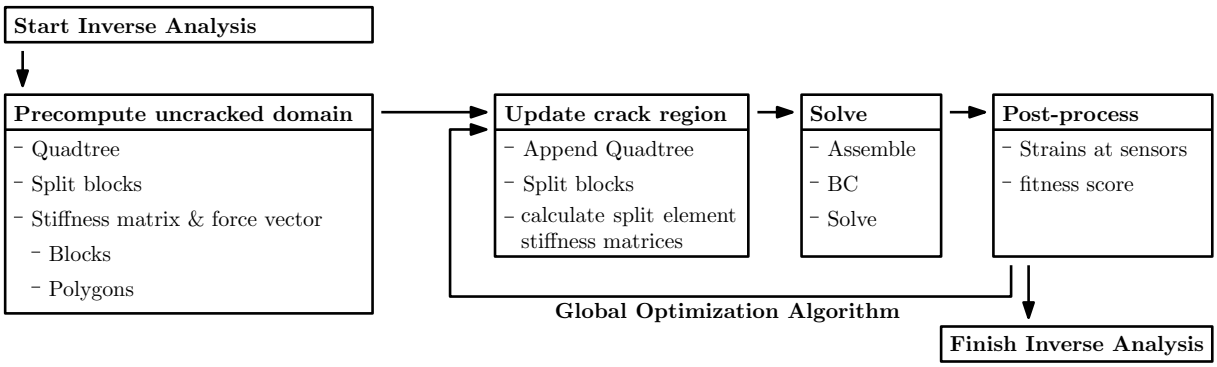

Fig. 6.2: Intermediate acceleration scheme referenced in sec. 6.2 for comparison purposes.

6.2 Numerical Examples

Unless otherwise mentioned (as in sec. 6.2.4), the "measured system response" stems from a fine mesh reference solution obtained by the commercial Software Abaqus, with the intent of avoiding the so-called inverse crime. However, in practice this is increasingly difficult, due to the high convergence rates associated with SBFEM on adaptive QT meshes: The norm, calculated by Matlab's built-in `norm` function, for example, considering the difference in strains between the fine mesh reference solution (Fig. 6.3a) and an SBFEM solution employing QT meshes (Fig. 6.3b), differs only by $||\{\epsilon^{(m)}\} - \{\epsilon^{(h)}\}|| = 0.009859$. This calculation is based on the 16 sensors (Fig. 6.3, red), each containing three strain components.

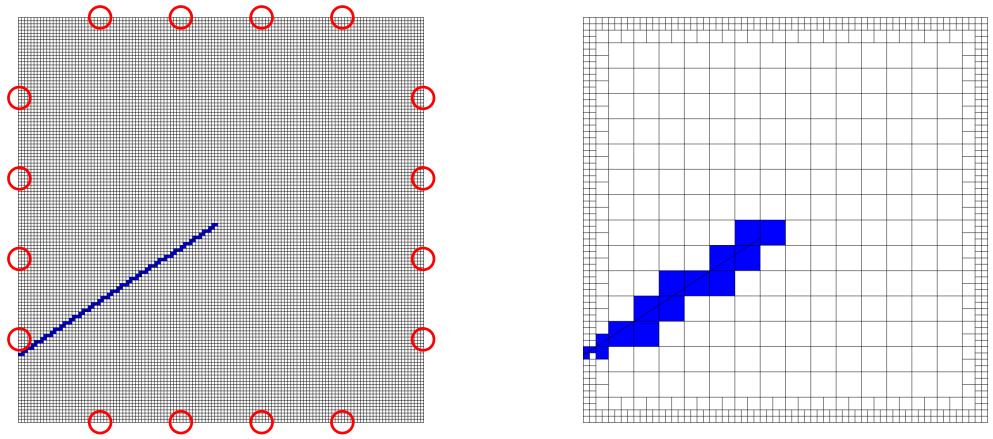

(a) (b)

Fig. 6.3: Example of reference and QT mesh. Sensor locations depicted in red. Elements affected by treatment of edge crack highlighted in blue.

6.2.1 Edge Crack in Square Plate

This first numerical example considers the detection of an edge crack in a square plate. To this end, the star-convex domain can be represented by one SBFEM subdomain, facilitating the algorithmic implementation. The Young's modulus E, Poisson ration ν and side length L are given as 200 [N/mm^2], 0.3 and 1 [mm] respectively. The crack length a, crack angle α, the number of sensors per edge and the loading conditions are considered as analysis parameters and treated in separate cases. GA is chosen as the optimizer and the fitness function considers displacements, i.e., $f(\theta) = ||\{u^m\} - \{u^h\}||/||\{u^m\}||$. The base of the square plate is clamped, while the top edge is subjected to loading. For this example the GA population type is specified as a bitstring, in which the design variables can only take on the discrete values of 0 and 1. Hence portions of the vector of design variables are grouped and function as a basis for the discretization of the feasible search space. The location of the associated crack tips results from a mapping of the binary digits to corresponding discrete Cartesian coordinates.

To this end, lower and upper bounds do not need to be specified explicitly, but are enforced by the underlying mapping. For this numerical example, a bitstring containing 13 entries is employed, of which 7 discretize the region outside the square plate into a grid of 64x64 feasible crack tip locations (Fig. 6.4, orange), while the remaining 6 define a 32x32 grid inside the domain (Fig. 6.4, blue). The resulting crack line is then clipped at the boundary resulting in the effectively introduced edge crack (Fig. 6.4, green). Results are reported by the following measure of detectability, which considers the distance between imposed (m) and identified (h) crack tip locations:

$$D = \sqrt{(x_1^m - x_1^h)^2 + (y_1^m - y_1^h)^2 + (x_2^m - x_2^h)^2 + (y_2^m - y_2^h)^2} \tag{6.7}$$

where x and y refer to the Cartesian crack tip locations and the subscripts 1 and 2 denote the individual crack tips. It follows that lower detectability scores equate to improved identification.

6.2.1.1 Case 1: Varying Crack Angles

For this case, the detection of cracks angled at $\alpha = \{-30, 0, 30, 60, 90°\}$ is considered. To this end, two load cases are treated. In the first setup, the specimen is loaded purely in tension, while in the second setup two orthogonal loads are considered by the addition of a shear loading (Fig. 6.5). The detectability scores are provided in Fig. 6.6 for single and double load cases respectively. For each test, 15 individual runs were performed with the results reported as box-plots.

Using both loading conditions significantly improved detectability is observed for vertical cracks. Since for pure tension loads, any vertical crack will minimize the fitness function, the problem is severely ill-conditioned. The addition of a second, orthogonal load, i.e., the shear load, significantly improves upon the detectability, though 6/15 of the runs converge to a local minimum.

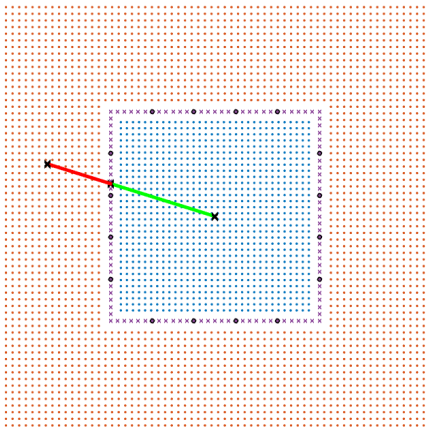

Fig. 6.4: Edge crack, case 1. Discretization of the domain into feasible crack tip locations by employing bitstrings. Points associated with the crack tip 1 in orange, crack tip 2 in blue and resulting edge crack in green.

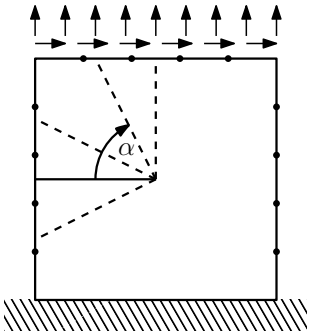

Fig. 6.5: Edge crack, case 1. Domain with investigated crack angles, loading and sensors per edge (black nodes).

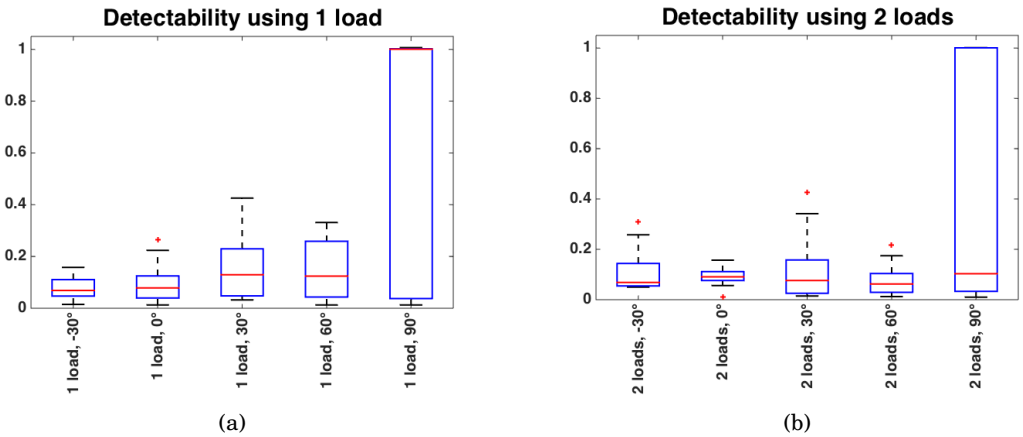

Fig. 6.6: Edge crack, case 1. Detectability scores for varying crack angles and load cases.

For the case of $\alpha = 0$, the outcome of 30 runs is plotted in Fig. 6.7a. While the crack tip location within the domain is well captured, the one outside is subject to large variability, bounded by the neighboring sensor locations. This becomes apparent when considering the associated response surface of the fitness function (Fig. 6.7b): Sharp transitions between plateaus are observed. While identification of the proper plateau is readily achieved, optimization within is not.

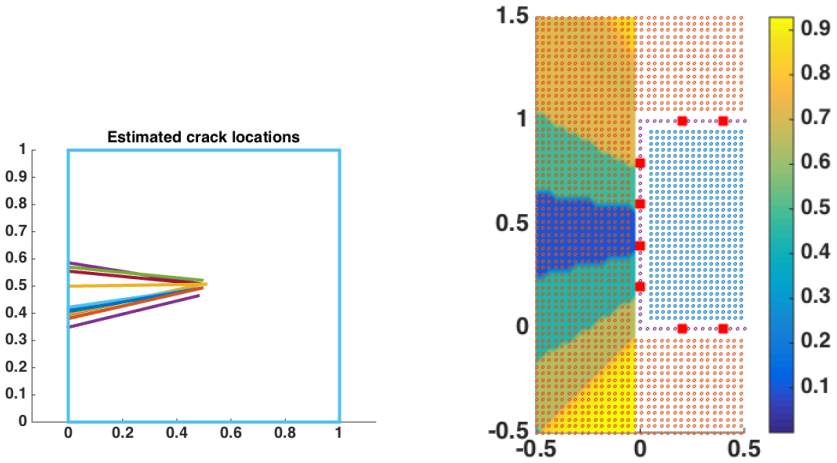

(a) (b)

Fig. 6.7: Edge crack, case 1. Effects of ill-posedness of the inverse problem on the accuracy of crack tip identification.

6.2.1.2 Case 2: Varying Amount of Sensors

In this case (Fig. 6.8), the effect of varying the amount of equally spaced sensors along with its influence on permitting the accurate detection of crack tips is studied. 15 runs are performed per test. Fig. 6.10 summarizes the detectability results, while Fig. 6.9 depicts the identified cracks. Although 200 generations and a population size of 50 seem sufficient to determine the crack tip locations using four or more sensors per edge, several non-converged results are observed when using 3 sensors per edge. In the case of 2 sensors per edge, the ill-posedness of the problem additionally suggests a strong local minimum. It is demonstrated that the amount of sensors plays a key role in the detection of damage. For the case of real-world structures, where sparse sensing networks are common, this imposes severe limitation.

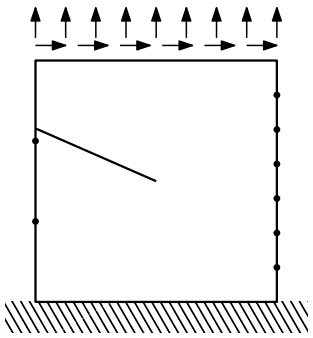

Fig. 6.8: Edge crack, case 2. Specimen geometry with imposed crack and sample sensor placement as black nodes.

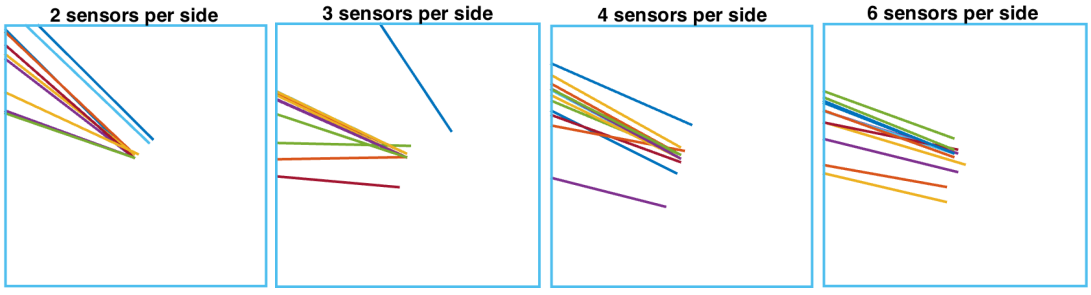

Fig. 6.9: Edge crack, case 2. Identified crack tip locations when employing a variable amount of sensors per edge.

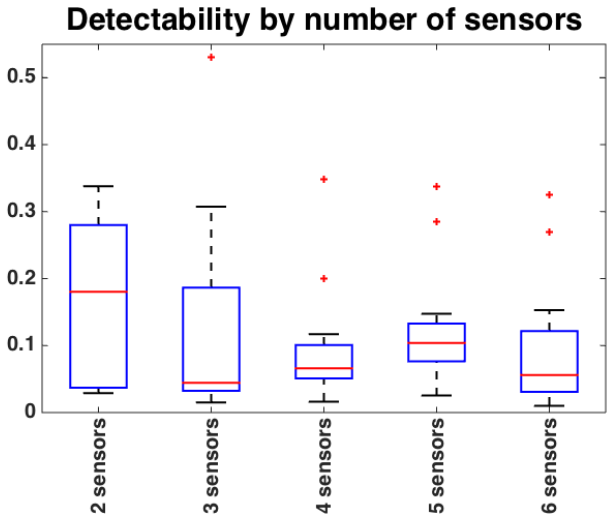

Fig. 6.10: Edge crack, case 2. Detectability score for variable amount of sensors.

6.2.1.3 Case 3: Varying Crack Length

In this case (Fig. 6.11), we study the effect of crack size on detectability. To this end, crack lengths with $a/L = \{0.33, 0.25, 0.2, 0.15, 0.1\}$ are studied. Crack lengths as small as a/L = 0.15 are accurately detected by the proposed scheme. However, due to the shallow characteristics of the response surface, the identified crack tips are scattered about the imposed crack. This is in part also attributed to the GA bitstring approach: The GA is exceptionally versatile in exploring a domain, at the expense of exploitability. Hence, it tends to identify depressions in the response surface, yet cannot efficiently determine its minimum. Although this may be alleviated by tuning the analysis parameters, a problem specific solution would be obtained. As is observed in Fig. 6.12b the use of four sensors per side admits outliers, i.e., unconverged runs, when specifying 200 generations. This is reflected in erroneous crack tip identifications. The use of a greater number of sensors per edge, e.g., six (Fig. 6.13) alleviates this issue and provides a tighter bound for the scattering of results.

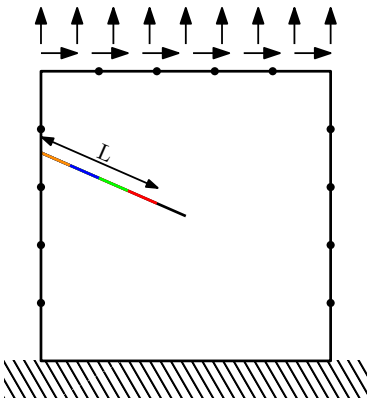

Fig. 6.11: Edge crack, case 3. Specimen geometry with imposed cracks of variable length.

6.2.2 Embedded Crack in Square Plate

This numerical example considers the detection of an embedded crack within a square plate. Such problems could be tackled with a similar approach to the one demonstrated in the first example, i.e., using two large subdomains, each containing one crack tip, to simulate the forward problem. Since this approach, however, breaks down in the presence of multiple flaws, the QT decomposition is employed for all remaining examples. The material properties and the domain description remain unchanged. Varying crack angles

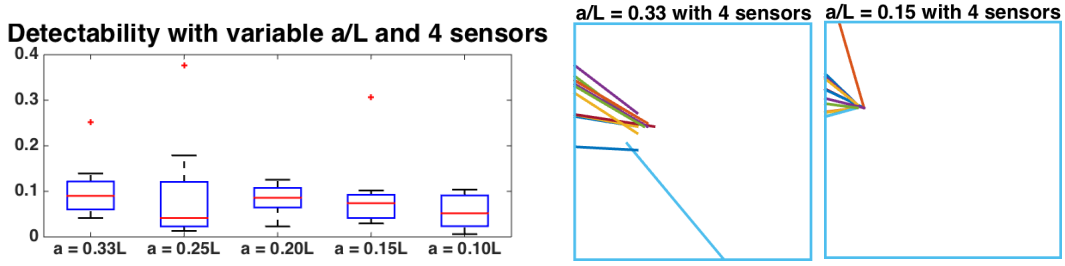

(a) (b)

Fig. 6.12: Edge crack, case 3. Detectability and resulting realizations for varying crack lengths and 4 sensors per edge.

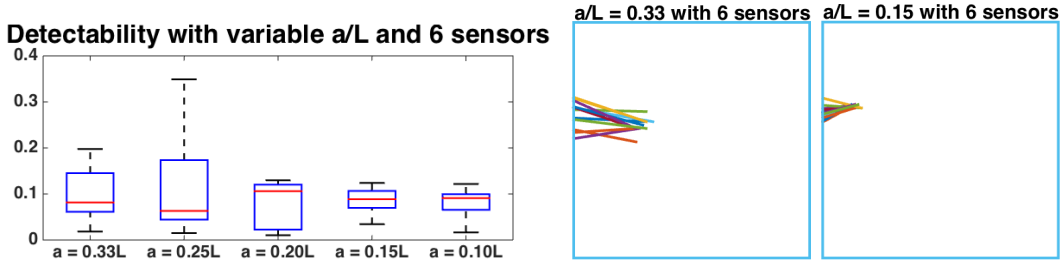

(a) (b)

Fig. 6.13: Edge crack, case 3. Detectability and resulting realizations for varying crack lengths and 6 sensors per edge.

α, crack length and number of sensors per edge are investigated. Four optimization algorithms are contrasted, GA, particle swarm optimization (PSO), covariance matrix adaptation evolution strategy (CMA-ES) and pattern search (PS). Further, the acceleration scheme proposed in sec. 6.1.4 is implemented and contrasted to the intermediate acceleration scheme (Fig. 6.2) and the conventional approach. The amount of design variables is limited to four continuous real numbers corresponding to the (x,y)-coordinates of the two crack tips. Their lower and upper bounds are chosen as [-0.05,1.05]. Initial analysis runs employing 1000 generations and 100 individuals per generation, where applicable, [1] indicated that 100 generations à 50 individuals are sufficient in order to arrive at converged results. The fitness function adopted for all following numerical examples is based on strains (Eq. 2.88), since the displacement-based response surface exhibited undesirable plateau characteristics, aggravating the ill-posedness of the inverse problem.

6.2.2.1 Case 1: Varying Crack Angles

This case study investigates the proposed scheme's ability to effectively identify cracks at varying orientations, as depicted in Fig. 6.14. The crack center is chosen slightly off-center with (x,y)-coordinates (0.6,0.6). Four sensors per edge are considered. 15 runs of each GA, PSO, CMA-ES and PS were performed and the detectability scores are summarized in Fig. 6.15. Both GA and PSO converge to within 1.5% of the imposed crack tip locations. However, both exhibit one run at crack angle $\alpha = 0$, i.e., the outlier, which converges towards a local minimum instead. Comparing to the previous numerical example implementing a displacement-based fitness function, the utilization of strain data results in tighter detectability bounds. The PS, however, suffers from convergence issues, often diverging towards a local minimum for crack angles of -30 and 0°, with outliers also present for crack angles of 60 and 90°. Convergence plots for $\alpha = -30°$ and a = 0.3 averaged over 15 runs are provided in Fig. 6.16a across iterations and Fig. 6.16b across function evaluations. The convergence issues of PS are apparent considering the values for the mean fitness function, where 4/15 runs diverge to a local minimum. The number of function evaluations required to reach a converged solution is directly proportional to the computational effort involved in an inverse analysis. Both GA and PSO, in their most basic form, require the specification of the amount of generations and

[1] This analysis performed with GA, traditionally the weakest of the methods compared, completed in just under 2 hours on a 4-core Intel Xeon E3-1225v3 @ 3.2 Ghz.

the associated population size. CMA-ES and PS contain inherent mechanisms to autonomously regulate the population size, thereby typically requiring fewer function evaluations. A representative analysis employing a conventional GA approach require 27 minutes, while the intermediate and proposed acceleration schemes conclude in 5.4 and 2.2 minutes respectively, manifesting a reduction in computational time by over an order of magnitude. Analyses by CMA-ES and PS typically complete at least twice as fast.

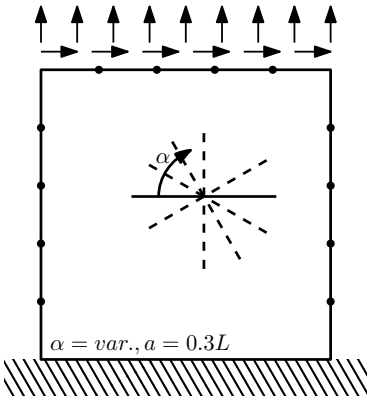

Fig. 6.14: Embedded crack, case 1. Specimen geometry with imposed crack at varying angles. Sensor placement at black nodes.

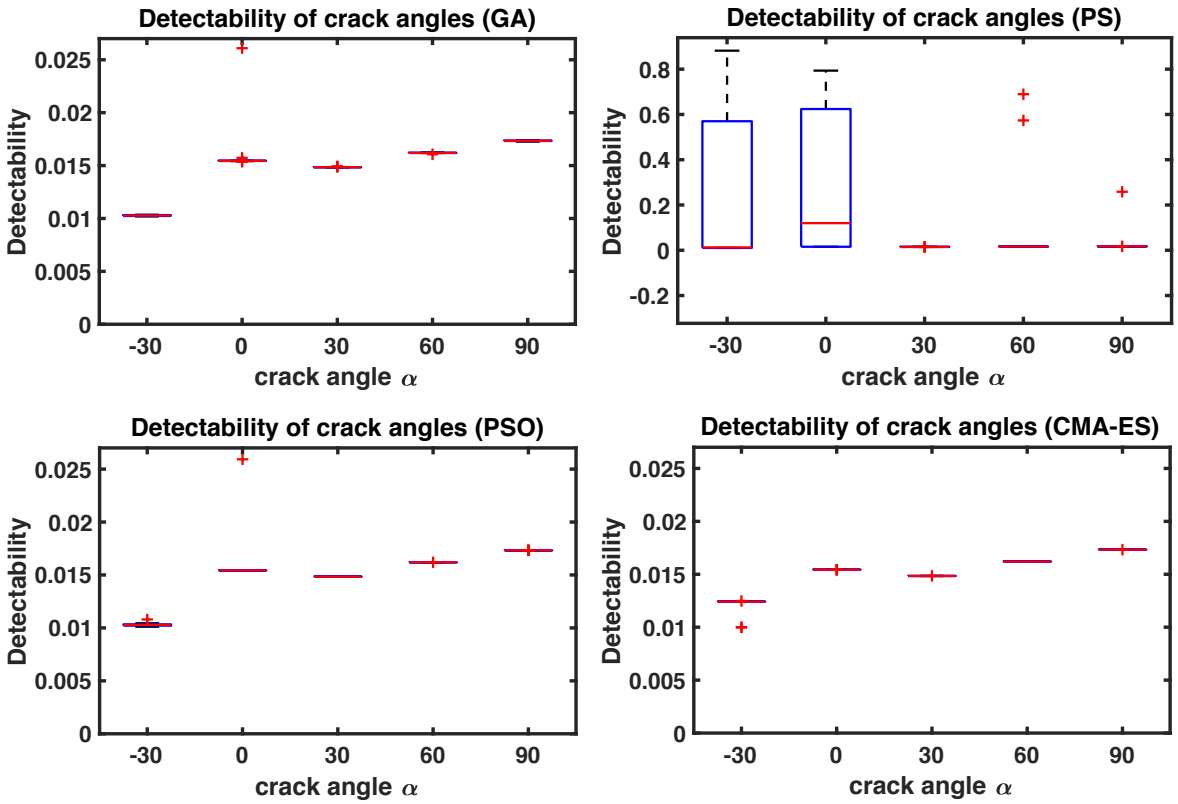

Fig. 6.15: Embedded crack, case 1. Detectability scores for global optimization algorithms across varying crack angles.

6.2.2.2 Case 2: Varying Crack Lengths

In this case study (Fig. 6.17), the proposed scheme's ability to localize cracks of varying lengths is investigated, with $a/L = \{0.5, 0.3, 0.2, 0.15, 0.1\}$. Four sensors per edge are considered. The resulting detectability

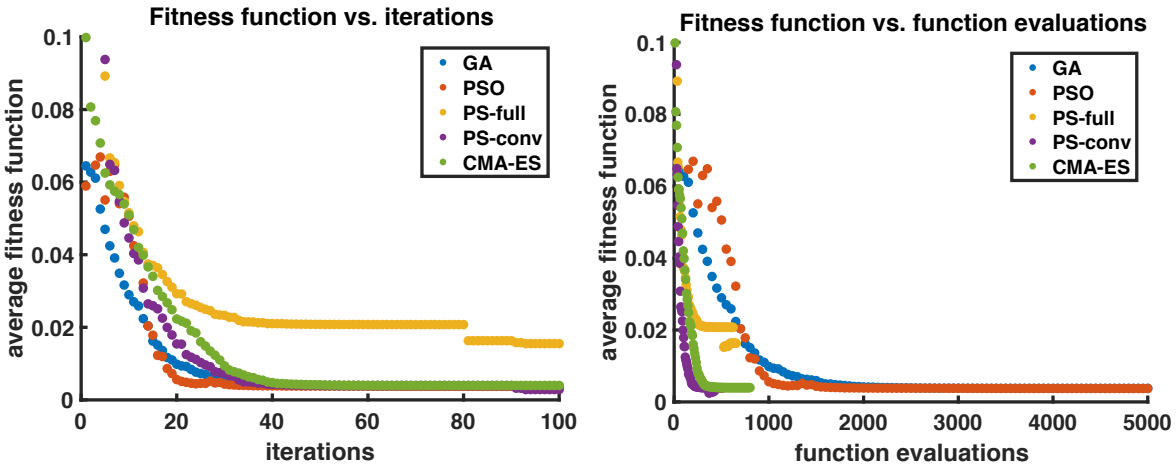

(a) (b)

Fig. 6.16: Embedded crack, case 1. Convergence plots for the global optimization schemes under consideration. In yellow the average of all PS-based runs. Purple only considers the converged subset.

scores are summarized in Fig. 6.18. Again GA, PSO and CMA-ES perform well and manage to accurately localize crack of various lengths. However, for crack lengths of 0.15 and 0.1, GA admits select outliers, which correspond to divergence towards local minima. Further, all methods demonstrate increased difficulty for the smallest imposed crack length. The mean crack localization by PS is of similar accuracy, however the frequent occurrence of diverging runs excludes its application to damage localization schemes. In Fig. 6.19 an outtake of the fitness function evolution vs. function evaluations is plotted for the case of a = 0.15. Therein, the rapid convergence of the CMA-ES is depicted as is evident by the slope of its curve. While GA admits a gradual convergence behavior, PSO tends to explore the entire domain in a first step (exploratory criterion) and then proceed with rapid convergence (exploitative criterion). In order to justify the use of global optimization algorithms over gradient based methods, a proxy fitness function response surface is plotted in Fig. 6.20. It is obtained by keeping one crack tip constant and varying the second across a grid. The resulting response surface is of a multi-nodal nature with areas of high boundary noise: Although the depression of the global minimum occupies a significant portion of the domain, the presence of select local minima warrant the adoption of global optimization methods.

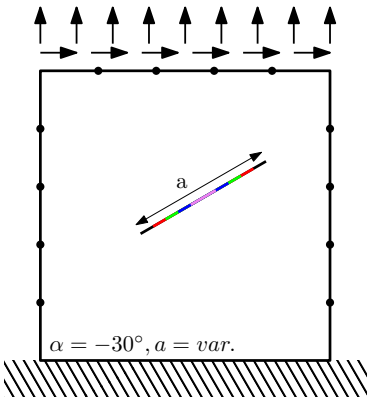

Fig. 6.17: Embedded crack, case 2. Specimen geometry with imposed crack of varying length. Sensor placement at black nodes.

6.2.2.3 Case 3: Varying Amount of Sensors

In this last case, the effect of the amount of sensors present during analysis is revisited. For the domain with geometry depicted in Fig. 6.21, between two to seven sensors per edge are considered. The detectabil-

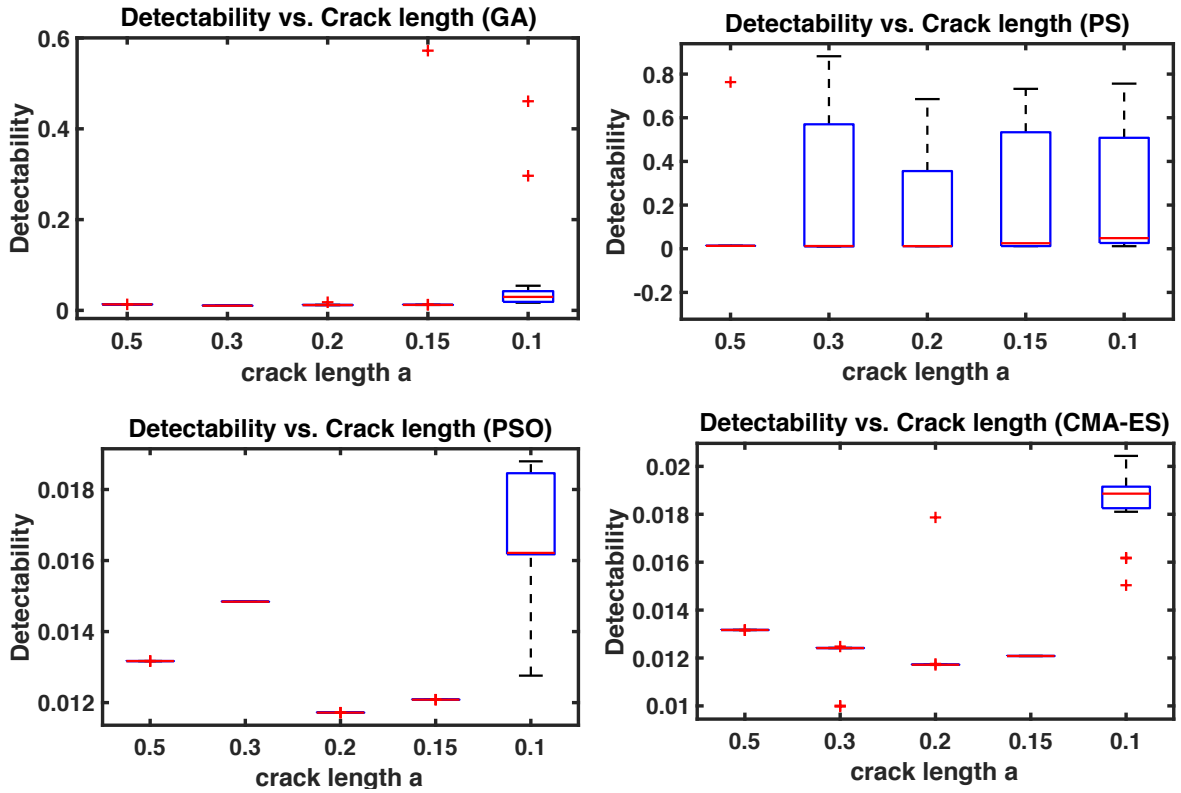

Fig. 6.18: Embedded crack, case 2. Detectability scores for global optimization algorithms across varying crack angles.

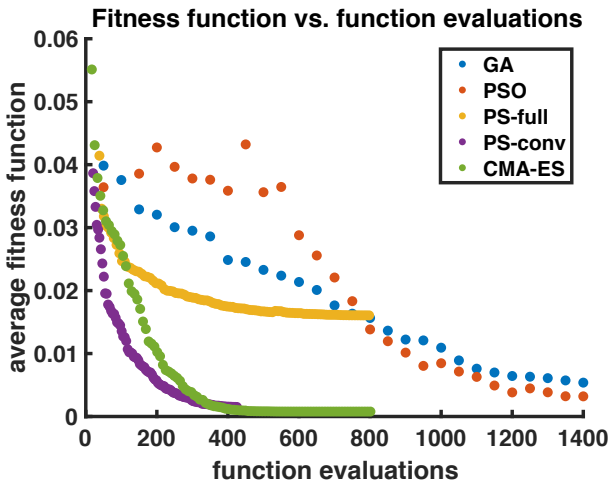

Fig. 6.19: Embedded crack, case 2. Convergence plots for the global optimization schemes under consideration. In yellow the average of all PS-based runs. Purple only considers the converged subset.

ity scores across 15 runs are given in Fig. 6.22. The PSO achieves best detection rates, whereas the GA admits outliers when only two or three sensors are present. PS does not converge reliably, mirroring the outcome of previous tests. CMA-ES manages to replicate the excellent detectability score of the PSO, however, it exhibits difficulty to converge towards a consistent result when only two sensors are present per side. This is mainly attributed to the difference in amount of function evaluations: While PSO obtains domain information though 5000 function evaluations, CMA-ES only relies on slightly over 800.

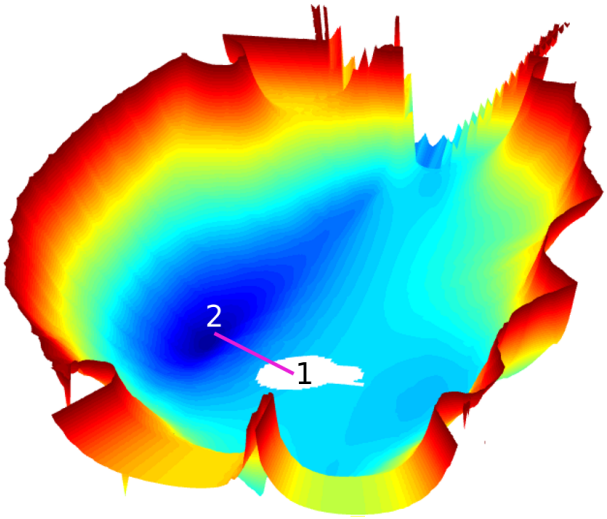

Fig. 6.20: Embedded crack, case 2. Response surface of the fitness function, given the impose crack in pink. The location of crack tip 1 is held constant, while for crack tip 2 it is variable.

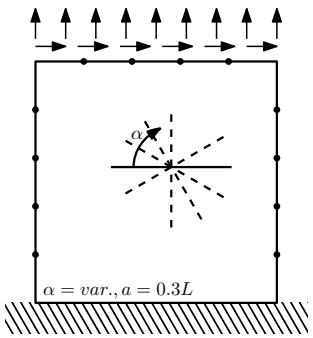

Fig. 6.21: Embedded crack, case 3. Specimen geometry with imposed crack and variable amount of sensors.

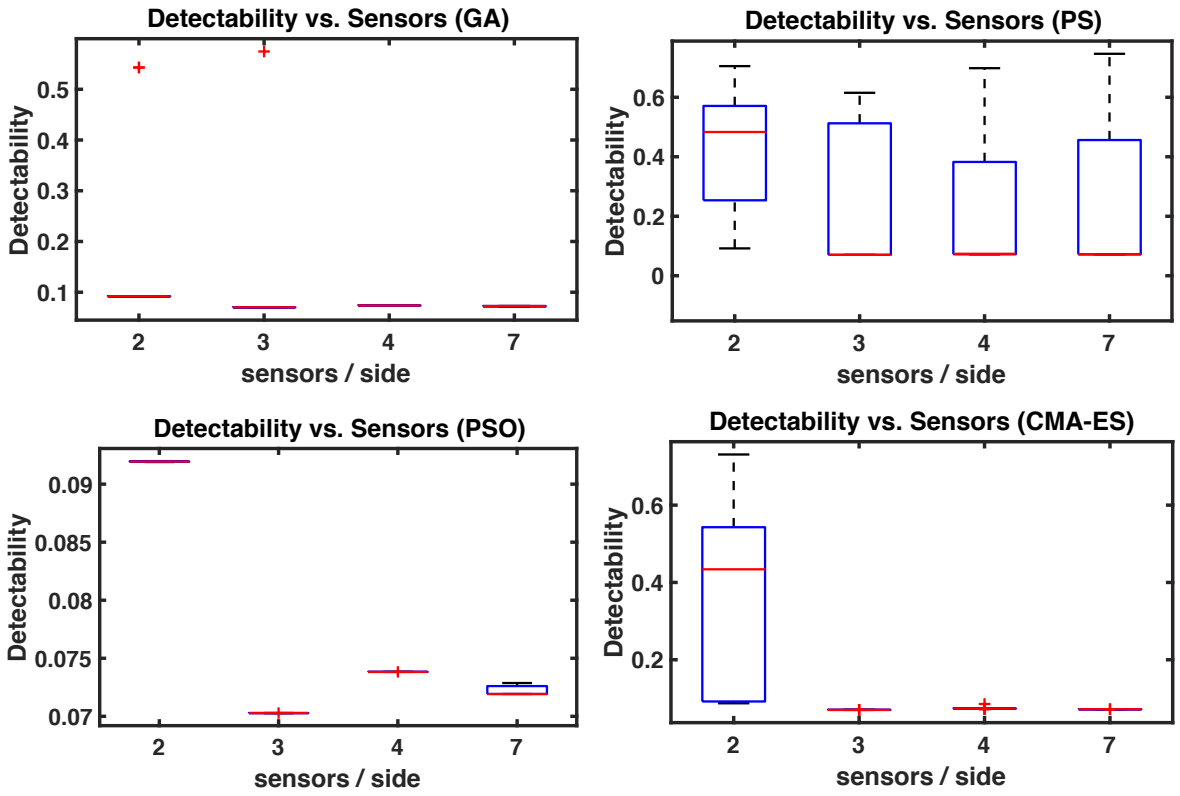

Fig. 6.22: Embedded crack, case 3. Detectability scores for global optimization algorithms across varying crack angles.

6.2.3 Multiple Inclusions in Square Plate

In this numerical example, the detection of multiple inclusions in a square plate is investigated (Fig. 6.23). The identical material parameters and geometric description of the domain from the previous two numerical examples is adopted.

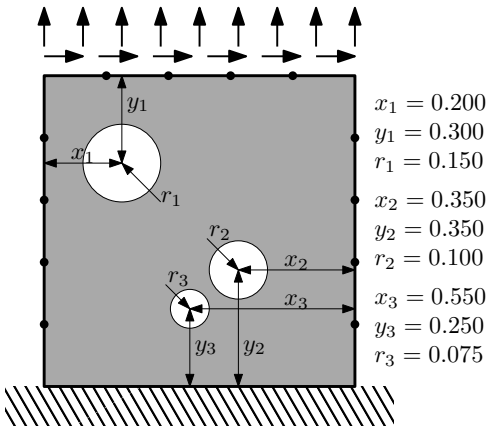

Fig. 6.23: Multiple inclusions. Specimen geometry with imposed inclusions.

The inclusions are incorporated by assigning a secondary material with Young's modulus three orders of magnitude smaller than its surroundings. Four sensors are utilized per edge. Only circular inclusions are considered, each described by three design parameters, i.e., the (x,y)-coordinates of its center and radius. Up to three inclusions are treated, each associated with a topological variable, which governs its de-/activation. Hence a total of 12 real, continuous design variables is considered. The design variables associated with the inclusion's center are prescribed an upper and lower bounds within the domain, while the inclusion's radius r is constrained to $0.05L \leq r \leq 0.6L$. Within the span [0,1], topological variables are seen to deactivate an inclusion for realizations less then 0.5. Only GA and PSO are considered. Fig. 6.24 depicts the best candidate solution after a given number of generations.

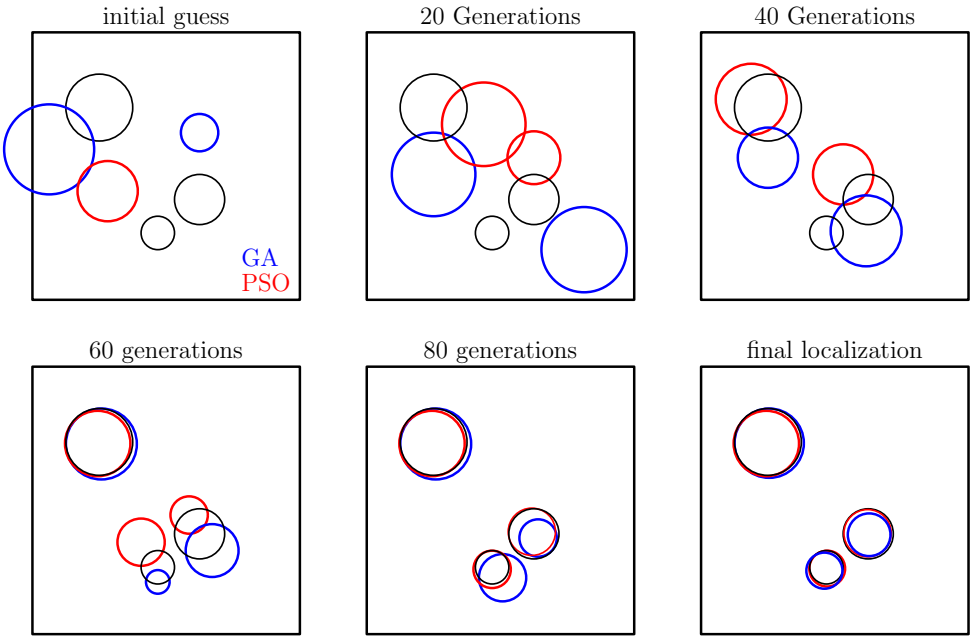

Fig. 6.24: Multiple inclusions. Evolution of the best candidate solution for the identified inclusions across generations for GA (blue) and PSO (red). The impose inclusions are in black.

Tbl. 6.1 lists the associated output data for the final identification for both the GA and PSO. In Fig. 6.25,

the convergence behavior of the GA and PSO is illustrated. Both optimizers manage to accurately capture all three inclusions accurately. The candidate inclusions predicted by the PSO are slightly closer to those imposed. At times the GA struggles to identify all inclusions and can return a local minimum, where the cluster of two small inclusions is replaced by a single, large one, as depicted in Fig. 6.26.

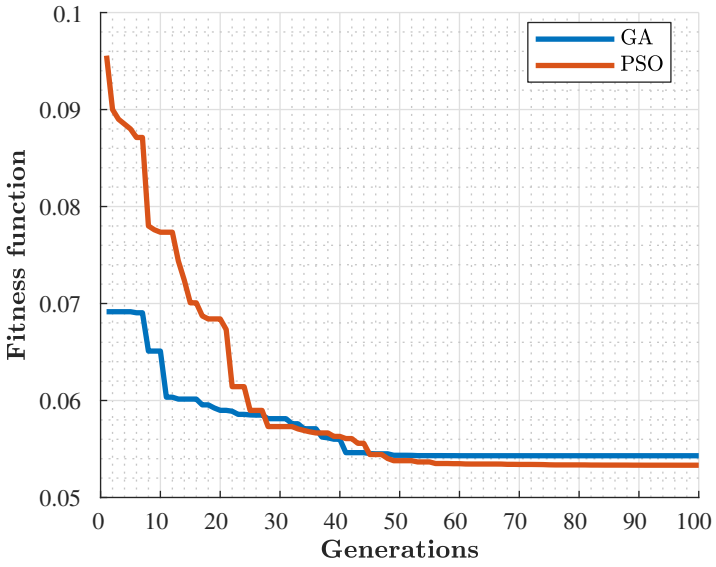

Fig. 6.25: Multiple inclusions. Convergence of the GA and PSO across generations.

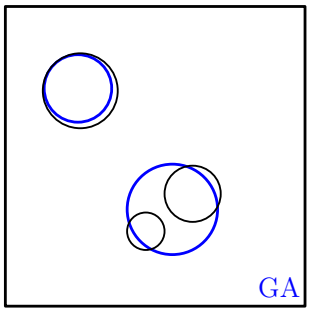

Fig. 6.26: Multiple inclusions. Example of divergence towards a local minima.

Tbl. 6.1: Multiple inclusions. Imposed and identified values describing the crack geometry.

Parameter	**Imposed**	**PSO**	**GA**
x_1	0.200	0.198	0.204
y_1	0.300	0.304	0.308
r_1	0.150	0.137	0.156
x_2	0.350	0.355	0.341
y_2	0.350	0.352	0.338
r_2	0.100	0.097	0.082
x_3	0.550	0.542	0.561
y_3	0.250	0.243	0.237
r_3	0.075	0.081	0.088

6.2.4 Embedded Crack in Rectangular Plate Employing Real-world Strain Measurements

In this numerical example, the proposed damage localization scheme is applied to real-world measurement data. The setup proposed and detailed in [66] is adopted (Fig. 6.27). The measured vertical and horizontal strain components are plotted against simulation results obtained by SBFEM (Fig. 6.28). While the overall response is captured, several sensors display readings, which do not match the numerical simulations well (both components of sensor 7 and one component of sensor 4). These components are disregarded and do not contribute to the fitness function. In [66], additional calibration of the model was performed after conducting the baseline strain reading to achieve a satisfactory fit between numerical prediction and measurement. This is omitted here with the intent of incorporating noise into the simulation. To permit a fair comparison, a GA optimizer is employed across 250 generations with population size 7. The upper and lower bounds imposed on the design variables are [1-11] inches for the x-component of the crack tips x_1 and x_2 as well as [1-23] inches for the y-component of the crack tips y_1 and y_2. The uncertainty in the measurement data manifests as a shift in global minimum of the response surface. A representative run is illustrated in Fig. 6.29. Although the general crack tip region is identified the precise location cannot. Tbl. 6.2 summarizes this finding.

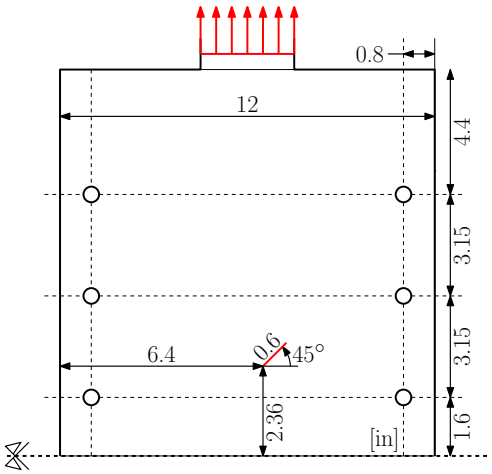

Fig. 6.27: Rectangular plate. Plate geometry, loading and sensor placement. Imposed crack in red.

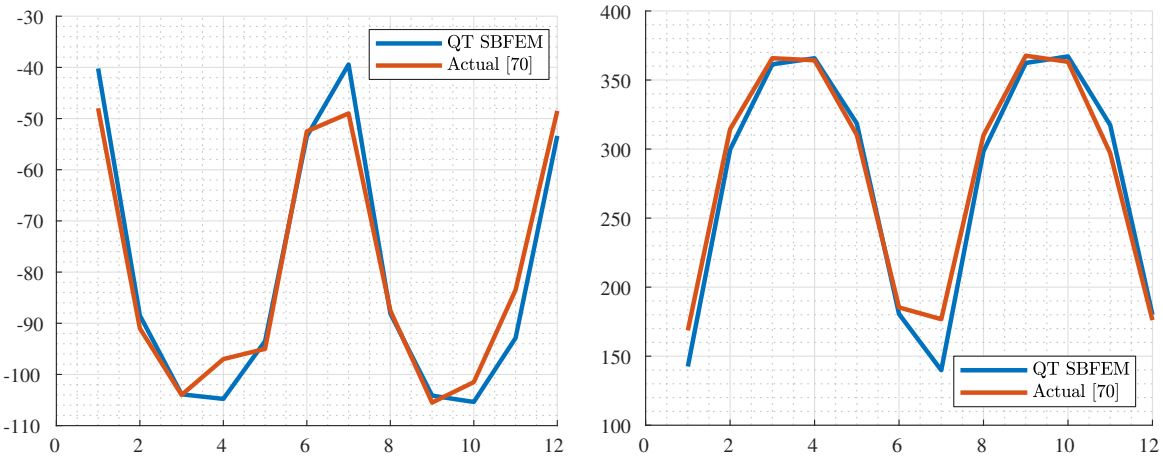

(a) Horizontal strain component.

(b) Vertical strain component.

Fig. 6.28: Rectangular plate. Comparison of measured and simulated strain for both horizontal and vertical directions.

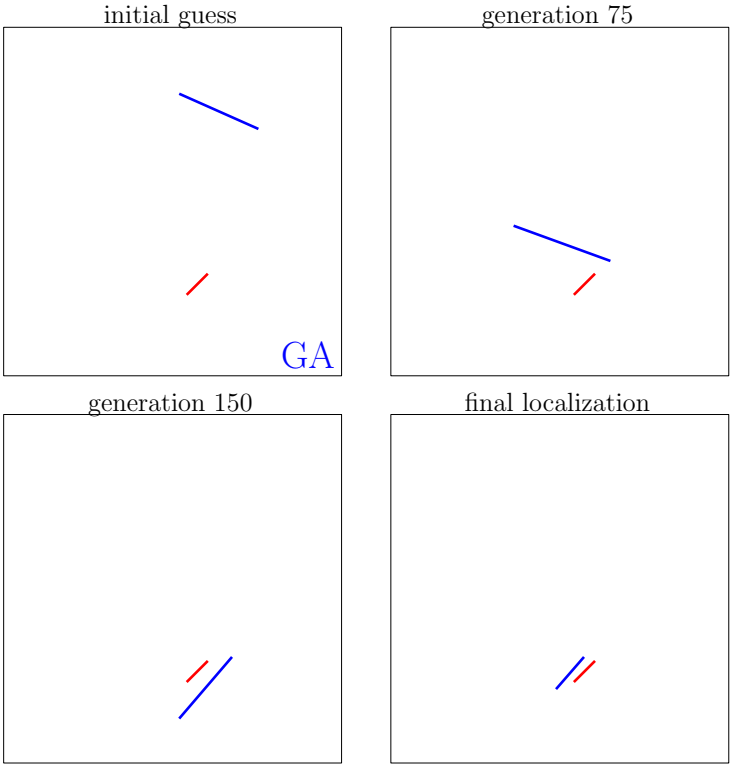

Fig. 6.29: Rectangular plate. Evolution of the best candidate solution for the identified crack across generations. Imposed crack in red, candidate crack in blue. One half of the domain is modeled.

Tbl. 6.2: Rectangular plate. Imposed [66] and identified values describing the crack geometry.

Parameter	**Imposed**	**Identified**
x_1	6.3976	5.92
y_1	14.6457	14.31
x_2	6.9882	6.76
y_2	14.6457	14.74

6.2.5 Embedded Crack in Wing

In this numerical example, the proposed damage localization scheme is extended to non-regular geometries. A wing-like structure with loading and boundary conditions as depicted in Fig. 6.30 is considered. The aim is to accurately localize one imposed crack. A reference solution is obtained from a high fidelity SBFEM analysis, with elements four times as fine as permitted in the inverse analysis. Sensors (Fig. 6.31, red) are placed about the perimeter and at specific QT nodes, known to exist across all simulation runs. Due to the non-regular geometry, specification of upper and lower bounds proves intricate for the design variables describing the candidate crack, i.e., the (x,y)-coordinates of the crack tips. Therefore, the bounds are specified spanning a unit square, combined with a mapping function that projects the design variables onto the wing span using conventional translation, rotation and stretch matrices. The CMA-ES is adopted for efficiency reasons. 100 generations are found to be sufficient in obtaining converged results. CMA-ES autonomously determines the amount of individuals required per generation. Fig. 6.32 depicts the evolution of the best candidate solution across function evaluations. In Tbl. 6.3 the identified values for the individual design variables are contrasted to the those imposed and the convergence graph of the fitness function is plotted in Fig. 6.33. The crack parameters are very well identified. This can be attributed to two factors: The use of an SBFEM-based reference solution and the increased amount of sensors available. Future studies should therefore include noise in simulation data in order to combat the former. The analysis comprises 801 function evaluations across 100 generations. The intermediate acceleration scheme

requires 186 seconds to complete, whereas the proposed acceleration scheme requires 114 seconds. In the process, the initial candidate crack, starts off as an and arbitrarily oriented edge crack and after several function evaluations aligns itself with the imposed crack direction. After a period of predominant translatory movement towards the imposed crack, the candidate crack's length estimate is refined. In a final phase, small adjustments to the design variables fine tune the identified crack parameters, although after approximately 400 function evaluations the crack is localized to sufficient accuracy for subsequent SHM applications.

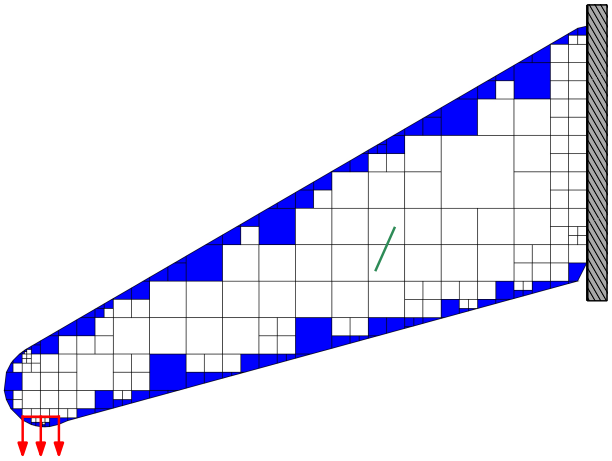

Fig. 6.30: Cracked wing. Specimen geometry with imposed crack (green), clamped boundary conditions on right edge and loading at wing tip.

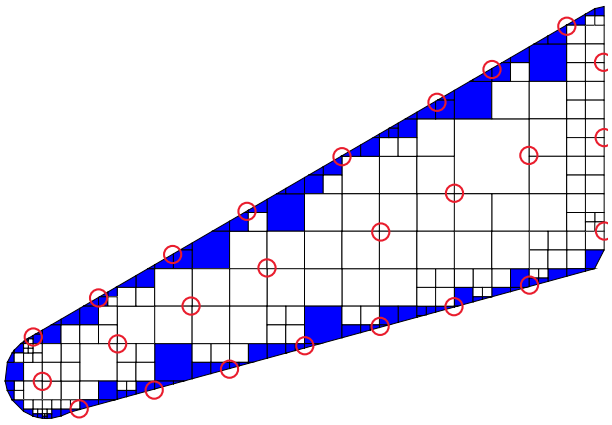

Fig. 6.31: Cracked wing. Sensor locations on wing boundary and within domain encircled in red.

Tbl. 6.3: Airplane wing. Imposed and identified values describing the crack geometry.

Parameter	**Imposed**	**Identified**
x_1	0.600	0.591
y_1	0.475	0.484
x_2	0.635	0.636
y_2	0.545	0.542

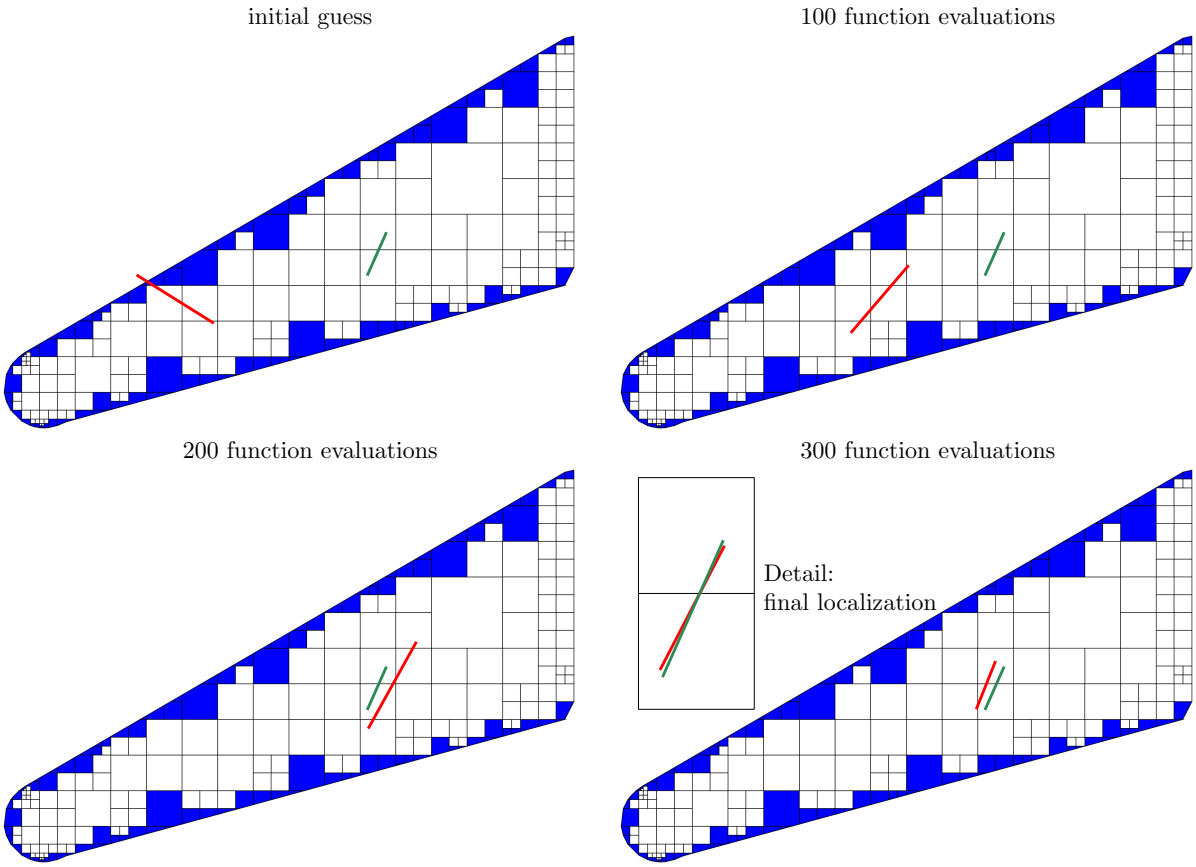

Fig. 6.32: Cracked wing. Evolution of the best candidate solution (red) for the identified crack across function evaluations. The impose crack is in green.

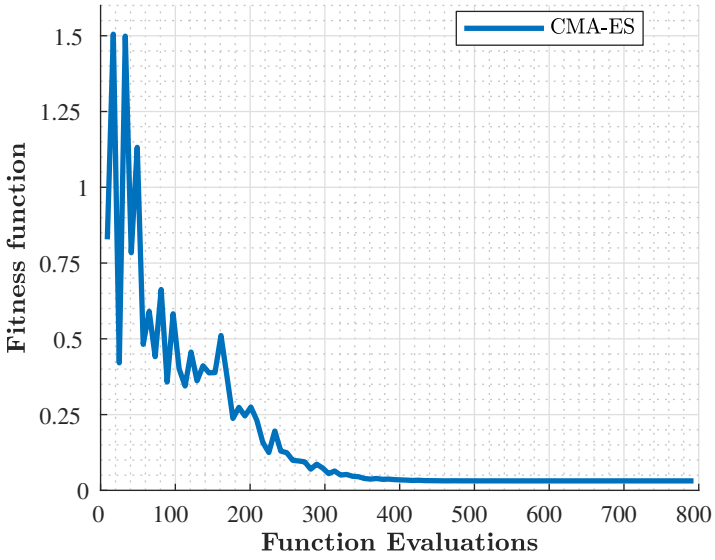

Fig. 6.33: Cracked wing. Convergence of the CMA-ES across function evaluations.

6.3 Conclusions

A methodology for localizing damage in 2D structures by fusion of SBFEM with global optimization algorithms is presented. Several numerical examples demonstrate its capability to detect the location of a crack

and multiple inclusions present in a domain, even when the geometry is non-regular. Further, sensing data extracted from real-world tests was successfully employed to accurately determine a crack's location within a metal plate. Moreover, parallel programming techniques combined with precomputation and reanalysis are exploited to accelerate conventional damage localization schemes by close to an order of magnitude for the presented numerical examples, enabling near real-time analyses.

However, in select instances, the detected cracks are physically meaningless due to insufficient loading case orthogonality, symmetry issues and crack overclosure. The latter two are closely related and can be effectively combated by enforcing contact during the forward solution phase; a direction of investigation for future work. A multitude of sensors are required to dampen the ill-posed nature of the inverse problem, though the application of strain gauges to structures is laborious, error-prone and for complex geometries often unfeasible. Hence the adoption of emerging sensor technologies utilizing piezoelectric materials, fiber optics and contactless imaging techniques, e.g, digital image correlation (DIC), should be explored. Due to the expedience of the proposed scheme, future studies towards optimal sensor placement constitute an interesting application within the framework of SHM.

7 Topology Optimization

With this contribution, we aim at accelerating TO by recasting the forward problem into a form that directly interacts with the structural solver: The polytope nature of SBFEM elements is exploited on quad-/octree meshes to alleviate issues associated with hanging nodes. Furthermore, a balancing operation applied to the mesh results in a manageable number of precomputable element configurations, which significantly accelerates the forward analysis. The analysis mesh for each optimization iteration is obtained via automated image-based decomposition of the design variables.

A number of benefits arise from this combination of methods. The ease with which higher-order elements may be incorporated, coupled with the use of unstructured meshes, combats the formation of checker-boarding [44]. Second, computational effort only arises where required by the problem definition, since adaptivity is automatically provided. Third, numerical examples in both 2D and 3D indicate that the amount of degrees of freedom present during analysis is reduced by more than an order or magnitude.

This work is motivated by the adoption of numerical methods capable of treating polytope-elements to alleviate issues commonly associated with hanging nodes. The proposed scheme is suited for fusion with, but not limited to, the boundary element method [177], polygonal finite element method [316], conforming shape functions [123] or virtual element method [36]. Here, we employ the SBFEM [294], a semi-analytical numerical method that permits the treatment of star-convex hp-polytopes. Although a mixed SBFEM has been employed for solving TO problems of incompressible materials [168], it follows the conventional fine-grid approach to TO and limits its treatment to linear elements and 2D applications.

The SBFEM has proven itself as a remarkably versatile tool in automatic image-based stress analysis [276, 187]. Such hierarchical meshes arising from tree-like image decompositions drastically reduce the amount of DOFs present, which accelerates the solution of the forward problem by alleviating computational effort and memory requirements. Image decomposition techniques, within the context of TO, produce fewer DOFs when material transition zones are eliminated. Hence, the BESO [138], SERA [21], SIMP combined with grayscale filters [20, 175] and level-set methods [244], for example, represent suitable algorithms. Since image decomposition operates on the design variables to produce analysis-ready meshes at each iteration, this family of techniques only requires interchanging the solver of the forward problem. Hence, incorporation into existing code bases requires minimal modification. Furthermore, as tree-like image decomposition techniques [47] utilize the uniformity of an element as a criterion for subdivision, multi-material TO [275] may be incorporated through extension to color-aware tree-like decompositions [161].

Subsequently, the proposed scheme is introduced in detail. Its novelty is i) the fusion of TO with automated image segmenting schemes, ii) the use of polytope-elements constructed by SBFEM to alleviate issues associated with hanging nodes, iii) color-encoding of domain and analysis parameters into the input images and iv) the extension to SBFEM-powered 3D TO. To this end, the SBFEM in 3D elastostatics is briefly treated. Based on three numerical examples, the proposed scheme is then verified, showcased and discussed.

7.1 Proposed Scheme

The proposed scheme primarily entails a drop-in replacement for calculating the displacement field. By exploiting hierarchical image decomposition techniques, regions with homogeneous material properties are identified and represented by a single element, such that coarser, adaptive meshes result with significantly fewer DOFs than with conventional grid approaches. Although remeshing is required for each iteration, the implemented decomposition techniques are economical and the resulting computational toll is easily recuperated by solving a forward problem with significantly fewer DOFs, even on modestly sized example domains. The steps differ slightly between 2D and 3D, since in 3D the precomputation procedure employed

for 2D would result in 4096 unique element realizations, whose construction requires building a substantial library and accompanying algorithmic logic. Instead, the unique element realizations for each 3D mesh are determined, which are computed once and subsequently cloned for the remaining mesh. Empirically, only a fraction of possible element realizations exist simultaneously on a mesh.

The proposed scheme comprises the following steps:

1. **Precompute**
   For the 2D case, the 16 possible element realizations are precomputed with Young's modulus equal to one.
2. **Initialize and begin TO loop**
   Only the filter must be prepared. Conversely to conventional approaches, remeshing at each iteration is required, rendering the preparation of sparse stiffness matrix assembly vectors [20] obsolete.
3. **Calculate displacement field**
   The grid of design variables is fed as a gray-scale image to the decomposition algorithm, which outputs an analysis-ready hierarchical mesh. Color-encoded regions are automatically recognized and resolved. Their inscribed operations are then applied. Once the stiffness properties of each element are identified, the displacement field is calculated analogous to the conventional FEM.
4. **Determine compliance**
   The compliance at each iteration is calculated as the product of the system displacement field and the force vector.
5. **Determine sensitivities**
   The sensitivities of the design variables are evaluated element-wise, by iterating over each subdomain. Since the subdomains are of variable size, the calculated sensitivities must be normalized per unit volume.
6. **Filter sensitivities**
   Standard mesh-independency filtering techniques may be applied as necessary.
7. **Design variable pro-/demotion**
   Solving the optimization problem, for example by OC approach, identifies, which design variables to promote or demote, i.e., assign or subtract material. While B/ESO, SERA and level-set approaches result in black-and-white outputs, SIMP-based approaches introduce intermediate material distributions. This is rectified by either employing a Heavyside projection [20] or a gray-scale filter [175, 284]. The updated design variables form the input for the subsequent iteration.
8. **Export of results**
   Upon completing the analysis, the hierarchical mesh is thresholded to yield the optimized system geometry. Simple methods permit exporting the hierarchical mesh to stereolithography (STL) format for subsequent additive manufacturing.

In order to further accelerate the analysis procedure, which is constrained by the solution of the forward problem, so-called hard-kill variants have been proposed. These differ from standard soft-kill approaches in how they treat void elements: Soft-kill approaches assign a very small stiffness, typically 10^{-9}, which impacts the conditioning of the numerical problem, while hard-kill approaches disregard such elements entirely. Not all problems, however, are amenable to this approach, since multiple independent substructures potentially arise during analysis, leading to numerical instabilities.

7.2 Numerical Examples

Three numerical examples are examined in this paper:

1. A thick cantilever subject to a point load at mid-height.
2. An L-shaped bracket with prescribed material distributions and multiple load cases.
3. The 3D wheel.

The first example verifies the proposed method, while the second showcases the extended capabilities, by color-encoding system and analysis information directly into the input image. Having thoroughly discussed the 2D behaviour, we extend the analysis to the 3D wheel problem. For each of the numerical examples, we couple the proposed method with a different TO variant, e.g., B/ESO, SERA and SIMP. One could have equally chosen to employ a level-set based method as an alternative to the ones listed prior.

7.2.1 Thick Cantilever

A thick cantilever subject to a point load at mid-height (Fig. 7.1) is considered. The width and height are discretized by 512 and 256 pixels respectively. The prescribed volume fraction f is chosen as 0.4. The penalty exponent of both SIMP and BESO approaches is equal to 3. Following [20], a filter utilizing Matlab's built-in `conv2` function is implemented with a radius of 16 pixels. For the BESO, the evolutionary volume ratio parameter is set to 0.1. Elements arising during quadtree decompositon are limited in size to ≤ 32 pixels. For the first iteration the discretization of the conventional grid is adopted. This is necessary, since the initial homogeneous material distribution would lead to a too coarse discretization, biasing the calculated sensitivities.

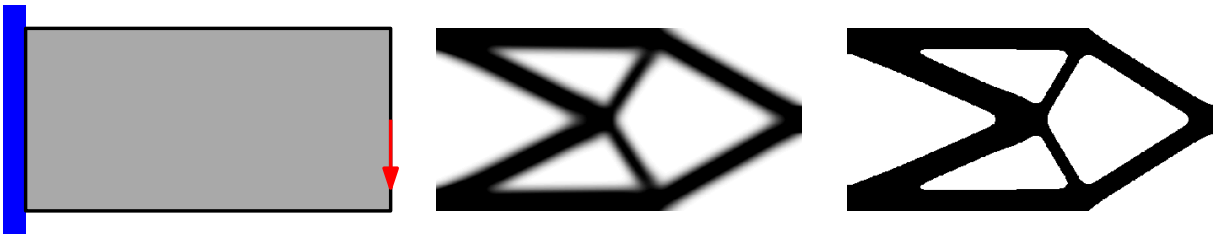

Fig. 7.1: From left to right: Thick cantilever setup, SIMP reference solution and BESO baseline.

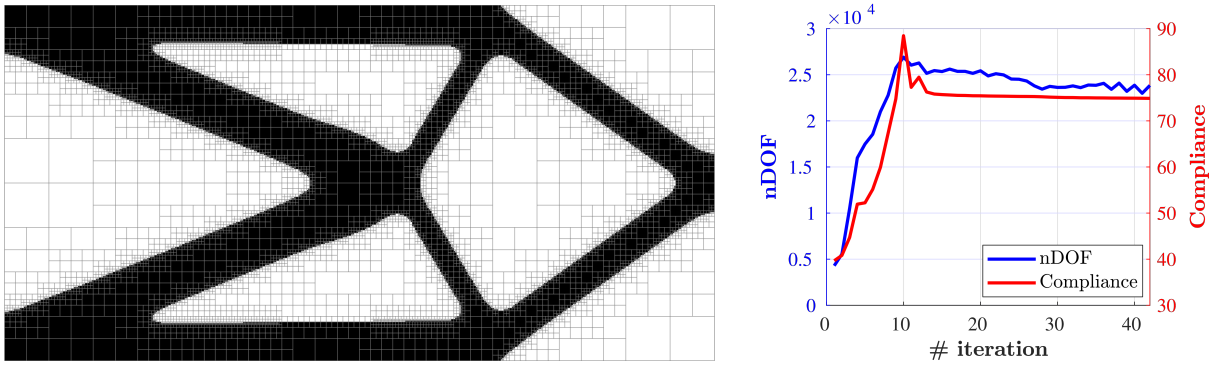

Fig. 7.2: BESO+QT optimized topology with evolution of DOFs and compliance across iterations.

In order to verify the proposed scheme, we investigate an elementary case: TO schemes, which result in black-and-white output, i.e., do not posses noticeable transitions in material distributions, permit the adaptive meshing algorithm to develop its full potential and minimize the DOFs required for analysis. Therefore, we contrast our scheme, which we term BESO+QT, to a BESO baseline [138]. Since, BESO follows a heuristic approach to TO, and it can therefore be mislead to local minima under certain circumstances [270], we first supply a SIMP reference solution [20]. Both the reference solution and the baseline depict the same resulting topology (Fig. 7.1). The BESO+QT (Fig. 7.2) is indistinguishable from the BESO baseline. The difference in compliance (Tab. 7.1) resulting from the SIMP and BESO approaches stems from the presence of transition material in the SIMP, leading to a slightly more flexible structure and therefore higher compliance. Given a higher value for the penalization parameter, this difference diminishes. The discrepancy in compliance between BESO and BESO+QT is attributed to the discretization: A coarse discretization results in a stiffer structure and therefore lower compliance. This is evident, since the amount of DOFs present during analysis is reduced by more than one order of magnitude. This in turn significantly alleviates the computational burden and associated memory requirements (Fig. 7.2, DOFs evolution). Employing higher order elements, e.g., quadratic or cubic elements, instead of conventional linear ones elevates the compliance to levels resembling the baseline BESO approach. Additional DOFs do not manifest during analysis, since these are condensed during the precomputation phase prior to analysis. The 1-2 additional iterations required to reach the stopping criterion, i.e., a 5% increase, represents a negligible difference to the base line case. In this contrived example, in which all three methods share a common implementation, differing only in the method of solving the forward problem, a glimpse of the com-

putational potential of the proposed scheme is possible: For this specific numerical example, an analysis concludes almost 5x faster, when employing the proposed scheme.

Tbl. 7.1: A comparison of results for SIMP reference solution, BESO baseline and proposed BESO+QT.

Method	**nIt.**	**Compliance**	**DOFs**	**time [s]**
SIMP	49	87.6	263'682	110
BESO	40	75.6	263'682	98
BESO+QT (linear elements)	42	74.8	23'846	20
BESO+QT (quadratic elements)	41	75.3	23'846	20
BESO+QT (cubic elements)	42	75.5	23'846	20

Further, behavior across problem sizes is investigated.

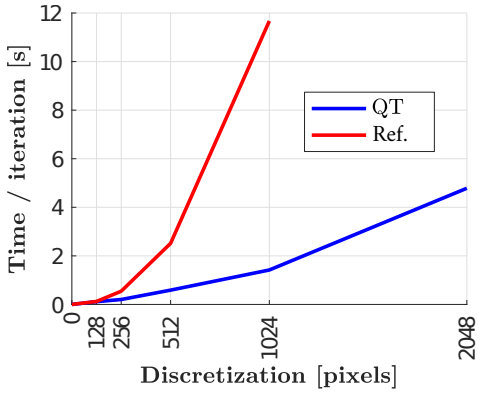

Fig. 7.3: Variant study of wall clock time spent per iteration at given discretization levels, comparing the convention BESO approach to the proposed BESO+QT.

Tbl. 7.2: Speedup in wall clock time compared to baseline BESO implementation at various discretization levels.

Discretization	**128**	**256**	**512**	**1024**
Speedup	1.08x	2.68x	4.27x	8.23x

Tbl. 7.3: Fraction of total wall clock time spent on key tasks.

Discretization	**256** [%]	**512** [%]	**1024** [%]	**2048** [%]
Initialize	0.44	0.11	0.32	0.99
SBFEM	60.52	61.59	55.21	31.38
Sensitivity	35.54	34.94	30.10	16.29
Filter	0.58	2.34	12.17	49.27
Update	0.64	0.80	1.97	1.93

Table 7.2 and Fig. 7.3 demonstrate that the proposed method manifest larger speedups as the discretization level is increased. The results reported are obtained after having invoke Matlab's `clear all` command and therefore do not take fully advantage of just-in-time compilation. Further, a shift in bottleneck from simulation to filtering is observed, when increasing the discretization level (Table 7.3). Hence, it would be worthwhile to investigate alternate filtering methods than Matlab's built-in `conv2` function. Considering the preliminary, unoptimized nature of the implementation, greater speedups are expected

in the future, when the implementation of the proposed method adopts vectorization, which is currently pervasive to the baseline implementation.

7.2.2 Modified L-bracket

A modified L-bracket setup is considered (Fig. 7.4). In this example the SERA is employed, which remedies the drawbacks of the BESO scheme [21], while maintaining black-and-white solutions. For this analysis, only a color-encoded input image is provided. The proposed scheme automatically recognizes significant regions and their associated operations during the automated decomposition phase. The colors blue, red, green, white and gray correspond to boundary conditions, loadings, solid, void and domain pixels respectively. Input images are easily constructed by small scripts or obtained from, e.g., medical imaging applications. Especially from the user perspective, manipulating analysis parameters by color-encoding simplifies the overall process and permits direct visual verification of the input prior to analysis. Further, it facilitates testing of variants. In this example, the domain is discretized by 512 pixels in each direction. A volume fraction of 0.3 is specified. The `conv2`-type filter is employed with radius equal 12 pixels. The SERA parameters PR, SR and B are chosen as 0.03, 1.3 and 0.003 respectively. All quadtree elements are of size ≤ 128.

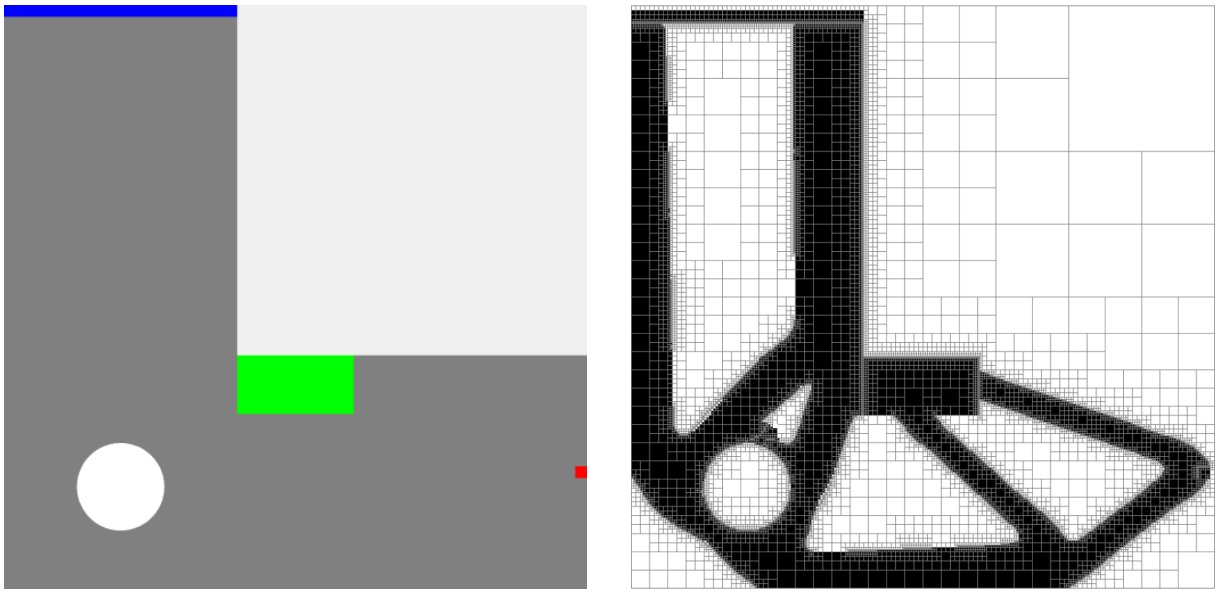

Fig. 7.4: Topology optimization of an L-bracket via automated image-based analysis. Input image (left) and resulting topology (right).

For more involved geometries, gratuitous discretization may arise due to slight misalignment with respect to the optimal quadtree meshing strategy. This is apparent surrounding the blue and red regions (Fig. 7.4), where a pertubation by 1 pixel triggers excessive refinement to accurately capture the domain's geometry. To demonstrate this general case, the L-bracket is treated as is by the quadtree decomposition, which results in 32'694 DOFs, while a shifted, scaled and therefore better aligned domain geometry results in 26'554 DOFs respectively. The conventional method employing the fine grid discretization treats 526'338 DOFs. In this example, the required DOFs are reduced by over an order of magnitude. For such small examples, a typical forward analysis completes in ≤ 0.6 seconds on a modest desktop computer running in serial.

7.2.3 3D Topology Optimization

7.2.3.1 The Scaled Boundary Finite Element Method in 3D Elastostatics

In order to treat 3D TO, a brief summary of the scaled boundary finite element method in 3D is given. For a more elaborate derivation and detailed explanations, the readers may consult references [297, 294].

The salient features of an SBFEM analysis are illustrated on the problem domain described by the volume V depicted in Fig. 7.5. V comprises the volume spanned by the scaling center O and the 2D surface element, describing the boundary. One minor constraint is required: The domain must remain star-convex, i.e., the entire surface must be visible from the scaling center. The introduction of this scaling center is accompanied by a transition from a Cartesian reference system into one resembling polar coordinates. In radial direction the analytic variable ξ is introduced, while for each tangential direction, η respectively ζ represent the local coordinates on the boundary. Therefore, each surface element may be described by 2D interpolation shape functions $[N(\eta,\zeta)]$ formulated in natural coordinates $-1 \le \eta \le 1$ and $-1 \le \zeta \le 1$. The interior of the domain is constructed by scaling the boundary (x,y,z) along the dimensionless radial coordinate $0 \le \xi \le 1$, which originates at the scaling center and ends on the boundary. The mapping of points employing the newly introduced scaled boundary coordinate system is therefore given as:

$$\hat{x}(\xi,\eta,\zeta) = \xi x(\eta,\zeta) = \xi[N(\eta,\zeta)]\{x\}, \tag{7.1a}$$

$$\hat{y}(\xi,\eta,\zeta) = \xi y(\eta,\zeta) = \xi[N(\eta,\zeta)]\{y\}, \tag{7.1b}$$

$$\hat{z}(\xi,\eta,\zeta) = \xi z(\eta,\zeta) = \xi[N(\eta,\zeta)]\{z\}. \tag{7.1c}$$

We denote the vectors of nodal coordinates of a surface element by $\{x\},\{y\},\{z\}$ respectively. The set (ξ,η,ζ) is termed the scaled boundary coordinates in the three-dimensional domain.

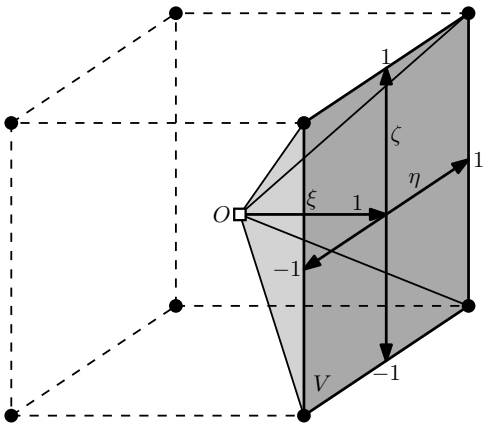

Fig. 7.5: Three-dimensional coordinates for a scaled boundary finite element.

Similarly, the iso-parametric mapping of the displacements $\{u(\xi,\eta,\zeta)\}$ at a point (ξ,η,ζ) comprises an analytic (ξ) and interpolatory (η,ζ) component:

$$\{u(\xi,\eta,\zeta)\} = \{u_x(\xi,\eta,\zeta), u_y(\xi,\eta,\zeta), u_z(\xi,\eta,\zeta)\}^{\mathrm{T}} = [N^u(\eta,\zeta)]\{u(\xi)\}, \tag{7.2}$$

where $\{u(\xi)\}$ represents an analytic displacement function along ξ, unique to each node on the boundary. These displacements functions are determined during the SBFEM solution. The interpolation shape function $[N^{\mathrm{u}}(\eta,\zeta)]$ in Eq. (7.2) are defined analogously to the conventional FEM:

$$[N^{\mathrm{u}}(\eta,\zeta)] = [N_1(\eta,\zeta)[I], N_2(\eta,\zeta)[I], \ldots, N_n(\eta,\zeta)[I]], \tag{7.3}$$

where n denotes the amount of nodes of the surface element and $[I]$ is the 3×3 identity matrix. Expressing the strains in scaled boundary coordinates requires splitting the linear differential operator into components $[B^1]$ and $[B^2]$, whose combined effect mimics the original transformation:

$$\{\epsilon(\xi,\eta,\zeta)\} = [B_1(\eta,\zeta)]\{u(\xi)_{,\xi}\} + \frac{1}{\xi}[B^2(\eta,\zeta)]\{u(\xi)\}, \tag{7.4}$$

The stresses are obtained conventionally by pre-multiplying the strains by the constitute matrix:

$$\{\sigma(\xi,\eta,\zeta)\} = [D]\left([B_1(\eta,\zeta)]\{u(\xi)_{,\xi}\} + \frac{1}{\xi}[B^2(\eta,\zeta)]\{u(\xi)\}\right). \tag{7.5}$$

The weak form for each subdomain may be derived by applying several methods [342, 82, 136]. Neglecting body loads and surface tractions, two equations arise (Eqs. 7.6 and 7.7):

$$[E^0]\xi^2\{u(\xi)_{,\xi\xi}\}+\Big(2[E^0]-[E^1]+[E^1]^{\mathrm{T}}\Big)\xi\{u(\xi)_{,\xi}\}+\Big([E^1]^{\mathrm{T}}-[E^2]\Big)\{u(\xi)\}=0, \tag{7.6}$$

The coefficient matrices $[E^0],[E^1],[E^2]$ bare a striking similarity to conventional FEM stiffness matrices, both in their structure and in that they are calculated for each element individually, with subsequent assembly for each subdomain. The internal nodal forces modes at the boundary $\{q(\xi)\}$ are derived as:

$$\{q(\xi)\}=\xi\Big([E^0]\xi\{u(\xi)_{,\xi}\}+[E_1]^{\mathrm{T}}\{u(\xi)\}\Big). \tag{7.7}$$

The scaled boundary finite element equation is solved by the matrix function solution proposed by Song [291]. Therein, the quadratic eigen-problem is recast into a system of first-order differential equations in ξ, at the expense of doubling the amount of unknowns:

$$\xi\left\{\begin{array}{c}\xi^{0.5}\{u(\xi)\}\\ \xi^{-0.5}\{q(\xi)\}\end{array}\right\}_{,\xi}=-[Z]\left\{\begin{array}{c}\xi^{0.5}\{u(\xi)\}\\ \xi^{-0.5}\{q(\xi)\}\end{array}\right\}, \tag{7.8}$$

with the Hamiltonian coefficient matrix $[Z]$ defined as:

$$[Z]=\left[\begin{array}{cc}[E^0]^{-1}[E^1]^{\mathrm{T}}-0.5[I] & -[E^0]^{-1}\\ -[E^2]+[E^1][E^0]^{-1}[E^1]^{\mathrm{T}} & -\big([E^1][E^0]^{-1}-0.5[I]\big)\end{array}\right]. \tag{7.9}$$

The Schur decomposition with subsequent block-diagonalization is employed to avoid numerical deficiencies in the solution and decompose Z to satisfy:

$$[Z][V]=[V][S], \tag{7.10}$$

where $[S]$ and $[V]$ are the real Schur form and the transformation matrix, respectively. In order to strip the bounded from the unbounded response, the diagonal blocks containing the eigen-values of $[S]$ are sorted in ascending order and the columns of $[V]$, which contain the associated eigen-modes, are reordered accordingly. The following partitioning is devised:

$$[S]=\left[\begin{array}{cc}S_{11} & 0\\ 0 & S_{22}\end{array}\right], \tag{7.11a}$$

$$[V]=\left[\begin{array}{cc}V_{11} & V_{12}\\ V_{21} & V_{22}\end{array}\right]. \tag{7.11b}$$

$[S_{11}]$ contains all eigenvalues with negative sign, i.e., $\texttt{real}(\lambda([S_{11}]))<0$, which can be shown to correspond to the bounded domain solution. The general solutions for the displacements and internal nodal forces for the bounded domain is sought in the form of a power series and can be expressed as:

$$\{u(\xi)\}=[V_{11}]\xi^{-[S_{11}]-0.5[I]}\{c\}, \tag{7.12a}$$

$$\{q(\xi)\}=[V_{21}]\xi^{-[S_{11}]-0.5[I]}\{c\}. \tag{7.12b}$$

The integration constants $\{c\}$, whose values are determined in post-processing, follow from the effective boundary conditions of the problem. Formulating Eq. (7.12) at the boundary ($\xi=1$), the nodal displacements $\{u\}=\{u(\xi=1)\}$ and the nodal forces $\{q\}=\{q(\xi=1)\}$ can be expressed as:

$$\{u\}=[V_{11}]\{c\}, \tag{7.13a}$$

$$\{q\}=[V_{21}]\{c\}. \tag{7.13b}$$

Since the static stiffness matrix $[K]$ is defined as $\{q\}=[K]\{u\}$, $[K]$ of a subdomain is determined by substituting Eq. (7.13):

$$[K]=[V_{21}][V_{11}]^{-1}. \tag{7.14}$$

Upon assembly of all individual subdomain stiffness matrices into a global stiffness matrix, the displacement solution is sought according to conventional FEM procedures.

The natural extension of 2D quadtree decompositions in 3D is termed octree decomposition. Therein the identical procedure is performed, with the addition of a third dimension, i.e., the vertical axis. Hence the criterion for subdivision now considers the contents of cubes. If the homogeneity criterion is not met, the parent cube is bisected in all three dimensions and therefore replaced by eight children, thus warranting the prefix “oc”.

7.2.3.2 3D-Wheel

In this example we extend SBFEM-powered TO to 3D problems. The established 3D wheel problem is studied (Fig. 7.6): The width, depth and height are discretized by 80, 80 and 40 pixels respectively. All four corners at the bottom edge are fully restrained. A point load is applied in downward direction in the middle of the bottom surface. A volume fraction of 0.075 is sought. The penalty parameters for SIMP and gray-scale filter are chosen as 3 and 2 respectively. The filter radius is given as 3 pixels. All octree elements are ≤ 16 pixels in size. A sensitivity filter is employed. A Young’s modulus of $E = 10^{-9}$ denotes material voids. The analysis concludes after 200 iterations.

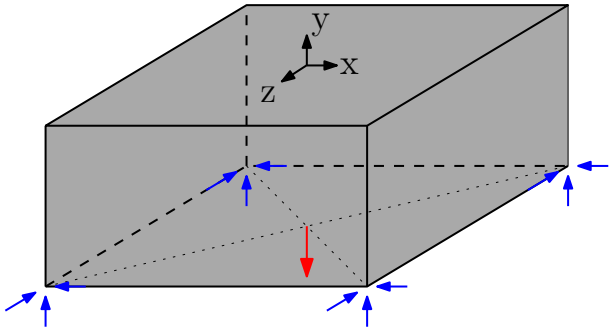

Fig. 7.6: Problem domain of the 3D wheel benchmark.

The SIMP with gray-scale filter is utilized. The addition of the gray-scale filter is crucial to obtaining computational efficiency, since regions of transitional material distributions, which impact the proposed hierarchical meshing techniques, are minimized. The preconditioned conjugate gradients method (pcg) is employed to obtain the solution of the forward problem. Scaling is performed to combat the conditioning issues due to the treatment of void elements [336] with secondary preconditioning by incomplete Cholesky decomposition. This significantly reduced the amount of iterations required for convergence. A strict convergence tolerance of 10^{-9} was specified to contain any divergence from the reference solution to the adaptive discretization choice. In Fig. 7.7 the final topology is depicted along with a sample of the octree mesh.

It is demonstrated, that the amount of DOFs and number of non-zero entries in the stiffness matrix (nnz) is significantly reduced (Fig. 7.8) by employing the proposed scheme, especially after the initial phase in the TO process. Although up to 4096 unique element realization are possible on the octree, only a handful exist at each iteration (Fig. 7.8). Computational effort is alleviated by only computing the element stiffness matrices for the unique elements and cloning the remainder. However, the overwhelming computational burden still resides in the solution of the forward problem.

The final topology is readily exported to STL format by operating on the octree, greatly facilitating subsequent additive manufacturing procedures.

7.3 Conclusions

This contribution advances the current state-of-the-art in TO by employing hierarchical meshes coupled with polytope-based numerical methods, which alleviate issues commonly associated with hanging nodes. Enforcing a balancing operation on the mesh further limits the amount of feasible element realizations, which is exploited through precomputation of element stiffness matrices and cloning of element properties. Moreover, we propose a novel and intuitive scheme for interacting with the analysis parameters by color-encoding input images, which the decomposition techniques automatically translate into analysis-ready

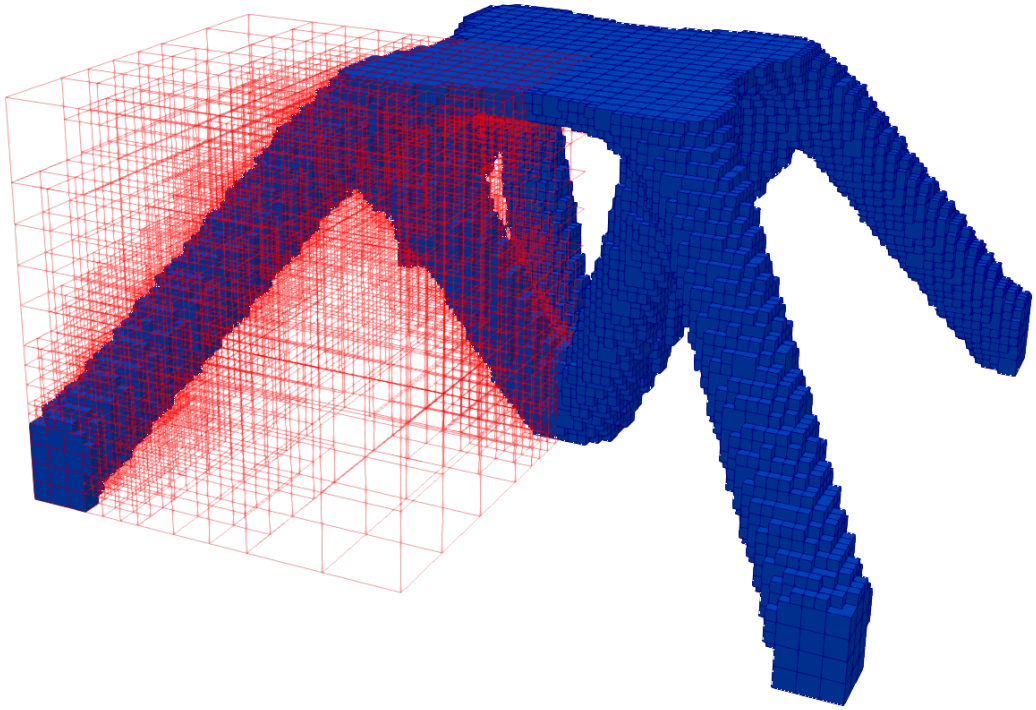

Fig. 7.7: Resulting topology for 3D wheel benchmark in blue with sample octree mesh in red.

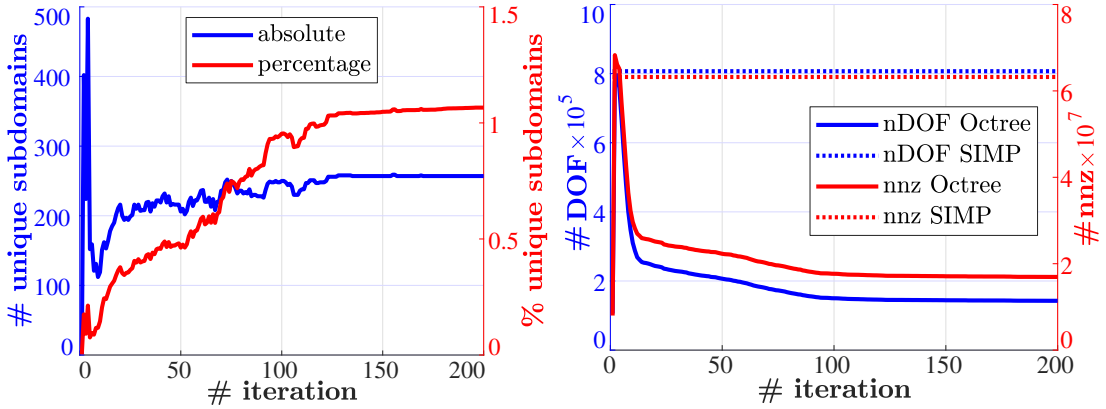

Fig. 7.8: Evolution of hierarchical mesh quantities across iterations.

meshes. Further, we extend SBFEM-powered TO to 3D problems and demonstrate an effective means for exporting results to STL format for subsequent additive manufacturing (3D printing).

TO relying on hierarchical meshes is shown to require only a fraction of the DOFs demanded by traditional grid approaches, significantly reducing the computational toll. The three investigated numerical examples consistently demonstrate a remarkable reduction in required DOFs and memory requirements, without incurring a perceivable loss of accuracy. Considering the generality of this approach in handling color-coded input, an extension to multi-material TO presents an intriguing direction for future work.

Part IV

Conclusions

8 Conclusions

8.1 Overview of Contributions

This thesis starts with providing a critical discussion on the capabilities and merits of numerical methods employing discrete and diffuse crack representations within the context of LEFM by proxy of SBFEM/XFEM and PFM. While the PFM's generality enables it to treat a wide range of complex problems that discrete methods cannot, it comes at the price of a comparatively severe computational toll.

The novel contributions towards accelerating forward problems are the following:

- The Hamiltonian Schur decomposition is adopted for the solution process of SBFEM. By preserving Hamiltonian symmetry, enhanced accuracy is obtained along near optimal convergence rates. Further, the doubling of system equations due to the linearization of the underlying quadratic eigenproblem is reversed, which is shown to reduce the approximate flops count of the method by close to an order of magnitude for larger problems. The SPR method of stress recovery is proposed within the computation of the gSIFs, which not only permits greater accuracy, but also admits an effective and efficient error estimator thereof. Numerical benchmark problems are solved with reference to XFEM, permitting a performance comparison.
- SBFEM based simulations are extended to multiscale analyses by fusion with the EMsFEM. Various types of h-refined CMX elements containing flaws on the fine scale are considered. Hybrid NBFs based on empirical observations are introduced, which aim at unburdening the analyst from having to chose a priori the type of NBFs. Further a scheme to improve the accuracy of the gSIFs calculated by SBFEM on coarse meshes is proposed, by internally elevating the approximation space of the crack tip element. These two finding are employed in the novel MSBFEM crack propagation scheme which only resolves the mesh locally about the crack front, resulting in a highly efficient method.

The novel contribution towards accelerating inverse problems comprise:

- Quadtree based approaches, are naturally complemented by polytope-based numerical methods, such as the SBFEM, since they can treat hanging nodes. Hence, the represent powerful means to provide adaptivity. Thus the computational toll suffered from the repeated solution of the forward problem can be efficiently dealt with. The proposed damage localization scheme, on the basis of SBFEM is accelerated by adopting precomputation, reanalysis and parallel programming techniques, to reduce the wall clock time of an analysis to near real time.
- Further, a drop-in replacement for the solver of TO problems is proposed. It significantly accelerates an analysis, by leveraging automated image compression techniques to arrive at adaptive analysis-ready meshes. This technique is exploited to permit a novel way of interacting with the problem: color-encoding of analysis information directly into an input image. Further, SBFEM-powered TO is extended to 3D problems.

Due to the generality and minimal invasiveness of the two methods proposed to accelerate the inverse problems, they can be freely combined with a multitude of algorithms, significantly increasing their range of application and significance.

8.2 Summary

In chapter 3, the merits of three alternative approaches, namely the XFEM/GFEM, SBFEM and PFMs, are surveyed and compared in the context of LEFM. The purpose of the study is to provide a critical literature review, emphasizing on the mathematical, conceptual and implementation particularities that lead

to the specific advantages and disadvantages of each method, as well as to offer numerical examples that help illustrate these features. SBFEM, the method of interest in this thesis occupies the same domain as the XFEM. SBFEM circumvents XFEM's shortcoming of having to specify enriched nodes and element sets, which pose potential conditioning problems, increase the DOFs present during analysis and require more involved numerical integration techniques at the cost of introducing a Hamiltonian eigen-problem, due to an analytic solution in radial direction. This permits SBFEM-based analysis to reduce the problem dimensionality and construct arbitrary star-convex hp-elements, which admit significantly relaxed meshing requirements. In the process no a priori assumptions must be made pertaining to the calculation of gSIFs. Unfortunately, incorporation of features with radial componenst are cumbersome, since they must be treated in the analytic formulation. During crack propagation, SBFEM, as apposed to XFEM, explicitly introduced double nodes which changes the topology of the mesh. Slicing of elements may induce unwanted artefacts, which must be corrected by further repositioning nodes. In the PFM, however, a crack is never explicitly propagated, but associated with the evolution of the phase field. The treatment of a second field, greatly increases the computational toll as it does the generality of the method, enabling the simultaneous incorporation of nucleation, branching, merging and coalescence of cracks, even in 3D applications where SBFEM/XFEM break down, confined to the limits of LEFM.

In chapter 4, the Hamiltonian Schur decomposition is adopted within the SBFEM context to reverse doubling the problem size incurred due to the linearization of the underlying quadratic eigen-problem. It is found to enhance the convergence properties of the SBFEM to near optimal rates, by respecting Hamiltonian symmetry and eliminating the need for a stabilization parameter during the solution process of the Hamiltonian eigen-problem, paving the way for applications to inverse problems. A comparison with the XFEM shows SBFEM to be highly competitive and outperform it for conventional LEFM applications, due to the ease with which hp-elements may be employed. One contributing factor is the novel recovery scheme for gSIFs, which permit an effective error estimator.

In chapter 5, SBFEM is extended towards multiscale analysis, by proposal of the MSBFEM: Exploiting SBFEM on the fine scale to account for fracture and the EMsFEM to map the fine scale information to a coarse one, where the governing equations are solved at significantly reduced computational cost. Simulation of a mock masonry wall indicates the accurate reconstruction of von Mises stresses using three orders of magnitudes fewer DOFs thereby reducing the wall clock time for analysis by over two orders of magnitude. The extension to a multiscale crack propagation scheme prompted a novel method to enhance the gSIFs computed on highly coarse QT meshes, which by virtue of elevating the crack tip element's approximation space, can reduce the error in recovered gSIFs by over an order of magnitude. Subsequent adoption in the MSBFEM crack propagation scheme, wherein only the RVE containing the crack tip is resolved and the remaining domain accounted for by coarse h-adaptive macro-elements, permits a significant reduction in DOFs required for analysis. For a sample problem solve, this equated to a 13-26x reduction of unknowns.

Starting with chapter 6, the proposed advancements pertaining to the solution of forward problems are applied to accelerating inverse analyses. The proposed scheme, which fuses concepts from parallel programming, precomputation and reanalysis to significantly accelerate damage localization, is verified, then validated with 5 numerical examples treating cracks, multiple inclusions, non-regular geometry and real-world sensing data. Early approaches employing a displacement-based fitness function are shown to be severely ill-posed, forcing frequent divergence toward local minima, given a sparse sensing network. The subsequent adoption of a strain-based fitness function, which is significantly more sensitive to variations of the candidate crack's design variables, permits their accurate identification. The effects of crack orientation, crack length and amount of sensors on the scheme's ability to accurately localize damage is examined. Of the four global optimization algorithms investigated, CMA-ES performs the best, followed by PSO and then GAs. PS is observed to frequently diverge and is thus not recommended for use in damage localization applications. Topological variables are employed to effectively study the detection of multiple inclusions. The incorporation of non-regular geometry is achieved by a function, mapping the lower and upper bounds of the design variables to the problem domain. On the basis of a simplified wing geometry, CMA-ES is shown to correctly and accurately identify the imposed crack location. The acceleration scheme permits the analysis to complete in less that two minutes on a conventional workstation. The use of real-world data still proves challenging due to the a priori unknown signal to noise ratio. Typically, the general location of the crack tip may still be inferred, which is sufficient for subsequent SHM applications.

In chapter 7, the current state-of-the-art in TO is extended by a drop-in replacement for the forward solver, which implements automated image compression techniques in conjunction with SBFEM to arrive at analysis-ready adaptive meshes at each iteration, with elements that are precomputable. By fusion with

multiple TO methods, the new approach is validated and shown to reduce the computational toll by over an order of magnitude without negatively affecting the structural layout. Any artifacts introduced due to the adaptive nature of the scheme are readily removed by the use of precomputed higher order elements. An unoptimized Matlab implementation manages to outperform existing schemes in terms of wall clock time required for analysis, by 5-8x on medium size problems. Further, this scheme extends SBFEM-powered TO to 3D problems. Even on a compact test case, where the adaptivity scheme cannot be deployed to its fullest potential, a reduction in DOF by over 75% is observed.

8.3 Limitations

Although the adoption of the Hamiltonian Schur decomposition in the SBFEM solution process admits many benefits, it does not resolve all issues. In select cases, where accuracy is of utmost importance, the rigid body translational modes should still be overwritten. Due to the recent discovery of the underlying method, user-friendly, high performance codes do not exist. Currently, a mixture of Fortran and Matlab codes, including mex-files requiring Matlab 7.3 (2006), exists. This unfortunate combination consumes any real world performance gains alluded to by the theoretical reduction in flops count.

The MSBFEM inherits all limitations of its parent method, the EMsFEM, i.e., it is limited by the choice of NBF typ. Further, it is not clear a priori, what level of coarse discretization induces how much error, especially in the presence of strong discontinuities on the fine mesh. This follows from the observed difficulty of accurately recovering the gSIFs when large crack are present or strong interactions with the boundary occur. The crack tip element enrichment scheme requires the addition of internal nodes, in order to construct the elevated approximation space, which are subsequently restrained to the surrounding mesh. In such cases, the use of higher order elements on the quadtree mesh is highly advantageous, but induces a considerable algorithmic burden to track and restrain the internal nodes. The MSBFEM crack propagation scheme is highly dependent on alterations to the strain field due to the introduction of CMX elements. Imprudent use can force erroneous crack paths. This is a consequence of the use of linear NBFs, to avoid iterations, and the absence of a clear criterion on when to resolve RVEs surrounding the crack tip. Though in principle this could be overcome to a certain degree by permitting periodic and oversampling based NBFs this would require an iterative process during each crack propagation step in order to enforce compatibility between fine and coarse meshes.

Within the context of LEFM, SBFEM and XFEM are similarly capable, yet current schemes for crack propagation using SBFEM on quadtree meshes limit themselves to linear elements, preventing SBFEM from making use of higher order elements. Further, they introduce spurious DOFs and require double nodes, i.e., topological changes to the mesh, to account for strong discontinuities. Crack tips contained within elements are limited to straight lines. Polytopes constructed by SBFEM must be star-convex.

The challenges inherent to the accelerated damage localization scheme stem primarily from the overall approach of tackling the inverse problem and are not directly SBFEM specific: Even the use of few design variables claims a considerable computational burden. Typically, the greater the amount of design variables, the more generations are required to reach the global minimum. The fact that no mathematical proof of convergence exists coupled with the lack of evidence that calculations have converged after the user-specified amount of generations have passed, implies having to perform multiple analysis runs. Although this considerably increases the computational burden, it helps detect symmetry issues or cases, where design variables are limited by their respective upper/lower bounds. For the case of more involved domains, specifying meaningful bounds can become involved and incur a considerable algorithmic burden. These combined issues pose significant challenges when trying to apply such damage localization techniques to real world structures, with the aspiration of near real time results.

The adaptivity criterion implemented for the drop-in replacement TO solver, is based purely on the geometric description of the problem domain. Special cases can be contrived, where perfect alignment with the underlying quadtree grid could result in very coarse discretizations. Due to the convergence properties inherent to the FEM-based methods, this forces the solution to overestimate the stiffness of the system, which the optimization scheme will interpret as a more desirable layout. Further the use of the SIMP approach introduces non-convexities and therefore local minima into the analysis. Although for most applications, the filtering techniques remedies this issue, adoption of a level-set approach would be advantageous. Even though significant reductions in wall clock time are reported when employing the proposed drop-in replacement for the forward solver, the unoptimized nature of the source code prohibits an accurate assessment of the methods potential.

8.4 Outlook

Popularizing SBFEM as a competitive alternative within the context of LEFM, requires convenient access to its underlying methods. With SBFEM finding increased application in 3D problems, due to its ability to treat complex meshing requirements, the need for robust and efficient numerical methods of performing Schur decompositions is of elevated importance. Rehabilitating the existing code-base for use with HPC libraries constitute a worthy direction of future work.

The tip enrichment scheme could be investigated on CMX elements containing discontinuities. Although it is expected to offer an increase in accuracy, it will most likely be overpowered by the use of NBFs. Indeed the pursuit of novel boundary conditions could prove quite fruitful within EMsFEM, e.g., prescribing a flux-based criterion across edges instead of displacements. Nevertheless, the use of hierarchical shape function for the tip enrichment scheme instead of internal nodes should provide similar levels of accuracy without the need to construct and treat a new crack tip element topology. The incorporation of plasticity into the the current MSBFEM formulation would provide a valuable contribution towards extending the methods capabilities, since, in this early stage, quasi-static crack propagation was researched within the context of LEFM. Extending SBFEM to more involved plasticity models such as Bouc-Wen or shape memory alloy material models would open up a new direction of exciting applications for the method and the proposed multiscale scheme.

Although several publications exist on damage localization techniques, few incorporate data from real-world measurements. Typically isotropic materials are considered. With the aspiration of successfully applying damage localization techniques to real-world problems, performance given inhomogeneous, e.g., functionally graded materials, could be investigated. Unfortunately, the applicability of most damage localization schemes is limited to the accuracy with which the forward problem can be solved. It would therefore be highly beneficial to construct a data set containing a suite of benchmark examples with measurements obtained from well documented testing campaigns. Further, different types of measurement instrumentation should be concurrently deployed to assess their adequacy for such problems.

Conventional TO requires a fine grid to overcome pixelated results and obtain a sufficiently accurate forward simulation. Specifically for TO implementing a stress-based approach, these step-like results can invoke spurious localizations. By combining level-set based TO with the featured based hybrid quadtree-polygon meshing, the domain boundary may be expressed continuously by clipping along the zero level-set. Further, stress-based TO could additionally benefit from the use of higher order polytope elements. At this point, the proposed adaptivity criterion, which is based on geometry might provide insufficient, such that alternatives should be explored. One possibility presents itself in a newly proposed, inexpensive error estimator specifically developed for SBFEM [298]. Unfortunately, only the forward analysis currently benefits from the reduced computational toll associated with the adaptive mesh, such that for higher discretization levels, the filtering technique dominates the computational effort. One intriguing possibility is to explore the effectiveness of PDE-based filters applied to the adaptive mesh. In an effort to tackle various structural optimization problems such as TO and shape optimization, the merits of higher order quadtree meshes must be considered. Two directions present themselves: First fusion of level-set TO and higher order polytope-based QT meshes. Second, shape optimization facilitated by isogeometric representations of QT meshes harnessing the scaled boundary isogeometric approach.

The combination of the proposed methods provides the basis for intriguing extensions, e.g., in SHM, a rapidly emerging field in engineering. Specifically the recent adoption of composite materials commonly encountered in fuselages, helicopter rotor and wind turbine blades, to name a few, has reinforced the need for accurate structural monitoring and assessment methods. Often, inspection of such structures by specialists is accompanied by long downtime, significant manual labor costs and procedures permitting only limited penetration depth at best, rendering it not only expensive, but potentially ineffective and prone to human error. This thesis provides the prospect of an automated near real-time damage localization scheme to accurately localize damage as it occurs in a structure during operation without the need for human intervention. Leveraging the MSBFEM component, the severity of the localized damage is determined and its affects on continued operation can be assessed. Deviation between measurements and MSBFEM simulation could be employed to update the numerical model as required. The ability to determine not only the failed component through damage localization, but also the damage path by MSBFEM, enables the TO process to automate the design of a more resilient component, which could be 3D printed on demand. Over time this combination of proposed methods will lead to safer structures and revolutionize the way in which maintenance is conducted.

Part V

Appendix

A A State-of-the-art Review of XFEM and PFM Theory

A.1 The eXtended/Generalized Finite Element Methods (XFEM/GFEM)

One of the main difficulties associated with the modeling of fracture by means of conventional finite element methods lies in the fact that a new mesh is needed at each propagation step. This, apart from increasing the computational cost, significantly limits the degree of automation that can be achieved in such simulations. The introduction of the partition of unity method (PUM) [27, 28, 194] has provided the background for the subsequent development of a suite of methods, including the extended [205] and generalized [304] finite element methods that have managed to overcome, to a large extent, this difficulty. In the following subsections, we provide a brief overview of these methods with the focus shed onto the methodological and implementational aspects relating to crack propagation problems. For a more detailed exposition of the methods and their applications we refer the reader to the several review papers available in existing literature, as for instance References [1, 39, 105] and more recently [306], as well as the references therein.

A.1.0.1 Partition of unity enrichment

Partition of unity enrichment, in general, allows the incorporation of known features of the solution in the numerical approximation in the form of enrichment functions. If finite elements are used as the basis for the numerical approximation, then partition of unity enrichment can be realized as follows:

$$\mathbf{u}(\mathbf{x}) = \underbrace{\sum_{\forall I} N_I(\mathbf{x})\mathbf{u}_I}_{\text{FE approximation}} + \underbrace{\sum_{\forall I} N_I^*(\mathbf{x})\Phi(\mathbf{x})\mathbf{b}_I}_{\text{enriched part}} \tag{A.1}$$

where $N_I(\mathbf{x})$ are the FE interpolation functions, $\mathbf{u}_I$ are FE degrees of freedom (dofs), $N_I^*(\mathbf{x})$ is a basis of functions that form a partition of unity, $\Phi(\mathbf{x})$ is the enrichment function and $\mathbf{b}_I$ are the enriched degrees of freedom.

Most commonly, finite element shape functions are employed to form the partition of unity basis:

$$N_I^*(\mathbf{x}) \equiv N_I(\mathbf{x}) \tag{A.2}$$

Alternative PU bases have can also be found in the literature Zhang, Banerjee, and Babuška [359], Griebel and Schweitzer [119], and Hong and Lee [133], aiming mostly at improving specific aspects of the method, such as conditioning of the resulting system matrices.

A.1.0.2 XFEM/GFEM enrichment functions for LEFM

In the original partition of unity finite element method (PU-FEM) [194], enrichment functions were used as a means of improving the overall accuracy of the approximation, thus enrichment was applied globally, i.e. for all nodes of the FE mesh. For problems involving localized phenomena, such as fracture, enrichment functions are only needed locally, thus, in the XFEM [38, 205] only a subset of the nodes is enriched to increase the efficiency of the method. This type of enrichment was subsequently also adopted in the GFEM rendering the two methods almost identical. In fact, in more recent publications [105] almost no distinction is made between the two methods.

For LEFM problems, two types of enrichment functions, i.e. specializations of function $\Phi(\mathbf{x})$, are most commonly used to represent the discontinuities and singularities introduced in the solution by the crack. In the following, these enrichment functions are presented along with possible alternatives from the literature. Furthermore, some common problems, associated with their use, are identified and possible remedies discussed.

A.1.0.3 Jump enrichment

The first type of enrichment functions consists of modified Heaviside step functions, usually referred to as jump enrichment functions, which allow to represent the displacement jump along the crack surface:

$$H(\mathbf{x}) = \begin{cases} 1 & \text{above the crack} \\ -1 & \text{below the crack} \end{cases} \tag{A.3}$$

These functions were introduced in the work of Moës, Dolbow, and Belytschko [205], and constitute perhaps the most distinctive feature of XFEM. Enrichment with these functions is realized locally, only for nodes whose nodal support is completely split in two by the crack.

Other types of discontinuous enrichment include the alternative formulation of Hansbo and Hansbo [127] and higher order discontinuous enrichment functions found both in the XFEM [189, 69, 4] and GFEM [87] literature. In the context of fracture mechanics, special discontinuous functions have also been proposed to handle branched and intersecting cracks [81].

A.1.0.4 Tip enrichment

The second type of enrichment functions is a set of asymptotic functions, also referred to as tip enrichment functions, that allow to represent the discontinuity at the crack tip or front:

$$F_j(r,\theta) = \left\{ \sqrt{r}\sin\frac{\theta}{2}, \sqrt{r}\cos\frac{\theta}{2}, \sqrt{r}\sin\frac{\theta}{2}\sin\theta, \sqrt{r}\cos\frac{\theta}{2}\sin\theta \right\} \tag{A.4}$$

where r, θ are spatial coordinates of a polar system with its origin at the crack tip/front. These functions were introduced by Belytschko and Black [38] and form a basis that can exactly represent the analytical solution of the Westergaard problem.

Initially [205], the use of asymptotic enrichment was limited to elements containing the crack tip/front, however in the works of Stazi et al. [302] and Laborde et al. [160] it was shown that this would lead to suboptimal convergence rates. In order to obtain the same rate of convergence as for smooth problems, the use of asymptotic enrichment in a domain of fixed size around the crack front is necessary [160, 34]. This alternative enrichment scheme was termed "geometrical enrichment" while the initial scheme is referred to as "topological enrichment". Usually, the domain where asymptotic enrichment is used is defined as the set of points whose distance from the crack tip/front is smaller that a predefined length r_e, called the enrichment radius.

An alternative to the enrichment functions of Eq. (A.4) consists of using the displacement expression of the Westergaard solution directly as an enrichment function. This approach was introduced by Duarte, Babuška, and Oden [86] and subsequently adopted in several works in the XFEM [350, 176, 356] and GFEM [124, 125] literature. This kind of enrichment results in different enrichment functions in each spatial dimension, thus in some works [231, 71] it was termed "vector enrichment" as opposed to "scalar enrichment" where the same enrichment functions are used in all spatial dimensions. As a disadvantage of this approach it is mentioned that it could complicate the implementation, especially in existing codes. On the other hand it leads to a decreased number of degrees of freedom compared to scalar enrichment and it can allow the direct estimation of stress intensity factors. Typically, to increase the accuracy of this estimation, higher order terms of the asymptotic expansion are also used as enrichment.

A.1.0.5 Kronecker delta property

From Eq. (A.1) it can be easily deduced that, for enriched nodes, the FE degrees of freedom will no longer correspond to displacements at the nodes. To restore this desirable property, enrichment functions can me modified such that they vanish at nodal points. A simple way to accomplish that, is through enrichment function "shifting" [365], which consists of subtracting from the enrichment functions, their values at the nodal points:

$$\Phi_I(\mathbf{x}) = \Phi(\mathbf{x}) - \Phi(\mathbf{x}_I) \tag{A.5}$$

where $\Phi_I(\mathbf{x})$ is the modified enrichment function and $\mathbf{x}_I$ are the spatial coordinates of nodal point I.

From the above, it becomes clear that shifting results in a different enrichment function for each node. Furthermore, when applied to the jump enrichment functions of Eq. (A.3), it causes the functions to vanish for elements that do not contain the crack, thus simplifying the implementation.

The Kronecker delta property can also be preserved by employing the stable GFEM [26, 124, 125], a technique where the FE interpolant of the enrichment functions is subtracted from the enrichment functions themselves. The main advantage of this technique however, lies in the fact that it can considerably improve the conditioning of the resulting stiffness matrices.

A.1.0.6 Blending

As already mentioned, enrichment in the XFEM and GFEM is mostly performed locally to increase efficiency. This leads to situations where only some of the nodes of an element are enriched with a specific enrichment function and the remaining nodes are either not enriched at all or enriched with a different enrichment function. In these elements, the shape functions pre-multiplying the enrichment functions no longer form a partition of unity leading to increased errors, also called "blending" errors. For the enrichment functions used in LEFM, these errors only result in some loss of accuracy, leaving the convergence rates unaffected. For other types of enrichment functions however, the convergence rate can also be affected [70].

Due to the above reasons, the "blending" problem has been extensively studied and several solutions have been proposed involving a variety of techniques such as assumed/enhanced strain formulations [70, 117, 319], directly matching displacements between the enriched and non enriched part of the approximation [160, 65, 5] and the use of weight functions [103, 64, 329] to smoothly blend different parts of the approximation. The later approach, also known as the corrected XFEM, is likely the most successful due to its relative simplicity and effectiveness.

A.1.0.7 Ill-conditioning

An additional problem related to enrichment is the linear dependence between the enriched and standard part of the approximation. As far as jump enrichment is concerned, linear dependence may arise if the crack either intersects, or lies very close to a node. Then, the enriched shape function of this node is identical or very close to its standard FE shape function leading to linear dependence problems. A commonly used technique to avoid this problem is "snapping", which consists of not enriching nodes if they are very close to the crack surface [81]. Other approaches involve pre-conditioning [195, 164] and stabilization in the element [178] or global equilibrium equations [330] level.

With respect to tip enrichment, ill-conditioning can arise when geometrical enrichment is used due to the fact that away from the singularity the tip enrichment functions tend to become linearly dependent both with respect to the FE part of the approximation and each other [3, 4]. To overcome this issue several alternatives have been proposed such as altering the partition of unity basis used to pre-multiply the tip enrichment functions [160, 6, 5], preconditioners [34, 195], stabilization [178] and enrichment function orthogonalization [3, 4]. Moreover, vector enrichment functions have been shown to lead to improved conditioning [71], and if further combined to the stable GFEM [124, 125] they can lead to optimal growth rates of the scaled condition number.

A.1.0.8 Displacement approximation

Using the enrichment functions of the previous subsection, the XFEM/GFEM displacement approximation can be obtained:

$$\mathbf{u}(\mathbf{x}) = \underbrace{\sum_{I \in \mathcal{N}} N_I(\mathbf{x})\mathbf{u}_I}_{\text{FE approximation}} + \underbrace{\sum_{J \in \mathcal{N}^j} N_J(\mathbf{x})H(\mathbf{x})\mathbf{b}_J}_{\text{jump enriched part}} + \underbrace{\sum_{T \in \mathcal{N}^t} \sum_j N_T(\mathbf{x})F_j(\mathbf{x})\mathbf{c}_{Tj}}_{\text{tip enriched part}} \tag{A.6}$$

where $\mathbf{b}_J$, $\mathbf{c}_{TJ}$ are enriched degrees of freedom.

The nodal sets of Eq. (A.6) are defined as follows:

$\mathcal{N}$ is the set of all nodes in the FE mesh.
$\mathcal{N}^j$ is the set of jump enriched nodes. This nodal set includes all nodes whose support is split in two by the crack.
$\mathcal{N}^t$ is the set of tip enriched nodes. This nodal set includes all nodes whose support includes the crack front.

The method resulting from the above approximation does not involve any modifications, for instance dealing with blending or conditioning issues, and is thus often referred to as the "standard XFEM".

A.1.0.9 Weak form and discretised equilibrium equations

For LEFM problems, the standard weak formulation for linear elasticity is typically used:

Find $\boldsymbol{u} \in \mathscr{U}$ such that $\forall \boldsymbol{v} \in \mathscr{V}^0$

$$\int_\Omega \boldsymbol{\sigma}(\boldsymbol{u}) : \boldsymbol{\varepsilon}(\boldsymbol{v})\, d\Omega = \int_\Omega \boldsymbol{b} \cdot \boldsymbol{v}\, d\Omega + \int_{\Gamma_t} \bar{\boldsymbol{t}} \cdot \boldsymbol{v}\, d\Gamma \tag{A.7}$$

where :

$$\mathscr{U} = \left\{ \boldsymbol{u} | \boldsymbol{u} \in \left(H^1(\Omega)\right)^3, \boldsymbol{u} = \bar{\boldsymbol{u}} \text{ on } \Gamma_u \right\} \tag{A.8}$$

and

$$\mathscr{V}^0 = \left\{ \boldsymbol{v} | \boldsymbol{v} \in \left(H^1(\Omega)\right)^3, \boldsymbol{v} = 0 \text{ on } \Gamma_u \right\} \tag{A.9}$$

Functions of $H^1(\Omega)$ are implicitly discontinuous along the crack surface.

By introducing the constitutive relationship of Eq. (2.3), the problem can be written as:
Find $\boldsymbol{u} \in \mathscr{U}$ such that $\forall \boldsymbol{v} \in \mathscr{V}^0$:

$$\int_\Omega \boldsymbol{\varepsilon}(\boldsymbol{u}) : \boldsymbol{D} : \boldsymbol{\varepsilon}(\boldsymbol{v})\, d\Omega = \int_\Omega \boldsymbol{b} \cdot \boldsymbol{v}\, d\Omega + \int_{\Gamma_t} \bar{\boldsymbol{t}} \cdot \boldsymbol{v}\, d\Gamma \tag{A.10}$$

The above equation can be discretised using the approximation of Eq. (A.6) to produce the discretised equilibrium equations.

A.1.0.10 Crack representation

To allow the evaluation of the enrichment functions as well as the definition of the nodal sets involved in the enriched approximation, some kind of geometrical representation of the crack is necessary. In early XFEM works, as well as some GFEM publications, crack surfaces were explicitly represented as a series of linear segments (2D) or triangles (3D) [205, 88, 308]. However, the combination of this kind of representation to the XFEM can render the implementation quite involved by requiring for instance the computation of intersections of the crack with elements of the FE mesh.

A.1.0.11 The level set method

An approach that is much better suited for combination to the XFEM, is the implicit representation of cracks using the level set method [243, 280]. Due to this fact, the method has been extensively used in the XFEM framework in 2D [303] and 3D [206, 118, 309] applications.

To implicitly represent closed surfaces, such as cracks, two level set functions are needed:

- The normal level set ϕ, defined as the signed distance from the crack surface.
- The tangent level set ψ, defined as the signed distance from a surface that is normal to the crack surface and intersects the crack surface at the crack tip/front.

The crack surface is then defined as the set of points for which the normal level set is equal to zero and the tangent level set assumes negative values.

Typically, these level set functions are only computed at nodal points and interpolated for the rest of the domain using the FE shape functions:

$$\phi = \phi(\mathbf{x}) = \sum_{\forall I} N_I(\mathbf{x}) \phi_I, \qquad \psi = \psi(\mathbf{x}) = \sum_{\forall I} N_I(\mathbf{x}) \psi_I \tag{A.11}$$

where ϕ_I, ψ_I are the nodal values of the level set functions.

From the above expressions, spatial derivatives of the level set functions can be conveniently obtained through the spatial derivatives of the FE shape functions. Also evaluation of the enrichment functions can be significantly simplified. More specifically, jump enrichment functions can be directly computed

as functions of the first level set, while the polar coordinates of Eq. (A.4), needed for the tip enrichment functions, can be computed as:

$$r = \sqrt{\phi^2 + \psi^2}, \qquad \theta = \arctan\left(\frac{\phi}{\psi}\right) \tag{A.12}$$

For the general case of evolving surfaces, level sets are usually updated based on some velocity field by integrating the Hamilton-Jacobi equation. The case of propagating cracks however, requires several additional steps due to the nature of the problem and the fact that cracks are closed surfaces. Firstly, the velocity field, needed to update the crack, is only known at the crack tip/front, thus an additional step is required to extend the field to the whole domain. Then, the crack surface that has already formed should remain unaffected by the level set update, thus the velocity field should be appropriately modified. Finally, an orthogonalization step is necessary to ensure that the two level sets are normal after the update. To simplify the above procedure, several approaches were proposed in the work of Duflot [89] that allowed the update of level set descriptions for cracks without requiring the integration of evolution equations. In Elguedj et al. [98] a similar approach was proposed and applied to dynamic 3D crack propagation. It should be noted that, both of these simplified methods rely on some geometric operations and are in fact very similar to methods from the category of the following paragraph.

A.1.0.12 Hybrid implicit/explicit methods

As an alternative, aiming at combining advantages of both explicit and implicit representations, Fries and Baydoun [104] proposed a method where level set functions were directly computed from explicit crack representations using linear segments (2D) or triangles (3D). Similarly, in the vector level set method [328, 7, 8] linear segments (2D) or quadrilaterals (3D) are used to update the level set description of the crack and are subsequently discarded. Another instance of a method combining elements from both types of representations is the method of Sadeghirad et al. [272], where an explicit representation is constructed in order to correct the level set representation by removing disconnected parts of the crack.

A.1.0.13 Numerical integration

Another challenge, associated with the use of discontinuous and singular enrichment functions, lies in the numerical integration of the weak form of Eq. (A.10). Since the functions to be integrated are not smooth, standard Gauss quadrature cannot be used and more sophisticated tools need to be employed.

For the discontinuous jump enrichment functions, the most common approach would be element partitioning where elements are divided into integration sub-cells based on the crack geometry [205, 308]. Extensions of this technique have also been proposed for higher order elements [69, 106, 250]. Alternatively, other works completely avoid the use of element partitioning by employing either equivalent polynomials [327, 331], or the Schwarz–Christoffel conformal mapping [219].

As far as asymptotic enrichment functions are concerned, the most widely used solution would involve element partitioning combined with some transformation aiming at removing the singularity. Several such transformations have been proposed, e.g., the almost polar mapping of Laborde et al. [160], the parabolic transformation of Béchet et al. [34], and the Duffy transformation by Mousavi and Sukumar [211]. Element partitioning is used to divide the element containing the crack tip in triangles with one node lying on the singularity, thus also accounting for the discontinuity present in this element. Subsequently, the transformation is used to map quadrilateral elements to the constructed triangles leading to an accumulation of Gauss points around the crack tip and additionally removing the singularity. A promising solution, also including the above steps, is the algorithm introduced in Chevaugeon, Moës, and Minnebo [71], where a mapping is used for all asymptotically enriched elements, rather than just the ones containing the crack tip, and an adaptive strategy is devised to determine the number of Gauss points required for each element. Similar element partitioning algorithms [179] and mappings [202] have also been introduced for the three dimensional case.

A.1.0.14 Crack propagation

The methods presented so far in this section mainly deal with discretising cracked domains using fixed meshes. For propagating cracks, principles of classic linear elastic fracture mechanics can be applied.

Within this framework, stress intensity factors (SIFs) are the main tool used to both indicate the occurrence and determine the direction of crack propagation under certain loading conditions.

A.1.0.15 Stress intensity factors

One of the most widely used techniques for the extraction of SIFs in extended, generalized or standard finite element simulations, involves the use of the interaction integral. This can be derived by initially converting the J integral in a domain form and subsequently evaluating it for a stress state resulting from the superposition of an auxiliary stress state and the computed numerical solution. Then the interaction term of the integral, for two dimensional problems, assumes the form:

$$I = -\int_V q_{,j}\left(\sigma_{kl}\epsilon^{\text{aux}}_{kl}\delta_{1j} - \sigma^{\text{aux}}_{kj}u_{k,1} - \sigma_{kj}u^{\text{aux}}_{k,1}\right)dV \tag{A.13}$$

where ϵ^{aux}, σ^{aux} and u^{aux} are the auxiliary stress, strain and displacement fields respectively which can be defined as in Moës et al. [205] and q is a virtual velocity field. Typically, q is chosen to assume a value of one for nodes within a disc of radius r_d around the crack tip and a value of zero for the remaining nodes.

In the interior of the elements, the values of q are interpolated using the FE basis functions. As a result, the expression of Eq. (A.13) needs to be evaluated only in a "ring" or layer of elements around the crack tip. The components of the tensors of Eq. (A.13), refer to a basis aligned with the crack, which for implicit crack representations can be conveniently defined using the level sets [206, 118]. By considering the relation between the J integral and the SIFs it is straightforward to show that with an appropriate selection of the SIF values of the auxiliary state, the SIFs can be directly obtained from the interaction integral.

It should be noted that in the derivation of Eq. (A.13) it has been assumed that the crack is straight. Of course, the expression can also be used for curved cracks, perhaps with some loss of accuracy, provided that the curvature of the crack is not very pronounced within the interaction integral domain. Alternatively, a more complicated formulation can be used [113], leading to more accurate results.

For three dimensional problems a more complicated expression for the interaction integral needs to be used as, for instance, in Gosz and Moran [116]. Furthermore, different alternatives exist for the definition of the virtual velocity field and the domain of integration [308, 114, 5] as well as the basis on which the tensor components refer to [113, 114].

Alternative methods of SIF extraction, employed in the XFEM/GFEM context, include direct extraction based on the enriched degree of freedom values [350, 176, 356, 71], Irwin's integral [162, 163, 299, 339, 338], and extraction through crack opening displacements [277]. The former technique relies on the fact that when vector enrichment is used, the physical meaning of the enriched degrees of freedom corresponding to the tip enriched nodes is by definition equivalent to the SIFs.

In several works [350, 176, 356], the technique is combined to degree of freedom gathering and the use of higher order terms of the Williams expansion to increase the accuracy of the extracted SIFs. Similarly, extraction using Irwin's integral also requires higher order enrichment. A relative advantage of both of these methods is their low computational cost and the fact that they do not require the use of auxiliary fields as in the interaction integral method. Extraction through crack opening displacements [277] does not require the use of higher order enrichment functions and is computationally inexpensive, it does however employ auxiliary fields. Finally, it should be mentioned that even though some of the above methods might be advantageous for certain problems, the interaction integral method is in general more accurate and has in general a wider field of applicability since domain integral formulations are available also for problems outside the LEFM domain.

A.1.0.16 Determination of the crack propagation increment

While the direction of crack propagation can be obtained using the SIFs through one of the available criteria, the length of the propagation increment is typically predefined and constant during the simulation. Nevertheless, this length is probably the parameter with the more pronounced effect on the crack paths obtained and should be set as small as possible. On the other hand, the length of this increment Δa is subject to the following constraint [307, 137]:

$$\Delta a > r_d > 1.5h \tag{A.14}$$

where h is the mesh size. This constraint is necessary to ensure that the crack will be indeed straight within the domain of integration, whose radius in turn needs to be larger than $1.5h$ in order to include a ring of elements around the crack tip. Thus, the length of the crack increment is essentially determined by the mesh size. Nonetheless, if an alternative interaction integral formulation or extraction method is used, as discussed in the previous section, the constraint could be removed or at least relaxed allowing to reduce the length of the crack increments without refining the mesh.

For the case of multiple cracks [61], a stability analysis is usually conducted to determine active cracks at each step, while in the three dimensional case, Paris's law is a common choice [118] for determining the propagation increment for different points along the crack front.

A.1.0.17 Applications in fracture mechanics and extensions

As a result of the extensive research conducted in almost two decades, the method has reached a level of maturity that allows its application in a wide range of problems of both academic and industrial interest. Some representative applications would include damage tolerance assessment of aerospace structures [49] and hydraulic fracturing [165]. Significant research effort has also been devoted in implementing the method both in a procedural [307, 314] and object oriented framework [50, 186]. Thus, implementations of the method can be found in several open source libraries and commercial software packages such as Ansys and Abaqus.

The range of possible applications includes problems far more challenging than two-dimensional linear elastic crack propagation. For instance, the method can be extended to three dimensions in a straightforward way [308, 206, 118], while the treatment of problems involving multiple cracks [61, 314, 313, 315] is also possible. The extension to dynamic crack propagation can be challenging, it is however possible and has been studied in several works, for instance references [42, 268, 196]. The method's flexibility also allows for application to problems involving different types of material models, for instance orthotropic [22], or in the nonlinear domain hyperelastic [166] and elastic-plastic [257]. Finally, other models for fracture, such as the cohesive zone model [204, 365], can also be incorporated with relative ease.

A.2 Phase Field Methods

PFM emerged as an alternative to discrete fracture aiming to address some of the challenges of computational fracture mechanics, e.g., automatic crack initiation, robust resolution of branching and merging and also the treatment of curved crack paths. The PFM diffusive crack interface is represented by a scalar variable, i.e., the phase field. The latter evolves according to a set of governing equations arising from a robust variational structure. As a result, the method does not require numerical tracking of the evolving discrete crack topologies and complex problems as in the case of 3D crack paths [see, e.g., 52, 174, 197, 122] and dynamic fragmentation are naturally resolved [278].

PFM emerged from the pioneering work of Francfort and Marigo [101] who proposed a variational theory of fracture based on energy minimization principles. Bourdin, Francfort, and Marigo [58] provided a regularised formulation by introducing a length scale parameter that rendered the approach more suitable for numerical approximations. The variational formulation was further modified and extended to multi-dimensional mixed-mode dynamic brittle fractures [198, 197, 155] also targeting the response of high performance composites [258, 220, 128]. The PFM for brittle fracture has been implemented in the commercial software Abaqus [290] via a User Element subroutine by Msekh et al. [214], which was later extended by Liu et al. [174]. Li, Zhang, and Zheng [170] (see, also, [167]) combined the variational phase field model of brittle fracture with an extended Cahn-Hilliard model [2, 322], and formulated a fourth-order phase field model suitable resolving crack propagation in anisotropic materials. Rate-dependent PFM models for modelling fracture in visco-elastic solids [282] have also been established.

The phase field representation of fracture has been extended to the ductile regime [14, 15, 53, 157] also within the context finite strains. The PFM has found application in the simulation of fractures in plates and shells [12, 149, 265], which involve a 3-D degradation of induced stresses whereas the element kinematics and damage are defined at the mid-surface. Attempts to experimentally validate the method have also been provided [see, e.g., 15].

Verhoosel and Borst [332] attempted to model cohesive fractures in composite materials using PFM by casting the cohesive zone approach in an energetic framework and introducing an auxillary field in addition to the displacement and phase field which represents the jump in displacement across the cracked domain. The motivation to use an auxillary field is to define the crack opening in cohesive fracture as a properly defined kinematic quantity, rather than an internal discontinuity as in the case of brittle fracture. Vignollet et al. [333] further extended the phase field based cohesive fracture formulation for the case of propagating cracks. This approach succeeds in achieving convergence with lesser number of elements and in contrast to brittle fracture, confines the length scale parameter only to topological approximations hence rendering it uninfluential for the mechanical behaviour of the structure. Nguyen et al. [225] proposed a new phase field formulation which could model the interaction between interfacial damage and bulk brittle damage for complex topologies arising from voxel-based models of microtomography images. The formulation used a level-set method to describe the diffused jump in displacement field and used the phase field variable, instead of an additional internal variable as in [332], to model crack opening and reclosure during cohesive fractures.

There have been several recent efforts emphasizing the requirement of a generalized cohesive description of fracture using the phase field method [107, 346], see, also Lorentz [181]. More specifically, Wu and Nguyen [346] proposed a unified phase field theory, namely the PF-CZM, for brittle and quasi-brittle fractures which converges to a cohesive zone model within the limits of a vanishing length-scale parameter. More importantly, the authors provided a method for the precise fitting of linear, exponential, and hyperbolic softening laws. PF-CZM was compared to the XFEM in [347] and further extended to the case of dynamic fracture in [227]. Furthermore, Geelen et al. [107] extended the work introduced in [183] to a dynamic cohesive fracture model incorporating phase field formulations.

The fundamental features of the phase field method are discussed in the following section.

A.2.0.1 PFM variational formulation

Griffith [121] postulated that the total potential energy Π of an elastic body undergoing elastic fracture comprises the contributions of the elastic strain energy Ψ_e and the fracture energy Ψ_f

$$\Pi(\mathbf{u},\Gamma) = \Pi_e + \Pi_f = \int_{\Omega} \psi_e d\Omega + \int_{\Gamma} \mathscr{G}_c d\Gamma \tag{A.15}$$

where ψ_e is the elastic energy density and $\mathscr{G}_c$ is the critical fracture energy density. The elastic energy density for the case of an isotropic medium is defined as

$$\psi_e(\boldsymbol{\varepsilon}) = \frac{1}{2}\lambda[\mathrm{Tr}(\boldsymbol{\varepsilon})]^2 + \mu\left[\mathrm{Tr}\left(\boldsymbol{\varepsilon}^2\right)\right] \tag{A.16}$$

where λ and μ are the Lamé constants.

Phase field modelling of fracture approximates the fracture surface integral expression introduced in Eq. (A.15) with a volume integral defined over the entire deformable domain Ω according to Eq. (A.17) below.

$$\int_{\Gamma} \mathscr{G}_c d\Gamma \approx \int_{\Omega} \mathscr{G}_c F_\Gamma(c, \nabla c) d\Omega \tag{A.17}$$

where $c = c(\mathbf{x}) \in [0,1]\ \forall \mathbf{x} \in \Omega$ is the scalar phase field representing crack.

Using Eq. (A.17), the expression of the potential energy of the elastic deformable body introduced in Eq. (A.15) can be modified into the following form

$$\Pi \approx \int_{\Omega} \psi_e d\Omega + \overbrace{\int_{\Omega} \mathscr{G}_c F_\Gamma d\Omega}^{Fracture\,Energy\,Approximation} - \left(\int_{\Omega} u_i b_i d\Omega + \int_{\partial\Omega_{\bar{\mathbf{t}}}} u_i \bar{t}_i d\Omega_{\bar{\mathbf{t}}} \right) \tag{A.18}$$

The functional F_Γ assumes the following generic form

$$F_\Gamma = \frac{1}{c_w}\left(\frac{1}{2l_0}\omega(c) + 2l_0 |\nabla c|^2 \right), \tag{A.19}$$

where $l_0 \in \mathbb{R}$ is a length scale parameter and $\omega(c)$ and c_w are the generic crack geometric function and associated constant; these assume different expressions based on the type of fracture surface energy approximation used.

With the introduction of the crack surface density function in Eq. (A.19), the discrete description of a sharp crack Γ_c in Fig. 2.1 is transformed onto a diffused crack description as shown in Fig. A.1 via the regularized crack functional $\Gamma_{l_0}(c)$ which is scaled by the length-scale parameter l_0 (A.20).

$$\Gamma_{l_0}(c) = \int_{\Omega} F_\Gamma(c, \nabla c) d\Omega \tag{A.20}$$

The length scale parameter l_0 is the regularisation length over which damage diffuses as shown in Fig. A.1. In the conventional phase field formulation, originally presented in Bourdin, Francfort, and Marigo [58], the peak force reached before the onset of fracture depends on the value of length-scale parameter l_0. Higher values of the length-scale parameter lead to lower peak forces and vice versa. In recent formulations, see, e.g., Wu and Nguyen [346] and Geelen et al. [107] this is alleviated, hence providing a significant advantage in enhancing the critical-stress predicting capabilities of the phase field method. In Miehe, Schaenzel, and Ulmer [201], generalized crack-driving forces with a failure criteria based on the maximum principal stress were introduced which also succeeded in predicting critical fracture loads unaffected by the length-scale parameter. However in notched structures, a crack nucleation principle based purely on the maximum principal stress criteria suffers from the curse of stress singularity at the notch-tip as also highlighted in [318].

Providing different expressions for $\omega(c)$ and c_w results in variants of the phase field approximation; key variants, i.e., the second and fourth order quadratic approximations and the second order linear phase field approximation are discussed in sections A.2.0.2, A.2.0.3 , and A.2.0.4, respectively. A schematic of the variation of the phase field c in the direction normal to the crack surface for all phase field variants considered as compared to the discrete fracture case is provided in Fig. A.2. In all cases, the phase field value $c = 1$ corresponds to an un-cracked region, whereas $c = 0$ corresponds to a cracked region.

Remark. *From a geometric standpoint, the length scale parameter regularises the width of the crack as shown in Figure A.1 in accordance with [58], see, also Borden et al. [52]. It is of interest to note that the length scale considered in Miehe, Hofacker, and Welschinger [198] (see, also, [197, 200]) is double the size of the one adopted in [58, 52]. Of course, both implementations are equivalent; one however should be careful*

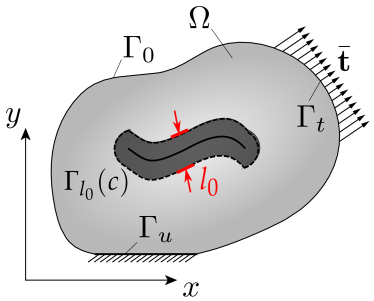

Fig. A.1: Description of diffused crack scaled by the length-scale parameter l_0 and boundary conditions.

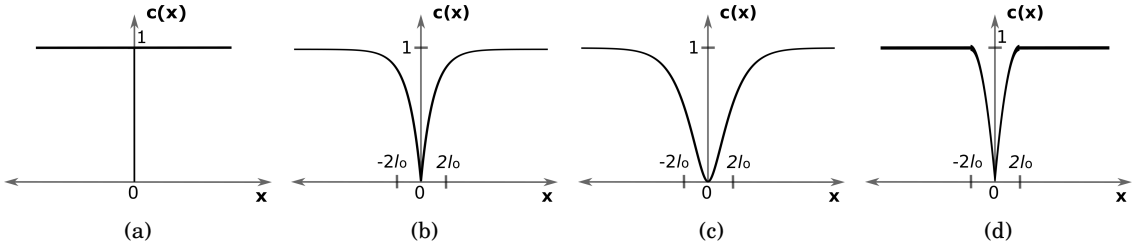

Fig. A.2: 1-D spatial variation of phase-field $c(x)$ for a) Discrete crack b) Diffused crack with second-order quadratic approximation c) Diffused crack with fourth-order quadratic approximation, and d) Diffused crack with second-order linear approximation.

to appropriately adapt the length scale parameter when comparing between the two. In this work, we comply with the former definitions.

A.2.0.2 Second-order quadratic approximation

For the second-order quadratic approximation, the 1-D spatial variation of phase-field variable $c(x)$ can be expressed as (Fig. A.2b):

$$c(x) = 1 - e^{-|x|/2l_0} \tag{A.21}$$

It is straight-forward to show that the width of diffusion zone decreases with decreasing the value of length-scale parameter l_0, which can also be seen in Fig. A.3.

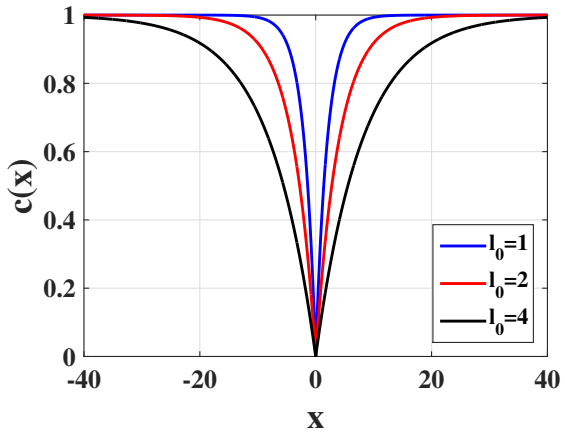

Fig. A.3: Second-order quadratic approximation: Effect on length-scale parameter l_0 on the width of diffusion

The specific second order functional proposed in Bourdin, Francfort, and Marigo [58] can be retrieved

by modifying the general form of Eqs. (A.17)-(A.19) and considering the following definitions in Eq. (A.22)

$$\begin{aligned} c_w &= 2 \\ \omega(c) &= (c-1)^2 \end{aligned} \tag{A.22}$$

Hence, the crack surface energy approximation assumes the following form

$$\begin{aligned} F_\Gamma &= \left[\frac{(c-1)^2}{4l_0} + l_0 |\nabla c|^2 \right] \\ \int_\Gamma \mathcal{G}_c d\Gamma &\approx \int_\Omega \mathcal{G}_c \left[\frac{(c-1)^2}{4l_0} + l_0 |\nabla c|^2 \right] d\Omega \end{aligned} \tag{A.23}$$

A.2.0.3 Fourth-order quadratic approximation

A fourth-order quadratic approximation is established considering the definition introduced in [51], i.e.,

$$\int_\Gamma \mathcal{G}_c d\Gamma \approx \int_\Omega \mathcal{G}_c \left[\frac{(c-1)^2}{4l_0} + \frac{l_0}{2} |\nabla c|^2 + \frac{l_0^3}{4} (\Delta c)^2 \right] d\Omega \tag{A.24}$$

The expression for $c(x)$ for the fourth-order quadratic approximation can be given as (also shown in Fig. A.2c):

$$c(x) = 1 - e^{-|x|/l_0} \left(1 + \frac{|x|}{l_0} \right) \tag{A.25}$$

The effect of the length-scale parameter on the diffusion width is illustrated in Fig. A.4. The higher-order term introduced in Eq. (A.24) leads to greater regularity of the phase-field solution, and improves its convergence rate and accuracy. However due to increased continuity requirements of the solution, the basis functions used for numerical interpolation must be at least (C^1) continuous, for e.g. hierarchically refined B-splines used within an isogeometric analysis framework [51]. It should also be noted that the use of 4^{th}-order model leads to a more accurate approximation of stresses, which in turn facilitates higher rates of crack growth. More applications of higher-order phase-field models can be found in [51, 85, 102].

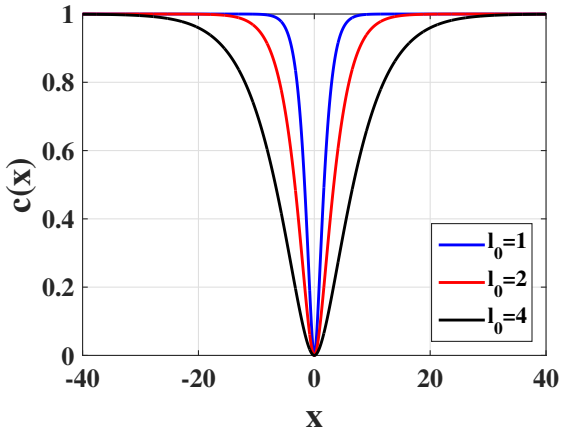

Fig. A.4: Fourth-order quadratic approximation: Effect of the length-scale parameter l_0 on the width of diffusion

A.2.0.4 Linear approximation

In the quadratic approximations shown in sections A.2.0.2 and A.2.0.3, the phase field variable and therefore the degradation function evolve as soon as the structure is loaded. This is clearly not the case in purely elastic brittle materials that demonstrate a linear elastic behavior until a crack initiates.

Pham et al. [255] addressed this issue by employing a linear approximation of the surface energy integral to achieve a diffused localization band and a purely elastic global response until the onset of damage. The 1-D expression for $c(x)$ in this case can be given as in Eq. (A.26), which is also illustrated in Fig. A.2d (See also Fig. A.5).

$$c(x) = 1 - \left(\frac{|x|}{2l_0} - 1\right)^2 \tag{A.26}$$

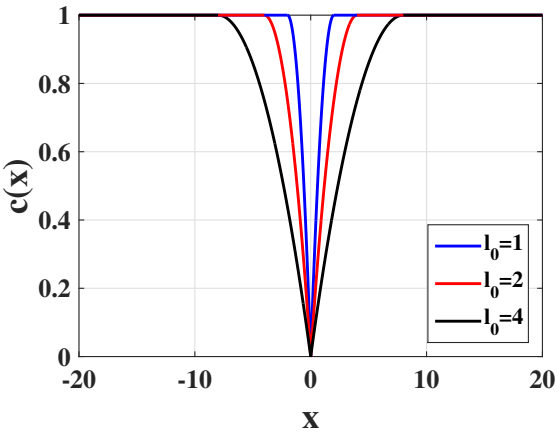

Fig. A.5: Second-order linear approximation: Effect of the length-scale parameter l_0 on the width of diffusion.

More recently, Geelen et al. [107] provided an analogous linear approximation based on the following expressions for c_w and $\omega(c)$

$$\begin{aligned} c_w &= \frac{16}{3} \\ \omega(c) &= 4(1-c) \end{aligned}, \tag{A.27}$$

which result in the following definition of the crack functional

$$F_\Gamma = \frac{3}{8l_0}\left[1 - c + l_0^2|\nabla c|^2\right]. \tag{A.28}$$

In view of Eq. (A.29), the approximation of the surface energy integral in Eq. (A.17) assumes the following form

$$\int_\Gamma \mathscr{G}_c d\Gamma \approx \int_\Omega \frac{3\mathscr{G}_c}{8l_0}\left[1 - c + l_0^2|\nabla c|^2\right] d\Omega \tag{A.29}$$

The linear approximation in Eq. (A.29) differs from the corresponding formulation in [107] in the sense that a fully cracked-state in the current study is represented by $c = 0$ in the current study, as opposed to $c = 1$ in [107]. In addition, the total diffusion width in the current model [Eq. (A.29) and Fig. A.2d] is twice the diffusion width in [107] to maintain consistency with other models.

It is of interest to note that the quadratic form (Eqs. (A.23)-(A.24)) implicitly guarantees the boundedness of the phase field variable c within the limits $[0,1]$. However, the solution obtained by Eq. (A.28) is not intrinsically bounded within this interval, and additional constraints must be imposed to ensure boundedness.

This is achieved by employing a Penalty [see, e.g., 110] or a Lagrange multiplier method [see, e.g, 107]. In both methods, a staggered iterative scheme is required for the solution of the resulting constrained system of governing phase-field equation. To guarantee both the boundedness and irreversibility of the phase field variable, Gerasimov and De Lorenzis [110] proposed a method to choose the value of an optimal or lower bound of the penalty parameter beyond which adequate constraint enforcement can be ensured.

A.2.0.5 Material Degradation

The expression of the potential energy introduced in Eq. (A.15) implies that in a given conservative system, any increase in the fracture energy due to a unit increase in the fracture surface has to be compensated by a corresponding decrease in the elastic strain energy. Hence, the expression of the elastic energy must be coupled to the evolution of the phase field c as the latter dictates the value of the fracture energy. In physical terms, the phase field has to account for the gradual degradation of material stiffness as cracks propagate through the medium.

Mathematically, this has been expressed through the definition of a degradation function, $g(c)$, which is then used to reduce the value material elastic energy density giving rise to the so called isotropic phase field methods. Driven from the fact that such an approach led to unrealistic and in cases erroneous results, e.g., cracks initiating and propagating due to pure compression later attempts postulated material degradation on the basis of an energy split, i.e.,

$$\psi_e = g(c)\,\psi_e^+ + \psi_e^- \tag{A.30}$$

where ψ_e^+ and ψ_e^- are the elastic strain energy densities whose expressions are specific to the type of energy split adopted, see, e.g., Miehe, Welschinger, and Hofacker [197] for an energy decomposition based on the spectral decomposition of the strain tensor and Amor, Marigo, and Maurini [17] for a volumetric/ deviatoric decomposition giving rise to the so called anisotropic degradation models. It is of interest to note that although anisotropic models mitigated the unrealistic crack patterns derived from the isotropic ones for most typical stress states, the problem is not yet fully resolved. The volumetric split defined in [17] may still result in degradation under a pure compressive stress state. The spectral decomposition model defined in [197] leads to a strongly non-linear stress-strain relation that has been shown to be computationally taxing (see e.g. [13] for a detailed comparison of these two models).

The expression of the degradation function $g(c)$ is not unique see, e.g., [345, 107, 57, 147, 53, 158, 183, 182, 11]. A widely used definition for the degradation function that is compatible with the first and second order quadratic approximations provided in Eq. (A.23) and (A.24), respectively is

$$g(c) = \left[(1-k)\,c^2 + k\right] \tag{A.31}$$

where k in Eq. (A.31) is a model parameter utilized in several applications, see, e.g., [17, 37] as a way to avoid ill-posedness. Geelen et al. [107] introduced an quasi-quadratic definition of $g(c)$ to be employed in conjuction with the linear approximation defined in Eq. (A.28) that is defined as

$$g(c) = \frac{c^2}{c^2 + m(1-c)[1+p(1-c)]} \;\text{ with } p \geq 1 \;\text{ and } l_0 < \frac{3E\mathcal{G}_c}{4(p+2)\sigma_c^2} \tag{A.32}$$

where $m = (3\mathcal{G}_c)/(8l_0\psi_c) = g'(c_0)$ is the initial slope of the degradation function $g(c)$ and p provides the initial slope and shape parameters for the softening curve assuming $c_0 = 1$ as the initial phase-field. Here, $\psi_c = (\sigma_c^2)/(2E)$ is the critical fracture energy per unit volume of the material, in which σ_c and E represent the critical tensile strength and Young's modulus of the material respectively. This definition, however, comes with an additional upper bound restriction on the value of length-scale parameter l_0 which is necessary to achieve optimal convergence. The upper bound on the regularization length is related to the characteristic length of the fracture process zone $l_{FPZ} = (E\mathcal{G}_c)/(\sigma_c^2)$, see [131, 107] for details.

Substituting Eq. (A.30) in Eq. (A.18), the expression for the brittle fracture potential energy assumes the following form

$$\Pi \approx \int_\Omega g(c)\psi_e^+ d\Omega + \int_\Omega \psi_e^- d\Omega + \int_\Omega \mathcal{G}_c F_\Gamma d\Omega - \left(\int_\Omega u_i b_i d\Omega + \int_{\partial\Omega_{\bar{\mathbf{t}}}} u_i \bar{t}_i d\Omega_{\bar{\mathbf{t}}} \right) \tag{A.33}$$

where definitions of ψ_e^+ and ψ_e^- are specific to the energy split adopted and $g(c)$, F_Γ may be chosen based on the table below.

$g(c)$	F_Γ	Reference
$\left[(1-k)c^2+k\right]$ Eq. (A.31)	$\left[\frac{(c-1)^2}{4l_0}+l_0\lvert\nabla c\rvert^2\right]$ Eq. (A.23)	Borden et al. [52]
$\frac{c^2}{c^2+m(1-c)[1+p(1-c)]}$ Eq. (A.32)	$\frac{3}{8l_0}\left[1-c+l_0^2\lvert\nabla c\rvert^2\right]$ Eq. (A.28)	Geelen et al. [107]

A.2.0.6 PFM strong form

The Euler-Lagrange equations of the displacement $\mathbf{u}(\mathbf{x},t)$ and phase field $c(\mathbf{x},t)$ coupled formulation of the Lagrangian functional are employed to derive the strong form of the quasi-static brittle-fracture phase field formulation. The latter assumes the following general form:

$$\nabla\boldsymbol{\sigma}+\mathbf{b}=0 \qquad \text{, on } \Omega \tag{A.34}$$

$$\mathscr{G}_c\delta_c(F_\Gamma)=-g'(c)\tilde{D} \qquad \text{, on } \Omega \tag{A.35}$$

where $\delta_c(F_\Gamma)$ denotes the derivative of surface energy approximation function F_Γ with respect to the phase field variable c, and $\tilde{D}$ is the energetic crack-driving force which depends on the phase field formulation used. A detailed description on the different crack-driving forces that can be employed in conjuction with Eq. (A.35) is provided in Miehe, Schaenzel, and Ulmer [201].

The coupled field Eqs. (A.34) and (A.34) are subject to boundary conditions introduced in Eq. (2.1) supplemented by

$$\frac{\partial c}{\partial x_i}n_i=0 \qquad \text{on} \qquad \Gamma_c^t. \tag{A.36}$$

where $n_i, i=1\ldots r$ is the outward-pointing normal vector to the crack boundary. The Cauchy stress tensor $\boldsymbol{\sigma}\in R^{r\times r}$ is defined as

$$\sigma_{ij,e}=\frac{\partial\psi_e}{\partial\varepsilon_{ij}} \tag{A.37}$$

Hence, substituting Eq. (A.30) into Eq. (A.37) gives rise to the degraded Cauchy stress tensor

$$\boldsymbol{\sigma}=\sigma_{ij}=g(c)\frac{\partial\psi_e^+}{\partial\varepsilon_{ij}}+\frac{\partial\psi_e^-}{\partial\varepsilon_{ij}}=g(c)\boldsymbol{\sigma}^++\boldsymbol{\sigma}^- \tag{A.38}$$

where $g(c)$ takes one of the forms shown in Eqs. (A.31) and (A.32) depending upon the formulation.

A.2.0.7 Derivation of phase field evolution equation in Borden et al. [52] from the general form

The phase field evolution equation employed in Borden et al. [52] can be obtained from the general expression of the strong form (Eqs. (A.34) and (A.35)), considering the expressions for F_Γ and $g(c)$ from Eq. (A.23) and (A.31), i.e.,

$$\begin{aligned} F_\Gamma&=\left[\frac{(c-1)^2}{4l_0}+l_0\lvert\nabla c\rvert^2\right] \;\;;\;\; \delta_c(F_\Gamma)=\left[\frac{(c-1)}{2l_0}-2l_0\Delta c\right] \\ g(c)&=(1-k)c^2+k \;\;;\;\; g'(c)=2(1-k)c \end{aligned} \tag{A.39}$$

In the original formulations of Miehe, Hofacker, and Welschinger [198], which is later also adopted in [52], the crack driving force $\tilde{D}$ was the positive part of the elastic strain energy density, i.e.,

$$\tilde{D}=\psi_e^+ \tag{A.40}$$

where ψ_e^+ is the tensile part of strain energy density taken from [197].
Substituting Eq.(A.40) in Eq. (A.35) and considering also Eqs. (A.39) the following evolution equation is derived, i.e.,

$$\left(\frac{4l_0(1-k)\psi_e^+}{\mathscr{G}_c}+1\right)c-4l_0^2\Delta c=1, \text{ on } \Omega \tag{A.41}$$

which is a linear differential equation with respect to c. It is of interest to note that the Laplacian of

the phase field in Eq. (A.41) is scaled by the squared value of the length scale parameter hence it rapidly vanishes for small values of l_0 compared to the c.

A.2.0.8 Derivation of cohesive phase field evolution equation in Geelen et al. [107] from general form

The phase field evolution equation presented in Geelen et al. [107] can be obtained from the general expression of the coupled strong form considering the following expressions for F_Γ, $\delta_c(F_\Gamma)$, and $g(c)$

$$\begin{aligned} F_\Gamma &= \frac{3}{8l_0}\left[1-c+l_0^2|\nabla c|^2\right] \quad ; \quad \delta_c(F_\Gamma) = \frac{3}{8l_0}\left[-1-2l_0^2\Delta c\right] \\ g(c) &= \frac{c^2}{c^2+m(1-c)[1+p(1-c)]} \text{ with } p \geq 1 \text{ and } l_0 < \frac{3E\mathscr{G}_c}{4(p+2)\sigma_c^2} \end{aligned} \tag{A.42}$$

Substituting Eqs. (A.42) into Eq. (A.35) and performing the necessary algebraic manipulations results in the following expression Geelen et al. [107].

$$\frac{3\mathscr{G}_c}{8l_0}\left[2l_0^2\Delta c+1\right] - g'(c)\tilde{D} = 0, \text{ on } \Omega \tag{A.43}$$

where

$$\tilde{D} = \max(\psi_c, \psi_e^+) \tag{A.44}$$

and $\psi_c = \sigma_c^2/2E$. Specific to this formulation, an additional augmented Lagrange constraint is incorporated to ensure the smooth monotonic evolution of the phase field variable c, such that $\dot{c} \leq 0$. In view of this, Eq. (A.43) transforms into the following expression:

$$\frac{3\mathscr{G}_c}{8l_0}\left[2l_0^2\frac{\partial^2 c}{\partial x_i^2}+1\right] - g'(c)\tilde{D} + \langle \lambda + \gamma(c-c^{n-1})\rangle_+ = 0, \text{ on } \Omega \tag{A.45}$$

where $\lambda \in L^2(\Omega)$ are Lagrange multipliers and $\gamma \in R_{>0}$ is the penalty kernel. c^{n-1} is the value of phase field at preceding $(n-1)^{th}$ time-increment.

A.2.0.9 Irreversibility Conditions

The expression of the potential energy defined in Eq. (A.33) implies that regardless of the value of the degradation function, the fracture energy would need to further increase in the case of unloading to compensate for the corresponding elastic energy decrease. This is also derived on the basis of Eqs. (A.41), i.e., the strong form of the coupled system. In particular, the second of Eqs. (A.41) would result in an increasing value of the phase field for decreasing values of the elastic energy potential in the case of unloading. This would correspond to a reduction in the crack length, thus negating the irreversibility condition

$$\Gamma^{(t+\Delta t)} \supseteq \Gamma^{(t)} \tag{A.46}$$

Amongst the various irreversibility constraints proposed within the phase field literature, the history variable approach given by Miehe, Hofacker, and Welschinger [198] is most widely applied. Based on the theoretical arguments provided in [198], irreversibility is enforced by introducing a so-called history variable such that the following Kuhn-Tucker conditions hold

$$\psi_e^+ - \mathscr{H} \leq 0 \quad \dot{\mathscr{H}} \geq 0 \quad \dot{\mathscr{H}}\left(\psi_e^+ - \mathscr{H}\right) = 0 \tag{A.47}$$

where $\mathscr{H}$ is a history field.

Some other recent works have also proposed penalty and augmented Lagrange methods for imposing the irreversibility constraints on the phase field equations, see for e.g. [110, 107], so that the monotonicity of the phase field variable constantly holds. It is to be noted that these methods provide a more natural way of imposing the constraints, and do not disrupt the original variational nature of the phase field equations. Eq. (A.45) employs such an augmented Lagrange constraint to ensure the monotonic evolution of phase field variable.

A.2.0.10 Effective critical energy release-rate

In the original variational formulation proposed by Bourdin, Francfort, and Marigo [58], it was shown that the fracture energy is slightly overestimated during simulations and the amount of this amplification depends upon the size of elements in the overall finite-element discretization. This amplification effect must be compensated by defining an effective critical energy release rate G_c^{eff} for the purpose of phase-field simulation (see also [254]).

$$G_c^{eff} = \frac{G_c^{actual}}{1+(h/4l_0)} \tag{A.48}$$

where G_c^{actual} and G_c^{eff} are the actual and effective critical energy release rates respectively. It must be emphasized that using the amplified value of material fracture energy G_c^{actual} leads to overestimation of critical fracture loads in comparison to discrete fracture methods, and hence for all practical purposes G_c^{eff} must be used while solving the phase-field evolution equation. This would also be highlighted in detail in the numerical examples section.

A.2.0.11 Galerkin approximation

The strong form of the coupled governing Eqs. (A.41) and (A.45) are set in a discrete form following standard Galerkin approximation. In this setting, the trial solution spaces are defined as

$$S_u = \left\{ \mathbf{u} \in \left(H^1(\Omega)\right)^d \middle| \mathbf{u} = \bar{\mathbf{u}} \text{ on } \partial\Omega_b \right\} \tag{A.49}$$

and

$$S_c = \left\{ c \in H^1(\Omega) \right\} \tag{A.50}$$

for the displacement field and the phase field respectively. Corresponding weighting functions spaces are further defined as

$$W_u = \left\{ \mathbf{w}^u \in \left(H^1(\Omega)\right)^d \middle| \mathbf{w}^u = \bar{\mathbf{w}}^u \text{ on } \partial\Omega_b \right\} \tag{A.51}$$

and

$$W_c = \left\{ w^c \in H^1(\Omega) \right\} \tag{A.52}$$

Multiplying Eq. (A.34) with the weighting functions (A.51) and performing the necessary integration by parts leads to the standard weak form of the equilibrium equation

$$\int_\Omega \boldsymbol{\sigma} \cdot \nabla \mathbf{w}^u \, d\Omega - \int_\Omega \boldsymbol{b} \cdot \mathbf{w}^u \, d\Omega - \int_{\partial\Omega_{\bar{\mathbf{t}}}} \bar{\boldsymbol{t}} \cdot \mathbf{w}^u \, d\partial\Omega_{\bar{\mathbf{t}}} = 0 \tag{A.53}$$

Multiplying Eq. (A.41) with the weighting functions (A.52) and performing the necessary algebraic manipulation gives rise to the phase field weak form employed in [52]

$$\int_\Omega \left(\left[\frac{4l_0(1-k)\mathscr{H}}{\mathscr{G}_c} + 1 \right] c, w^c \right) d\Omega + \int_\Omega \left(4l_0^2 \nabla c, \nabla w^c \right) d\Omega - \int_\Omega \left(1, w^c\right) d\Omega = 0 \tag{A.54}$$

Similarly, the cohesive phase field weak form derived from Eq. (A.45) assumes the following form

$$\int_\Omega (g'(c)\tilde{D}, w^c) \, d\Omega + \int_\Omega \frac{3\mathscr{G}_c}{8l_0} \left[-(1, w^c) + \left(2l_0^2 \nabla c, \nabla w^c \right) \right] d\Omega + \int_\Omega (\langle \lambda + \gamma(c - c^{n-1}) \rangle_+, w^c) \, d\Omega = 0 \tag{A.55}$$

The weak forms introduced in Eqs.(A.54) or (A.55) can be further discretised employing either mesh-based, i.e., the FEM, mesh-less methods, see, e.g., [281] or MPM [143]. The resulting discrete equations are then solved in an incremental fashion. Due to the nonlinear nature of $g(c)$, the resulting discrete problem is a nonlinear one, even for the case of elastic fracture, hence necessitating the use of iterative solvers.

B List of Figures

C List of Tables

Bibliography

[1] Y. Abdelaziz and A. Hamouine. “A survey of the extended finite element”. In: *Computers & structures* 86.11 (2008), pp. 1141–1151.

[2] T. Abinandanan and F. Haider. “An extended Cahn-Hilliard model for interfaces with cubic anisotropy”. In: *Philosophical Magazine A* 81.10 (2001), pp. 2457–2479.

[3] K. Agathos, S. Bordas, and E. Chatzi. “Improving the conditioning of XFEM/GFEM for fracture mechanics problems through enrichment quasi-orthogonalization”. In: *Computer Methods in Applied Mechanics and Engineering* (2018).

[4] K. Agathos, E. Chatzi, and S. Bordas. “A unified enrichment approach addressing blending and conditioning issues in enriched finite elements”. In: *Computer Methods in Applied Mechanics and Engineering* (2018 (under review)).

[5] K. Agathos, E. Chatzi, and S. Bordas. “Stable 3D extended finite elements with higher order enrichment for accurate non planar fracture”. In: *Computer Methods in Applied Mechanics and Engineering* 306 (2016), pp. 19–46.

[6] K. Agathos et al. “A well-conditioned and optimally convergent XFEM for 3D linear elastic fracture”. In: *International Journal for Numerical Methods in Engineering* 105.9 (2016), pp. 643–677.

[7] K. Agathos et al. “Stable 3D XFEM/vector level sets for non-planar 3D crack propagation and comparison of enrichment schemes”. In: *International Journal for Numerical Methods in Engineering* 113.2 (2018), pp. 252–276.

[8] K. Agathos et al. “Well Conditioned Extended Finite Elements and Vector Level Sets for Three-Dimensional Crack Propagation”. In: *Geometrically Unfitted Finite Element Methods and Applications*. Springer, 2017, pp. 307–329.

[9] F. Aldakheel et al. “Phase-field modeling of brittle fracture using an efficient virtual element scheme”. In: *Computer Methods in Applied Mechanics and Engineering* 341 (2018), pp. 443–466.

[10] R. Alessi, S. Vidoli, and L. De Lorenzis. “A phenomenological approach to fatigue with a variational phase-field model: The one-dimensional case”. In: *Engineering Fracture Mechanics* 190 (2018), pp. 53–73.

[11] R. Alessi, J.-J. Marigo, and S. Vidoli. “Gradient damage models coupled with plasticity: variational formulation and main properties”. In: *Mechanics of Materials* 80 (2015), pp. 351–367.

[12] M. Ambati and L. De Lorenzis. “Phase-field modeling of brittle and ductile fracture in shells with isogeometric NURBS-based solid-shell elements”. In: *Computer Methods in Applied Mechanics and Engineering* 312 (2016), pp. 351–373.

[13] M. Ambati, T. Gerasimov, and L. De Lorenzis. “A review on phase-field models of brittle fracture and a new fast hybrid formulation”. In: *Computational Mechanics* 55.2 (2015), pp. 383–405.

[14] M. Ambati, T. Gerasimov, and L. De Lorenzis. “Phase-field modeling of ductile fracture”. In: *Computational Mechanics* 55.5 (2015), pp. 1017–1040.

[15] M. Ambati, R. Kruse, and L. De Lorenzis. “A phase-field model for ductile fracture at finite strains and its experimental verification”. In: *Computational Mechanics* 57.1 (2016), pp. 149–167.

[16] L. Ambrosio and V. M. Tortorelli. “Approximation of functional depending on jumps by elliptic functional via Γ -convergence”. In: *Communications on Pure and Applied Mathematics* 43.8 (1990), pp. 999–1036.

[17] H. Amor, J.-J. Marigo, and C. Maurini. “Regularized formulation of the variational brittle fracture with unilateral contact: numerical experiments”. In: *Journal of the Mechanics and Physics of Solids* 57.8 (2009), pp. 1209–1229.

[18] T. L. Anderson. *Fracture mechanics: fundamentals and applications*. CRC press, 2017.

[19] J. E. Andrade and X. Tu. “Multiscale framework for behavior prediction in granular media”. en. In: *Mechanics of Materials* 41.6 (June 2009), pp. 652–669.

[20] E. Andreassen et al. “Efficient topology optimization in MATLAB using 88 lines of code”. en. In: *Structural and Multidisciplinary Optimization* 43.1 (Jan. 2011), pp. 1–16.

[21] R. Ansola Loyola et al. “A sequential element rejection and admission (SERA) topology optimization code written in Matlab”. en. In: *Structural and Multidisciplinary Optimization* 58.3 (Sept. 2018), pp. 1297–1310.

[22] A. Asadpoure, S. Mohammadi, and A. Vafai. “Modeling crack in orthotropic media using a coupled finite element and partition of unity methods”. In: *Finite Elements in Analysis and Design* 42.13 (2006), pp. 1165–1175.

[23] F. Auricchio et al. “A simple algorithm for obtaining nearly optimal quadrature rules for NURBS-based isogeometric analysis”. en. In: *Computer Methods in Applied Mechanics and Engineering* 249-252 (Dec. 2012), pp. 15–27.

[24] D. Azócar, M. Elgueta, and M. C. Rivara. “Automatic LEFM crack propagation method based on local Lepp–Delaunay mesh refinement”. en. In: *Advances in Engineering Software* 41.2 (Feb. 2010), pp. 111–119.

[25] B. S. Kirk et al. “`libMesh`: A C++ library for parallel adaptive mesh refinement/coarsening simulations”. In: *Engineering with Computers* 22.3–4 (2006). `http://dx.doi.org/10.1007/s00366-006-0049-3`, pp. 237–254.

[26] I. Babuška and U. Banerjee. “Stable generalized finite element method (SGFEM)”. In: *Computer Methods in Applied Mechanics and Engineering* 201 (2012), pp. 91–111.

[27] I. Babuška, G. Caloz, and J. Osborn. “Special finite element methods for a class of second order elliptic problems with rough coefficients”. In: *SIAM Journal on Numerical Analysis* 31.4 (1994), pp. 945–981.

[28] I. Babuška and J. Melenk. “THE PARTITION OF UNITY METHOD”. In: *International Journal for Numerical Methods in Engineering* 40.4 (1996), pp. 727–758.

[29] I. Babuška. “Homogenization Approach In Engineering”. In: *Computing Methods in Applied Sciences and Engineering*. Ed. by M. Beckmann et al. Vol. 134. Berlin, Heidelberg: Springer Berlin Heidelberg, 1976, pp. 137–153.

[30] E. Barbieri and M. Meo. “A Meshless Cohesive Segments Method for Crack Initiation and Propagation in Composites”. In: *Applied Composite Materials* 18 (2011), pp. 45–63.

[31] G. I. Barenblatt. “The Mathematical Theory of Equilibrium Cracks in Brittle Fracture”. In: *Advances in Applied Mechanics* 7 (1962), pp. 55–129.

[32] R. Barsoum. “On the use of isoparametric finite elements in linear fracture mechanics”. In: *International journal for numerical methods in engineering* 10.1 (1976), pp. 25–37.

[33] K.-J. Bathe. *Finite element procedures*. eng. OCLC: 732251900. Boston, Mass.: Bathe, 2006.

[34] E. Béchet et al. “Improved implementation and robustness study of the X-FEM for stress analysis around cracks”. In: *International Journal for Numerical Methods in Engineering* 64.8 (2005), pp. 1033–1056.

[35] M. Beckers. “Topology optimization using a dual method with discrete variables”. en. In: *Structural Optimization* 17.1 (Feb. 1999), pp. 14–24.

[36] L. Beirão Da Veiga et al. “BASIC PRINCIPLES OF VIRTUAL ELEMENT METHODS”. en. In: *Mathematical Models and Methods in Applied Sciences* 23.01 (Jan. 2013), pp. 199–214.

[37] G. Bellettini and A. Coscia. “Discrete approximation of a free discontinuity problem”. In: *Numerical Functional Analysis and Optimization* 15.3-4 (1994), pp. 201–224.

[38] T. Belytschko and T. Black. “Elastic crack growth in finite elements with minimal remeshing”. In: *International Journal for Numerical Methods in Engineering* 620.July 1998 (1999), pp. 601–620.

[39] T. Belytschko, R. Gracie, and G. Ventura. “A review of extended/generalized finite element methods for material modeling”. In: *Modelling and Simulation in Materials Science and Engineering* 17.4 (2009), p. 043001.

[40] T. Belytschko, L. Gu, and Y. Lu. “Fracture and crack growth by element free Galerkin methods”. In: *Modelling and Simulation in Materials Science and Engineering* 2.3A (1994), p. 519.

[41] T. Belytschko, Y. Lu, and L. Gu. “Element-free Galerkin methods”. In: *International journal for numerical methods in engineering* 37.2 (1994), pp. 229–256.

[42] T. Belytschko et al. “Dynamic crack propagation based on loss of hyperbolicity and a new discontinuous enrichment”. In: *International journal for numerical methods in engineering* 58.12 (2003), pp. 1873–1905.

[43] M. P. Bendsøe. “Optimal shape design as a material distribution problem”. en. In: *Structural Optimization* 1.4 (Dec. 1989), pp. 193–202.

[44] M. P. Bendsøe and O. Sigmund. *Topology Optimization*. en. Berlin, Heidelberg: Springer Berlin Heidelberg, 2004.

[45] M. P. Bendsøe and N. Kikuchi. “Generating optimal topologies in structural design using a homogenization method”. en. In: *Computer Methods in Applied Mechanics and Engineering* 71.2 (Nov. 1988), pp. 197–224.

[46] P. Benner and D. Kressner. “New Hamiltonian Eigensolvers with Applications in Control”. In: IEEE, 2005, pp. 6551–6556.

[47] M. de Berg et al. *Computational Geometry*. en. Berlin, Heidelberg: Springer Berlin Heidelberg, 2008.

[48] T. Bittencourt et al. “Quasi-automatic simulation of crack propagation for 2D LEFM problems”. en. In: *Engineering Fracture Mechanics* 55.2 (Sept. 1996), pp. 321–334.

[49] S. Bordas and B. Moran. “Enriched finite elements and level sets for damage tolerance assessment of complex structures”. In: *Engineering Fracture Mechanics* 73.9 (2006), pp. 1176–1201.

[50] S. Bordas et al. “An extended finite element library”. In: *International Journal for Numerical Methods in Engineering* 71.January (2007), pp. 703–732.

[51] M. J. Borden et al. “A higher-order phase-field model for brittle fracture: Formulation and analysis within the isogeometric analysis framework”. In: *Computer Methods in Applied Mechanics and Engineering* 273 (2014), pp. 100–118.

[52] M. J. Borden et al. “A phase-field description of dynamic brittle fracture”. In: *Computer Methods in Applied Mechanics and Engineering* 217 (2012), pp. 77–95.

[53] M. J. Borden et al. “A phase-field formulation for fracture in ductile materials: Finite deformation balance law derivation, plastic degradation, and stress triaxiality effects”. In: *Computer Methods in Applied Mechanics and Engineering* 312 (2016), pp. 130–166.

[54] R. de Borst and C. V. Verhoosel. “Gradient damage vs phase-field approaches for fracture: Similarities and differences”. In: *Computer Methods in Applied Mechanics and Engineering* 312 (2016), pp. 78–94.

[55] R. Bouc. “Forced vibration of mechanical systems with hysteresis”. In: *Proceedings of the fourth conference on non-linear oscillation*. Prague, Czechoslovakia, 1967.

[56] P. Bouchard, F. Bay, and Y. Chastel. “Numerical modelling of crack propagation: automatic remeshing and comparison of different criteria”. en. In: *Computer Methods in Applied Mechanics and Engineering* 192.35-36 (Aug. 2003), pp. 3887–3908.

[57] B. Bourdin, G. A. Francfort, and J.-J. Marigo. “Numerical experiments in revisited brittle fracture”. In: *Journal of the Mechanics and Physics of Solids* 48.4 (2000), pp. 797–826.

[58] B. Bourdin, G. A. Francfort, and J.-J. Marigo. “The variational approach to fracture”. In: *Journal of elasticity* 91.1-3 (2008), pp. 5–148.

[59] C. Brebbia and J. Dominguez. “Boundary element methods for potential problems”. en. In: *Applied Mathematical Modelling* 1.7 (Dec. 1977), pp. 372–378.

[60] M. K. Brun et al. “An iterative staggered scheme for phase field brittle fracture propagation with stabilizing parameters”. In: *arXiv preprint arXiv:1903.08717* (2019).

[61] E. Budyn et al. “A method for multiple crack growth in brittle materials without remeshing”. In: *International Journal for Numerical Methods in Engineering* 61.10 (2004), pp. 1741–1770.

[62] G. T. Camacho and M. Ortiz. “Computational modelling of impact damage in brittle materials”. In: *International Journal of Solids and Structures* 33.20 (1996), pp. 2899–2938.

[63] F. Cazes and N. Moës. “Comparison of a phase-field model and of a thick level set model for brittle and quasi-brittle fracture”. In: *International Journal for Numerical Methods in Engineering* 103.2 (2015), pp. 114–143.

[64] E. Chahine and P. Laborde. “Crack tip enrichment in the XFEM using a cutoff function”. In: *International journal for numerical methods in engineering* 75.January (2008), pp. 629–646.

[65] E. Chahine, P. Laborde, and Y. Renard. “A non-conformal eXtended Finite Element approach: Integral matching Xfem”. In: *Applied Numerical Mathematics* 61.3 (2011), pp. 322–343.

[66] E. N. Chatzi et al. “Experimental application and enhancement of the XFEM–GA algorithm for the detection of flaws in structures”. en. In: *Computers & Structures* 89.7-8 (Apr. 2011), pp. 556–570.

[67] X. Chen et al. “A quadtree-polygon-based scaled boundary finite element method for crack propagation modeling in functionally graded materials”. en. In: *Theoretical and Applied Fracture Mechanics* 94 (Apr. 2018), pp. 120–133.

[68] Z. Chen et al. “Cohesive zone finite element-based modeling of hydraulic fractures”. In: *Acta Mechanica Solida Sinica* 22 (2009), pp. 443–452.

[69] K. Cheng and T. Fries. “Higher-order XFEM for curved strong and weak discontinuities”. In: *International Journal for Numerical Methods in Engineering* 82.5 (2010), pp. 564–590.

[70] J. Chessa, H. Wang, and T. Belytschko. “On the construction of blending elements for local partition of unity enriched finite elements”. In: *International Journal for Numerical Methods in Engineering* 57.7 (2003), pp. 1015–1038.

[71] N. Chevaugeon, N. Moës, and H. Minnebo. “Improved crack tip enrichment functions and integration for crack modeling using the extended finite element method”. In: *Journal for Multiscale Computational Engineering* 11 (2013), pp. 597–631.

[72] S. R. Chidgzey and A. J. Deeks. “Determination of coefficients of crack tip asymptotic fields using the scaled boundary finite element method”. en. In: *Engineering Fracture Mechanics* 72.13 (Sept. 2005), pp. 2019–2036.

[73] I. Chiong et al. “Scaled boundary polygons with application to fracture analysis of functionally graded materials: SCALED BOUNDARY POLYGONS FOR FUNCTIONALLY GRADED MATERIALS”. en. In: *International Journal for Numerical Methods in Engineering* 98.8 (May 2014), pp. 562–589.

[74] M. S. Chowdhury, C. Song, and W. Gao. “Highly accurate solutions and Padé approximants of the stress intensity factors and T-stress for standard specimens”. en. In: *Engineering Fracture Mechanics* 144 (Aug. 2015), pp. 46–67.

[75] D. Chu, X. Liu, and V. Mehrmann. “A numerical method for computing the Hamiltonian Schur form”. en. In: *Numerische Mathematik* 105.3 (Dec. 2006), pp. 375–412.

[76] G.-H. Cottet and P.-A. Raviart. “On particle-in-cell methods for the Vlasov-Poisson equations”. In: *Transport Theory and Statistical Physics* 15.1-2 (1986), pp. 1–31.

[77] J. A. Cottrell, T. J. R. Hughes, and Y. Bazilevs. *Isogeometric analysis: toward integration of CAD and FEA*. English. OCLC: 441875062. Chichester, West Sussex, U.K.; Hoboken, NJ: Wiley, 2009.

[78] S. Courtin et al. “Advantages of the J-integral approach for calculating stress intensity factors when using the commercial finite element software ABAQUS”. en. In: *Engineering Fracture Mechanics* 72.14 (Sept. 2005), pp. 2174–2185.

[79] P. Cundall. “A Computer Model for Simulating Progressive Large Scale Movements in Blocky Rock Systems”. In: *Proc. Int. Symp. Rock Fracture, ISRM*. Nancy (F), 1971, pp. 2–8.

[80] G. Dasgupta. “A Finite Element Formulation for Unbounded Homogeneous Continua”. In: *Journal of Applied Mechanics* 49.1 (Mar. 1982), pp. 136–140.

[81] C. Daux et al. “Arbitrary branched and intersecting cracks with the extended finite element method”. In: *International journal for numerical methods in engineering* 48.12 (2000), pp. 1741–1760.

[82] A. J. Deeks and J. P. Wolf. “A virtual work derivation of the scaled boundary finite-element method for elastostatics”. In: *Computational Mechanics* 28.6 (June 2002), pp. 489–504.

[83] A. J. Deeks and J. P. Wolf. “Stress recovery and error estimation for the scaled boundary finite-element method”. en. In: *International Journal for Numerical Methods in Engineering* 54.4 (June 2002), pp. 557–583.

[84] G. Deodatis et al., eds. *Safety, reliability, risk and life-cycle performance of structures and infrastructures: proceedings of the 11th International Conference on Structural Safety and Reliability, New York, USA, 16-20 June 2013*. eng. A Balkema Book. OCLC: 935489672. Boca Raton, Fla.: CRC Press, 2014.

[85] M. Dittmann et al. “Variational phase-field formulation of non-linear ductile fracture”. In: *Computer Methods in Applied Mechanics and Engineering* 342 (2018), pp. 71–94.

[86] C. Duarte, I. Babuška, and J. Oden. “Generalized finite element methods for three-dimensional structural mechanics problems”. In: *Computers & Structures* 77.2 (2000), pp. 215–232.

[87] C. Duarte, L. Reno, and A. Simone. “A high-order generalized FEM for through-the-thickness branched cracks”. In: *International Journal for Numerical Methods in Engineering* 72.3 (2007), pp. 325–351.

[88] C. Duarte et al. “A generalized finite element method for the simulation of three-dimensional dynamic crack propagation”. In: *Computer Methods in Applied Mechanics and Engineering* 190.15 (2001), pp. 2227–2262.

[89] M. Duflot. “A study of the representation of cracks with level sets”. In: *International Journal for Numerical Methods in Engineering* 70.November 2006 (2007), pp. 1261–1302.

[90] D. S. Dugdale. “Yielding of Steel Sheets Containing Slits”. In: *Journal of Mechanics and Physics of Solids* 8 (1960), pp. 100–104.

[91] Y. Efendiev and T. Y. Hou. *Multiscale finite element methods: theory and applications*. Surveys and tutorials in the applied mathematical sciences 4. OCLC: ocn233933416. New York, NY: Springer, 2009.

[92] A. W. Egger, E. N. Chatzi, and S. P. Triantafyllou. “An enhanced scaled boundary finite element method for linear elastic fracture”. en. In: *Archive of Applied Mechanics* 87.10 (Oct. 2017), pp. 1667–1706.

[93] A. Egger, S. Triantafyllou, and E. Chatzi. “A scaled boundary multiscale approach to crack propagation”. In: *Proceedings of the 10th International Conference on Fracture Mechanics of Concrete and Concrete Structures*. IA-FraMCoS, June 2019.

[94] A. Egger, S. Triantafyllou, and E. Chatzi. “Improving the Accuracy of Stress Intensity Factors Obtained by the Scaled Boundary Finite Element Method on Hierarchial Meshes”. In: *Proceedings of the International Conference on Computational Methods*. Vol. 6. Singapore: Scientech, June 2019, pp. 479–492.

[95] A. Egger et al. “Discrete and Phase Field Methods for Linear Elastic Fracture Mechanics: A Comparative Study and State-of-the-Art Review”. en. In: *Applied Sciences* 9.12 (June 2019), p. 2436.

[96] A. Egger et al. “Exploring Topology Optimization on Hierarchical Meshes by Scaled Boundary Finite Element Method”. In: *Proceedings of the International Conference on Computational Methods*. Vol. 6. Singapore: Scientech, June 2019, pp. 464–478.

[97] W. Ehlers and C. Luo. “A phase-field approach embedded in the Theory of Porous Media for the description of dynamic hydraulic fracturing”. In: *Computer Methods in Applied Mechanics and Engineering* 315 (2017), pp. 348–368.

[98] T. Elguedj et al. “Extended finite element modeling of 3D dynamic crack growth under impact loading”. In: *Finite Elements in Analysis and Design* 151 (2018), pp. 1–17.

[99] H. L. Ewalds and R. J. H. Wanhill. *Fracture mechanics*. London : Delft, Netherlands: E. Arnold ; Delftse Uitgevers Maatschappij, 1984.

[100] Fett. “Stress intensity factors for edge-cracked plates under arbitrary loading”. en. In: *Fatigue <html_ent glyph="@amp;" ascii="&" /> Fracture of Engineering Materials and Structures* 22.4 (Apr. 1999), pp. 301–305.

[101] G. A. Francfort and J.-J. Marigo. “Revisiting brittle fracture as an energy minimization problem”. In: *Journal of the Mechanics and Physics of Solids* 46.8 (1998), pp. 1319–1342.

[102] M. Franke, C. Hesch, and M. Dittmann. “Phase-field approach to fracture for finite-deformation contact problems”. In: *PAMM* 16.1 (2016), pp. 123–124.

[103] T. Fries. “A corrected XFEM approximation without problems in blending elements”. In: *International Journal for Numerical Methods in Engineering* 75.November 2007 (2008), pp. 503–532.

[104] T. Fries and M. Baydoun. “Crack propagation with the extended finite element method and a hybrid explicit-implicit crack description”. In: *International Journal for Numerical Methods in Engineering* 89.November 2011 (2012), pp. 1527–1558.

[105] T. Fries and T. Belytschko. “The extended/generalized finite element method: an overview of the method and its applications”. In: *International Journal for Numerical Methods in Engineering* 84.3 (2010), pp. 253–304.

[106] T. Fries et al. “Higher-order meshing of implicit geometries—part I: Integration and interpolation in cut elements”. In: *Computer methods in applied mechanics and engineering* 313 (2017), pp. 759–784.

[107] R. J. Geelen et al. “A phase-field formulation for dynamic cohesive fracture”. In: *arXiv preprint arXiv:1809.09691* (2018).

[108] M. Geers, V. Kouznetsova, and W. Brekelmans. “Multi-scale computational homogenization: Trends and challenges”. en. In: *Journal of Computational and Applied Mathematics* 234.7 (Aug. 2010), pp. 2175–2182.

[109] T. Gerasimov and L. De Lorenzis. “A line search assisted monolithic approach for phase-field computing of brittle fracture”. In: *Computer Methods in Applied Mechanics and Engineering* 312 (2016), pp. 276–303.

[110] T. Gerasimov and L. De Lorenzis. “On penalization in variational phase-field models of brittle fracture”. In: *arXiv preprint arXiv:1811.05334* (2018).

[111] T. Gerasimov et al. “A non-intrusive global/local approach applied to phase-field modeling of brittle fracture”. In: *Advanced Modeling and Simulation in Engineering Sciences* 5.1 (2018), p. 14.

[112] C. Geuzaine and J.-F. Remacle. “Gmsh: A 3-D finite element mesh generator with built-in pre- and post-processing facilities”. en. In: *International Journal for Numerical Methods in Engineering* 79.11 (Sept. 2009), pp. 1309–1331.

[113] V. González-Albuixech et al. “Convergence of domain integrals for stress intensity factor extraction in 2-D curved cracks problems with the extended finite element method”. In: *International Journal for Numerical Methods in Engineering* 94.8 (2013), pp. 740–757.

[114] V. González-Albuixech et al. “Domain integral formulation for 3-D curved and non-planar cracks with the extended finite element method”. In: *Computer Methods in Applied Mechanics and Engineering* 264 (2013), pp. 129–144.

[115] O. González-Estrada et al. “Locally equilibrated stress recovery for goal oriented error estimation in the extended finite element method”. en. In: *Computers & Structures* 152 (May 2015), pp. 1–10.

[116] M. Gosz and B. Moran. “An interaction energy integral method for computation of mixed-mode stress intensity factors along non-planar crack fronts in three dimensions”. In: *Engineering Fracture Mechanics* 69 (2002), pp. 299–319.

[117] R. Gracie, H. Wang, and T. Belytschko. “Blending in the extended finite element method by discontinuous Galerkin and assumed strain methods”. In: *International Journal for Numerical Methods in Engineering* 74.November 2007 (2008), pp. 1645–1669.

[118] A. Gravouil, N. Moës, and T. Belytschko. “Non-planar 3D crack growth by the extended finite element and level sets-Part II: Level set update”. In: *International Journal for Numerical Methods in Engineering* 53.11 (2002), pp. 2569–2586.

[119] M. Griebel and M. Schweitzer. “A particle-partition of unity method part VII: adaptivity”. In: *Meshfree Methods for Partial Differential Equations III*. Springer, 2007, pp. 121–147.

[120] A. Griffith. “The phenomena of rupture and flow in solids”. In: *The Phenomena of Rupture and Flow in Solids* (1920), pp. 163–198.

[121] A. A. Griffith. “The phenomena of rupture and flow in solids”. In: *Philosophical transactions of the royal society of london. Series A, containing papers of a mathematical or physical character* 221 (1921), pp. 163–198.

[122] O. Gültekin, H. Dal, and G. A. Holzapfel. “A phase-field approach to model fracture of arterial walls: theory and finite element analysis”. In: *Computer methods in applied mechanics and engineering* 312 (2016), pp. 542–566.

[123] A. K. Gupta. “A finite element for transition from a fine to a coarse grid”. en. In: *International Journal for Numerical Methods in Engineering* 12.1 (1978), pp. 35–45.

[124] V. Gupta et al. “A stable and optimally convergent generalized FEM (SGFEM) for linear elastic fracture mechanics”. In: *Computer methods in applied mechanics and engineering* 266 (2013), pp. 23–39.

[125] V. Gupta et al. “Stable GFEM (SGFEM): Improved conditioning and accuracy of GFEM/XFEM for three-dimensional fracture mechanics”. In: *Computer Methods in Applied Mechanics and Engineering* 289 (2015), pp. 355–386.

[126] W. Hackbusch. “A Sparse Matrix Arithmetic Based on H-Matrices. Part I: Introduction to H-Matrices”. In: *Computing* 62.2 (Apr. 1999), pp. 89–108.

[127] A. Hansbo and P. Hansbo. “A finite element method for the simulation of strong and weak discontinuities in solid mechanics”. In: *Computer methods in applied mechanics and engineering* 193.33-35 (2004), pp. 3523–3540.

[128] A. C. Hansen-Dörr et al. “Phase-field modelling of interface failure in brittle materials”. In: *Computer Methods in Applied Mechanics and Engineering* 346 (2019), pp. 25–42.

[129] Y. Heider and B. Markert. “A phase-field modeling approach of hydraulic fracture in saturated porous media”. In: *Mechanics Research Communications* 80 (2017), pp. 38–46.

[130] T. Heister, M. F. Wheeler, and T. Wick. “A primal-dual active set method and predictor-corrector mesh adaptivity for computing fracture propagation using a phase-field approach”. In: *Computer Methods in Applied Mechanics and Engineering* 290 (2015), pp. 466–495.

[131] A. Hillerborg, M. Modéer, and P.-E. Petersson. “Analysis of crack formation and crack growth in concrete by means of fracture mechanics and finite elements”. In: *Cement and concrete research* 6.6 (1976), pp. 773–781.

[132] M. Hofacker and C. Miehe. “A phase field model of dynamic fracture: Robust field updates for the analysis of complex crack patterns: A PHASE FIELD MODEL OF DYNAMIC FRACTURE”. en. In: *International Journal for Numerical Methods in Engineering* 93.3 (Jan. 2013), pp. 276–301.

[133] W. Hong and P. Lee. “Mesh based construction of flat-top partition of unity functions”. In: *Applied Mathematics and Computation* 219.16 (2013), pp. 8687–8704.

[134] T. Y. S. Hoshina, I. F. M. Menezes, and A. Pereira. “A simple adaptive mesh refinement scheme for topology optimization using polygonal meshes”. en. In: *Journal of the Brazilian Society of Mechanical Sciences and Engineering* 40.7 (July 2018), p. 348.

[135] T. Y. Hou and X.-H. Wu. “A Multiscale Finite Element Method for Elliptic Problems in Composite Materials and Porous Media”. en. In: *Journal of Computational Physics* 134.1 (June 1997), pp. 169–189.

[136] Z. Hu et al. “A Hamiltonian-based derivation of Scaled Boundary Finite Element Method for elasticity problems”. In: *IOP Conference Series: Materials Science and Engineering* 10 (June 2010), p. 012213.

[137] R. Huang, N. Sukumar, and J. Prévost. “Modeling quasi-static crack growth with the extended finite element method Part II: Numerical applications”. In: *International Journal of Solids and Structures* 40.26 (2003), pp. 7539–7552.

[138] X. Huang and Y. M. Xie. *Evolutionary Topology Optimization of Continuum Structures: Methods and Applications*. Chichester, UK: John Wiley & Sons, Ltd, Apr. 2010.

[139] T. Hughes, J. Cottrell, and Y. Bazilevs. “Isogeometric analysis: CAD, finite elements, NURBS, exact geometry and mesh refinement”. en. In: *Computer Methods in Applied Mechanics and Engineering* 194.39-41 (Oct. 2005), pp. 4135–4195.

[140] T. J. R. Hughes. *The finite element method: linear static and dynamic finite element analysis*. Mineola, NY: Dover Publications, 2000.

[141] A. R. Ingraffea and V. Saouma. “Numerical modelling of discrete crack propagation in reinforced and plain concrete”. In: *Fracture Mechanics of Concrete. Martinus Nijhoff Publishers: Dordrecht* (1985), pp. 171–225.

[142] M. Janssen. *Fracture mechanics*. Delft: DUP Blue Print, 2002.

[143] E. G. Kakouris and S. P. Triantafyllou. “Phase-field material point method for brittle fracture”. en. In: *International Journal for Numerical Methods in Engineering* 112.12 (Dec. 2017), pp. 1750–1776.

[144] E. Kakouris and S. Triantafyllou. “Material point method for crack propagation in anisotropic media: a phase field approach”. In: *Archive of Applied Mechanics* 88.1-2 (2018), pp. 287–316.

[145] P. Kanouté et al. “Multiscale Methods for Composites: A Review”. en. In: *Archives of Computational Methods in Engineering* 16.1 (Mar. 2009), pp. 31–75.

[146] B. L. Karihaloo and Q. Z. Xiao. “Asymptotic fields at the tip of a cohesive crack”. en. In: *International Journal of Fracture* 150.1-2 (Mar. 2008), pp. 55–74.

[147] A. Karma, D. A. Kessler, and H. Levine. “Phase-field model of mode III dynamic fracture”. In: *Physical Review Letters* 87.4 (2001), p. 045501.

[148] E. Kausel. “Thin-layer method: Formulation in the time domain”. en. In: *International Journal for Numerical Methods in Engineering* 37.6 (Mar. 1994), pp. 927–941.

[149] J. Kiendl et al. “Phase-field description of brittle fracture in plates and shells”. In: *Computer Methods in Applied Mechanics and Engineering* 312 (2016), pp. 374–394.

[150] J.-H. Kim and G. H. Paulino. “The interaction integral for fracture of orthotropic functionally graded materials: evaluation of stress intensity factors”. en. In: *International Journal of Solids and Structures* 40.15 (July 2003), pp. 3967–4001.

[151] U. Kirsch. *Reanalysis of Structures: A Unified Approach for Linear, Nonlinear, Static and Dynamic Systems (Solid Mechanics and Its Applications)*. Springer, 2008.

[152] E. Kita and N. Kamiya. “Trefftz method: an overview”. en. In: *Advances in Engineering Software* 24.1-3 (Jan. 1995), pp. 3–12.

[153] P. A. Klein et al. “Physics-based modeling of brittle fracture: cohesive formulations and the application of meshfree methods”. In: *Theoretical and Applied Fracture Mechanics* 37 (2001), pp. 99–166.

[154] R. Krueger. “Virtual crack closure technique: History, approach, and applications”. en. In: *Applied Mechanics Reviews* 57.2 (2004), p. 109.

[155] C. Kuhn and R. Müller. “A continuum phase field model for fracture”. In: *Engineering Fracture Mechanics* 77.18 (2010), pp. 3625–3634.

[156] C. Kuhn and R. Müller. “Phase field simulation of thermomechanical fracture”. In: *PAMM: Proceedings in Applied Mathematics and Mechanics*. Vol. 9. 1. Wiley Online Library. 2009, pp. 191–192.

[157] C. Kuhn, T. Noll, and R. Müller. “On phase field modeling of ductile fracture”. In: *GAMM-Mitteilungen* 39.1 (2016), pp. 35–54.

[158] C. Kuhn, A. Schlüter, and R. Müller. “On degradation functions in phase field fracture models”. In: *Computational Materials Science* 108 (2015), pp. 374–384.

[159] M. Kuna. *Finite elements in fracture mechanics: theory - numerics - applications*. eng. Solid mechanics and its applications 201. OCLC: 858004580. Dordrecht: Springer, 2013.

[160] P. Laborde et al. "High-order extended finite element method for cracked domains". In: *International Journal for Numerical Methods in Engineering* 64.3 (2005), pp. 354–381.

[161] L. T. T. Lan and A. Boucher. "Simplified Quadtree Image Segmentation for Image Annotation". In: 2011.

[162] M. Lan, H. Waisman, and I. Harari. "A direct analytical method to extract mixed-mode components of strain energy release rates from Irwin's integral using extended finite element method". In: *International Journal for Numerical Methods in Engineering* 95.12 (2013), pp. 1033–1052.

[163] M. Lan, H. Waisman, and I. Harari. "A High-order extended finite element method for extraction of mixed-mode strain energy release rates in arbitrary crack settings based on Irwin's integral". In: *International Journal for Numerical Methods in Engineering* 96.12 (2013), pp. 787–812.

[164] C. Lang et al. "A simple and efficient preconditioning scheme for heaviside enriched XFEM". In: *Computational Mechanics* 54.5 (2014), pp. 1357–1374.

[165] B. Lecampion. "An extended finite element method for hydraulic fracture problems". In: *Communications in Numerical Methods in Engineering* 25.2 (2009), pp. 121–133.

[166] G. Legrain, N. Moes, and E. Verron. "Stress analysis around crack tips in finite strain problems using the extended finite element method". In: *International Journal for Numerical Methods in Engineering* 63.2 (2005), pp. 290–314.

[167] B. Li and C. Maurini. "Crack kinking in a variational phase-field model of brittle fracture with strongly anisotropic surface energy". In: *Journal of the Mechanics and Physics of Solids* (2019).

[168] C. Li and L. Tong. "Topology optimization of incompressible materials based on the mixed SBFEM". en. In: *Computers & Structures* 165 (Mar. 2016), pp. 24–33.

[169] C. Li et al. "Analysis of cracks and notches in piezoelectric composites using scaled boundary finite element method". en. In: *Composite Structures* 101 (July 2013), pp. 191–203.

[170] H. Li, H. Zhang, and Y. Zheng. "A coupling extended multiscale finite element method for dynamic analysis of heterogeneous saturated porous media". In: *International Journal for Numerical Methods in Engineering* 104.1 (2015), pp. 18–47.

[171] K. Li and X. Qian. "Isogeometric analysis and shape optimization via boundary integral". In: *Computer-Aided Design* 43.11 (2011), pp. 1427–1437.

[172] G. Lin et al. "Scaled boundary isogeometric analysis for 2D elastostatics". en. In: *Science China Physics, Mechanics and Astronomy* 57.2 (Feb. 2014), pp. 286–300.

[173] J. Lindemann and W. Becker. "Free-Edge Stresses around Holes in Laminates by the Boundary Finite-Element Method". In: *Mechanics of Composite Materials* 38.5 (Sept. 2002), pp. 407–416.

[174] G. Liu et al. "Abaqus implementation of monolithic and staggered schemes for quasi-static and dynamic fracture phase-field model". In: *Computational Materials Science* 121 (2016), pp. 35–47.

[175] K. Liu and A. Tovar. "An efficient 3D topology optimization code written in Matlab". en. In: *Structural and Multidisciplinary Optimization* 50.6 (Dec. 2014), pp. 1175–1196.

[176] X. Liu, Q. Xiao, and B. Karihaloo. "XFEM for direct evaluation of mixed mode SIFs in homogeneous and bi-materials". In: *International Journal for Numerical Methods in Engineering* 59.8 (2004), pp. 1103–1118.

[177] Y. J. Liu et al. "Recent Advances and Emerging Applications of the Boundary Element Method". en. In: *Applied Mechanics Reviews* 64.3 (Mar. 2012), p. 030802.

[178] S. Loehnert. "A stabilization technique for the regularization of nearly singular extended finite elements". In: *Computational Mechanics* 54.2 (2014), pp. 523–533.

[179] S. Loehnert, D. Mueller-Hoeppe, and P. Wriggers. "3D corrected XFEM approach and extension to finite deformation theory". In: *International Journal for Numerical Methods in Engineering* 86.October 2010 (2011), pp. 431–452.

[180] X. Long et al. "Sensitivity analysis of the scaled boundary finite element method for elastostatics". en. In: *Computer Methods in Applied Mechanics and Engineering* 276 (July 2014), pp. 212–232.

[181] E. Lorentz. “A nonlocal damage model for plain concrete consistent with cohesive fracture”. In: *International Journal of Fracture* 207.2 (2017), pp. 123–159.

[182] E. Lorentz, S. Cuvilliez, and K. Kazymyrenko. “Modelling large crack propagation: from gradient damage to cohesive zone models”. In: *International journal of fracture* 178.1-2 (2012), pp. 85–95.

[183] E. Lorentz and V. Godard. “Gradient damage models: Toward full-scale computations”. In: *Computer Methods in Applied Mechanics and Engineering* 200.21-22 (2011), pp. 1927–1944.

[184] Y. Lu, T. Belytschko, and L. Gu. “A new implementation of the element free Galerkin method”. In: *Computer methods in applied mechanics and engineering* 113.3-4 (1994), pp. 397–414.

[185] C. Ma et al. “An effective computational approach based on XFEM and a novel three-step detection algorithm for multiple complex flaw clusters”. en. In: *Computers & Structures* 193 (Dec. 2017), pp. 207–225.

[186] M. Malekan et al. “Two-dimensional fracture modeling with the generalized/extended finite element method: An object-oriented programming approach”. In: *Advances in Engineering Software* 115 (2018), pp. 168–193.

[187] H. Man et al. “Towards Automatic Stress Analysis using Scaled Boundary Finite Element Method with Quadtree Mesh of High-order Elements”. In: *arXiv:1402.5186 [math]* (Feb. 2014). arXiv: 1402.5186.

[188] T. K. Mandal, V. P. Nguyen, and A. Heidarpour. “Phase field and gradient enhanced damage models for quasi-brittle failure: A numerical comparative study”. In: *Engineering Fracture Mechanics* 207 (2019), pp. 48–67.

[189] S. Mariani and U. Perego. “Extended finite element method for quasi-brittle fracture”. In: *International Journal for numerical methods in engineering* 58.1 (2003), pp. 103–126.

[190] D. Maringer. *Portfolio management with heuristic optimization*. Advances in computational management science v. 8. Dordrecht: Springer, 2005.

[191] K. Markov, L. Preziosi, and N. Bellomo, eds. *Heterogeneous Media: Micromechanics Modeling Methods and Simulations*. en. Modeling and Simulation in Science, Engineering and Technology. Boston, MA: Birkhäuser Boston, 2000.

[192] H.-G. Maschke and M. Kuna. “A review of boundary and finite element methods in fracture mechanics”. en. In: *Theoretical and Applied Fracture Mechanics* 4.3 (Dec. 1985), pp. 181–189.

[193] V. Mehrmann, C. Schröder, and D. Watkins. “A new block method for computing the Hamiltonian Schur form”. en. In: *Linear Algebra and its Applications* 431.3-4 (July 2009), pp. 350–368.

[194] J. Melenk and I. Babuška. “The partition of unity finite element method: basic theory and applications”. In: *Computer methods in applied mechanics and engineering* 139.1-4 (1996), pp. 289–314.

[195] A. Menk and S. Bordas. “A robust preconditioning technique for the extended finite element method”. In: *International Journal for Numerical Methods in Engineering* 85.October 2010 (2011), pp. 1609–1632.

[196] T. Menouillard et al. “Efficient explicit time stepping for the eXtended Finite Element Method (X-FEM)”. In: *International Journal for Numerical Methods in Engineering* 68.9 (2006), pp. 911–939.

[197] C. Miehe, F. Welschinger, and M. Hofacker. “Thermodynamically consistent phase-field models of fracture: Variational principles and multi-field FE implementations”. In: *International Journal for Numerical Methods in Engineering* 83.10 (2010), pp. 1273–1311.

[198] C. Miehe, M. Hofacker, and F. Welschinger. “A phase field model for rate-independent crack propagation: Robust algorithmic implementation based on operator splits”. In: *Computer Methods in Applied Mechanics and Engineering* 199.45 (2010), pp. 2765–2778.

[199] C. Miehe and S. Mauthe. “Phase field modeling of fracture in multi-physics problems. Part III. Crack driving forces in hydro-poro-elasticity and hydraulic fracturing of fluid-saturated porous media”. In: *Computer Methods in Applied Mechanics and Engineering* 304 (2016), pp. 619–655.

[200] C. Miehe, S. Mauthe, and S. Teichtmeister. “Minimization principles for the coupled problem of Darcy–Biot-type fluid transport in porous media linked to phase field modeling of fracture”. In: *Journal of the Mechanics and Physics of Solids* 82 (2015), pp. 186–217.

[201] C. Miehe, L.-M. Schaenzel, and H. Ulmer. “Phase field modeling of fracture in multi-physics problems. Part I. Balance of crack surface and failure criteria for brittle crack propagation in thermoelastic solids”. In: *Computer Methods in Applied Mechanics and Engineering* 294 (2015), pp. 449–485.

[202] H. Minnebo. “Three-dimensional integration strategies of singular functions introduced by the XFEM in the LEFM”. In: *International Journal for Numerical Methods in Engineering* 92.July (2012), pp. 1117–1138.

[203] H. P. Mlejnek. “Some aspects of the genesis of structures”. en. In: *Structural Optimization* 5.1-2 (Mar. 1992), pp. 64–69.

[204] N. Moës and T. Belytschko. “Extended finite element method for cohesive crack growth”. In: *Engineering fracture mechanics* 69.7 (2002), pp. 813–833.

[205] N. Moës, J. Dolbow, and T. Belytschko. “A finite element method for crack growth without remeshing”. In: *International Journal for Numerical Methods in Engineering* 46.1 (1999), pp. 131–150.

[206] N. Moës, A. Gravouil, and T. Belytschko. “Non-planar 3D crack growth by the extended finite element and level sets-Part I: Mechanical model”. In: *International Journal for Numerical Methods in Engineering* 53.11 (2002), pp. 2549–2568.

[207] N. Moës, J. Dolbow, and T. Belytschko. “A finite element method for crack growth without remeshing”. en. In: *International Journal for Numerical Methods in Engineering* 46.1 (Sept. 1999), pp. 131–150.

[208] N. Moës et al. “A level set based model for damage growth: the thick level set approach”. In: *International Journal for Numerical Methods in Engineering* 86.3 (2011), pp. 358–380.

[209] S. Mohammadi. *XFEM fracture analysis of composites*. Chichester, West Sussex, United Kingdom: John Wiley & Sons, Ltd, 2012.

[210] B. Moran and C. Shih. “Crack tip and associated domain integrals from momentum and energy balance”. In: *Engineering fracture mechanics* 27.6 (1987), pp. 615–642.

[211] S. Mousavi and N. Sukumar. “Generalized Gaussian quadrature rules for discontinuities and crack singularities in the extended finite element method”. In: *Computer Methods in Applied Mechanics and Engineering* 199.49-52 (2010), pp. 3237–3249.

[212] G. Moutsanidis et al. “Hyperbolic phase field modeling of brittle fracture: Part II-immersed IGA-RKPM coupling for air-blast–structure interaction”. In: *Journal of the Mechanics and Physics of Solids* 121 (2018), pp. 114–132.

[213] G. Moutsanidis et al. “Modeling strong discontinuities in the material point method using a single velocity field”. In: *Computer Methods in Applied Mechanics and Engineering* 345 (2019), pp. 584–601.

[214] M. A. Msekh et al. “Abaqus implementation of phase-field model for brittle fracture”. In: *Computational Materials Science* 96 (2015), pp. 472–484.

[215] A. Müller et al. “The boundary finite element method for predicting directions of cracks emerging from notches at bimaterial junctions”. en. In: *Engineering Fracture Mechanics* 72.3 (Feb. 2005), pp. 373–386.

[216] S. Murakami. *Continuum damage mechanics: a continuum mechanics approach to the analysis of damage and fracture*. Vol. 185. Springer Science & Business Media, 2012.

[217] S. Nagaraja et al. “Phase-field modeling of brittle fracture with multi-level hp-FEM and the finite cell method”. In: *Computational Mechanics* (2017), pp. 1–18.

[218] J. A. Nairn. “Material point method calculations with explicit cracks”. In: *Computer Modeling in Engineering and Sciences* 4.6 (2003), pp. 649–664.

[219] S. Natarajan, D. Mahapatra, and S. Bordas. “Integrating strong and weak discontinuities without integration subcells and example applications in an XFEM/GFEM framework”. In: *International Journal for Numerical Methods in Engineering* 83.January (2010), pp. 269–294.

[220] S. Natarajan, R. K. Annabattula, et al. “Modeling crack propagation in variable stiffness composite laminates using the phase field method”. In: *Composite Structures* 209 (2019), pp. 424–433.

[221] S. Natarajan and C. Song. “Representation of singular fields without asymptotic enrichment in the extended finite element method: SINGULAR FIELDS WITHOUT ASYMPTOTIC ENRICHMENT IN THE XFEM”. en. In: *International Journal for Numerical Methods in Engineering* 96.13 (Dec. 2013), pp. 813–841.

[222] S. Natarajan et al. “Isogeometric analysis enhanced by the scaled boundary finite element method”. en. In: *Computer Methods in Applied Mechanics and Engineering* 283 (Jan. 2015), pp. 733–762.

[223] R. Nelson, S. Dong, and R. Kalra. “Vibrations and waves in laminated orthotropic circular cylinders”. en. In: *Journal of Sound and Vibration* 18.3 (Oct. 1971), pp. 429–444.

[224] T. C. Nguyen et al. “Modelling rock fracture unsing smoothed particle hydrodynamics and cohesive cracks”. In: *EUROCK* October (2012), pp. 7–10.

[225] T.-T. Nguyen et al. “A phase-field method for computational modeling of interfacial damage interacting with crack propagation in realistic microstructures obtained by microtomography”. In: *Computer Methods in Applied Mechanics and Engineering* 312 (2016), pp. 567–595.

[226] V. P. Nguyen, P. Kerfriden, and S. P. Bordas. “Two- and three-dimensional isogeometric cohesive elements for composite delamination analysis”. en. In: *Composites Part B: Engineering* 60 (Apr. 2014), pp. 193–212.

[227] V. P. Nguyen and J.-Y. Wu. “Modeling dynamic fracture of solids with a phase-field regularized cohesive zone model”. In: *Computer Methods in Applied Mechanics and Engineering* 340 (2018), pp. 1000–1022.

[228] V. P. Nguyen et al. “Isogeometric analysis: An overview and computer implementation aspects”. en. In: *Mathematics and Computers in Simulation* 117 (Nov. 2015), pp. 89–116.

[229] V. P. Nguyen et al. “Meshless methods: A review and computer implementation aspects”. en. In: *Mathematics and Computers in Simulation* 79.3 (Dec. 2008), pp. 763–813.

[230] V. P. Nguyen et al. “Modelling hydraulic fractures in porous media using flow cohesive interface elements”. In: *Engineering Geology* 225 (2017), pp. 68–82.

[231] S. Nicaise, Y. Renard, and E. Chahine. “Optimal convergence analysis for the extended finite element method”. In: *International Journal for Numerical Methods in Engineering* 86.4-5 (2011), pp. 528–548.

[232] Niconet e.V. *Subroutine Library in Systems and Control Theory*. Version 5.0. Oct. 20, 2016.

[233] E. T. Ooi and Z. J. Yang. “Modelling dynamic crack propagation using the scaled boundary finite element method”. en. In: *International Journal for Numerical Methods in Engineering* 88.4 (Oct. 2011), pp. 329–349.

[234] E. T. Ooi, Z. J. Yang, and Z. Y. Guo. “Dynamic cohesive crack propagation modelling using the scaled boundary finite element method: DYNAMIC COHESIVE CRACK PROPAGATION MODELLING”. en. In: *Fatigue & Fracture of Engineering Materials & Structures* 35.8 (Aug. 2012), pp. 786–800.

[235] E. T. Ooi et al. “Crack propagation modelling in concrete using the scaled boundary finite element method with hybrid polygon–quadtree meshes”. en. In: *International Journal of Fracture* 203.1-2 (Jan. 2017), pp. 135–157.

[236] E. Ooi and Z. Yang. “Efficient prediction of deterministic size effects using the scaled boundary finite element method”. en. In: *Engineering Fracture Mechanics* 77.6 (Apr. 2010), pp. 985–1000.

[237] E. Ooi and Z. Yang. “Modelling multiple cohesive crack propagation using a finite element–scaled boundary finite element coupled method”. en. In: *Engineering Analysis with Boundary Elements* 33.7 (July 2009), pp. 915–929.

[238] E. Ooi et al. “Adaptation of quadtree meshes in the scaled boundary finite element method for crack propagation modelling”. en. In: *Engineering Fracture Mechanics* 144 (Aug. 2015), pp. 101–117.

[239] E. Ooi et al. “Dynamic crack propagation simulation with scaled boundary polygon elements and automatic remeshing technique”. en. In: *Engineering Fracture Mechanics* 106 (July 2013), pp. 1–21.

[240] E. T. Ooi and Z. J. Yang. “Modelling crack propagation in reinforced concrete using a hybrid finite element–scaled boundary finite element method”. en. In: *Engineering Fracture Mechanics* 78.2 (Jan. 2011), pp. 252–273.

[241] E. T. Ooi et al. “Dynamic fracture simulations using the scaled boundary finite element method on hybrid polygon–quadtree meshes”. en. In: *International Journal of Impact Engineering* 90 (Apr. 2016), pp. 154–164.

[242] E. T. Ooi et al. “Polygon scaled boundary finite elements for crack propagation modelling: SCALED BOUNDARY POLYGON FINITE ELEMENTS FOR CRACK PROPAGATION”. en. In: *International Journal for Numerical Methods in Engineering* 91.3 (July 2012), pp. 319–342.

[243] S. Osher and J. Sethian. “Fronts propagating with curvature-dependent speed: algorithms based on Hamilton-Jacobi formulations”. In: *Journal of computational physics* 79.1 (1988), pp. 12–49.

[244] M. Otomori et al. “Matlab code for a level set-based topology optimization method using a reaction diffusion equation”. en. In: *Structural and Multidisciplinary Optimization* 51.5 (May 2015), pp. 1159–1172.

[245] A. Panesar et al. “Hierarchical remeshing strategies with mesh mapping for topology optimisation: Hierarchical remeshing strategies with mesh mapping for topology optimisation”. en. In: *International Journal for Numerical Methods in Engineering* 111.7 (Aug. 2017), pp. 676–700.

[246] J. Panetier, P. Ladevèze, and F. Louf. “Strict bounds for computed stress intensity factors”. en. In: *Computers & Structures* 87.15-16 (Aug. 2009), pp. 1015–1021.

[247] C. Papadimitriou and D.-C. Papadioti. “Component mode synthesis techniques for finite element model updating”. en. In: *Computers & Structures* 126 (Sept. 2013), pp. 15–28.

[248] A. T. Patera. “A spectral element method for fluid dynamics: Laminar flow in a channel expansion”. en. In: *Journal of Computational Physics* 54.3 (June 1984), pp. 468–488.

[249] R. Patil, B. Mishra, and I. Singh. “An adaptive multiscale phase field method for brittle fracture”. In: *Computer Methods in Applied Mechanics and Engineering* 329 (2018), pp. 254–288.

[250] B. Paul et al. “An integration technique for 3D curved cracks and branched discontinuities within the extended Finite Element Method”. In: *Finite Elements in Analysis and Design* 123 (2017), pp. 19–50.

[251] G. A. Pavliotis and A. M. Stuart. *Multiscale methods: averaging and homogenization*. Texts in applied mathematics 53. OCLC: ocn166384346. New York: Springer, 2008.

[252] R. d. Peerlings et al. “Gradient enhanced damage for quasi-brittle materials”. In: *International Journal for numerical methods in engineering* 39.19 (1996), pp. 3391–3403.

[253] X. Peng et al. “Isogeometric boundary element methods for three dimensional static fracture and fatigue crack growth”. In: *Computer Methods in Applied Mechanics and Engineering* 316 (2017), pp. 151–185.

[254] K. Pham, K. Ravi-Chandar, and C. Landis. “Experimental validation of a phase-field model for fracture”. In: *International Journal of Fracture* 205.1 (2017), pp. 83–101.

[255] K. Pham et al. “Gradient damage models and their use to approximate brittle fracture”. In: *International Journal of Damage Mechanics* 20.4 (2011), pp. 618–652.

[256] U. Pillai, Y. Heider, and B. Markert. “A diffusive dynamic brittle fracture model for heterogeneous solids and porous materials with implementation using a user-element subroutine”. In: *Computational Materials Science* 153 (2018), pp. 36–47.

[257] B. Prabel et al. “Level set X-FEM non-matching meshes: application to dynamic crack propagation in elastic–plastic media”. In: *International Journal for Numerical Methods in Engineering* 69.8 (2007), pp. 1553–1569.

[258] A. Quintanas-Corominas et al. “A phase field approach to simulate intralaminar and translaminar fracture in long fiber composite materials”. In: *Composite Structures* (2019).

[259] T. Rabczuk and G. Zi. “A Meshfree Method based on the Local Partition of Unity for Cohesive Cracks”. In: *Computational Mechanics* 39 (2007), pp. 743–760.

[260] D. Rabinovich, D. Givoli, and S. Vigdergauz. “Crack identification by ‘arrival time’ using XFEM and a genetic algorithm”. en. In: *International Journal for Numerical Methods in Engineering* 77.3 (Jan. 2009), pp. 337–359.

[261] D. Rabinovich, D. Givoli, and S. Vigdergauz. “XFEM-based crack detection scheme using a genetic algorithm”. en. In: *International Journal for Numerical Methods in Engineering* 71.9 (Aug. 2007), pp. 1051–1080.

[262] I. Raju. “Calculation of strain-energy release rates with higher order and singular finite elements”. In: *Engineering Fracture Mechanics* 28.3 (1987), pp. 251–274.

[263] B. N. Rao and S. Rahman. “An efficient meshless method for fracture analysis of cracks”. In: *Computational Mechanics* 26.4 (Oct. 2000), pp. 398–408.

[264] Y. Rashid. “Ultimate strength analysis of prestressed concrete pressure vessels”. In: *Nuclear engineering and design* 7.4 (1968), pp. 334–344.

[265] J. Reinoso, M. Paggi, and C. Linder. “Phase field modeling of brittle fracture for enhanced assumed strain shells at large deformations: formulation and finite element implementation”. In: *Computational Mechanics* 59.6 (2017), pp. 981–1001.

[266] J. J. C. Remmers, R. de Borst, and A. Needleman. “A cohesive segments method for the simulation of crack growth”. In: *Computational mechanics* 31.1-2 (2003), pp. 69–77.

[267] J. J. C. Remmers, R. de Borst, and A. Needleman. “The simulation of dynamic crack propagation using the cohesive segments method”. In: *Journal of the Mechanics and Physics of Solids* 56.1 (2008), 70–92], year = [2008.

[268] J. Réthoré, A. Gravouil, and A. Combescure. “An energy-conserving scheme for dynamic crack growth using the extended finite element method”. In: *International Journal for Numerical Methods in Engineering* 63.5 (2005), pp. 631–659.

[269] V. Rokhlin. “Rapid solution of integral equations of classical potential theory”. en. In: *Journal of Computational Physics* 60.2 (Sept. 1985), pp. 187–207.

[270] G. I. N. Rozvany. “A critical review of established methods of structural topology optimization”. en. In: *Structural and Multidisciplinary Optimization* 37.3 (Jan. 2009), pp. 217–237.

[271] E. Rybicki and M. Kanninen. “A finite element calculation of stress intensity factors by a modified crack closure integral”. In: *Engineering fracture mechanics* 9.4 (1977), pp. 931–938.

[272] A. Sadeghirad et al. “A novel hybrid approach for level set characterization and tracking of non-planar 3D cracks in the extended finite element method”. In: *Engineering Fracture Mechanics* 160 (2016), pp. 1–14.

[273] M. A. Salazar de Troya and D. A. Tortorelli. “Adaptive mesh refinement in stress-constrained topology optimization”. en. In: *Structural and Multidisciplinary Optimization* 58.6 (Dec. 2018), pp. 2369–2386.

[274] A. L. Salen and M. H. Aliabadi. “Crack growth analysis in concrete using boundary element method”. In: *Engineering Fracture Mechanics* 51 (1995), pp. 533–545.

[275] E. D. Sanders et al. “PolyMat: an efficient Matlab code for multi-material topology optimization”. en. In: *Structural and Multidisciplinary Optimization* 58.6 (Dec. 2018), pp. 2727–2759.

[276] A. Saputra et al. “Automatic image-based stress analysis by the scaled boundary finite element method: AUTOMATIC IMAGE-BASED STRESS ANALYSIS BY THE SCALED BOUNDARY FEM”. en. In: *International Journal for Numerical Methods in Engineering* 109.5 (Feb. 2017), pp. 697–738.

[277] M. Schätzer and T.-P. Fries. “Stress Intensity Factors Through Crack Opening Displacements in the XFEM”. In: *Advances in Discretization Methods*. Springer, 2016, pp. 143–164.

[278] A. Schlüter et al. “Phase field approximation of dynamic brittle fracture”. In: *Computational Mechanics* 54.5 (2014), pp. 1141–1161.

[279] M. Scott et al. “Isogeometric boundary element analysis using unstructured T-splines”. In: *Computer Methods in Applied Mechanics and Engineering* 254 (2013), pp. 197–221.

[280] J. Sethian. *Level set methods and fast marching methods: evolving interfaces in computational geometry, fluid mechanics, computer vision, and materials science*. Vol. 3. Cambridge university press, 1999.

[281] Y. Shao, Q. Duan, and S. Qiu. “Adaptive consistent element-free Galerkin method for phase-field model of brittle fracture”. In: *Computational Mechanics* (2019), pp. 1–27.

[282] R. Shen, H. Waisman, and L. Guo. “Fracture of viscoelastic solids modeled with a modified phase field method”. In: *Computer Methods in Applied Mechanics and Engineering* 346 (2019), pp. 862–890.

[283] O. Sigmund and J. Petersson. “Numerical instabilities in topology optimization: A survey on procedures dealing with checkerboards, mesh-dependencies and local minima”. en. In: *Structural Optimization* 16.1 (Aug. 1998), pp. 68–75.

[284] O. Sigmund. “Morphology-based black and white filters for topology optimization”. en. In: *Structural and Multidisciplinary Optimization* 33.4-5 (Feb. 2007), pp. 401–424.

[285] G. Sih. “Strain-energy-density factor applied to mixed mode crack problems”. In: *International Journal of fracture* 10.3 (1974), pp. 305–321.

[286] P. Silvester et al. “Exterior finite elements for 2-dimensional field problems with open boundaries”. en. In: *Proceedings of the Institution of Electrical Engineers* 124.12 (1977), p. 1267.

[287] A. Simone, G. N. Wells, and L. J. Sluys. “From continuous to discontinuous failure in a gradient-enhanced continuum damage model”. In: *Computer Methods in Applied Mechanics and Engineering* 192.41-42 (2003), pp. 4581–4607.

[288] R. N. Simpson et al. “A two-dimensional isogeometric boundary element method for elastostatic analysis”. In: *Computer Methods in Applied Mechanics and Engineering* 209 (2012), pp. 87–100.

[289] N. Singh et al. “A fracture-controlled path-following technique for phase-field modeling of brittle fracture”. In: *Finite Elements in Analysis and Design* 113 (2016), pp. 14–29.

[290] M. Smith. *ABAQUS/Standard User’s Manual, Version 6.9*. English. Simulia, 2009.

[291] C. Song. “A matrix function solution for the scaled boundary finite-element equation in statics”. en. In: *Computer Methods in Applied Mechanics and Engineering* 193.23-26 (June 2004), pp. 2325–2356.

[292] C. Song. “A super-element for crack analysis in the time domain”. en. In: *International Journal for Numerical Methods in Engineering* 61.8 (Oct. 2004), pp. 1332–1357.

[293] C. Song. “Evaluation of power-logarithmic singularities, T-stresses and higher order terms of in-plane singular stress fields at cracks and multi-material corners”. en. In: *Engineering Fracture Mechanics* 72.10 (July 2005), pp. 1498–1530.

[294] C. Song. *The scaled boundary finite element method: intorduction to theory and implementation*. Hoboken, New Jersey: John Wiley & Sons, 2018.

[295] C. Song, E. T. Ooi, and S. Natarajan. “A review of the scaled boundary finite element method for two-dimensional linear elastic fracture mechanics”. en. In: *Engineering Fracture Mechanics* 187 (Jan. 2018), pp. 45–73.

[296] C. Song, F. Tin-Loi, and W. Gao. “A definition and evaluation procedure of generalized stress intensity factors at cracks and multi-material wedges”. en. In: *Engineering Fracture Mechanics* 77.12 (Aug. 2010), pp. 2316–2336.

[297] C. Song and J. P. Wolf. “The scaled boundary finite-element method—alias consistent infinitesimal finite-element cell method—for elastodynamics”. en. In: *Computer Methods in Applied Mechanics and Engineering* 147.3-4 (Aug. 1997), pp. 329–355.

[298] C. Song et al. “A novel error indicator and an adaptive refinement technique using the scaled boundary finite element method”. In: *Engineering Analysis with Boundary Elements* 94 (2018), pp. 10–24.

[299] G. Song et al. “Extraction of stress intensity factors from Irwin’s integral using high-order XFEM on triangular meshes”. In: *International Journal for Numerical Methods in Engineering* 102.3-4 (2015), pp. 528–550.

[300] P. Soparat and P. Nanakorn. “Analysis of Cohesive Crack Growth by the Element-Free Galerkin Method”. In: *Journal of Mechanics* 24 (2008), pp. 45–54.

[301] M. Spiridonakos and E. Chatzi. “Metamodeling of dynamic nonlinear structural systems through polynomial chaos NARX models”. en. In: *Computers & Structures* 157 (Sept. 2015), pp. 99–113.

[302] F. Stazi et al. “An extended finite element method with higher-order elements for curved cracks”. In: *Computational Mechanics* 31.1-2 (2003), pp. 38–48.

[303] M. Stolarska et al. “Modelling crack growth by level sets in the extended finite element method”. In: *International journal for numerical methods in Engineering* 51.8 (2001), pp. 943–960.

[304] T. Strouboulis, I. Babuška, and K. Copps. “The design and analysis of the generalized finite element method”. In: *Computer methods in applied mechanics and engineering* 181.1 (2000), pp. 43–69.

[305] N. Sukumar et al. “Modeling holes and inclusions by level sets in the extended finite-element method”. en. In: *Computer Methods in Applied Mechanics and Engineering* 190.46-47 (Sept. 2001), pp. 6183–6200.

[306] N. Sukumar, J. Dolbow, and N. Moës. “Extended finite element method in computational fracture mechanics: a retrospective examination”. In: *International Journal of Fracture* 196.1-2 (2015), pp. 189–206.

[307] N. Sukumar and J. Prévost. “Modeling quasi-static crack growth with the extended finite element method Part I: Computer implementation”. In: *International journal of solids and structures* 40.26 (2003), pp. 7513–7537.

[308] N. Sukumar et al. “Extended finite element method for three-dimensional crack modelling”. In: *International Journal for Numerical Methods in Engineering* 48.November 1999 (2000), pp. 1549–1570.

[309] N. Sukumar et al. “Three-dimensional non-planar crack growth by a coupled extended finite element and fast marching method”. In: *International Journal for Numerical Methods in Engineering* 76.5 (2008), pp. 727–748.

[310] D. Sulsky, Z. Chen, and H. L. Schreyer. “A particle method for history-dependent materials”. In: *Computer Methods in Applied Mechanics and Engineering* 118.1-2 (1994), pp. 179–196.

[311] H. Sun, H. Waisman, and R. Betti. “Nondestructive identification of multiple flaws using XFEM and a topologically adapting artificial bee colony algorithm: XFEM-EABC ALGORITHM FOR MULTIPLE FLAWS DETECTION”. en. In: *International Journal for Numerical Methods in Engineering* 95.10 (Sept. 2013), pp. 871–900.

[312] O. J. Sutton. “The virtual element method in 50 lines of MATLAB”. en. In: *Numerical Algorithms* 75.4 (Aug. 2017), pp. 1141–1159.

[313] D. Sutula and S. Bordas. “Minimum energy multiple crack propagation. Part II: Discrete Solution with XFEM.” In: *Engineering Fracture Mechanics* (2017).

[314] D. Sutula and S. Bordas. “Minimum energy multiple crack propagation. Part III: XFEM computer implementation and applications.” In: *Engineering Fracture Mechanics* (2017).

[315] D. Sutula et al. “Minimum energy multiple crack propagation. Part I: Theory and state of the art review”. In: *Engineering Fracture Mechanics* 191 (2018), pp. 205–224.

[316] A. Tabarraei and N. Sukumar. “Adaptive computations on conforming quadtree meshes”. en. In: *Finite Elements in Analysis and Design* 41.7-8 (Apr. 2005), pp. 686–702.

[317] C. Talischi et al. “PolyMesher: a general-purpose mesh generator for polygonal elements written in Matlab”. en. In: *Structural and Multidisciplinary Optimization* 45.3 (Mar. 2012), pp. 309–328.

[318] E. Tanné et al. “Crack nucleation in variational phase-field models of brittle fracture”. In: *Journal of the Mechanics and Physics of Solids* 110 (2018), pp. 80–99.

[319] J. Tarancón et al. “Enhanced blending elements for XFEM applied to linear elastic fracture mechanics”. In: *International Journal for Numerical Methods in Engineering* 77.July 2008 (2009), pp. 126–148.

[320] I. The MathWorks. *eig*. 2016. URL: `https://ch.mathworks.com/help/matlab/ref/eig.html` (visited on 12/01/2016).

[321] M. Tootkaboni and L. Graham-Brady. “A multi-scale spectral stochastic method for homogenization of multi-phase periodic composites with random material properties”. en. In: *International Journal for Numerical Methods in Engineering* (2010), n/a–n/a.

[322] S. Torabi and J. Lowengrub. “Simulating interfacial anisotropy in thin-film growth using an extended Cahn-Hilliard model”. In: *Physical Review E* 85.4 (2012), p. 041603.

[323] S. P. Triantafyllou and E. N. Chatzi. “A hysteretic multiscale formulation for nonlinear dynamic analysis of composite materials”. en. In: *Computational Mechanics* 54.3 (Sept. 2014), pp. 763–787.

[324] S. P. Triantafyllou and V. K. Koumousis. “Hysteretic Finite Elements for the Nonlinear Static and Dynamic Analysis of Structures”. en. In: *Journal of Engineering Mechanics* 140.6 (June 2014), p. 04014025.

[325] S. P. Triantafyllou and E. N. Chatzi. “A hysteretic multiscale formulation for validating computational models of heterogeneous structures”. en. In: *The Journal of Strain Analysis for Engineering Design* 51.1 (Jan. 2016), pp. 46–62.

[326] W. S. Ventu. *Boundary element method in geomechanics*. eng. Lecture Notes in engineering 4. Berlin: Springer, 1983.

[327] G. Ventura. “On the elimination of quadrature subcells for discontinuous functions in the eXtended Finite-Element Method”. In: *International Journal for Numerical Methods in Engineering* 66.5 (2006), pp. 761–795.

[328] G. Ventura, E. Budyn, and T. Belytschko. “Vector level sets for description of propagating cracks in finite elements”. In: *International Journal for Numerical Methods in Engineering* 58.10 (2003), pp. 1571–1592.

[329] G. Ventura, R. Gracie, and T. Belytschko. “Fast integration and weight function blending in the extended finite element method”. In: *International journal for numerical methods in engineering* 77.July 2008 (2009), pp. 1–29.

[330] G. Ventura and C. Tesei. “Stabilized X-FEM for Heaviside and nonlinear enrichments”. In: *Advances in Discretization Methods*. Springer, 2016, pp. 209–228.

[331] G. Ventura and E. Benvenuti. “Equivalent polynomials for quadrature in Heaviside function enriched elements”. In: *International Journal for Numerical Methods in Engineering* 102.3-4 (2015), pp. 688–710.

[332] C. V. Verhoosel and R. de Borst. “A phase-field model for cohesive fracture”. In: *International Journal for numerical methods in Engineering* 96.1 (2013), pp. 43–62.

[333] J. Vignollet et al. “Phase-field models for brittle and cohesive fracture”. In: *Meccanica* 49.11 (2014), pp. 2587–2601.

[334] E. L. Wachspress. “A Rational Basis for Function Approximation”. en. In: *IMA Journal of Applied Mathematics* 8.1 (1971), pp. 57–68.

[335] H. Waisman, E. Chatzi, and A. W. Smyth. “Detection and quantification of flaws in structures by the extended finite element method and genetic algorithms”. en. In: *International Journal for Numerical Methods in Engineering* (2009), n/a–n/a.

[336] S. Wang, E. d. Sturler, and G. H. Paulino. “Large-scale topology optimization using preconditioned Krylov subspace methods with recycling”. en. In: *International Journal for Numerical Methods in Engineering* 69.12 (Mar. 2007), pp. 2441–2468.

[337] S. Wang, E. de Sturler, and G. H. Paulino. “Dynamic Adaptive Mesh Refinement for Topology Optimization”. In: *arXiv:1009.4975 [cs, math]* (Sept. 2010). arXiv: 1009.4975.

[338] Y. Wang and H. Waisman. “An arc-length method for controlled cohesive crack propagation using high-order XFEM and Irwin’s crack closure integral”. In: *Engineering Fracture Mechanics* (2018).

[339] Y. Wang et al. “XFEM with high-order material-dependent enrichment functions for stress intensity factors calculation of interface cracks using Irwin’s crack closure integral”. en. In: *Engineering Fracture Mechanics* 178 (June 2017), pp. 148–168.

[340] Z. A. Wilson and C. M. Landis. “Phase-field modeling of hydraulic fracture”. In: *Journal of the Mechanics and Physics of Solids* 96 (2016), pp. 264–290.

[341] B. J. Winkler. *Traglastuntersuchungen von unbewehrten und bewehrten Betonstrukturen auf der Grundlage eines objektiven Werkstoffgesetzes für Beton*. Innsbruck University Press, 2001.

[342] J. P. Wolf. *The scaled boundary finite element method*. Chichester, West Sussex, England ; Hoboken, NJ, USA: J. Wiley, 2003.

[343] J. P. Wolf and C. Song. "Consistent infinitesimal finite-element cell method: in-plane motion". en. In: *Computer Methods in Applied Mechanics and Engineering* 123.1-4 (June 1995), pp. 355–370.

[344] J. P. Wolf and C. Song. *Finite-element modelling of unbounded media*. Chichester, England ; New York: Wiley, 1996.

[345] J.-Y. Wu. "A unified phase-field theory for the mechanics of damage and quasi-brittle failure". In: *Journal of the Mechanics and Physics of Solids* 103 (2017), pp. 72–99.

[346] J.-Y. Wu and V. P. Nguyen. "A length scale insensitive phase-field damage model for brittle fracture". In: *Journal of the Mechanics and Physics of Solids* (2018).

[347] J.-Y. Wu et al. "Computational modeling of localized failure in solids: XFEM vs PF-CZM". In: *Computer Methods in Applied Mechanics and Engineering* 345 (2019), pp. 618–643.

[348] J.-Y. Wu et al. "Phase field modeling of fracture". In: *Advances in Applied Mechancis: Multi-scale Theory and Computation* 52 (2018).

[349] T. Wu and L. D. Lorenzis. "A phase-field approach to fracture coupled with diffusion". In: *Computer Methods in Applied Mechanics and Engineering* 312 (2016). Phase Field Approaches to Fracture, pp. 196–223.

[350] Q. Xiao and B. Karihaloo. "Direct evaluation of accurate coefficients of the linear elastic crack tip asymptotic field". In: *Fatigue & Fracture of Engineering Materials & Structures* 26.November 2002 (2003), pp. 719–729.

[351] X.-P. Xu and A. Needleman. "Numerical simulations of fast crack growth in brittle solids". In: *Journal of the Mechanics and Physics of Solids* 42.9 (1994), pp. 1397–1434.

[352] Z. J. Yang and A. J. Deeks. "Modelling cohesive crack growth using a two-step finite element-scaled boundary finite element coupled method". en. In: *International Journal of Fracture* 143.4 (June 2007), pp. 333–354.

[353] Z. Yang and A. Deeks. "Fully-automatic modelling of cohesive crack growth using a finite element–scaled boundary finite element coupled method". en. In: *Engineering Fracture Mechanics* 74.16 (Nov. 2007), pp. 2547–2573.

[354] Z. Yang. "Fully automatic modelling of mixed-mode crack propagation using scaled boundary finite element method". en. In: *Engineering Fracture Mechanics* 73.12 (Aug. 2006), pp. 1711–1731.

[355] Q. Yu and J. Fish. "Multiscale asymptotic homogenization for multiphysics problems with multiple spatial and temporal scales: a coupled thermo-viscoelastic example problem". en. In: *International Journal of Solids and Structures* 39.26 (Dec. 2002), pp. 6429–6452.

[356] A. Zamani, R. Gracie, and M. Eslami. "Cohesive and non-cohesive fracture by higher-order enrichment of XFEM". In: *International Journal for ...* 90.January (2012), pp. 452–483.

[357] H. Zhang, Z. Fu, and J. Wu. "Coupling multiscale finite element method for consolidation analysis of heterogeneous saturated porous media". en. In: *Advances in Water Resources* 32.2 (Feb. 2009), pp. 268–279.

[358] H.-W. Zhang et al. "Extended multiscale finite element method for mechanical analysis of heterogeneous materials". en. In: *Acta Mechanica Sinica* 26.6 (Dec. 2010), pp. 899–920.

[359] Q. Zhang, U. Banerjee, and I. Babuška. "Higher order stable generalized finite element method". In: *Numerische Mathematik* 128.1 (2014), pp. 1–29.

[360] Z. Zhang et al. "Nonlocal damage modelling by the scaled boundary finite element method". en. In: *Engineering Analysis with Boundary Elements* 99 (Feb. 2019), pp. 29–45.

[361] Z. Zhang et al. "Three-dimensional damage analysis by the scaled boundary finite element method". en. In: *Computers & Structures* 206 (Aug. 2018), pp. 1–17.

[362] M. Zhou and G. Rozvany. "The COC algorithm, Part II: Topological, geometrical and generalized shape optimization". en. In: *Computer Methods in Applied Mechanics and Engineering* 89.1-3 (Aug. 1991), pp. 309–336.

[363] S. Zhou, X. Zhuang, and T. Rabczuk. “Phase-field modeling of fluid-driven dynamic cracking in porous media”. In: *Computer Methods in Applied Mechanics and Engineering* (2019).

[364] C. Zhu, G. Lin, and J. Li. “Modelling cohesive crack growth in concrete beams using scaled boundary finite element method based on super-element remeshing technique”. en. In: *Computers & Structures* 121 (May 2013), pp. 76–86.

[365] G. Zi and T. Belytschko. “New crack-tip elements for XFEM and applications to cohesive cracks”. In: *International Journal for Numerical Methods in Engineering* 57.15 (2003), pp. 2221–2240.

[366] O. C. Zienkiewicz, R. L. Taylor, and J. Z. Zhu. *The finite element method: its basis and fundamentals*. Seventh edition. Amsterdam: Elsevier, Butterworth-Heinemann, 2013.

[367] O. C. Zienkiewicz and J. Z. Zhu. “The superconvergent patch recovery anda posteriori error estimates. Part 1: The recovery technique”. en. In: *International Journal for Numerical Methods in Engineering* 33.7 (May 1992), pp. 1331–1364.

[368] O. C. Zienkiewicz and J. Z. Zhu. “The superconvergent patch recovery anda posteriori error estimates. Part 2: Error estimates and adaptivity”. en. In: *International Journal for Numerical Methods in Engineering* 33.7 (May 1992), pp. 1365–1382.